Energy Extraction from a Steady Flow Using Vortex Induced Vibration

by
Kamaldev Raghavan

A dissertation submitted in partial fulfillment
of the requirements for the degree of
Doctor of Philosophy
(Naval Architecture and Marine Engineering)
in The University of Michigan
2007

Doctoral Committee:

Professor Michael. M. Bernitsas, Chair
Professor Michael. G. Parsons
Professor Armin. W. Troesch
Assistant Professor Bogdan. I. Epureanu

"It is the nature of great research that one cannot predict what basic new insights about the workings of nature will emerge, nor can one dream of what practical applications will follow."

- John Rigden

Dedication

To my parents (Achchan and Amma), who have constantly provided the unconditional love. It is their belief in me that made me to accomplish this work.

Acknowledgements

I would like to express my deep and sincere gratitude to my supervisor, Professor Michael M Bernitsas. His wide knowledge and his logical way of thinking have been of great value to me. His understanding, encouragement to free thinking and personal guidance has provided a good basis for the present thesis. Even though he has, in my opinion, a very hectic schedule, always found adequate time to oversee my research and to share his knowledge and expertise with me.

I wish to express my sincere gratitude to Professor Armin. W. Troesch., for his constant encouragement to do a Ph.D during my master's study. Without his encouragement during my master's study I wouldn't have made this leap.

I appreciate the advice of my dissertation committee members, Professor. Michael. G. Parsons, Assistant Professor. Bogdan. I. Epureanu, for their critical comments, which enabled me to notice the weaknesses of my Dissertation and make the necessary improvements according to their comments.

I would like to thank Dr. Owen H Oakley and Mr. Yiannis Constandinies for their constructive discussions on my research topic during my internship at Chevron.

During this work I have collaborated with many colleagues for whom I have great regard, and I wish to extend my warmest thanks to Ms. Elisha Maloney-Hahn Garcia, Mr. Dimitri Maroulis, Mr. Gaetan Duchene, Mr. Yaron Bensimon, Mr. Jim Chang, Ms. Rebecca Macklem, Mr. Nathan Hill, and Mr. Kazuya Sasahara. I would like to thank Mr. James Gerard Bretl (Jim), Ms. Elisha Maloney-Hahn Garcia, and Mr. Varun Raghunathan for taking time to proof read my chapters and the constructive review they provided.

My friends at University of Michigan made my graduate school life a memorable experience (in a good way). In no particular order, some of them are Mr. Madhusudhan Chellappa, Mr. Nagraj Kashyap, Mr. Magesh Jayapandian, Mr. Walid El Asmar, Mr. Atin Tandon, Mr. Oscar Tascon, Mr. Jingting Guo, Mr. Junghoon Hyun, Mr. Khalid, Ms. Rong Wu, Ms. Jing Ying, Ms. Ellie Nick, Ms. Yaning Li, Mr. Taemin Earmme, Mr. Javid Moraveji, Mr. Sina Aragh and Mr. Sai Mohan Majhi. I have learnt a great deal from them. My friends not from the University of Michigan but still who have provided constant support and encouragement are Mr. Basil Theckumpurath, Mr. Muneerudheen Neduvanchery, Mr Aadil Adam Mohammed, Mr. Suresh Rajendran, and Mr. Ramesh Raghavan.

The most important of all, I would like to thank my closest friend Xiaoyan Yan for her constant encouragement and support during my research.

None of this would have been possible without the love and patience of my parents, my sister and my brother in law.

I would like to thank The Link foundation and the department of Naval Architecture and Marine Engineering, University of Michigan, for their fellowships during my graduate studies.

Table of Contents

List of Figures

List of Tables

Glossary

Roman symbols

A	Oscillation amplitude
A_{Max}	Maximum oscillation amplitude
A^*	Nondimensional oscillation amplitude
A^*_{Max}	Nondimensional maximum oscillation amplitude
b	Breadth of the surface roughness strips
C_D	Drag coefficient
C_p	Pressure coefficient
C_{pb}	Base pressure coefficient
Ca	Potential added mass coefficient of a cylinder ($C_a = 1$)
C_L	Mean lift coefficient
$c_y(t)$	$\frac{F_{transverse} \text{ in phase with velocity}}{\frac{1}{2}\rho U^2 DL}$
C_L'	Fluctuating lift coefficient
c_{system}	From damping test with transmission disconnected
c_{tra}	From damping tests with transmission connected minus the c_{system}
c_{gen}	From damping tests with transmission and generator connected minus c_{tra} minus c_{system}
c_{harn}	From damping tests with transmission and generator connected minus c_{tra} minus c_{system} minus c_{gen}

c_{total}	$= c_{system} + c_{tra} + c_{gen} + c_{harn}$
D	Cylinder diameter
F_{fluid}	Fluid force (total)
F_L	Transverse lift force (total)
F_L'	Root-mean-square lift fluctuations (total)
$f_{n,air}$	$\frac{1}{2\pi}\sqrt{\frac{k}{m_{osc}}}$, system natural frequency in air
$f_{n,water}$	$\frac{1}{2\pi}\sqrt{\frac{k}{(m_{osc}+m_a)}}$, system natural frequency in water
$f_{V,form}$	Vortex formation frequency
f_{osc}	Oscillating cylinder frequency
f_{St}	$\frac{St \cdot U}{D}$, fixed cylinder shedding frequency, St = 0.2
f_{fluid}	Fluid force frequency
$f_{V,mode}$	Frequency of vortex mode
f^*_{index}	$\frac{f_{index}}{f_{n,water}}$
Fr_D	Froude number based on diameter
Fr_h	Froude number based on gap height
G	Gap between cylinder and the bottom boundary
h	Gap between cylinder and the free surface
i	Imaginary number
K_{spring}	Total system elasticity (stiffness)
k	Sandpaper grit size
L	Cylinder length
L_f	Vortex formation length
L_r	Roughness spanwise segment length
m_{osc}	Oscillating mass including one third of spring mass.
m_d	$\frac{\pi}{4}\rho_w D^2 L$, fluid mass displaced by the cylinder
m_a	$C_a m_d$, added mass of the cylinder

m^*	$\frac{m_{osc}}{m_d}$, nondimensional mass, mass ratio
P	Sandpaper thickness (including roughness size)
P_{VIVACE}	Power harnessed by VIVACE
$P_{UL\text{-}VIVACE}$	Upper limit of Power that can be harnessed by VIVACE
p_1	Horizontal distance between cylinders in a VIVACE bank
R_{arm}	Generator armature (internal) resistance
R_L	Load resistance from the resistor
Re	Reynolds number based on the diameter
Re_x	Reynolds number based on the distance from the entrance of the channel
Re_k	Reynolds number of the roughness element
Re_{k+P}	Reynolds number of the roughness including the sand paper thickness
S_G	Skop-Griffin parameter, $2\pi^3 St^2 (m^* \zeta_a)$
St	Strouhal number
t	Time
t_1	Vertical distance between cylinders in a VIVACE bank
U	Free-stream fluid velocity
U^*	$\frac{U}{f_{n,water} D}$, reduced velocity
$U^*_{fn,air}$	$\frac{U}{f_{n,air} D}$, reduced velocity
U^*_{true}	$\frac{U}{f_{osc} D}$, true reduced velocity
u'	Fluctuating wake velocity
V_{load}	Voltage at the load resistor
x_1	Distance from the entrance of the channel
y	Displacement
$\dot{y}$	Velocity
$\ddot{y}$	Acceleration
y^*	$\frac{y}{D}$, nondimensional displacement

$y^*_{\max}$	$\frac{y_{\max}}{D}$, nondimensional maximum displacement
y^*_{rms}	$\frac{y_{rms}}{D}$, nondimensional RMS displacement
$\dot{y}^*$	Nondimensional velocity
$\ddot{y}^*$	Nondimensional acceleration

Greek symbols

ζ	$\frac{c}{2\sqrt{k\ m}}$, damping coefficient in air
ζ_{index}	$\frac{c_{index}}{2\sqrt{k\left(m+C_a m_d\right)}}$, generalized damping coefficient
δ_b	Boundary layer thickness
δ^*	Displacement thickness
θ^*	Momentum thickness
μ	Fluid dynamic viscosity
ν	Fluid kinematic viscosity
ρ_{fluid}	Fluid density
ω_{index}	$\frac{1}{2\pi f_{index}}$,
λ_z	Correlation length
α	Product of sum of mass ratio and added mass coefficient with damping coefficient $(m^*+C_a)\zeta$
α_{bu}	Upper initial angle of the roughness strip
α_{bl}	Lower initial angle of the roughness strip
θ_u	Upper initial minus final angle of the roughness strip
θ_l	Lower initial minus final angle of the roughness strip

Abstract

Ocean renewable energy is abundant and worldwide available in the form of waves, currents, tides, thermal gradient, and salinity gradient. Several pilot and patented devices exist to harness ocean energy. They face challenges related to environmental compatibility, low density, obtrusion to coastal property, grid compatibility, and high load threshold for efficient operation.

The **VIVACE Converter** (Vortex Induced Vibration Aquatic Clean Energy) is introduced (patent pending) to extract energy from a steady flow using Vortex Induced Vibrations (VIV). In our early experiments on energy harnessing using VIVACE, energy density of $51W/m^3$ was achieved for U = 0.84 m/s = 1.63 knots which is 3-10 times higher than other current energy converter and 2-5 times higher than wave energy converters. Based on test measurements, an upper limit of $86W/m^3$ was calculated. The range of synchronization and the amplitude of oscillation were reduced at the expense of energy generation. Scalability of VIV and the VIVACE Converter makes it possible to harness energy even from low current speeds where turbines are not viable financially.

Experiments were performed in the TrSL3 regime (2×10^4- 4×10^4 < Re < 1×10^5- 2×10^5). This regime had not been explored before. A **strong dependence of VIV on Reynolds number** was observed. In the TrSL3 regime, amplitude of oscillation of 1.9 diameters was achieved for a smooth cylinder in VIV even with high damping imposed. Our VIV tests fall in the tail-end of the Griffin-plot. Amplitudes achieved and maintained are 2-3 times higher than previously measured data.

Our experiments showed that proximity of the VIVACE Converter to **free surface** reduces the range of synchronization of VIV and the amplitude ratio. A strong dependence of VIV response on Froude number was shown by further model tests.

Proximity to free surface introduced hysteresis due to flipping between wake states. At low gap ratio hysterisis was observed at both ends of the synchronization range. For moderate gap ratio hysterisis was observed at the end of synchronization range. At a critical value of the Froude number, VIV is suppressed and it is attributed to change in stability of vortex shedding. At high Froude numbers and low gap ratios, the vortex formation transforms from absolute to convective instability.

Our experiments showed that proximity of the VIVACE Converter to **bottom boundary** reduced the amplitude of oscillation for intermediate gap ratio ($0.65 < G/D < 3.0$), but the range of synchronization remained unaffected. For low gap ratios ($G/D < 0.65$), the positive amplitude of oscillation was higher than the VIV of a cylinder in unbounded fluid. The positive amplitude of oscillation reached a value of 2 diameters.

Surface roughness of predetermined distribution and magnitude was added to the surface of the VIVACE cylinder in VIV. The added roughness, when designed and implemented appropriately, affects in a predetermined way the boundary layer, the separation of the boundary layer, the level of turbulence, the wake, the drag and lift forces, and consequently the VIV (Two patents pending). In our experiments properly designed and applied surface roughness increased the range of synchronization and amplitude ratio (A/D) of VIV. In our experiments, amplitude of oscillation of 2.7 diameters was achieved and the range of synchronization opened up to the point that it exceeded the Low Turbulence Free Surface Water (LTFSW) Channel capability.

Chapter 1

VIVACE: A NEW CONCEPT IN OCEAN ENERGY CONVERSION

1.1. INTRODUCTION

Ocean energy comes in five forms: waves, currents, tides, thermal gradient and salinity gradients. It can provide an abundant supply of clean and renewable energy (Pontes and Falcao 2001; Schiller and Linke 1933). Several studies attest to the abundance of ocean energy in general (WEC 2001) and more specifically to ocean current energy (Pontes and Falcao 2001). The VIVACE (Vortex Induced Vibration Aquatic Clean Energy) Converter introduced in this dissertation is patented by Bernitsas and Raghavan (2005a; 2005b) to convert ocean/river current energy to electricity.

The VIVACE Converter uses Vortex Induced Vibrations (VIV) for the first time to generate energy successfully and with high energy density from a fluid flow. VIV normally cause tremendous damage to aero, civil, mechanical, marine, offshore, and nuclear engineering structures. Ever since Leonardo da Vinci first observed VIV, circa 1500AD, in the form of "Aeolian Tones," engineers have been trying to spoil vortex shedding and suppress VIV to prevent damage to equipment and structures. Further, Von Kármán at Cal Tech proved that the Tacoma Narrows bridge collapse in 1940 was due to VIV. This fluid-structure interaction phenomenon occurs due to nonlinear resonance of cylinders (or spheres) through vortex shedding lock-in. VIV is also called synchronization between vortex shedding and cylinder (or sphere) oscillations. In this

dissertation, the terms VIV, synchronization, vortex shedding lock-in, and nonlinear resonance are used to refer to the same phenomenon.

The VIVACE Converter design is based on the very simple idea of enhancing rather than spoiling vortex shedding and maximizing under significant damping rather than suppressing Vortex Induced Vibrations (VIV), and harnessing rather than mitigating VIV energy. None of the hundreds of known or patented (Pontes and Falcao 2001; USPTO USPTO; WaveNet 2003) devices which can generate significant usable energy is based on this concept. VIVACE is scalable and can extract energy from currents of velocities from 0.5 to 5 knots and above (Bernitsas and Raghavan 2005a). It is a robust system in the sense of low sensitivity to environmental conditions because vortex shedding synchronization occurs over a broad and continuous range of frequencies, not just at natural frequencies as in linear resonance. For stationary cylinders, the Kármán Street (stream of generated vortices) occurs over very broad ranges of Reynolds (Re) number. Only in two transition regions, VIV is suppressed. Similarly, the Kármán Street may occur over the same Reynolds number ranges.

1.2. LITERATURE REVIEW

Three areas of the literature are relevant to this dissertation: ocean energy conversion, Vortex Induced Vibrations, and the VIVACE Converter. The first two are very extensive and only a limited overview follows as it relates to defining challenges in designing the VIVACE Converter.

1.2.1. Ocean energy conversion

Due to public pressure, the California Energy Commission (CEC) and the Department of Energy (DOE) of the USA have defined general requirements, which ocean energy conversion devices must satisfy to be considered for license to operate in the USA. Those are: (1) have high energy density, (2) be unobstructive to navigation, (3) not diminish the value of expensive coastal real estate, (4) be friendly to marine life and the environment, (5) have low maintenance, (6) be robust, (7) meet life cycle cost targets, and (8) have a minimum life of 10-20 years.

The challenge of meeting all of these requirements has been the focus of more than 40 years of worldwide efforts – particularly in Europe and Japan and to a lesser extent in the USA (Pontes and Falcao 2001; Thorpe 1998; WaveNet 2003). Numerous devices have been designed and patented and several pilot devices have been launched (Pontes and Falcao 2001; Technomare 1996; WMCE 2003). A universally acceptable converter, however, has not yet been developed (Thorpe 1998; WaveNet 2003).

There are five sources of ocean energy: waves, currents, tides, thermal gradient, and salinity gradient. Some examples of how ocean energy converters fail to satisfy some of the CEC/DOE criteria follow:

(i) Converters based on surface oscillation, such as water column, buoy, flap, or pendulum (Pontes and Falcao 2001; WaveNet 2003; WMCE 2003), have high energy output only in a very narrow band of wave frequencies near resonance. At any particular location, waves are random allowing for a small window of optimal performance. In addition, waves occasionally apply extreme loads to structures.

(ii) Converters of wind or tidal current energy (turbines, watermills) can extract energy proportionally to their projected surface at efficiency of 15-30% (Website: Marine turbines; Technomare 1996) and only for currents stronger that 2m/sec (~4 knots), below which they do not function efficiently (Website: Marine turbines).

(iii) Tidal energy converters require at least a 5m head, and are very large and as obtrusive as water dams. They also require a 5-7 year construction period and significant initial capital cost (Website: Marine turbines).

(iv) Most of the converters operate on the surface and near shore and occupy valuable coastal real estate.

(v) Converters such as watermills, turbines, or tidal dams disturb marine life.

1.2.2. Vortex induced vibrations

The literature on Vortex Induced Vibrations of circular cylinders is very extensive and new knowledge is developed continuously using experiments (Carberry 2002; Gharib 1999; Govardhan 2000; Khalak and Williamson 1996; Klamo 2006; Sumer and Fredsoe 1997), field tests (Sumer and Fredsoe 1997), and numerical simulations (Sumer and

Fredsoe 1997; Williamson and Govardhan 2004). At this point in time, many of the aspects of VIV are understood well or the next research steps are well defined. Some new phenomena though still are being revealed as more research is conducted. Separate reviews of literature on different aspects of VIV of circular cylinders and vortex shedding around circular cylinders that are pertinent to each chapter in this dissertation are presented more extensively in those. A quick introductory overview of some aspects of VIV, which pertains to all the forthcoming chapters and to performance of the VIVACE Converter, is presented next.

In its simplest form, a modulo of the VIVACE Converter, consists of a rigid circular cylinder mounted on elastic springs and connected to a Power Take – Off (PTO) system via a transmission mechanism. Accordingly, literature related to free vibrations of elastically supported rigid cylinders; forced vibrations of such structures; with cylinders having one or two degrees of freedom (Govardhan 2000; Khalak and Williamson 1996; Triantafyllou et al. 2006; Williamson and Govardhan 2004; Williamson and Jauvtis 2004) is relevant.

For a VIVACE modulo, the primary response mode is transverse to the flow. In-line oscillations of smaller magnitude are also observed in VIV and strengthen transverse oscillations (Jauvtis and Williamson 2004). As the flow velocity U increases, lock-in for a high mass ratio system is reached when the vortex formation frequency $f_{V,form}$ is close enough to the body's natural frequency $f_{n,water}$ as seen in Figure 1.1**.** Lock-in or vortex synchronization occurs over a broad range of the reduced velocity factor U^* defined as

$$U^* = \frac{U}{f_{n,water} D}. \tag{1.1}$$

The mass ratio m^* is defined as the total oscillating mass of the cylinder in VIV, including with all oscillating appendages and 1/3 of the spring mass, divided by the displaced fluid mass m_d

$$m^* = \frac{m_{osc}}{m_d} \quad , \tag{1.2}$$

where

$$m_d = \frac{\pi}{4}\rho_w \mathrm{D}^2\mathrm{L} \quad , \tag{1.3}$$

D is the cylinder diameter, L is the cylinder length, and ρ_w is the water density, and the rest of the symbols are defined in Table 1.1. That is, for high m* values, up until lock-in occurs $f_{V,form} = f_{St}$. When synchronization occurs at U* of about 6 in Figure 1 (for m* = 8.63), $f_{V,mode}$ appears and becomes equal to $f_{osc,}$ the frequency of oscillation of the cylinder. The difference between $f_{V,form}$ and $f_{V,mode}$ is explained later in this Section under "wake structures".

The phenomenon of lock-in or synchronization traditionally means that the ratio $f^*_{osc} = \frac{f_{osc}}{f_{n,water}}$ remains close to unity, for high mass ratio (Feng 1968; Sumer and Fredsoe 1997; Williamson and Govardhan 2004). For low mass ratio, the body oscillates at a distinctly higher frequency as seen in Figure 1.1 and the range of synchronization opens up. Experimentally, the departure of $f^*_{osc} = f_{osc}/f_{n,water}$ from unity, through the lock-in regime, was shown in (Sumer and Fredsoe 1997) and more recently was reported in (Brankovic and Bearman 2006; Govardhan and Williamson 2002; Williamson and Govardhan 2004). Synchronization is defined as the "matching of the frequency of the periodic wake vortex mode with the body oscillation frequency" (Khalak and Williamson 1999) or $f_{V,mode}=f_{osc}$. Correspondingly, the fluid force frequency f_{fluid} must match the oscillation frequency, which is the definition of lock-in used by Sarpkaya (Sarpkaya 1995; Sarpkaya 2004). The fluid frequency consists of a spectrum with $f_{V,mode}=f_{osc}$ as the dominant frequency at lock-in. The rest of the components are explained under "wake structures".

The next important issue is the cylinder's amplitude of oscillation in VIV. In Figure 1.2**,** Feng's minimum damping case and Khalak and Williamson's case are compared. In Figure 1.2 it is apparent that in Feng's case there are only two amplitude branches, namely the "initial" branch and the "lower" branch (Williamson and Govardhan 2004) with a hysteretic transition between branches. The mass ratio m* in Feng's case is very large because the experiments were conducted in air (m* ≈ 250). In the case of Khalak and Williamson (Khalak and Williamson 1997b), we see three branches with higher amplitudes namely the "initial" branch, the "upper" branch, and the

"lower" branch. In the Khalak and Williamson case m* = 2.4. There is a hysteretic transition between initial and upper branches and intermittency between upper and lower branches for the low mass ratio case. In recent work, however, much higher amplitudes of oscillation have been observed for higher Reynolds numbers.

m_{osc}	Oscillating mass including one third of spring mass.	m_d	$\frac{\pi}{4}\rho_w \mathrm{D}^2\mathrm{L}$	c_{system}	From damping test with transmission disconnected
m^*	m_{osc}/m_d	m_a	$C_a m_d$	c_{tra}	From damping tests with transmission connected minus the c_{system}
y^*	y/D	$y^*_{\max}$	$y_{\max}/D$	c_{total}	$= c_{system} + c_{tra} + c_{gen} + c_{harn}$
y^*_{rms}	y_{rms}/D	$f_{n,water}$	$\frac{1}{2\pi}\sqrt{\frac{K_{spring}}{(m+m_a)}}$	c_{gen}	From damping tests with transmission and generator connected minus c_{tra} minus c_{system}
f_{St}	$\frac{St \cdot U}{D}$	$f_{V,form}$	Vortex formation frequency	c_{harn}	From damping tests with transmission and generator connected minus c_{tra} minus c_{system} minus c_{gen}
f_{fluid}	Fluid force frequency	f_{osc}	Oscillating cylinder frequency	ζ_{index}	$\frac{c_{index}}{2\sqrt{K_{spring}\left(m + C_a m_d\right)}}$
$f_{V,mode}$	Frequency of vortex mode	f^*_{index}	$f_{index}/f_{n,water}$	$\mathrm{S_G}$	$2\pi^3 St^2 (m^* \zeta_a)$
ω_{index}	$\frac{1}{2\pi f_{index}} = \frac{T_{index}}{2\pi}$	T_{index}	$1/f_{index}$	$c_y(t)$	$\frac{\mathrm{F_{transverse}\ in\ phase\ with\ velocity}}{\frac{1}{2}\rho U^2 DL}$
U^*	$\frac{U}{f_{n,water} D}$				

Table 1.1. Definition of dimensional and dimensionless variables for the VIVACE Converter.

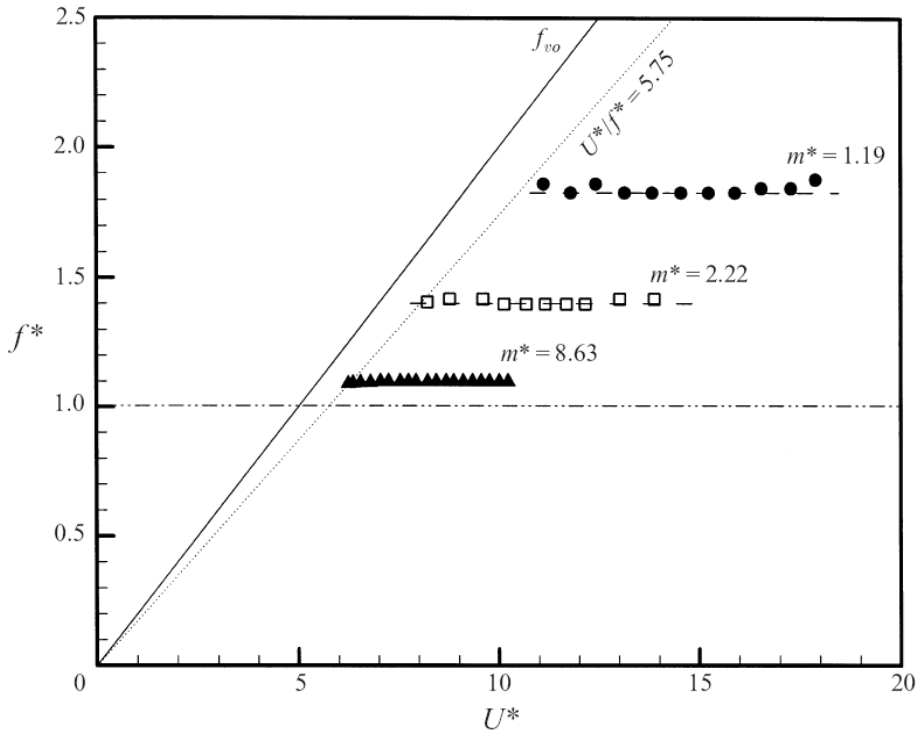

Figure 1.1. Lower branch frequency response for different mass ratio vs. varying U*. [Reproduced from Govardhan (2000) here $f^* = f^*_{osc}$].

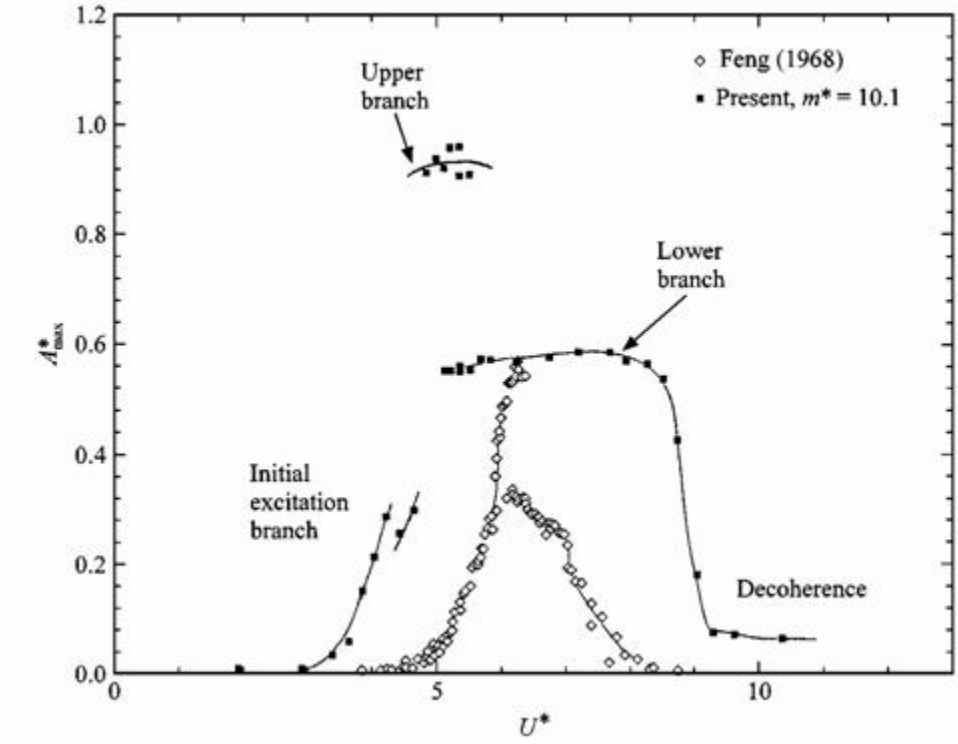

Figure 1.2. Amplitude of oscillation Feng's (1968) for experiments in air by Feng and experiments in water by Khalak and Williamson (1999).

In recent papers on free VIV, wake structures that are different from the classical Kármán vortex street have been reported (Govardhan and Williamson 1999; Jauvtis and Williamson 2003; Williamson 1985; Williamson and Govardhan 2004; Williamson and Roshko 1988). In chapter 7 of this dissertation, wake structures comprising of four vortices are discussed and these were not seen before by previous researchers. Wake structures that can be induced by the body motion are explained below. The wake-mode terminology was introduced by Williamson and his associates (Govardhan and Williamson 1999; Jauvtis and Williamson 2003; Williamson 1985; Williamson and Govardhan 2004; Williamson and Roshko 1988):

(a) The 2S mode: Two single vortices shed per cylinder oscillation cycle of period T_{osc}. This is like the classical Kármán street. The frequency of vortex formation $f_{V,form}$ is equal to $f_{osc}= 1/ T_{osc}$. The frequency of vortex wake-mode $f_{V,mode}$ is also equal to f_{osc}. Finally, the fluid forcing frequency f_{fluid} is also equal to $f_{V,form}$ and f_{osc}.

(b) The 2P mode: Two pairs of vortices shed per cylinder oscillation cycle of period T_{osc}. The frequency of vortex wake-mode $f_{V,mode}$ is always equal to f_{osc}. The frequency of vortex formation $f_{V,form}=2\times f_{V,mode}$. Finally, the fluid forcing frequency f_{fluid} has a major component at $f_{osc}= f_{V,mode}$ and a secondary one at $2\times f_{V,mode}$.

(c) The P+S mode: One vortex pair and a single vortex shed per cylinder oscillation cycle of period T_{osc}. The frequency of vortex wake-mode $f_{V,mode}$ is always equal to f_{osc}. The frequency of vortex formation $f_{V,form}=3/2\times f_{V,mode}$. Finally, the fluid forcing frequency f_{fluid} has a major component at $f_{osc}= f_{V,mode}$ and a diminished secondary one at $2\times f_{V,mode}$ and another diminished one at $3\times f_{V,mode}$.

(d) The 2T mode: Three vortex pairs shed per cylinder oscillation cycle of period T_{osc}. The frequency of vortex wake-mode $f_{V,mode}$ is always equal to f_{osc}. The frequency of vortex formation $f_{V,form}=3\times f_{V,mode}$. Finally, the fluid forcing frequency f_{fluid} has a major component at $f_{osc}= f_{V,mode}$ and a secondary one at $3\times f_{V,mode}$.

(e) The 2Q mode: Four vortex pairs shed per cylinder oscillation cycle of period T_{osc}. The frequency of vortex wake-mode $f_{V,mode}$ is always equal to f_{osc}. The frequency of vortex formation $f_{V,form}=4\times f_{V,mode}$. Finally, the fluid forcing frequency f_{fluid} has a major component at $f_{osc}= f_{V,mode}$ and secondary ones at $2\times f_{V,mode}$, and $4\times f_{V,mode}$.

Brika and Laneville (1993), were the first to show evidence of the 2P vortex wake mode in free vibration of cable due to vortex shedding. The mode of vortex shedding clearly affects the amplitude of oscillation. An important issue to consider is that tests are typically performed with as small damping as possible. In the present work, damping is not small as a rather high value induced by the PTO system is mandatory for energy extraction (Ben Simon 2005; Bernitsas et al. 2006a).

The aspect ratio (L/D) of the cylinder in VIV is an important design parameter for the operation of VIVACE. It has been studied extensively (Norberg 1994; Szepessy and Bearman 1992). The aspect ratio as well as VIV have a major impact on the correlation length of the flow along the cylinder. Obviously, higher correlation length induces higher overall forces on the oscillating cylinder. In practice for VIVACE, we keep the aspect length around 20. High Reynolds numbers and end plate design also have an impact on the correlation length and the maximum lift (Bearman and Davies 1975; Norberg 1994; Stansby 1974; Szepessy and Bearman 1992). The wake properties depend on the aspect ratio of the cylinder (Norberg 1994; Williamson and Govardhan 2004)

Higher Reynolds number results in higher lift forces and amplitudes of oscillation (Govardhan and Williamson 2006). Most previously reported amplitudes of oscillation are between 0.54 and 1.13 cylinder diameters (Williamson and Govardhan 2004). Amplitude of oscillation of 1.9 diameters (Bernitsas et al. 2006a; 2006b; Raghavan et al. 2007b) in the smooth case and 2.7 for modified cylinders were observed in the present experiments.

Proximity of a cylinder mounted on springs to free surface and bottom affects VIV. Even though the VIVACE Converter operates fully submerged and not too close to the free surface so that it will not be obtrusive to navigation and visually unpleasant to valuable coastal real estate, tests have been conducted to ensure that the free surface impact on VIVACE can be assessed. Free surface would impact VIVACE in shallow water flows such as those in rivers. The free surface effect on VIV of cylinders is important because when the flow is bounded by a surface the topology of the wake and the forces on the cylinder can be significantly altered (Carberry 2002).

Finally, high damping is mandatory for energy extraction using VIVACE Converter. As it will become obvious in the Chapter 3, the design optimization process

requires that high VIV amplitude is maintained, under high damping, over a broad range of synchronization. The peak response amplitude $y_{\max}$ varies as a function of m^* and ζ the damping ratio. This point is discussed, concerning especially the product of $m^*\zeta$, in (Williamson and Govardhan 2004). In VIVACE, the generated power is maximized by adding damping to the system in the form of electrical resistance. Too much damping reduces the amplitude and may suppress VIV as shown in Griffin's plot (Govardhan and Williamson 2006; Williamson and Govardhan 2004). Increase in damping can be counteracted by decreasing the mass ratio m* and Reynolds number (Govardhan and Williamson 2006; Williamson and Govardhan 2004). In the review papers of Williamson and Sarpkaya (Sarpkaya 2004; Williamson and Govardhan 2004), it is mentioned that the product of $m^* \zeta$ is the parameter controlling the maximum amplitude of oscillation.

1.3. VIVACE CONVERTER

Even though the phenomenon of Vortex Induced Vibrations has been known since 1500AD, no device has ever been built to generate efficiently and at significant level electricity or other form of usable energy from a fluid flow using VIV. A patent by R. O. Clark (1999) was granted in 1999 based on a formula attributed to Rayleigh, which is similar to the Strouhal formula for St =0.2.

$$St = \frac{f_{St} D}{U} \tag{1.4}$$

Clark's design, however, will not likely work in a practical way as its design and way of operation suppresses VIV in a multitude of ways. Y. Yoshitake et al. (2004) generated miniscule amounts of energy as a byproduct of suppressing VIV of tower structures in airflow. The underlying concepts of VIVACE, design particulars, test results, dimensions for various scales of application, the principles of modularity and scaling, and some performance measures were revealed and are presented in Chapter 3.

1.3.1. VIVACE – Modeled as an elastically supported cylinder

This dissertation is focused on energy extraction using VIV. Accordingly, literature related to free vibrations of elastically supported rigid cylinders; forced

vibrations of such structures; with cylinders having one or two degrees of freedom (Jauvtis and Williamson 2002; 2003) is reviewed.

In this dissertation, an elastically mounted cylinder restrained to move transversely to the flow is considered. As the flow speed (U) increases, lock-in for high mass ratio system is reached when the vortex formation frequency (f_V) is close enough to the body's natural frequency (f_n) as seen in Figure 1.1.

The vortex-excited oscillations are accompanied by an increase in the vortex strength (Atsavapranee et al. 1998; Davies 1976) when the amplitude in the transverse direction exceeds a value of about 0.1 diameter. The threshold value is about 0.02D for the in-line oscillations (Okajima et al. 2002; Sainsbury and King 1971; Sugimoto et al. 2002). The vortex induced vibration leads to an increase of the correlation length of the vortex shedding process for free vibrating oscillating cylinder (Ferguson and Parkinson 1967; Koopmann 1967; Ramberg and Griffin 1976; Toebes 1969).

Feng (1968) noted that the jump in response amplitude was reflected by a significant jump in the phase of the pressure fluctuations relative to body motion. Zdravkovich (1982) showed that the jump in the phase is due to the shift in the timing of vortex shedding using visualizations. Ongoren and Rockwell (1988a; 1988b), Gu, Chyu and Rockwell (1994) confirmed the switch from forced vibrations at small $A^* = 0.2$, in the first study of this problem using PIV. Vortex switching phenomenon has also been studied using numerical simulations (Meneghini and Bearman, (1993; 1995); Lu and Dalton (1996), Blackburn and Henderson (1999), Anagnostopoulos (2000a; 2000b), Guilmineau and Queutey (2002)), and further experiments by Krishnamoorthy et al. (2001).

The phenomenon of lock-in, or synchronization in Blevins (1990) and Sumer and Fredsøe (1997), traditionally means that the ratio $f^*=f_{osc}/f_{n,air}$ remains close to unity, for high mass ratio. For low mass ratio, the body oscillates at a distinctly higher frequency as seen in Figure 1.1 and the range of synchronization opens up. Experimentally, the departure of f^* from unity, through the lock-in regime, was shown by Moe and Wu (1990), and more recently was reported in Khalak and Williamson (1997a; 1999), Govardhan and Williamson (2000); Williamson and Govardhan (2004), and in Gharib M R (1999). Therefore, synchronization can be defined as the "matching of the frequency of

the periodic wake vortex mode with the body oscillation frequency" Williamson and Govardhan (2004). Correspondingly, the force frequency must match the oscillation frequency, which is the definition of lock-in used by Sarpkaya (1995).

1.3.2. Effect of aspect ratio on VIVACE:

The aspect ratio (L/D) is an important design parameter for the operation of VIVACE, because of its effect on vortex shedding and VIV. It has been studied in detail by Szepessy and Bearman (1992). They studied the effect of aspect ratio on lift coefficient of a stationary cylinder by using movable end-plates. They found that the lift induced by vortex shedding on a stationary cylinder showed a maximum for an aspect ratio of one due to the increase in correlation length. The aspect ratio for maximum lift increases for an oscillating cylinder. This increase in the lift coefficient amplitude was found to be accompanied by increase in spanwise correlation of the flow or the correlation length of the cylinder which is related to the amplitude of oscillation.

To induce parallel shedding, end modifications are required; see Williamson (1996) for a review. At higher Reynolds numbers, the minimum aspect ratio for maximum correlation varies with Reynolds number which is also dependent on the end conditions (Norberg 1994; Szepessy 1993; Szepessy and Bearman 1992; West and Apelt 1982). For a stationary cylinder with end-plates attached, a decrease in aspect ratio below 10 for $Re = 10^4$ and below 6 for $Re = 10^5$ increased the lift coefficient (Keefe 1962; Szepessy and Bearman 1992). In his experiments Norberg (1994) observed that there is a transition of characteristics in mean pressure loading at an approximate Reynolds number ($Re \approx 8 \times 10^3$). Norberg (1994) observed a critical Reynolds number ($Re=8\times10^3$) above which the mean pressure loading increased with end-plates attached with increase in aspect ratio. He also observed that below the critical value ($Re=8\times10^3$) the mean pressure loading decreased along with decrease in aspect ratio.

The wake properties depend on the aspect ratio of the stationary cylinder (Williamson (1996), Norberg (2001)). Norberg (1994) showed that at low aspect ratios the vortex shedding frequency, the onset of vortex shedding and the base pressure coefficient are dependent on aspect ratio for a stationary cylinder. In general for $L/D > 7$

when end-plates are fitted, the effect of aspect ratio becomes relatively small (Norberg (1994; 2001)).

1.3.3. Effect of Reynolds number on VIVACE

VIVACE operates at both high and low Reynolds number. So, the effect of Reynolds number on the amplitude of VIV should be thoroughly understood. This study has been recently gaining impetus (Bernitsas et al. 2006a; Bernitsas et al. 2006b; Govardhan and Williamson 2005; Govardhan and Williamson 2006; Raghavan et al. 2007b). The previous studies on high Reynolds number were done to measure the drag values and the Strouhal number for stationary cylinder. Also, the experiments by Anatol Roshko (1961) are for a stationary cylinder at high Reynolds number. To the author's knowledge, the experiments on VIV of cylinders at high Reynolds number are scarce and are limited to studies by Bernitsas et al. (2006a; 2006b), Raghavan et al. (Raghavan et al. 2007b), Moe et al. (1994), Vikestad (1998), and Ding et al. (2004).

1.3.4. Effect of free surface on VIVACE

Free surface plays an important role on VIVACE in shallow water flow (Bernitsas et al. 2007). The free surface effect on VIV of cylinders is important because when the flow is bounded by a surface, the topology of the wake and the forces on the cylinder can be significantly altered as shown by Bearman and Zdravkovich (1978), Miyata et al. (1990), Zhu et al. (2000), Sheridan et al. (1997), and Carberry (2002; 2002a; 2002b). The curvature of the free surface induce additional vorticity into the flow (Lundgren and Koumoutsakos 1999). This is due to the boundary conditions at a free surface being different from those at a solid boundary as mentioned by Rood (1995) and Gharib and Weigand (1996). The free surface effect on vortex shedding and VIV for forced vibration cases was recently studied by using PIV imaging and quantitative measurements were taken (Sheridan et al. 1997; Zhu et al. 2000). In this work the effect of free surface is studied.

1.3.5. Amplitude and frequency response for low mass ratio and damping

VIVACE operates by maximizing VIV. The power output of VIVACE depends on the amplitude of oscillation and damping. It needs to be understood how the peak response amplitude ($A_{\max}$) varies as a function of m^*, ζ where ζ is the damping ratio. Much discussion on this point, concerning especially the effect of m*, and m*ζ, is reviewed in the "Review and preliminary results" section of Khalak and Williamson (1999). In VIVACE, the generated power is maximized by adding extra damping to the system. In turn, damping reduces the amplitude and may completely suppress the VIV as shown in Figure 1.3 (Griffin's plot). The increase in the damping can be counteracted by decreasing the mass ratio (Khalak and Williamson (1999)). In the review papers of Williamson and Govardhan (Williamson and Govardhan 2004), and Sarpkaya (Sarpkaya 2004), it is mentioned that the product of $m^* \zeta$ is the parameter which controls the maximum amplitude of oscillation.

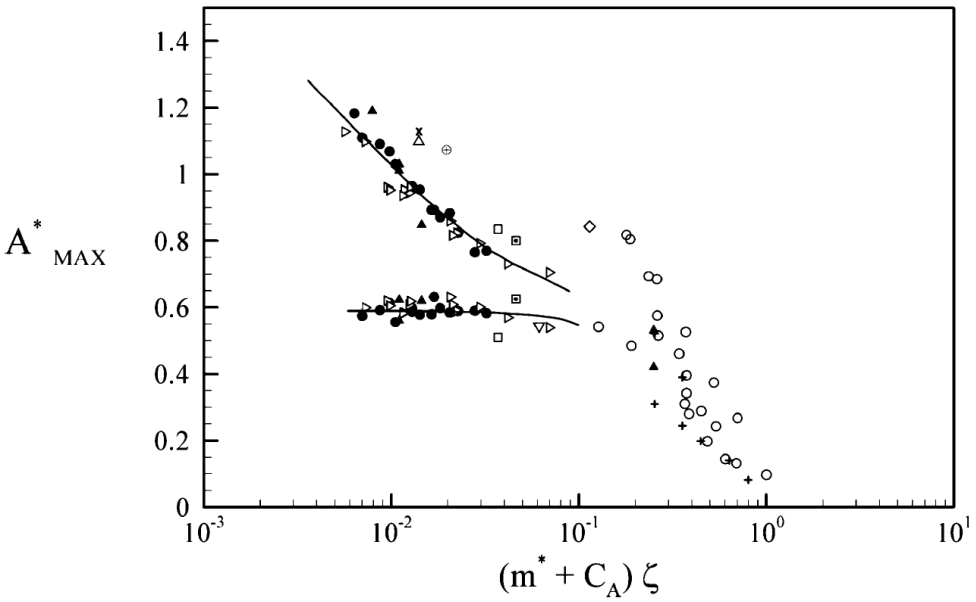

Figure 1.3. The Griffin plot. Peak-amplitude data plotted versus $(m^*+C_a)\zeta$. This indicates a large scatter at a low $(m^*+C_a)\zeta$. [Reproduced from Williamson and Govardhan (2004)].

In Figure 1.2**,** the amplitude response plot for m^*=2.4 and ζ=0.0045 is compared to the amplitude response measured by Feng (1968) in whose experiments m^*= 248. Khalak and Williamson (1996) found much greater amplitudes, with nearly twice the

maximum amplitude ($A_{\max} \sim 1$). Khalak and Williamson also found a four-fold increase in the range of velocity U^* over which the cylinder is in VIV. The difference in the results of Khalak and Williamson from those of Feng, in Figure 1.2**,** is attributed to a much lower mass-damping ($m^* \zeta$) of Khalak and Williamson than those of Feng (3% of his value).

In the case of low $m^* \zeta$, the oscillation frequency follows neither the vortex-shedding frequency (for the stationary cylinder case), nor the structural natural frequency (Khalak and Williamson, 1996) as seen in Figure 1.4. But in classical "lock-in" the oscillation frequency "locks onto" the natural frequency as seen in Figure 1.4 and Figure 1.1**.**

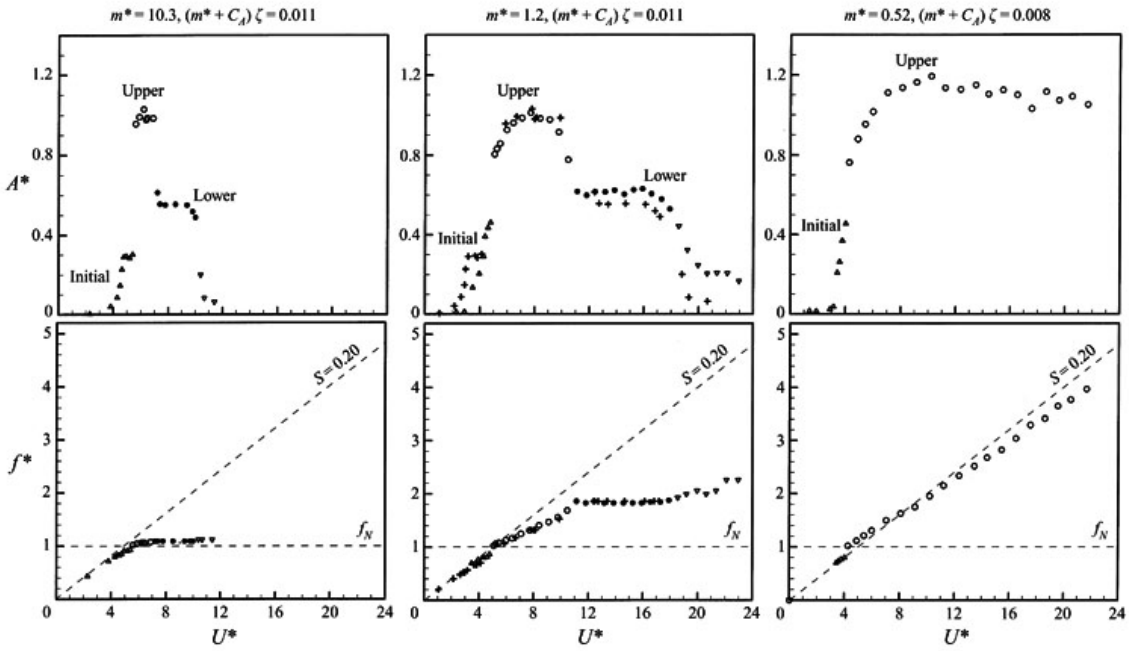

Figure 1.4. Pairs of amplitude ratio and frequency plots for decreasing mass ratio m*. [Reproduced from Govardhan and Williamson (2002)].

1.3.6. Effect of parallel shedding

The power of VIVACE is directly proportional to C_L' (fluctuating lift coefficient) and the amplitude of oscillation is also directly related to C_L'. Hereafter lift coefficient refers to fluctuating lift coefficient. The term mean lift coefficient is used explicitly when appropriate. In Figure 1.5, the dependence of lift coefficient on the Reynolds number is

plotted. C_L' has an increasing trend with the Reynolds number. In Figure 1.5 and Figure 1.6, the change in magnitude of force due to parallel shedding can be observed. Parallel shedding can be induced by altering the end conditions and there are few papers dedicated on this subject (Hammache and Gharib 1989; 1991; Williamson 1989). Williamson mentions that parallel shedding can be induced by increasing the velocity at the end conditions which can be attained by the methods mentioned in the above papers.

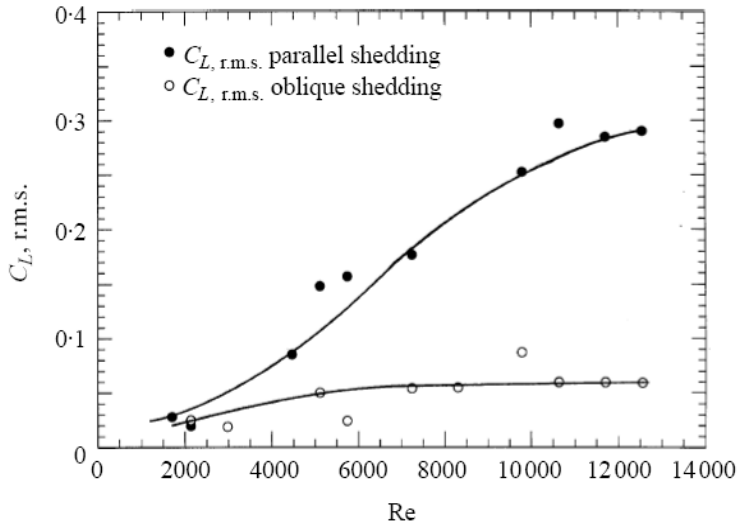

Figure 1.5. Increase in fluctuating lift coefficient with Reynolds number due to parallel shedding. [Reproduced from Khalak and Williamson (1999)].

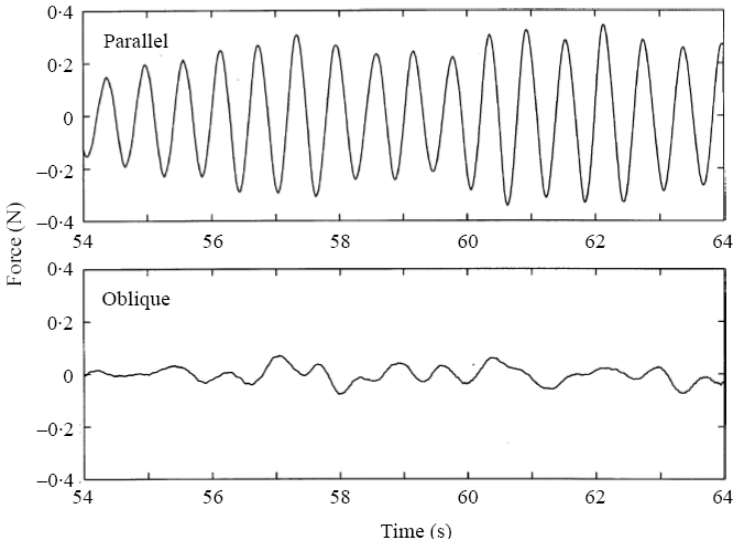

Figure 1.6. A comparison of force curve with respect to time for parallel and oblique vortex shedding. [Reproduced from Khalak and Williamson (1999)].

1.3.7. Dependence of lift coefficient on the wake mode

The relation of wake mode on the amplitude of response was established by Williamson and Roshko (1988) in their experiments which are shown in Figure 1.7 and Figure 1.8. Zdravkovich (1982); Ongoren and Rockwell (1988a; 1988b), Gu et al. (1994); Govardhan and Williamson (2000) confirmed this by Particle Image Velocimetry (PIV).

A link between the wake mode and forces on the cylinder was established numerically by Blackburn and Henderson (1999); and Lu and Dalton (1996). They found that a change in the timing of the vortex shed is accompanied by the change in the lift force in different branches on the oscillating cylinder. Following that, Carberry et al. (2001) did an experimental investigation to understand the changes in the topology of the wake of an oscillating cylinder and the forces on the cylinder.

In the free VIV case, as the reduced velocity decreases, the shift in the oscillation mode from the upper or lower branch to the initial branch corresponds to a change in the mode of vortex shedding from 2P to 2S, and a 180 degree phase shift of the vortex lift force (Govardhan and Williamson 2000). They observed a change in the timing of vortex shedding and therefore a change in the sign of the initially formed vortex.

Griffin and Ramberg (1974) and Ongoren and Rockwell (1988a; 1988b) observed 2P and P+S modes when a cylinder oscillated in-line with a flow at a period roughly half the shedding period corresponding for stationary cylinder. Griffin and Ramberg (1974) found that the shedding of a third vortex per cycle, which corresponds with the P+S mode, occurs at higher amplitudes of oscillation.

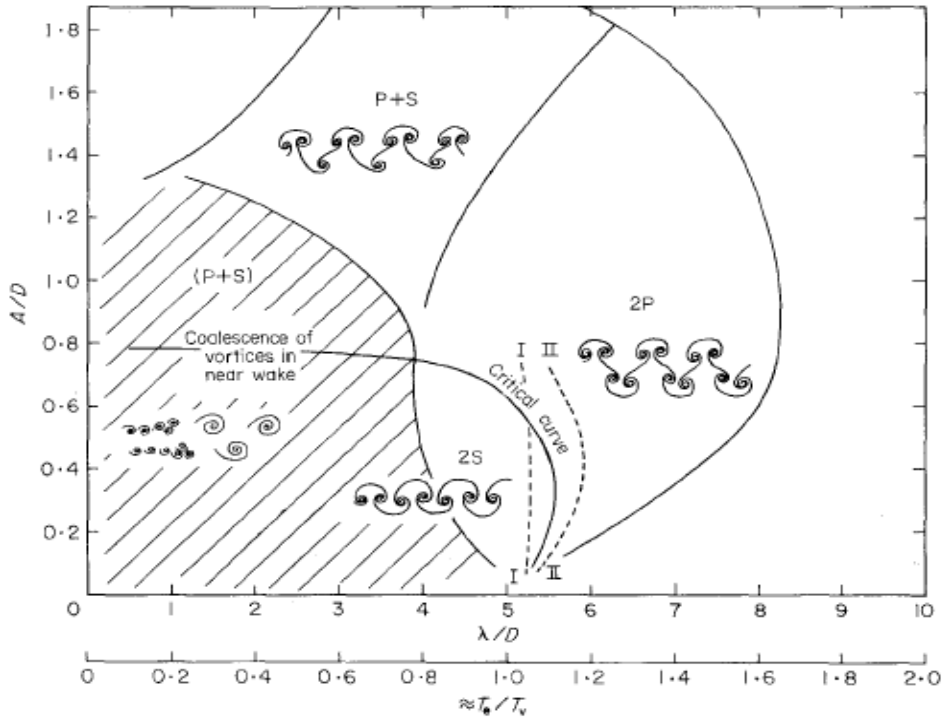

Figure 1.7. Williamson-Roshko Map of vortex shedding modes. [Reproduced from Williamson and Roshko (1988)].

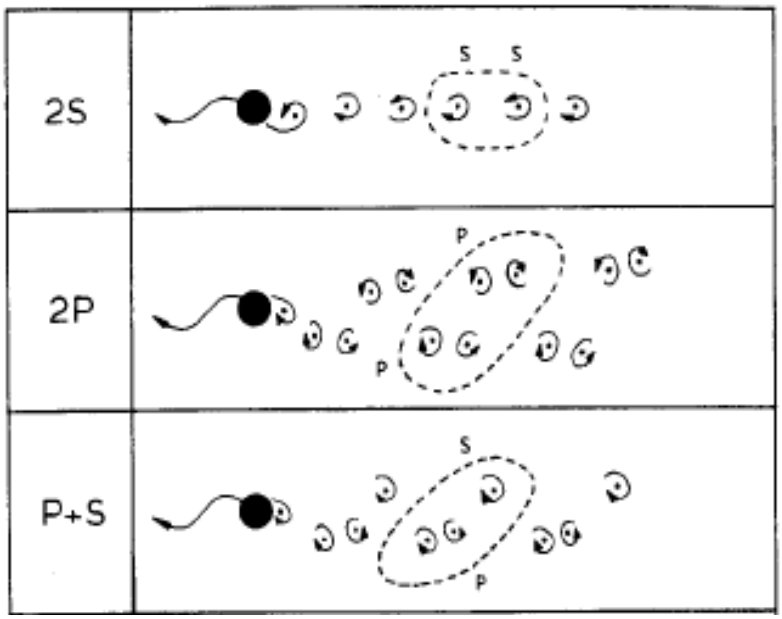

Figure 1.8. Vortex shedding modes. [Reproduced from Williamson and Roshko (1988)].

1.4. BASIC RESEARCH REQUIRED FOR THE DESIGN OF VIVACE

Generation of energy by a VIVACE Converter is based on extracting kinetic energy from a fluid flow by exciting a rigid cylinder on elastic supports in VIV and converting this motion to electricity. A brief literature review on VIV, ocean energy conversion, and VIVACE was presented in the Sections 1.2.1, 1.2.2, and 1.3. Suffice to discuss here only some important issues directly relating to the domain of operation of VIVACE so the relevant problem can be defined.

There are several issues in VIV that affect the design and operation of the VIVACE Converter. These are the following:

(a) Synchronization or lock-in between vortex shedding and cylinder oscillation. As the flow velocity U increases, lock-in for a high mass ratio system is reached when the vortex formation frequency $f_{V,form}$ is close enough to the body's natural frequency $f_{n,water}$. The two frequencies involved, $f_{V,form}$ and $f_{n,water}$, involved may be far apart depending on the mass ratio m*. This also affects the wake pattern mode.

(b) Range of synchronization. Unlike linear systems, which achieve large amplitude response in a narrow band around their natural frequency, systems in VIV achieve large amplitudes over broad ranges around $f_{n,water}$. This is a major advantage for a VIVACE Converter as it results in robustness with respect to sensitivity to relatively large changes in flow velocity.

(c) Self-limiting amplitude. On the other hand, the amplitude of oscillation of a smooth cylinder in VIV is self-limiting as large motions break the wake mode, lock-in frequency and vortex pattern. Modification of the surface of the cylinder with rough strips (Chapter 7) alters the wake mode and allows the sustenance of large amplitude motions which are not self limiting. The lock-in frequency is modified when the surface of cylinder is modified with roughness strips.

(d) Amplitude of oscillation and associated branches: initial, upper, lower. Over the synchronization regime these three branches correspond to different amplitudes and wake structures. It is important for VIVACE to operate under high damping and sustain high amplitude oscillations (upper branch) over wide ranges of synchronization.

(e) Wake structures defined as 2S, 2P, P+S, 2T 2Q. Manifestation of wake structures is determined by $m*$, modification of the surface with roughness strips and a second degree of freedom.

(f) Ratio of oscillating mass to displaced fluid mass m* Govardhan and Williamson (2000) observed that there exist two distinct types of response, depending on high or low combined mass-damping $m^*\varsigma$. In the classical high $m^*\varsigma$ case, the 'initial' and 'lower' amplitude branches are separated by a discontinuous mode transition, whereas in the case of low $m^*\varsigma$, the upper branch appears. For large mass ratios $m^* = O(100)$ (Williamson and Govardhan 2004), the vibration frequency for synchronization lies close to the natural frequency $f_{V,form} / f_{n,water} \approx 1$. As the mass ratio is reduced to $m^* = O(1)$, $f^*_{V,form}$ can reach high values. They also derived the following expression for the vortex formation frequency in the lower branch of vibration $f_{lower} = \sqrt{\frac{\left(m^* + C_A\right)}{m^* - 0.54}}$, where C_A is the potential flow added mass taken as one for a circular cylinder. It reveals the existence of a critical mass ratio m^*_{critic}= 0.54, where $f^*_{V,form}$ becomes very large. When $m^* < m^*_{critic}$, the lower branch ceases to exist.

(g) Multiple degrees of freedom It has also been observed experimentally that a two degree of freedom cylinder in VIV allows larger amplitudes of oscillation in the direction perpendicular to the fluid flow.

(h) Correlation length. In VIV, this is an order of magnitude higher than the correlation length of a stationary cylinder in current. The larger it is, the higher are the forces exerted on the VIVACE cylinder as a whole.

(i) Synchronization under high damping This has received no attention up to date and it is the regime applicable to the VIVACE Converter. The higher the damping imposed by the PTO, the higher the energy that can be extracted provided that high amplitude VIV is optimally maintained.

(j) Increase of lift with Reynolds number. To the author's knowledge, experiments on VIV of cylinders at high Reynolds number are scarce. Yet, recent work (Bernitsas et al. (2006a; 2006b), Raghavan et al. (Raghavan et al. 2007b)) has shown that the amplitude of oscillation increases for high Reynolds numbers.

(k) Proximity to free surface or solid boundaries The free surface effect on VIV of cylinders is important because when the flow is bounded by a surface the structure of the wake and the forces on the cylinder can be significantly altered. The boundary conditions at a free surface are significantly different from those at a solid boundary.

1.5. SCOPE OF THIS Ph.D DISSERTATION

As the prior discussion indicates, the design of VIVACE involves a number of parameters resulting in a thorough need of understanding the different aspects of VIV.
The major aims of the current investigation are as follows:

(a) To confirm analytically and experimentally that VIVACE can be an economically viable and environmentally compatible device to extract energy from fluid flow.
(b) To understand the effect of damping on VIV.
(c) To understand the effect of higher Reynolds number on VIVACE and use it as an input parameter for VIVACE.
(d) To understand the effect of proximity to free surface on VIVACE because when the flow is bounded by a surface the structure of the wake and the forces on the cylinder can be significantly altered. This is an important design parameter for VIVACE in shallow water.
(e) To understand the effect of proximity to solid rigid boundaries on VIVACE because the boundary conditions at a free surface are significantly different from those at a solid boundary. This is an important design parameter for VIVACE in shallow water.
(f) To understand the effect of strategically located roughness on the amplitude of oscillation and synchronization range of VIVACE.

This dissertation is organized as follows:

- Chapter 2 explains the experimental setup in general.
- Chapter 3 details the design and validation of the VIVACE concept.
- Chapter 4 studies the effect of Reynolds number on VIVACE.
- Chapter 5 studies the effect of the proximity of free surface on VIVACE.
- Chapter 6 studies the effect of the proximity of bottom boundary on VIVACE.

- Chapter 7 studies the effect of strategically located surface roughness on VIVACE.
- Chapter 8 contains some concluding remarks and suggestions for future work.

Chapter 2

EXPERIMENTAL APPARATUS AND CALIBRATION

2.1. FACILITY, APPARATUS, CALIBRATION

All model tests performed on the simple VIVACE modulo considered in this dissertation were conducted in the Low Turbulence Free Surface Water (LTFSW) Channel of the Marine Hydrodynamics Laboratory (MHL) of the University of Michigan. The LTFSW Channel is described in Section 2.1.1 along with the reasons of selecting that facility for the VIVACE model tests. The particulars of the physical model, which was built and tested, are presented in Section 2.1.2. Calibration of the LTFSW Channel with the VIVACE modulo in place is discussed in Section 2.2. The specifics of the experimental set up for each topic dealt in this dissertation are discussed individually in their own respective chapters 3 - 7. In this chapter, only the common features of the experimental set up for different experiments are discussed.

2.1.1. Low Turbulence Free Surface Water (LTFSW) Channel

A continuous flow past a VIVACE cylinder can be provided in the LTFSW Channel (see Figure 2.1). Alternatively, the current effect can be created by towing the cylinder at a constant speed in otherwise calm water. The relative flow past the cylinder is identical. Each method, however, has particular benefits and limitations. Careful use of a towing tank with sufficient time between runs reduces the free-stream turbulence to negligible levels but the length of the towing tank limits the number of oscillations per experiment. In the LTFSW Channel, the flow is generated by an impeller and there is no

limit on the number of oscillations per experiment. It is difficult, however, to achieve low turbulence levels because of the turbulence induced by the impeller and the cylinder in VIV. The length of the cylinder is limited by the width of the channel. The LTFSW Channel was selected because of its advantages and acceptable turbulence level.

The purpose of the LTFSW Channel is to facilitate the study of the fundamental structural aspects of turbulent flows. The water channel is two stories high and re-circulates approximately 8,000 gallons of softened and filtered water by making use of a 0.787m diameter four-bladed bronze impeller connected to a 20 hp three-phase induction motor. The maximum flow speed is 2 m/s. The test section is 2.44 m long, 1 m across and aprroximately0.8 m deep. All walls at the test section are acrylic to allow for flow visualization experiments and to facilitate measurements with optical instrumentation. The turbulence intensity normalized by the free-stream velocity was reported at 0.095% (Walker et al. 1996).

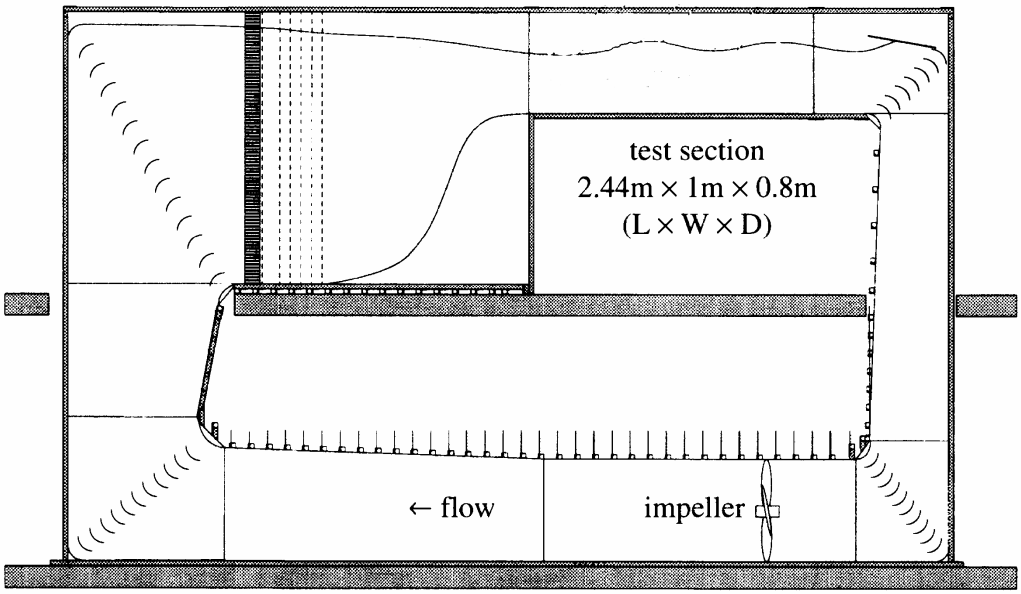

Figure 2.1. Schematic of LTFSW Channel. [Reproduced from Walker et al. (1996)].

2.1.2. Apparatus

A simple schematic of a single modulo of the VIVACE Converter considered in this dissertation is depicted in Figure 2.2. The elements of this modulo are: a circular rigid cylinder of diameter D and length L, two supporting linear springs each of stiffness

$K_{spring}/2$, system damping c_{system} , damping of transmission mechanism c_{tra}, a generator with damping c_{gen},and the energy harnessing damping c_{harn}. Depending on the type of experiments c_{tra}, c_{gen} and c_{harn} may or may not be present. The cylinder is placed with its axis in the z-direction perpendicular to the flow velocity U, which is in the x-direction. The cylinder oscillates in the y-direction, which is perpendicular to its axis in z and the flow velocity in x.

To study the energy generation aspect of VIVACE, three gradually improved models of the VIVACE modulo were built and tested until the system was debugged. All data and results reported in this dissertation pertain to the third model. The third VIVACE Model has *D*=125.7 mm, *L*=914.4 mm, and is made of aluminum. The aspect ratio of this cylinder is small, 7.274. The blockage ratio is 14.3% in the working section of the water channel for this particular model. Cylinders with lower blockage ratio (≈7%) and high aspect ratio (≈15) were studied and those experiments showed similar character to the 5″ cylinder. The cylinder is suspended by two compression coil-springs attached to the end-plates. The cylinder is constrained by linear bearings to oscillate freely in the *y*-direction. Narrow gaps of about 10 mm are maintained between the walls of the water-channel and the end-plates of the model. The natural frequency $f_{n,water}$ of the oscillating cylinder system was controlled in the range of 0.88-1.037 Hz by adjusting the number of active coils in the coil-springs. The values of Reynolds number Re=UD/ν (ν= kinematic viscosity, 1.1389×10^{-6} for fresh water at 15^{o}C) used in the experiments are in the range of Re $\in$ [0.44×10^{5}-1.34×10^{5}]. Figure 2.3 shows a picture of the third VIVACE Converter Model with parts 1 through 6 identified and listed in Table 2.1. The weights of the oscillating parts sum to 16.79 kg, this includes one third of the spring mass. The displaced fluid mass equals to 11.58 kg. This results in a ratio of oscillating mass over displaced fluid mass of m*= 1.45.

This model was later improved and the system was made lighter to study the effect of Reynolds number, free surface, bottom boundary, and the effect of roughness distribution on VIVACE. The studies on the above mentioned aspects of VIVACE were done using four sets of cylinders and their characteristics are compiled in Table 2.2

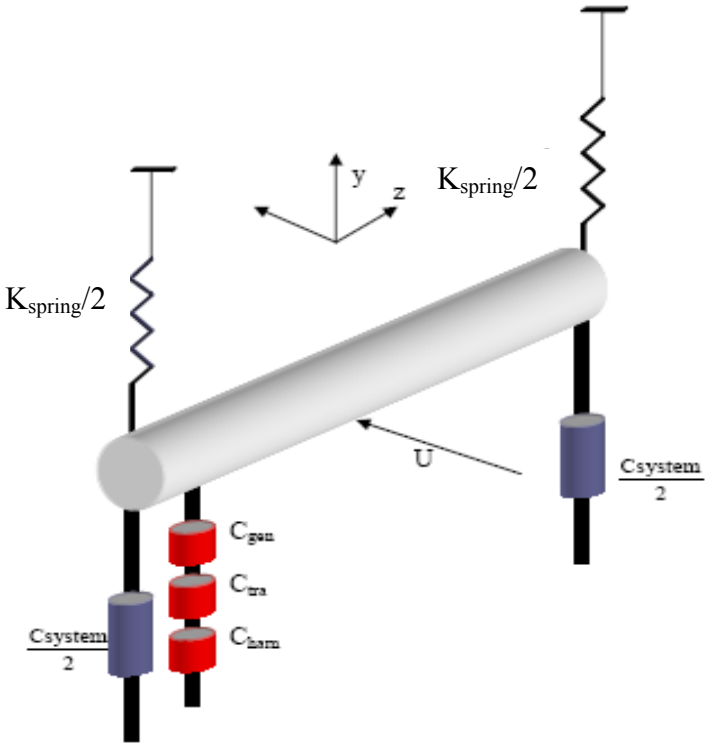

Figure 2.2. Simple schematic of a VIVACE modulo with coordinate system.

End Plates: When a cylinder spans a wind/water tunnel, boundary effects may be significant, especially on the lift coefficient and the correlation length (Norberg 1994; Szepessy and Bearman 1992). At higher Reynolds number, three dimensionality is induced in vortex shedding (Williamson 1996). At higher Reynolds numbers (4×10^3-4.8×10^3), a reduction of pressure correlation occurs due to shedding of vortices in cells each with a different shedding phase (Norberg 1994; Szepessy and Bearman 1992). Vortex shedding becomes irregular and affects the pressure fluctuations associated with vortex shedding (Norberg 1994; Szepessy and Bearman 1992). It has been observed that flow around a stationary cylinder for Reynolds number around 10^4 has a spanwise correlation of 3-4 diameters (Norberg 1994; Szepessy and Bearman 1992; Szepessy and Bearman 1993), which increases for an oscillating cylinder in VIV. The end plates of the VIVACE Models were designed to the size of the diameter of the cylinder to induce parallel shedding at high Reynolds number tests.

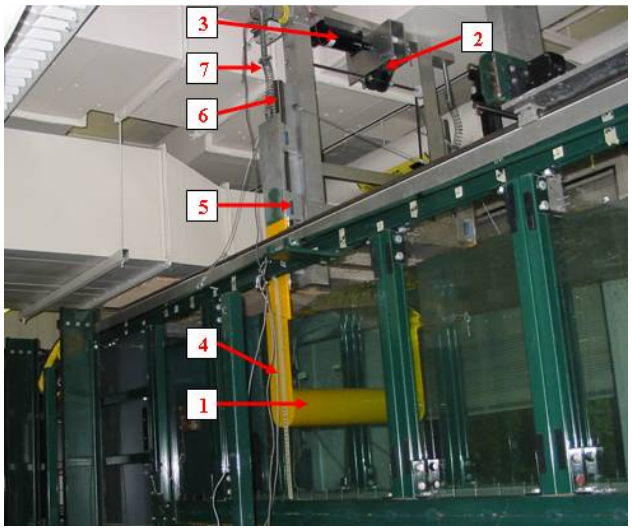

Figure 2.3. VIVACE model in the Low Turbulence Free Surface Water (LTFSW) Channel.

Part no.	Description	No. of parts
1	Cylinder	1
2	Rotatory generator	1
3	Gear	2
4	Side strut	2
5	Linear bearings	4
6	Fixed shafts	2

Table 2.1. Main components of VIVACE model.

In the Marine Hydrodynamics Laboratory of the University of Michigan, models that have been tested for energy extraction had aspect ratios of 7.20. The description of the models that were used to test the effect of Reynolds number, free surface, bottom boundary, and roughness strips are tabulated in Table 2.2

Diameter	2.5″	3″	3.5″	5.0″	6.0″
Length (m)	0.9144	0.9144	0.9144	0.9144	0.9144
Total mass (kg)	8.95	9.11	10.28	12.7	13.3
Displaced mass (kg)	2.86	4.11	5.60	11.43	16.46
Mass ratio	3.14	2.21	1.84	1.11	0.808
Aspect ratio	14.40	12.00	10.29	7.20	6.00

Table 2.2. Characteristics of models used to study the effect of Reynolds number, boundary conditions, and roughness strips on VIVACE.

2.2. CALIBRATION

The vertical displacement y(t) was measured using a Celesco cable extension position transducer (yo-yo potentiometer). The voltage measurement was done by directly connecting the generator to the data acquisition system. The data acquisition system from the position transducer and the generator consisted of a 16 bit analog to digital converter with four pole, low-pass, Butterworth filters. All data were collected at a 100 Hz sampling rate. The pressures are reported as an average over the steady-state portion of the time series. The record length was 30 seconds for large amplitude oscillations.

Calibration of the LTFSW Channel: Using a Pitot tube, velocity surveys were conducted to measure the velocity of the flow at different water depths of the tunnel. This produced a factor for various water depths which, when multiplied by the frequency of the impeller, determines the flow velocity. The Pitot tubes were positioned at 30 cm above the bottom of the tank and at half-width of the tank. Next, the velocity profiles were measured at one downstream location but at four other frequency settings on the drive motor at six different depths. The purpose of these profiles was to provide a calibration between the impeller frequency and the free-stream velocity. The equation derived by correlation for the free stream velocity is

$$\text{U (m/s)} = (-0.000034 \times (\text{Depth (mm)}) + 0.061177) \times \text{Impeller Frequency} \quad (2.1)$$

The correlation coefficient for the above linear equation between free stream velocity and the water depth is $R^2 = 0.994211$. These values matched very well with the averaged value measured using the formula in K.Maki's Ph.D dissertation (Maki 2005).

2.3. MEASUREMENTS AND DATA ANALYSIS

Using the LTFSW Channel and the VIVACE model described in Chapter 3, the following quantities were recorded in each run:

(i) The cylinder vertical displacement *y(t)*

(ii) The water velocity *U*

(iii) The voltage generated at the load resistance R_L used to harness electricity

(iv) The harnessed power *P(t)*

Fourier transform analysis was performed on the displacement to study the frequency character of the VIV experiments conducted.

2.4. ERROR ANALYSIS

All experimental measurements, however carefully measured, are subject to uncertainties. Error analysis is the study and evaluation of these uncertainties. All experimental uncertainty is due to either random errors or systematic errors.

In our experiments the only measurement that was used was the displacement measurement. The Error analysis showed a variation of ± 5% in the displacement value and the oscillation frequency measured was accurate to 0.03%. The accuracy of the oscillation amplitude was of concern only in the synchronization regime.

2.5. DAMPING TESTS

Several damping tests were conducted to evaluate the design, fabrication, and mounting of the various VIVACE models built and tested. Damping tests with different configurations of the model were conducted to study the energy extraction aspect of VIVACE. The configurations tested constituted of the VIVACE model with gear disconnected, gear connected, generator connected, and generator connected with loading. In the cases of experiments conducted to study the effects of Reynolds number, free surface, bottom boundary, and roughness strip on VIVACE, the damping tests were conducted with gear disconnected. Damping tests were conducted in air and water. A few sample results presented here are from the measurements conducted on VIVACE models (see Figure 2.4 and Figure 2.5). Damping tests were conducted on a regular basis every few hours of model tests. The calculated damping factor corresponds to ζ_{system} for different initial displacement values. The results are plotted in Figure 2.6 and compare very well to damping test results for similar apparatuses as compiled by Sumer and Fredsoe (1997).

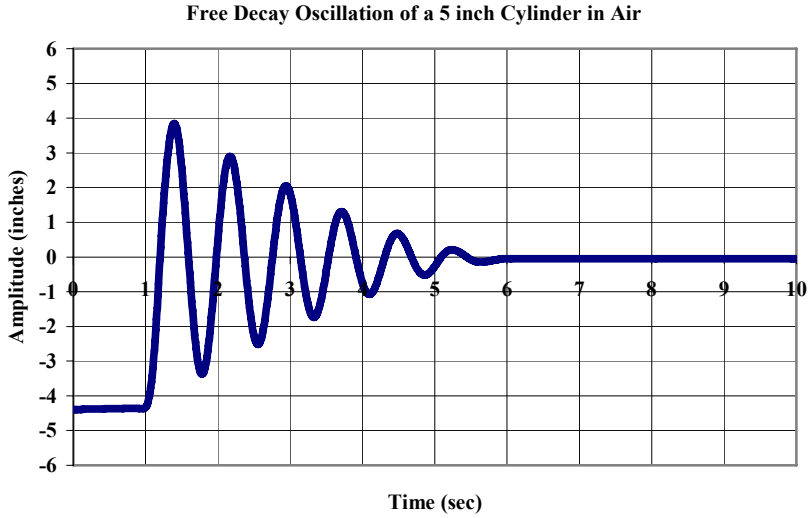

Figure 2.4. Typical recorded time histories of free decay oscillation in air for VIVACE model with gear disconnected.

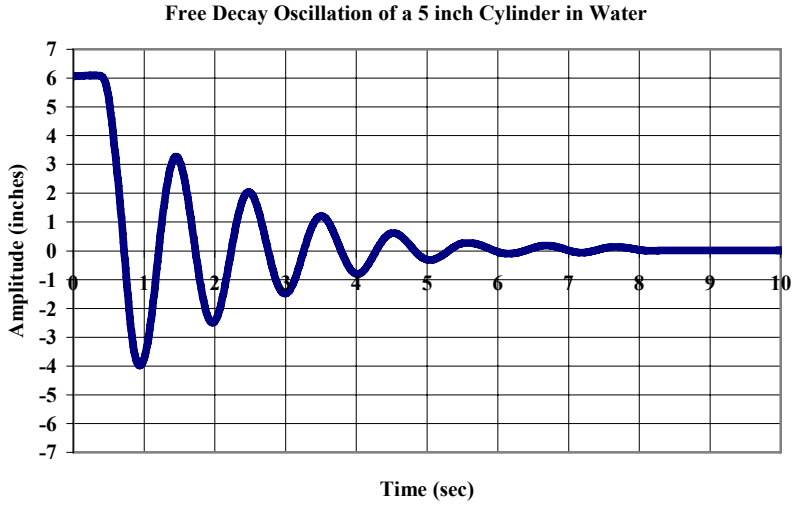

Figure 2.5. Typical recorded time histories of free decay oscillation in water for VIVACE model with gear disconnected.

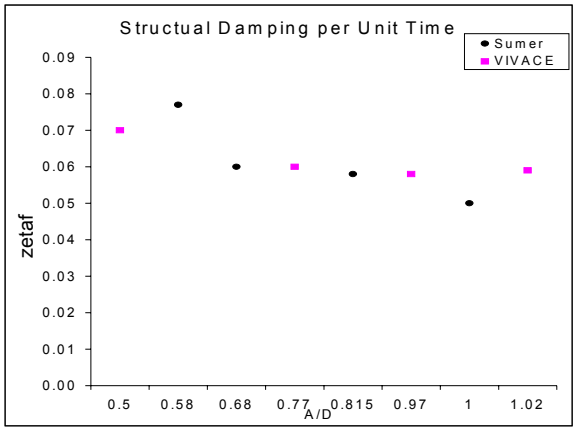

Figure 2.6. Free decay damping test results in water: comparison between VIVACE model with gear disconnected and Sumer's compiled data (Bernitsas et al. 2006a).

Chapter 3

THE VIVACE CONVERTER

3.1. CHAPTER OVERVIEW

The VIVACE Converter consists of a bluff body, which is rigid and elastically mounted or flexible, placed in a fluid flow. The body undergoes Vortex Induced Vibrations and through a transmission system transmits the mechanical energy to a generator for conversion to electricity or directly to a mechanical or hydraulic form of usable energy. The subclass of the VIVACE Converter presented in this chapter is that of a rigid circular cylinder mounted on linear springs and placed perpendicularly to a steady uniform current (Figure 2.1 and Figure 3.1). The resulting mechanical energy is transmitted via a gear-belt system to a generator and converted to electricity. First the fundamental principles of operation of the VIVACE Converter are discussed. Then, the geometry of module and assemblies of module are presented.

3.2. THE UNDERLYING PRINCIPLES OF VIVACE

The VIVACE technology is based on four principles: (a) Vortex Induced Vibrations, (b) nonlinear resonance, (c) correlation length, and (d) energy generation. All of these concepts are interrelated.

(a) Vortex Induced Vibrations of a rigid circular cylinder mounted on linear springs: The phenomenon of VIV of such cylinders has been studied extensively in the past one hundred years. Alternating vortex shedding creates asymmetry and oscillatory lift. The cylinder in VIV oscillates perpendicularly to its axis and transversely to the flow velocity

(Figure 2.1). VIV result in negative drag in the direction of the cylinder oscillation. Thus, the cylinder in VIV absorbs energy from the fluid. This phenomenon has been observed in several engineering disciplines: offshore (pipelines, marine risers, cables, legs of drilling and production platforms, etc) (Morison et al. 1950; Sarpkaya 1995; Sumer and Fredsoe 1997; Williamson and Govardhan 2004); nuclear (control rods in reactors); mechanical (heat exchangers); civil (bridges, towers, flag poles). In all occasions, systematic effort has been made to spoil vortex shedding and suppress VIV. VIVACE, enhances VIV to maximize energy harnessing at high damping while maintaining a high VIV amplitude and synchronization range.

(b) Nonlinear resonance: This phenomenon is inherently related to VIV. In a broad range around the natural frequency, vortex shedding locks into the oscillation frequency of the cylinder in VIV. The vortex shedding frequency f_{St} as calculated for a stationary cylinder in a steady flow ($\frac{St \cdot U}{D}$, where St = 0.2) ceases to exist. Frequency $f_{V,mode}$ appears and becomes equal to the oscillating cylinder frequency f_{osc}. The vortex formation frequency $f_{V,form}$ depends on the wake pattern as explained in the Introduction. Hence, this phenomenon is called synchronization – between vortex shedding mode and oscillations. Synchronization may occur (depending on the oscillating mass ratio) over a broad range around the cylinder's natural frequency in water, not just at the natural frequency. In addition, the amplitude of oscillation of the cylinder in VIV is self-limiting. Due to these last two properties, VIV is clearly a self-excited nonlinear resonance phenomenon. Ocean energy converting devices based on oscillating parts (buoys, water columns, flaps) are designed to achieve linear resonance to maximize the amplitude of oscillation. Linear resonance has a very limited bandwidth of large amplitude oscillations. The VIVACE Converter is based on nonlinear resonance and enhances VIV by pushing oscillation as close as possible to its self-limiting amplitude over the entire range of nonlinear resonance while adding electrical resistance for optimal energy generation. The fact that the VIV nonlinear resonance is self-limiting in amplitude has an advantage. Specifically, the steady state electricity generation is very close to the maximum and the electrical generator rating does not have to be much higher to accommodate extreme load increases.

(c) Correlation Length: In VIV, the correlation length of the flow past the cylinder is defined as the length of the cylinder along which vortices shed in phase within certain allowance. Higher correlation length results in higher total vortex induced forces. For a circular cylinder in VIV, the correlation length is theoretically infinite. In practice, a minimum aspect ratio of 7 and a maximum of 20 are recommended. The VIVACE Converter is designed with an aspect ratio in the above range. The actual choice depends on other issues tailored to the specific application and the requirements/restrictions on the values of U, m*, m_d and required power output. For example, the VIVACE models tested in the lab had an aspect ratio of 7.2. Large ocean converters will have an aspect ratio as high as 20.

(d) Electrical Generation: The mechanical energy of a cylinder in VIV can be converted into other forms of usable energy. In VIVACE models, a belt and gear system transmitted the mechanical VIV energy to a generator to convert it to electrical energy. Conversion to mechanical energy is possible, say, by using hydraulics to pump water or pressurize it for desalination. Regardless of the final form of energy, the energy converter induces mechanical damping back to the VIV system. Too much damping suppresses VIV resulting in zero harnessed energy. Too little damping will result in little harnessed energy. An optimized amount of damping needs to be applied to the VIV system for an optimized energy extraction. The total system damping ζ_{total}, the stiffness K_{spring} of the supporting springs, and the oscillating mass m* (equation 3.3) can be adjusted resulting in a high degree of flexibility of the system when combined with the broad range of VIV synchronization.

3.2.1. Physical model

A simple schematic of a single module of the VIVACE Converter considered in this chapter is depicted in Figure 2.2 and Figure 3.1. The elements of this module are: a circular rigid cylinder of diameter D and length L, two supporting linear springs each of stiffness $K_{spring}/2$, system damping c_{system}, one or more generators, generator damping c_{gen}, transmission damping c_{tra}, and the energy generating damping c_{harn}. In Figure 2.2, the cylinder is placed with its axis in the z direction perpendicular to the flow velocity U,

which is in direction x. The cylinder oscillates in the y direction, which is perpendicular to its axis in z and the flow velocity in x.

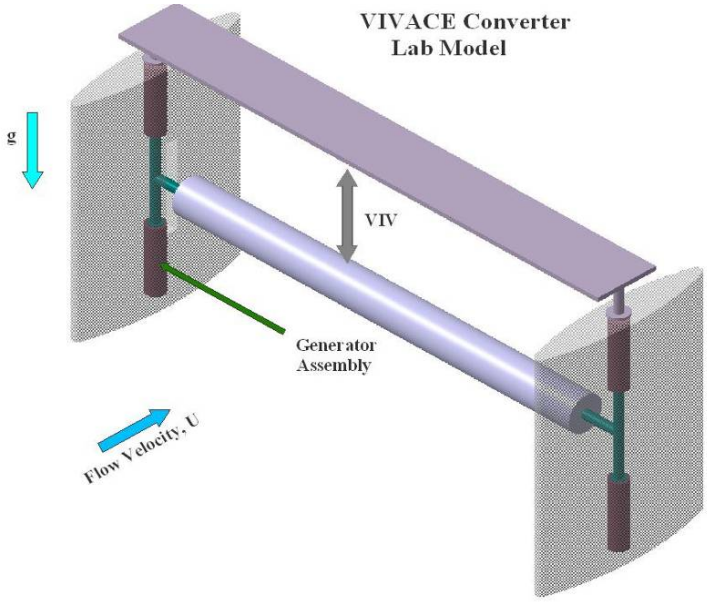

Figure 3.1. VIVACE Converter module.

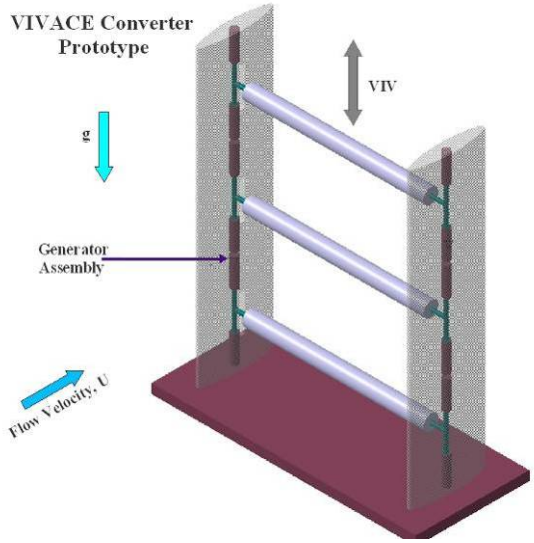

Figure 3.2. Vertical VIVACE Converter bank.

The VIVACE Converter design is modular, scalable, and flexible in the sense of geometry and configuration. Thus, converters of various sizes can be developed by assembling module of various sizes and properties in a variety of configurations. Figure 3.1, Figure 3.2, and Figure 3.3 shows artist's renditions of VIVACE Converters for a

single module, a small vertical bank for river currents, and a small array for an offshore power plant, respectively. The supporting piles, which house all the transmission and electricity generating components, are hydrodynamically faired to prevent their own VIV. The oscillating cylinders are attached by small pins to sliding bearings on a steel rod with springs and damping to provide an elastic support to achieve VIV of the cylinders.

The VIV mechanical energy can be converted to electricity or directly into other forms of usable mechanical energy. Figure 3.4 depicts the system presently used in the VIVACE Converter lab models. It consists of a gear-belt transmission system and an off-the-shelf rotary generator. Alternatives such as a hydraulic system (WaveNet 2003) or a linear generator (WaveNet 2003) are possible.

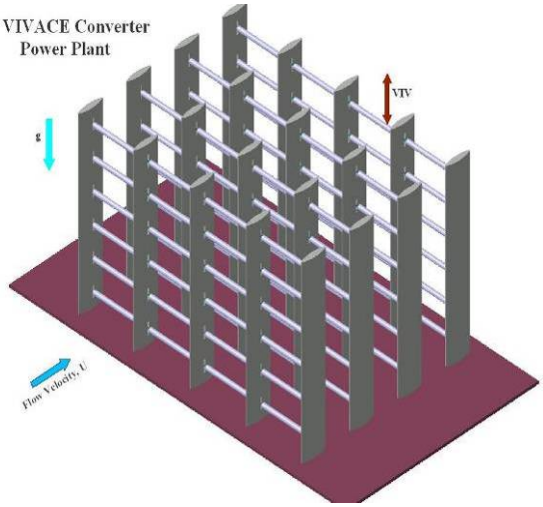

Figure 3.3. Small conceptual VIVACE Converter power plant.

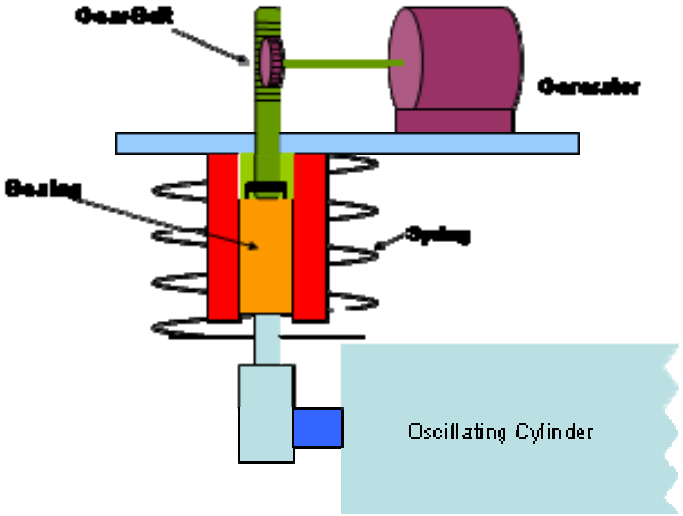

Figure 3.4. Rotary generator system.

For multiple cylinders, a hydraulic system can be connected to multiple VIVACE modules and then to one generator. Direct transmission to mechanical energy through hydraulics can be used to pump water for irrigation or raise pressure for water desalination. An extensive study would be required to study the effect of proximity of multiple cylinders. Data available on this issue are very limited (Sumer and Fredsoe 1997).

In addition to the quantities that define the VIVACE module, for a VIVACE Converter assembly, the following geometric variables need to be defined as shown in Figure 3.5: h_1 = water depth, d = draft of the VIVACE Converter assembly, t_1 = vertical distance between centers of cylinders, p_1 = horizontal distance between centers of cylinders.

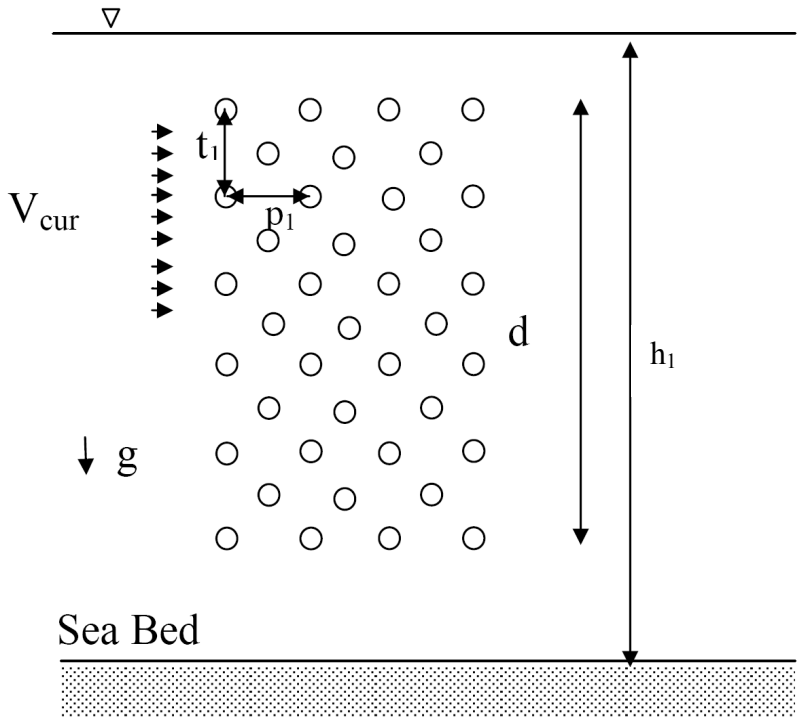

Figure 3.5. Geometry, dimensions, and arrangement of cylinders in a VIVACE Converter assembly.

3.3. MODELING OF VIVACE

Most of the information available in the literature on free (not forced) VIV of circular cylinders, falls into one of two categories: (i) Laboratory tests of rigid cylinders on elastic supports at relatively low Reynolds numbers and low damping (Sarpkaya 2004;

Williamson and Govardhan 2004). (ii) Field tests of flexible cylinders at high Reynolds numbers, possibly with helical strakes or other devices to suppress VIV (Ding et al. 2004; Sumer and Fredsøe 1997). The type of tests needed for VIVACE are for a rigid cylinder mounted on elastic supports, at high Reynolds numbers, and at high damping. Accordingly, in spite of the large amount of experimental information available in the literature, the specific domain of operation of VIVACE requires model tests. A series of such tests was performed on a VIVACE model in the LTFSW Channel of the Marine Hydrodynamics Lab of the University of Michigan. In Section 3.3.1, some information on those lab tests is provided. Many mathematical models have been developed since the early 1900's (Prandtl and Tietjens 1957) but none actually solves the boundary/initial value problem of the Navier – Stokes equations. Those models are based on numerous phenomenological assumptions and/or numerical solution techniques and consequently require extensive calibration to match measurements. A simple math model is used in Section 3.3.2 to help understand the behavior of the VIVACE Converter and verify compatibility of test measurements.

3.3.1. Lab model

Some of the properties of the VIVACE model are listed in Table 3.1. The VIVACE cylinder is made of aluminum and coated for surface smoothness and protection as shown in Figure 3.6. The aspect ratio of this cylinder is, 7.274. The blockage ratio in the test section of the water channel is, 14.3%. An oscillating cylinder model is suspended by two compression coil-springs attached to the end-plates. The cylinder is constrained to vibrate freely in the transverse direction by linear bearings. There were narrow gaps of about 10 mm between the walls of water-tunnel and the end-plates of the model. To convert VIV into electricity, a rotary electrical generator is used. The generator is a low-RPM type, typically used for wind energy generation. A gear-belt transmission system is used to transmit the VIV linear oscillatory motion to rotational oscillatory motion of the generator shaft.

The first objective of the model tests was to confirm that the VIVACE Converter can remain in nonlinear resonance at the high value of damping throughout the design

range of water current velocities, without stalling and without adjusting the spring stiffness.

Figure 3.6. VIVACE model in the Low Turbulence Free Surface Water Channel of the Marine Hydrodynamics Laboratory of the University of Michigan.

VIVACE Model Particulars	
Diameter (mm)	127
Length (mm)	914.4
K_{spring} of each spring (N/m)	518
Mass of the system (kg)	16.8
Mass ratio (m*)	1.45
$f_{n,water}$ (Hz)	0.96
Velocity of current (m/s)	0.4-1.2
Reynolds number	$0.44\text{-}1.34 \times 10^5$
Generator resistance (Ohm)	7

Table 3.1. VIVACE model particulars for test results in Figure 10.

3.3.2. Mathematical model

A simple mathematical model of the system dynamics and fluid forces is presented next. The motion of the cylinder in the y-direction (see Figure 2.1 and Figure 3.1) is modeled by a second-order linear equation as

$$m_{osc}\ddot{y} + c_{total}\dot{y} + K_{spring}y = \mathrm{F}_{\mathrm{fluid}}\hat{\mathrm{y}}, \tag{3.1}$$

where y is the direction perpendicular to the flow and the cylinder axis, $\hat{\mathrm{y}}$ is the unit normal vector in the y-direction. $\mathrm{m_{osc}}$ is the oscillating system mass which includes one third of the spring mass, $\mathrm{K_{spring}}$ is the spring stiffness, c_{total} is the total damping coefficient, and $\mathrm{F}_{\mathrm{fluid}}$ is the force exerted by the fluid on the body in the y-direction. In this model, we separate the fluid force into viscous and inviscid components (Khalak and Williamson 1996; 1997a; 1999) as follows

$$m_{osc}\ddot{y} + c_{total}\dot{y} + K_{spring}y = \mathrm{F}_{\mathrm{viscous}}\hat{\mathrm{y}} + \mathrm{F}_{\mathrm{inviscid}}\hat{\mathrm{y}}. \tag{3.2}$$

The inviscid force may be defined in terms of the inviscid added mass m_a. The added mass inclusion through a constant added mass coefficient (from potential theory) on the left hand side is still debated. The added mass is defined as "the impulse given to the fluid during an incremental change of body velocity, divided by that incremental velocity." Further,

$$\mathrm{F}_{\mathrm{inviscid}}\hat{\mathrm{y}} = -m_a\ddot{y}, \tag{3.3}$$

$$\mathrm{F}_{\mathrm{viscous}}\hat{\mathrm{y}} = \frac{1}{2}c_y(t)\rho U^2 DL. \tag{3.4}$$

At this stage, we introduce m_d, the mass of the displaced fluid, which for a cylinder is $\frac{\pi}{4}\rho_w \mathrm{D}^2\mathrm{L}$. This reduces the equation of motion to

$$\left(m_{osc} + m_a\right)\ddot{y} + c_{total}\dot{y} + K_{spring}y = \frac{2}{\pi D}c_y(t)m_d U^2. \tag{3.5}$$

We can non-dimensionalize the above equation by introducing the dimensionless variables defined in Table 1.1.

Use of the natural frequency of VIVACE in water rather than in vacuum or air is necessary due to the big difference in the density of air and water. After substituting the non-dimensional values into equation (3.5), the equation of motion becomes

$$\left(m^* + C_a\right)\bullet\left(\frac{\ddot{y}^*}{f_{n,water}^2} + \frac{4\pi\zeta_{total}\dot{y}^*}{f_{n,water}} + 4\pi^2 y^*\right) = \frac{2}{\pi}c_y(t)U^{*2}. \tag{3.6}$$

When the system is in resonance, the cylinder motion is nearly sinusoidal and VIV can be modeled using a linear oscillator model. Outside of the resonance range, the model has to be described by a nonlinear model, and several wake–oscillator models have been proposed in the literature (Blevins 1990). To obtain a simple approximation to the resonant response without experiments, the traditional approach is to assume a sinusoidal form for the fluctuating transverse force coefficient and amplitude (Bearman 1984) as

$$y = y_{\max} \sin\left(2\pi f_{fluid} t\right) \text{ , therefore } y^* = y^*_{\max} \sin\left(2\pi f_{fluid} t\right), \tag{3.7}$$

$$c_y(t) = C_y \sin(2\pi f_{fluid} t + \phi), \tag{3.8}$$

where f_{fluid} is the dominant fluid forcing frequency which relates to the cylinder in VIV frequency as explained in Chapter 1. For the ensuing analysis, f_{fluid} is assumed equal to f_{osc} which is the dominant fluid forcing frequency. Matching of these two quantities defines resonance. Further, ϕ is the phase difference between the fluid forcing and the displacement. That is, the displacement lags the forcing by an angle ϕ, which is near $\frac{\pi}{2}$ for linear systems at resonance. The phase angle ϕ between the fluid force and the body displacement is important in determining the energy transfer from the fluid to VIVACE. From equations (3.7) and (3.8) we can deduce that $C_y \sin\phi$ has to be positive for VIVACE to generate energy. For forced vibration, Gopalkrishnan (1993) reported that for A/D =0.3, $C_y \sin\phi$ is positive for reduced velocity in the range of 5.5 < U*< 8.0. In his experimental setup, the value of $C_y \sin\phi$ becomes negative as the amplitude of the forced oscillation increases to over 0.85. In free vibration experiments, $C_y \sin\phi$ can never be negative and for lower mass ratio the value of $C_y \sin\phi$ is positive for higher values of dimensionless amplitude (up to 1.13) as reported in (Williamson and Govardhan 2004) .

Next, we derive expressions for the various stages of available power and for the VIVACE energy density.

Power in fluid: In the present analysis the power in the flowing fluid is taken over the projected area of the cylinder in the direction perpendicular to the flow direction and

can be calculated as follows. The kinetic pressure head in the fluid from Bernoulli's equation is $\frac{1}{2}\rho U^2$. The force acting over the projected area DL of the cylinder in direction-x of the flow (see Figure 2.1) is $\frac{1}{2}\rho U^2 DL$. For an oscillating cylinder, the projected area where the cylinder encounters the fluid is (2A+D)×L but this area would not be completely representative of fluid power utilized because the fluid in this projected area doesn't encounter the oscillating cylinder for the whole oscillating period, but it is the DL projected area that always encounters the flowing fluid by the cylinder. In the case of multiple cylinders, the cylinders downstream encounter unaffected fluid due to the staggered arrangement. Since there is no clear way of defining how much power from the fluid is utilized by the oscillating cylinder and for simplicity, the projected area is used (DL). Then, the power in the fluid, being the product of the acting force times the velocity in that same direction-x is

$$\text{Power in the fluid} = \frac{1}{2}\rho U^3 DL\,. \tag{3.9}$$

Equation (3.9) provides a fluid power for reference and nondimensionalization. It is not appropriate to use it in the denominator in energy density calculations. A more appropriate measure of efficiency is the one used by Department of Energy for ocean energy converters, where energy density is measured in kW/m^3. The implications of using energy density instead of efficiency is that it takes into consideration the entire space affected by the converter. For example, a ducted turbine like the Lunar Power needs a downstream clearance of about 10 duct lengths and a vertical clearance of about one duct diameter (Bedard and Previsic 2005; Bedard et al. 2005). Further, moored wave energy converters obstruct use of the entire footprint volume.

Fluid power in VIVACE: The work done by the fluid force acting on a VIVACE cylinder during a vibration cycle is obtained from the inner vector product of the force by the displacement vector $d\vec{x}$ integrated over one cycle. Therefore, the work done on the body during a cycle of oscillation of the cylinder is

$$W_{\text{VIVACE-Fluid}} = \int_0^{T_{osc}} F_{fluid}\,\dot{y}\;\mathrm{d}t \tag{3.10}$$

Then, the fluid power in VIVACE is

$$P_{\text{VIVACE-Fluid}} = \frac{W_{\text{VIVACE-Fluid}}}{T_{\text{osc}}}. \tag{3.11}$$

The force exerted on the VIVACE cylinder by the fluid is given by the right hand side of equation (3.5). If we multiply the force by the instantaneous velocity, integrate the right hand side and average it over the cycle period T_{osc} we have:

$$P_{\text{VIVACE-Fluid}} = \frac{1}{T_{osc}} \int_0^{T_{osc}} \frac{2}{\pi D} c_y(t) m_d U^2 2\pi f_{fluid} y_{\max} \cos\left(2\pi f_{fluid} t\right) dt \tag{3.12}$$

In synchronization, we have

$$f_{fluid} = f_{v,\text{mode}} = f_{osc} = \frac{1}{T_{osc}}.$$

Therefore,

$$P_{\text{VIVACE-Fluid}} = f_{osc} \int_0^{\frac{1}{f_{osc}}} \frac{2}{\pi D} C_y m_d U^2 2\pi f_{osc} y_{\max} \sin\left(2\pi f_{osc} t + \phi\right) \cos\left(2\pi f_{osc} t\right) dt, \tag{3.13}$$

$$= \frac{2}{D} C_y m_d U^2 2\pi f_{osc}^2 y_{\max} \left(\frac{1}{f_{osc}} \sin(\phi) + \cos\left(4\pi f_{osc} + \phi\right) - \cos(\phi) \right) = \frac{2}{D} C_y m_d U^2 2\pi f_{osc} y_{\max} \sin(\phi). \tag{3.14}$$

Inserting the definition of m_d from Table 1.1, $m_d = \frac{\pi}{4} \rho D^2 L$, yields

$$P_{\text{VIVACE-Fluid}} = \frac{1}{2} \rho \pi C_y U^2 f_{osc} y_{\max} DL \ \sin(\phi). \tag{3.15}$$

<u>Mechanical power in VIVACE:</u> Next, from equation (3.5), we integrate the left hand side after multiplying it by the instantaneous velocity and we average it over the cycle period T_{osc}. That yields the mechanical power in VIVACE as

$$P_{\text{VIVACE-Mech}} = \frac{1}{T_{osc}} \int_0^{T_{osc}} \left(\left(m_{osc} + m_a \right) \ddot{y} + c_{total} \dot{y} + K_{spring} y \right) \dot{y} \ \mathrm{d}t. \tag{3.16}$$

Only the term in phase with the velocity generates a non-zero energy term. Thus,

$$P_{\text{VIVACE-Mech}} = \frac{1}{T_{osc}} \int_0^{T_{osc}} 4\pi (m_{osc} + m_a) \zeta_{total} \dot{y}^2 f_{n,water} \ \mathrm{d}t. \tag{3.17}$$

Using the sinusoidal expression for y(t) from equation (3.7) into the above integral, we have the R.H.S as

$$P_{\text{VIVACE-Mech}} = 8\pi^3 (m_{osc} + m_a)\zeta_{total} \left(y_{\max} f_{osc} \right)^2 f_{n,water} . \quad (3.18)$$

Equating fluid power in VIVACE to mechanical power in VIVACE: Now, equating the VIVACE power from the fluid in equation (3.15) to the mechanical power in VIVACE in equation (3.18) – since they are integrals of the two sides of equation (3.6) – we have

$$\frac{1}{2}\rho\pi C_y U^2 f_{osc}\ y_{\max} DL\ \sin(\phi) = 8\pi^3 (m_{osc} + m_a)\zeta_{total} \left(y_{\max} f_{osc} \right)^2 f_{n,water} , \quad (3.19)$$

or

$$\frac{1}{2}\rho\pi C_y U^2 f_{osc}\ y_{\max} DL\ \sin(\phi) = 8\pi^3 \frac{\pi}{4}\rho D^2 L(m^* + C_a)\zeta_{total} \left(y_{\max} f_{osc} \right)^2 f_{n,water} , \quad (3.20)$$

or

$$C_y U^2 \sin(\phi) = 4\pi^3 D(m^* + C_a)\zeta_{total} y_{\max} f_{osc} f_{n,water} \quad (3.21)$$

It is assumed that we can measure experimentally three of the four quantities C_y, $\sin(\phi)$, y_{max}, ζ_{total} and solve for the fourth quantity.

Upper limit of VIVACE: The actual energy harnessed of the VIVACE Converter, can be calculated based only on the harnessed energy measured during lab tests of the VIVACE model in the LTFSW Cannel. Nevertheless, an upper limit, can be calculated as the power in VIVACE – either in fluid form (equation 3.15) or in mechanical form (equation 3.18).

$$P_{\text{UL-VIVACE}} = \frac{1}{2}\rho\pi C_y U^2 f_{cyl} y_{\max} DL \sin\phi , \quad (3.22)$$

where, for a given experiment, U, D, L, ρ, m* are specified; f_{osc}, $y_{\max}$, ϕ are measured; and C_y is calculated as follows.

In equation (3.7), for t = $\frac{1}{4}T_{osc}$ and for t = $\frac{3}{4}T_{osc}$, the displacement is at its maximum. So,

$$y(t = \tfrac{1}{4}T_{osc}) = y_{\max} \sin\left(2\pi f_{fluid}\ \tfrac{1}{4}T_{osc}\right) = y_{\max} . \quad (3.23)$$

The velocity is zero, thus eliminating the term with the unknown damping; and the acceleration is at its maximum, with

$$\ddot{y}(t=\tfrac{1}{4}\mathrm{T}_{\mathrm{osc}}) = -\omega_{osc}^2 y_{\max} \sin\left(2\pi f_{fluid}\,\tfrac{1}{4}\mathrm{T}_{\mathrm{osc}}\right) = -\omega_{osc}^2 y_{\max} \tag{3.24}$$

Using the potential value of m_a for inviscid flow and equations (3.5, 3.7, 3.8), we derive the following expression from which C_y can be calculated

$$-\left(m_{osc}+m_a\right)\omega_{osc}^2 y_{\max} + 0 + K_{spring} y_{\max} = \frac{1}{2}\rho C_y U^2 DL \sin(\tfrac{\pi}{2}+\phi) \tag{3.25}$$

Table 3.2 shows some sample calculations of $\mathrm{P}_{\mathrm{UL\text{-}VIVACE}}$ based on equation (3.22) and experimental data. The first two cases use data from (Khalak and Williamson 1999) and the third case uses data from VIVACE model tests. It should be noted that the value of C_y increases with lower mass ratio, increases with Reynolds number, and decreases with increasing damping (Khalak and Williamson 1996; 1999). Comparing cases 1 and 2 to case 3 we observe that m_{osc} decreases and Re increases both supporting higher values of C_y. The present tests, however, are performed for high damping values which result in decreasing values for C_y. Of course this points out to the need of optimizing for maximum output by trading-off between $y_{\max}$ amplitude of oscillation and c_{harn}. Experimentally, the process is shown later in Figure 3.13.

Case	***m****	**Re**	C_y	**U***	$\mathbf{y^*_{max}}$	$\sin\phi$	$P_{\mathrm{UL\text{-}VIVACE}} \Big/ \frac{1}{2}\rho U^3 DL$
1	10.3	5×10^3-1.6×10^4	2.83	5	1.18	0.1132	0.24
2	3.3	5×10^3-1.6×10^4	4.5	5	1.18	0.1132	0.38
3	1.45	9.4×10^4	4.54	6.5	1.36	0.1132	0.37

Table 3.2. Estimation of an Upper Limit of the harnessed power ofVIVACE.

Harnessable energy using VIVACE: The power that can be harnessed using the VIVACE Converter is the power extracted by the generator which is equal to the power VIVACE extracts from the fluid minus the power dissipated by structural, transmission, and internal generator losses. To simplify calculations, we assume that the damping force due to the generator, which converts the mechanical energy to electrical energy, is in phase with the velocity term and it behaves in the same way as structural and transmission damping. The total damping, as defined in Table 1.1 in dimensionless form, is

$$\zeta_{total} = \zeta_{tra} + \zeta_{sys} + \zeta_{gen} + \zeta_{harn} \tag{3.26}$$

Using equation (3.24), we have

$$\zeta_{total} = \frac{C_y U^2 \sin(\phi)}{4\pi^3 D(m^* + C_a) y_{\max} f_{cyl} f_{n,water}}. \tag{3.27}$$

and in terms of the reduced velocity factor U^*, ζ_{total} can be written as

$$\zeta_{total} = \frac{C_y U^{*2} f_{n,water} \sin(\phi)}{4\pi^3 (m^* + C_a) y^*_{\max} f_{cyl}}. \tag{3.28}$$

Combining the last two equations we derive equation (3.29) for the damping ζ_{harn} used to harness energy

$$\zeta_{harn} = \left(\frac{C_y U^{*2} f_{n,water} \sin(\phi)}{4\pi^3 (m^* + C_a) y^*_{\max} f_{osc}} - (\zeta_{tra} + \zeta_{sys} + \zeta_{gen}) \right). \tag{3.29}$$

With further manipulation we have

$$8\pi^3 (m + m_a)\zeta_{har} \left(y_{\max} f \right)^2 f_{n,water} =$$
$$\frac{\pi}{4} \rho D^2 L \left(2C_y U^2 f_{osc} y^*_{\max} \sin(\phi) - 8\pi^3 (m^* + C_a)(\zeta_{tra} + \zeta_{sys} + \zeta_{gen}) \left(y_{\max} f_{osc} \right)^2 f_{n,water} \right) \text{'} \tag{3.30}$$

which results in the final expression for the harnessed power

$$\mathrm{P}_{\text{VIVACE-Harn}} = \frac{\pi}{4} \rho D^2 L \left(2C_y U^2 f_{osc}\ y^*_{\max} \sin(\phi) - 8\pi^3 (m^* + C_a)(\zeta_{tra} + \zeta_{sys} + \zeta_{gen}) \left(y_{\max} f_{osc} \right)^2 f_{n,water} \right) \tag{3.31}$$

3.3.3. Effect of damping ratio on the response of VIVACE

The energy generation of VIVACE is accomplished by the damping term from the generator. So, it is very important to understand the effect of damping on VIV response. $A_{\max}$ is often plotted versus parameter $\mathrm{S_G}$, which is proportional to the product of mass and damping and is defined as

$$\mathrm{S_G} = 2\pi^3 St^2 (m^* \zeta_a) \tag{3.32}$$

where St is the Strouhal number for the stationary cylinder. This 'Skop-Griffin' parameter ($\mathrm{S_G}$) was used in Griffin et al. (1975), and the plot has been popularly called Griffin plot (see Figure 3.7).

From equation (3.21)

$$A_{\max} \propto \frac{C_y \sin\phi}{(m^* + C_a)\zeta_a} \tag{3.33}$$

From the above equation, $A_{\max}$ is a function of the product of sum of mass ratio and added mass coefficient with damping coefficient $\left(m^* + C_a\right)\zeta_a$. The use of a combined mass damping parameter at low mass ratios has been clearly discussed and is supported by Sarpkaya (1978; 1979); Zdravkovich (1990b) and Khalak and Williamson (1999). In Figure 3.7, it can be observed how this product affects the amplitude of VIV. This is the reason why we see high amplitude oscillation for experiments in water rather than in air. Between water and air m* is reduced by an order of 2. In Figure 3.8, it is observed that introduction of damping reduces the synchronization range and the amplitude of oscillation. The effect of damping ratio on maximum amplitude using eddy current damping has been studied by Klamo, Leonard and Roshko (2005; 2006). Their results are compiled in Table 3.3 keeping in mind that the damping they introduced is the power that can be extracted. In the runs 4(a), 4(b), and 4(c) we can observe that 3% damping is the damping from the structure and the rest 28% can be utilized.

Run	**Stiffness**	**Re**	**Zeta**	**m***	**A^*_{max}**	**U**	**f_s (hz)**	**Power**	$\frac{P_{\text{Harnessed}}}{\frac{1}{2}\rho U^3 DL} \times 100$
	(N/m)	**(A^*_{max})**				**(m/s)**		**watt**	
1(a)	65	525	0.0008	49.85	0.53	0.053	1.103	1.18×10^{-5}	7
1(b)	65	525	0.0017	49.85	0.5	0.053	1.103	2.24×10^{-5}	13
2(a)	134	525	0.0005	99.76	0.56	0.053	1.103	1.68×10^{-5}	10
2(b)	134	525	0.0011	99.76	0.49	0.053	1.103	2.82×10^{-5}	17
3(a)	264	1000	0.0006	49.85	0.66	0.100	2.100	1.01×10^{-4}	9
3(c)	264	1000	0.0026	49.85	0.5	0.100	2.100	2.50×10^{-4}	21
4(a)	15	2600	0.0014	4.52	0.73	0.068	0.378	3.64×10^{-5}	3
4(c)	15	2600	0.0107	4.52	0.7	0.068	0.378	2.56×10^{-4}	18
4(e)	15	2600	0.0211	4.52	0.65	0.068	0.378	4.35×10^{-4}	31

Table 3.3. Compilation of results from Klamo et al. (2005).

The total damping coefficient is defined as

$$c_{total} = c_{system} + c_{tra} + c_{gen} + c_{harn} \tag{3.34}$$

Analytical estimation of c_{total} for a VIVACE cylinder in VIV is not possible. Consequently, damping is measured experimentally.

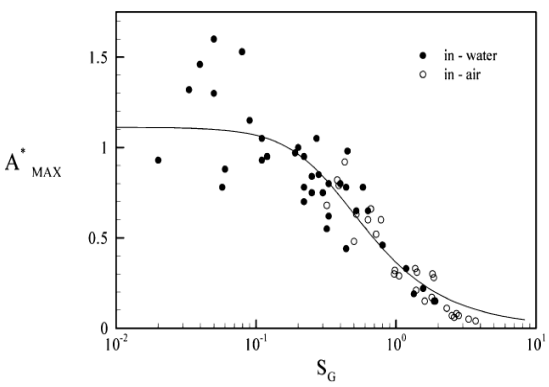

Figure 3.7. Griffin plot showing peak amplitude ratio $A^*_{\max}$ versus S_G. [Reproduced from Williamson and Govardhan, (2004)].

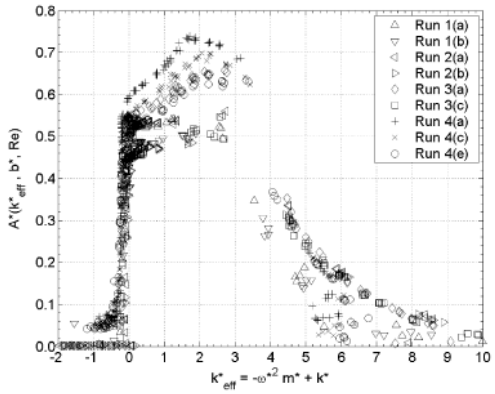

Figure 3.8. Amplitude ratio versus effective elasticity for different damping ratios. [Reproduced from Klamo et al. (2005)].

For a VIVACE cylinder in VIV, there are four sources of damping as shown in equation (3.34). The system damping c_{system} includes structural damping and fluid damping. The former is caused by friction at the component and the material scales. It is measured by performing a damping test in air (ideally in vacuum). The fluid damping is the result of energy dissipation, as the structure vibrated in a stationary fluid. The transmission damping c_{tra} is due to friction in the gear system and frictional losses of the generator as frictional bearing losses. The generator damping c_{gen} is due to the generator armature (internal) resistance R_{arm} (magnetic losses are neglected at this stage for the linear mathematical model). Finally, c_{harn} is the damping due to the load resistance R_L used to harness energy. The following damping tests are conducted to assess the quality of the VIVACE model and some of the measurements can be used to calculate the components of equation (3.35).

(i) In air with gear disconnected: It provides data to calculate the component of c_{system} due to structural damping.

(ii) In water with gear disconnected: It provides data to calculate the sum of c_{system} due to structural damping plus damping due to stationary fluid.

(iii) In water with transmission connected and generator connected to the transmission (without electrical load) : It provides data to calculate the sum of the c_{system} part due to structural damping, plus fluid damping due to the cylinder motion in stationary fluid, plus frictional losses due to the gear transmission and generator. This provides data to calculate c_{tra}.

The generator damping c_{gen} (due to the generator armature internal resistance R_{arm}), is a function of the load resistance.

The above damping coefficients (except of course for the electrical damping coefficients c_{gen} and c_{harn}) are calculated by performing a free decay test of the corresponding system. An initial displacement is given to the structure (cylinder), resulting in a damped oscillation of the structure. If y_n and y_{n+1} are two consecutive peaks of a linear system, we have

$$\frac{y_n}{y_{n+1}} = \frac{A_y \exp\left(-\zeta\omega_d t\right)}{A_y \exp\left(-\zeta\omega_d \left(t+T_d\right)\right)} = \exp\left(\zeta\omega_d T_d\right) \tag{3.35}$$

where T_d is the period of the oscillation $T_d = \frac{2\pi}{\omega_d}$. Hence, the damping ratio ζ is

$$\zeta = \frac{1}{2\pi} \ln \frac{y_n}{y_{n+1}} \tag{3.36}$$

where y_n and y_{n+1} are measured experimentally. Figure 3.9, Figure 3.10, and Figure 3.11 shows a sequence of damping tests in still water with additional components connected progressively. The test results reveal that there is a significant amount of energy that can be harnessed and a lot that is dissipated in various forms of loss. Results also imply that there is a significant room for improvement in the model. The response with the damping connected is shown in Figure 3.13.

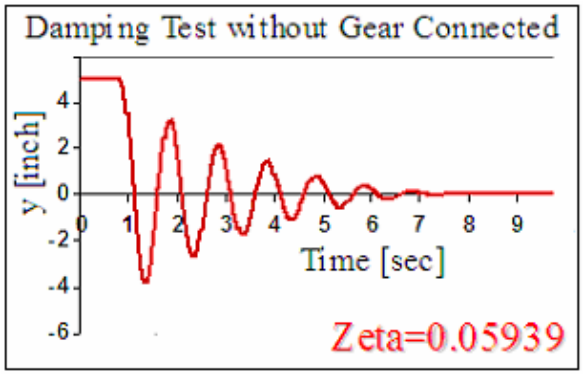

Figure 3.9. Free decay damping test in water for VIVACE model with disconnected transmission (Bernitsas et al. 2006a).

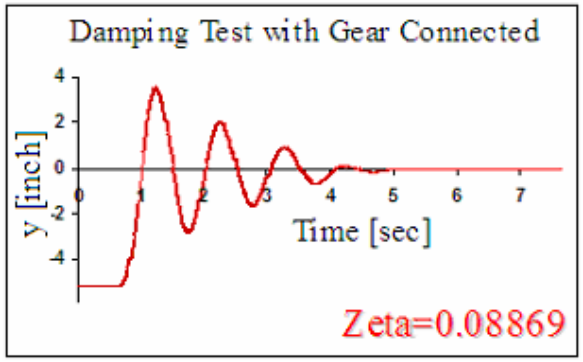

Figure 3.10. Free decay damping test in water for VIVACE model with connected transmission but disconnected generator (Bernitsas et al. 2006a).

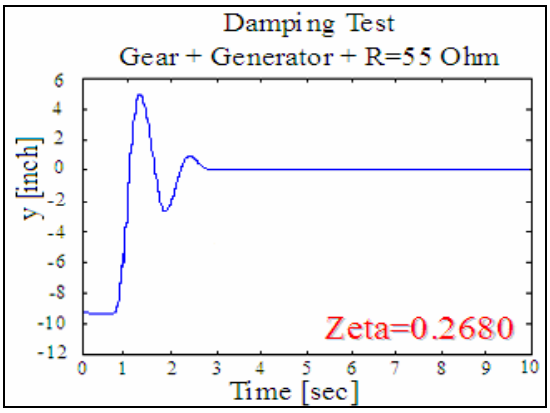

Figure 3.11. Free decay damping test in water for VIVACE model with connected transmission, generator, and R_L = 55 ohm (Bernitsas et al. 2006a).

3.3.4. Measured power

Several tests were conducted spanning a broad range of velocities and energy harnessing resistors R_L. The resistor voltage was measured along with the harnessed power. In the case considered here, the test velocity was U = 0.840m/sec = 1.63knots, the load resistor was R_L=80 Ohm (see Figure 3.13, Figure 3.14, and Figure 3.15). This particular combination resulted in the highest measured energy in comparison to the power in the fluid flowing through the projected area of the cylinder (DL).

Based on the results reported, even at these early stages of development of the VIVACE Converter, the harnessed power achieved experimentally is

$$P_{\text{VIVACE}} = 0.22 \times \frac{1}{2} \rho U^3 DL \tag{3.37}$$

for U= 0.840 m/s.

The maximum peak power harnessed for the tested VIVACE module is (see Figure 3.15)

$$P_{\text{Peak}} = 0.308 \times \frac{1}{2} \rho U^3 DL \tag{3.38}$$

It should be noted that the upper limit of the VIVACE Converter harnessed power based on the model tests is (see Table 3.2)

$$P_{\text{UL-VIVACE}} = 0.37 \times \frac{1}{2} \rho U^3 DL \tag{3.39}$$

On the basis of test measurements and evaluation of the system damping and set up, there is a lot of room for increase in values of both numbers in future developments.

Figure 3.12 shows 60 seconds of recorded signals for R_L = 80 Ohm and U = 0.805 m/s. The measured cylinder displacement *y(t)*, the voltage at the load resistor ends $V_{load}(t)$, and power; and calculated cylinder velocity $\dot{y}(t)$ are shown in Figure 3.12. The cylinder velocity is calculated by time differentiation of the cylinder displacement.

3.4. TEST RESULTS

Figure 3.13 and Figure 3.14 show the measured dimensionless amplitude of VIV and the measured power output, respectively. Figure 3.15 shows the measured power in comparison to the power in the fluid flowing through the projected area of the cylinder

(DL) calculated by integrating the voltage measured. We can make several observations based on these results.

(a) Figure 3.13 shows that as R_L increases, that is damping decreases, the VIV amplitude and range of synchronization increase.

(b) For R_L of infinity, the electrical power take-off goes to zero as the generator ends are open and electrical current is zero.

(c) Figure 3.13 shows that the amplitude of oscillation and range of synchronization remain high even at the high damping values used. This is necessary for extracting generating energy using VIV.

(d) Figure 3.15 shows that the maximum power harnessed reaches a value of $0.3077\times\frac{1}{2}\rho U^3 DL$ corresponding to an integrated power harnessed in a cycle of $0.22\times\frac{1}{2}\rho U^3 DL$ and an upper limit of $0.3663\times\frac{1}{2}\rho U^3 DL$. This is achieved by approximately optimizing the system with respect only to one variable R_L and even at the low speed of 0.840m/sec. In most of the cases, the peak power harnessed was around $0.25\times\frac{1}{2}\rho U^3 DL$.

(e) It appears that the relatively high Reynolds number at which the experiments are conducted supports higher amplitudes of oscillation than those typically reported in the literature. Indeed, in the present experiments with the VIVACE model, maximum amplitude of about 2×D at a Reynolds number of 0.44×10^5-1.34×10^5 was measured. Recent experiments by Exxon (Ding et al. 2004), also concluded that high amplitude oscillation is possible at high Reynolds numbers.

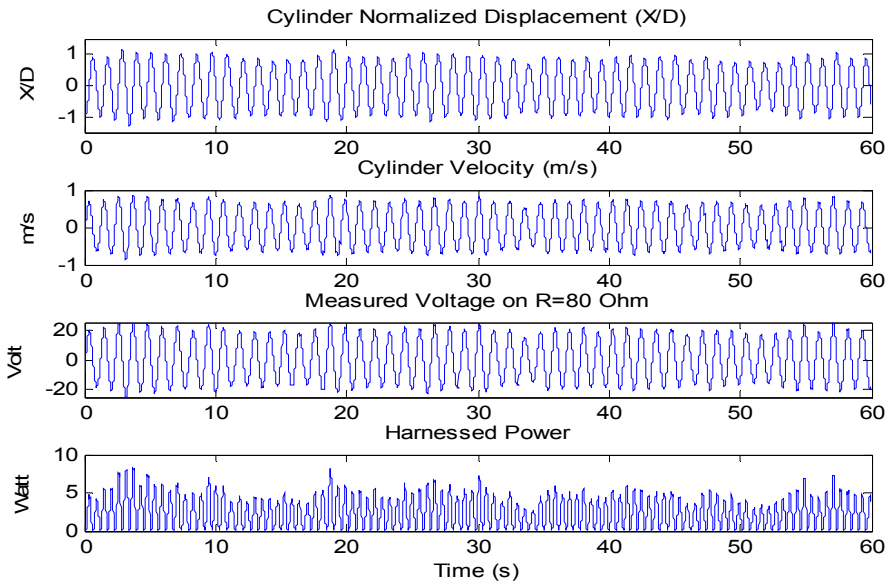

Figure 3.12. Time histories of measured cylinder displacement, potential, and power; and calculated cylinder velocity (Bernitsas et al. 2006a).

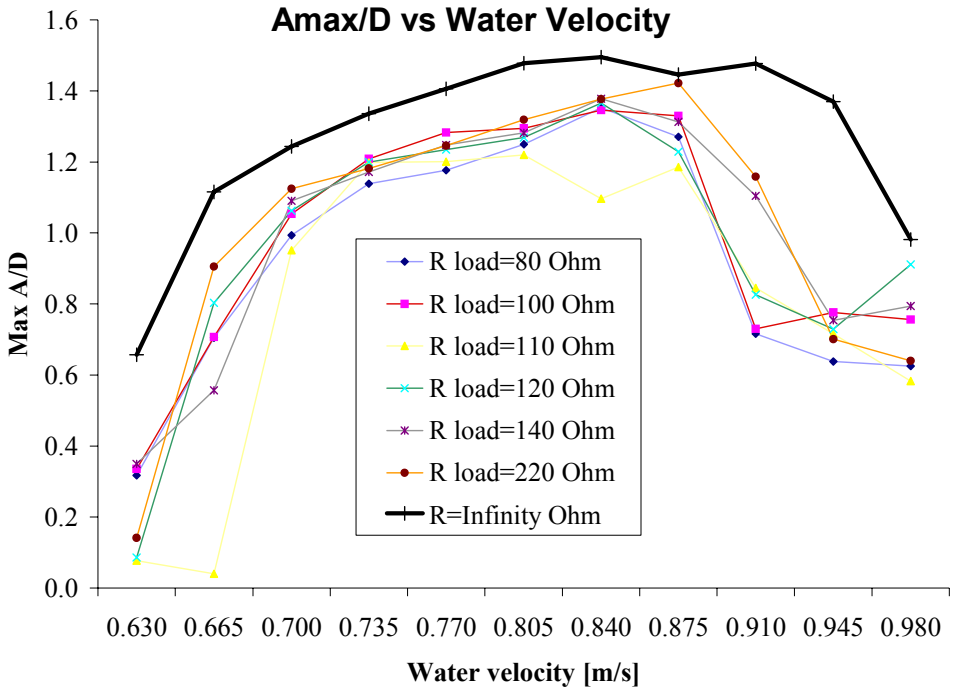

Figure 3.13. Normalized amplitude vs. water velocity for different resistance load (Bernitsas et al. 2006a).

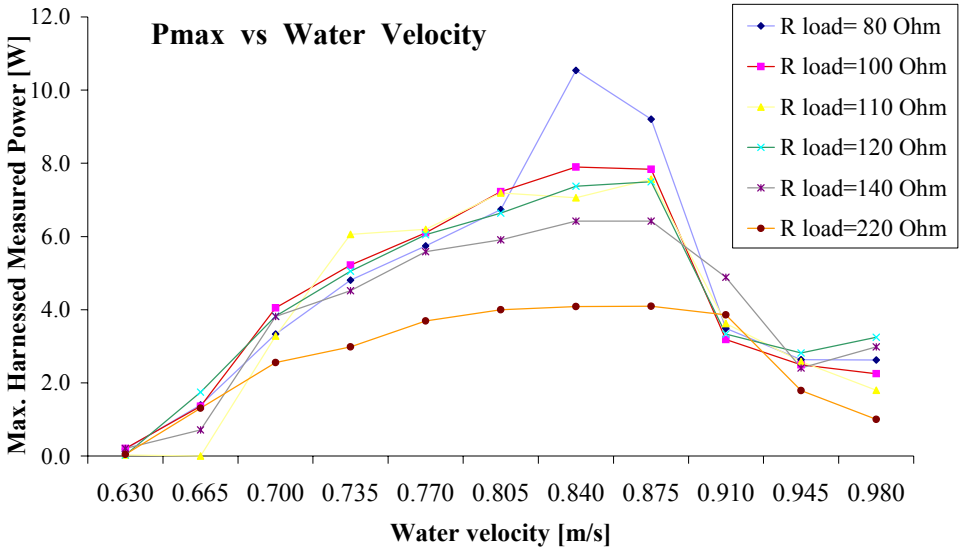

Figure 3.14. Generated power vs. water velocity for different resistance load (Bernitsas et al. 2006a).

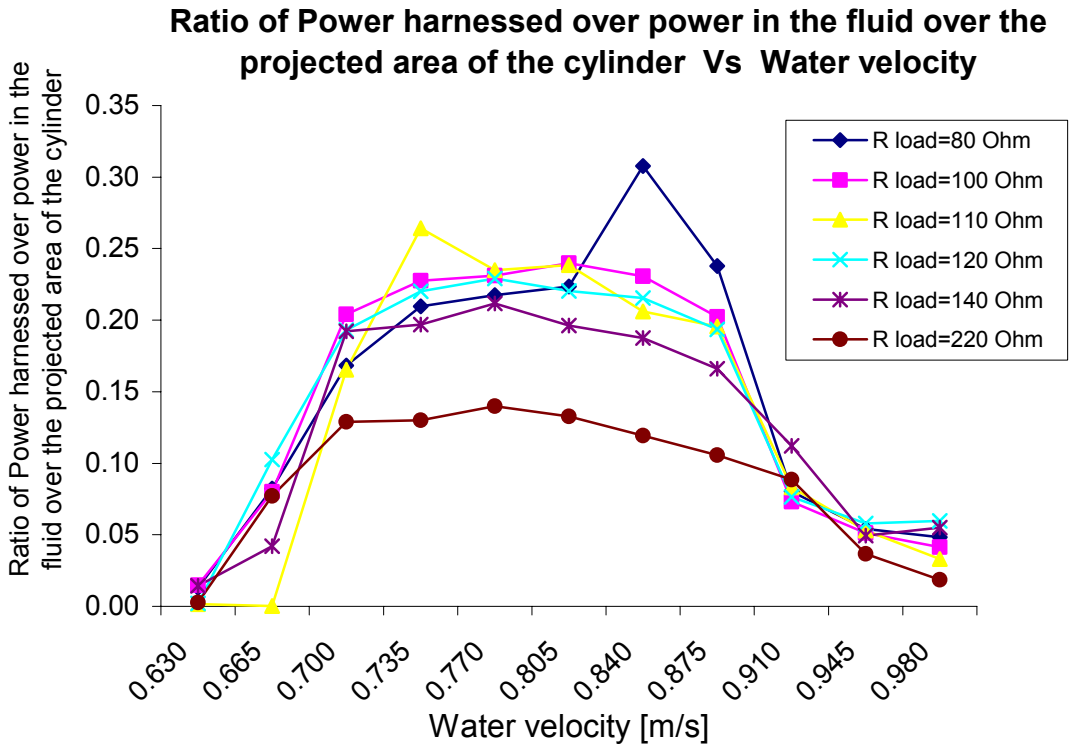

Figure 3.15. Ratio of Power harnessed over power in the fluid within the projected area of the cylinder Vs Water velocity for different resistance load

3.5. DESIGN, APPLICATIONS, BENCHMARKING

In this Section, the VIVACE Converter design is discussed as it may apply to various applications from small devices of a few Kilo-Watts to offshore power plants of a Giga-Watt. Calculations are based on the most recent lab measurements of the power harnessed using a VIVACE Converter.

3.5.1. Design

A VIVACE Converter, generating usable energy from ocean/river currents is modular, flexible, and scalable. Thus, it can be designed, manufactured, and installed to generate electricity in diverse applications. These three key words as used in this chapter are defined next.

Modular: A VIVACE Converter is an assembly of VIVACE modules. It may consist of a single module with a diameter of 2cm and length of 30-40cm to thousands of modules with cylinders of 1m in diameter and 20m in length.

Flexible: The VIVACE Converter is flexible in the sense that it can be designed to generate electricity from ocean/river currents in a variety of configurations for a given power output. The following design variables of a VIVACE Converter and of the oscillating VIVACE cylinders allow great flexibility (Figure 3.5): number of cylinders, density of cylinders in space, cylinder dimensions (D, L), cylinder surface properties such as roughness and turbulence stimulators, cylinder relative arrangement with respect to each other (t_1, p_1), cylinder relative arrangement with respect to the water velocity profile, cylinder relative location in the body of water (d) from which they extract energy, cylinder oscillating mass ratio m*, spring stiffness K_{spring}, useful damping to harness energy c_{harn}.

Scalable: The VIVACE Converter is scalable in the sense that it can be designed - based on the same four concepts presented in Section 3.2– using small or large module. As explained in the principles below special attention has to be paid to the hydrodynamic scale defined by the Reynolds number.

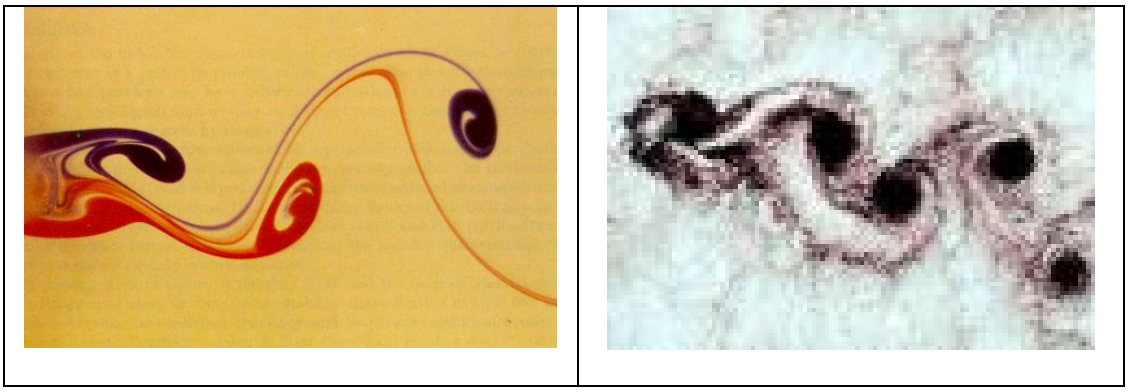

Figure 3.16 Vortex shedding behind a cylinder at different scales of Reynolds number, the left picture is a small scale (lab) Re ≈ O(10^2) and the right picture is a large scale (island) Re ≈ O(10^{12}).

Scalability and flexibility of the design of a VIVACE Converter are based on the following four principles:

Principle #1: Vortex Induced Vibrations (VIV) of circular cylinders occurs practically over the entire range of Reynolds number (Re) (see Figure 3.16). VIV doesnot occur for a smooth cylinder in two ranges of Re, which correspond to the two ranges of noncoherent alternate vortex shedding in a steady flow past a stationary cylinder. Hereafter we refer to these ranges as the no vortex shedding zones or dead zones.

(i) $Re < 40$ corresponding to the pre-vortex-shedding range.

(ii) $3\times10^5<Re<5\times10^5$ corresponding to the transition region from laminar to turbulent flow.

These ranges are obtained experimentally and are valid for smooth cylinders. They are affected by various factors such as the condition of the cylinder surface, ambient flow vorticity, fluid conditions affecting water viscosity such as salinity and temperature. Some of these factors can be modified in the design or operation state in a passive or active manner to ensure that the VIVACE cylinders remain in VIV as explained in the next principle. The technique for modification of the surface to sustain in the high Reynolds number dead zone is discussed in Chapter 7.

Principle #2: Modifications to the basic geometry of the oscillating cylinder in a passive or active manner can be designed and built to ensure that a VIVACE cylinder can remain in VIV for the entire practical range of Reynolds numbers. Following, is a non-

exhaustive list of techniques which can be used to implement this principle to achieve scalability and flexibility of the VIVACE Converter:

(i) Change the cylinder diameter. Reynolds number changes linearly proportionally with the diameter. This change is practical only when small changes in Re is sufficient to move a flow out of a dead zone.

(ii) Introduce surface roughness. It has a strong impact on the location of the dead zones on the Re scale. Introducing surface roughness passively is very effective when the incoming flow conditions are known a priori and do not change significantly in time.

(iii) Introduce fixed (passive) turbulence stimulators. Like surface roughness, turbulence stimulators, have a strong impact on the location of the dead zones on the Re scale. They are very effective when the incoming flow conditions are known a priori and do not change significantly in time.

(iv) Introduce controllable (active) turbulence stimulators. In the unlikely case of strong variation of the incoming flow velocity in time, active control through turbulence stimulators remains the last resort.

Principle #3: For a given Reynolds number, a VIVACE cylinder can be in synchronization over broad ranges depending on the oscillating mass, the displaced fluid mass, and the stiffness of the supporting springs. The synchronization range may be very long for $m^* < 0.54$ (Govardhan and Williamson 2002) and this was not tried in the present experiments.

Principle #4: For a given Reynolds number, m^* defined in Principle #3, controls the range of synchronization. The amplitude of oscillation depends on m^* as well. To maximize the power harnessed by the VIVACE Converter as given by equation (3.31), the following non-exclusive list of design variables can be controlled both passively and actively:

(i) The supporting spring stiffness

(ii) The oscillating mass of the cylinder plus appendages

(iii) The damping C_{har} induced back into the VIV system by the harnessed electrical energy.

(iv) The length of each VIVACE cylinder that has to be long enough to ensure low m* but not too long to result in flexural mode excitation which will reduce the VIV correlation length.

An extensive study on the effect of Reynolds number on VIVACE operation is studied in Chapter 4.

3.5.2. Applications

Modularity, flexibility, and scalability of the VIVACE Converter make it suitable for a wide variety of applications. A non-exhaustive list of applications is provided below classified in terms of scale of harnessed electrical power. The latter is proportional to the overall dimensions of the converter even though the dimensions of the VIVACE cylinders in VIV and their relative positions vary dramatically. The power calculated in the examples below is based on:

(i) Flow velocity U = 1.5 m/s

(ii) Power harnessed, $P_{VIVACE} = 0.22 \times \frac{1}{2} \rho U^3 DL$ which is the RMS of harnessed power measured in the VIVACE model tests. It should be noted that this value is conservative since the system has not been optimized in any way.

(iii) Spacing between cylinders of $p_1 = 8 \times D$ and $t_1 = 5 \times D$. This is greater than the required minimum of 4×D for minimal interference between stationary cylinders (Chen 1987; Zdravkovich 1997). Also it is significantly larger than the in-flow and transverse clearance is of 2×D and 1×D, respectively, for a cylinder in VIV upstream from a fixed cylinder (Sumer and Fredsoe 1997). Further it is larger than the in-flow and transverse clearances of 3×D and 1×D, respectively, for a cylinder in VIV downstream from a fixed cylinder (Sumer and Fredsoe 1997). Further, as shown in Figure 3.5, cylinder rows are staggered in the flow direction and aligned in the other two directions.

(iv) The weight of the foundation and the supporting struts has been calculated based on DNV regulations for similar marine foundation templates and a 25% penalty for safety.

Based on these conservative assumptions, the basic design variables of VIVACE Converters for a given power output can be calculated. It should be noted that there are infinite solutions for each power plant configuration. We have selected several variables

and particularly D and L in such a way that the number of cylinders is not excessive. Higher number of cylinders results in higher energy density but increased complexity. Further, it is assumed that a typical household uses 1kW (IEIA 2006). This provides a measure of the utility magnitude of the six scales of the VIVACE Converter considered in the examples below.

3.5.3. Benchmarking

Two benchmarking methods are used in this Section. First, VIVACE is compared to traditional and alternative energy resources based on data from the Michigan Public Service Commission (MPSC 2005). The comparison results are shown in Figure 3.17 in terms of $/kWh. The assumptions behind these calculations are summarized in Table 3.4, Table 3.5, Table 3.6, and Table 3.7. Table 3.5 shows the fuel cost per Btu; Table 3.6, and Table 3.7 show the assumptions for conventional and alternative energy generation, respectively. The assumptions behind the VIVACE Converter are summarized in Table 3.8.

Scale	Power $P_{VIVACE\text{-}Har}$ (MW)	Number of Cylinders	D (m)	L (m)	h (m)	S (m^2)	W (ktons)
Giga	1000	32,849	2	40	60	1,497,335	1,775
Mega	100	6,570	2	20	30	258,998	159.0
Large	10	1,314	1	20	15	14,569	11.4
Medium	1	526	0.5	10	15	2,428	1.1
Small	0.1	328	0.2	4	5	92	0.10
Micro	0.05	657	0.1	2	5	45	0.05

Table 3.4. Design particulars of six different scales of the VIVACE Converter.

Assumptions	$/MMBtu
Pulverized Coal	1.25
Bituminous Coal	2.75
Powder River Basin Coal	1.25
Uranium	0.5
Natural Gas	6
Landfill Gas	1.8
Capital Charge	14%

Table 3.5. Fuel cost assumptions.

The second benchmarking is performed by comparing the VIVACE Converter to leading wave energy converters. This benchmarking is much more difficult to do

correctly as complete sets of consistent data are not available. The three devices selected are the Pelamis (Pelamis), the OPT buoy (OPT; OPT 2001) and the Energetech (Energetech) converters. The data collected about these three devices are summarized in Table 3.10, and Table 3.11 below. The data for the VIVACE Converter are summarized in Table 3.15. Comparison measures are presented in Figure 3.29, Figure 3.30, and Figure 3.31.

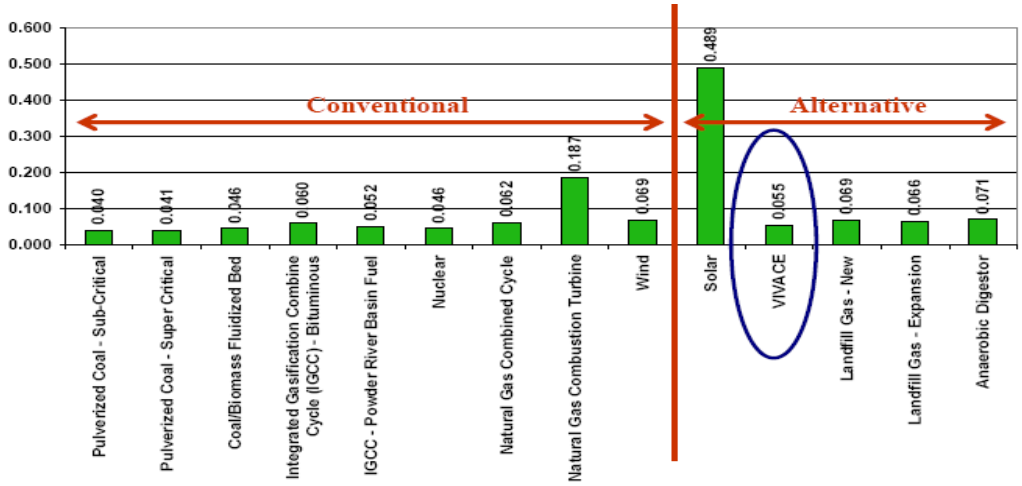

Figure 3.17. Cost comparison between conventional and alternative sources of energy and the VIVACE Converter.

Conventional Technology	Size	Capital Cost	Fixed OandM	Fuel Cost	Variable OandM	Availa -bility	Cost / kWh
	MW	$/kW	$/kW	$/kWh	$/MWh		$/kWh
Pulverized Coal – Sub-Critical	500	1370	42.97	0.012	1.80	85%	0.040
Pulverized Coal - Super Critical	500	1437	43.60	0.011	1.70	85%	0.041
Coal/Biomass Fluidized Bed	350	1,505	44.77	0.012	4.24	85%	0.046
IGCC- Bituminous	550	1,647	59.52	0.025	0.95	80%	0.060
IGCC - Powder River Basin Fuel	550	1,845	59.52	0.013	0.95	80%	0.052
Nuclear	1000	2,180	67.90	0.005	0.53	90%	0.046
Natural Gas Combined Cycle	500	467	5.41	0.043	2.12	45%	0.062
Natural Gas Combustion Turbine	160	375	2.12	0.063	3.71	5%	0.187

**Integrated Gasification Combine Cycle (IGCC)

Table 3.6 Assumptions for cost estimate of conventional energy generation.

Technology	Capital Cost	Fixed OandM	Fuel Cost	Variable OandM	Availability	Cost per kWh
Alternative Generation	**$/kW**	**$/kW**	**$/kWh**	**$/MWh**		**$/kWh**
Wind	1200	156.43	0.000	-18.00*	25%	0.069
Solar	6000	125.14	0.000	0.00	20%	0.489
VIVACE	3000	70.72	0.000	0.00	90%**	0.055
Landfill Gas New	1200	100.00	0.018	28.22	90%	0.069
Landfill Gas Expansion	1000	100.00	0.018	28.22	90%	0.066
Anaerobic Digestor	2500	100.00	0.000	24.82	90%	0.071

* Includes tax credits $18/MWh.

** Accounts for availability of energy source and maintenance time.

Table 3.7 Assumptions for cost estimate of Alternative energy generation.

Power $P_{VIVACE\text{-}Har}$	**100 MW**
D	1 m
L	20 m
m	1880 kg
m_a	16100 kg
m*	1
Number of cylinders	13094
VIVACE Model III power harnessed	$0.22\times\frac{1}{2}\rho U^3 DL$
Calculated upper limit	$0.37\times\frac{1}{2}\rho U^3 DL$
Vcur	1.5m/s
p	8D
t	5D
water depth h	20 m
draft d	15 m
Footprint	128 acres
Weight + foundation	148,714 tons
Footprint volume of power plant	10,359,953 m^3
kW/ton	0.6701
kW/m^3 footprint volume of power plant	0.0096

Table 3.8. Data regarding the 100MWatt VIVACE Converter.

Pelamis : It is a semi-submersible ocean wave energy converter moored to the seabed. It is designed to be used as a module of a wave farm. It is a long cylinder with four sections and three hinges which make it flexible to follow the free surface deformation. Hinges include a hydraulic ram system to capture the energy of the relative motion of the hinged cylindrical sections. It was designed in January 1998 and a prototype was built and deployed in May 2005. It is expected to become competitive in the year 2010. It is moored in water 50-60 m deep at a location 5-10 km offshore. Some relevant data are presented in Table 3.9.

Length	150 m
Diameter	3.5 m
Weight	380 tons
Weight with ballast	700 tons
Water depth	50 m
Life between refits	10 years
Rated Power	750 kW
Actual Power (Availability 40 %)	300 kW

Table 3.9 Pelamis data.

Figure 3.18: Pelamis, the wave energy converter.

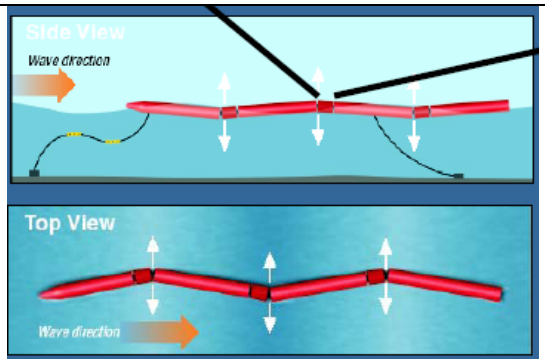

Figure 3.19: Schematic version of the Pelamis wave energy converter in action.

OPT Power Buoy : It is a semi-submersible wave energy converter moored to the sea bed. The OPT Power Buoy experiences controlled oscillations in heave. The electric

generator converts the mechanical energy in the oscillations to electricity. It is designed to be used as a part of a wave farm. Electricity is transported to land through underwater cable. It was developed in 1994 and the first tests were conducted in New Jersey in 1997. A 50 kW Power Buoy is in place in Hawaii. The company has plans to build a 10MW wave farm in the UK. Some relevant data are presented in Table 3.10.

Figure 3.20. Power buoy deployed in the ocean.

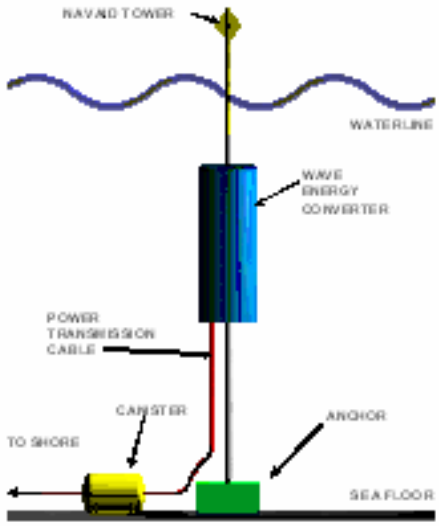

Figure 3.21. Schematic diagram of OPT power buoy system.

Length	14.63 m
Diameter	4.27 m
Water depth	30 m
Life	30 years
Rated Power	20 kW
Actual Power (Availability 40 %)	8 kW

Table 3.10. OPT Power buoy data.

Energetech Oscillating Water Column: The Energetech OWC was first developed in Australia in 1992. The first model and testing were completed in 1997. The first full scale prototype is operating in the Port Kembla Harbor. It is placed on the sea bed or is

moored at a low depth and has a parabolic wave focuser. Waves push air through a turbine, which in drives an electric generator. Some relevant data are presented in Table 3.11.

Length	36m
Width	35 m
Diameter	4.27 m
Weight	485 tons
Water depth	15 m
Life	10 Years
Rated Power	500 kW
Volume of the device	18585 m^3
Foot print volume	18900 m^3
Actual Power (Availability 33 %)	165 kW

Table 3.11. Energetech oscillating water column data.

Figure 3.22. Energetech's oscillating water column.

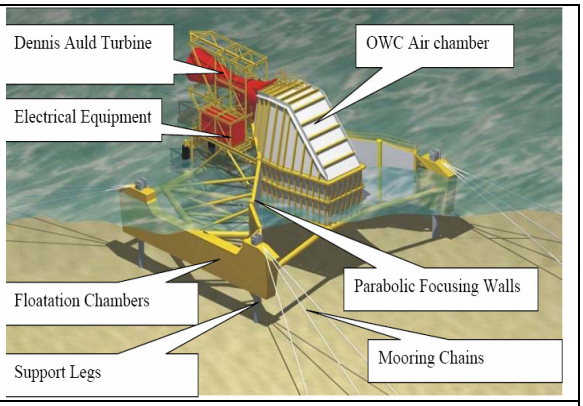

Figure 3.23. Conceptual model of Energetech's oscillating water column.

Marine Current Turbines (MCT): Marine Current Turbines (MCT) work like submerged windmills, but driven by flowing water rather than air. The MCT has twin open axial flow rotors mounted on "wings" either side of a monopole structure. The

important feature of this technology is that the wing can be raised above the water surface for maintenance. Some relevant data are presented in Table 3.12.

Figure 3.24. Marine Current Turbine during maintenance.

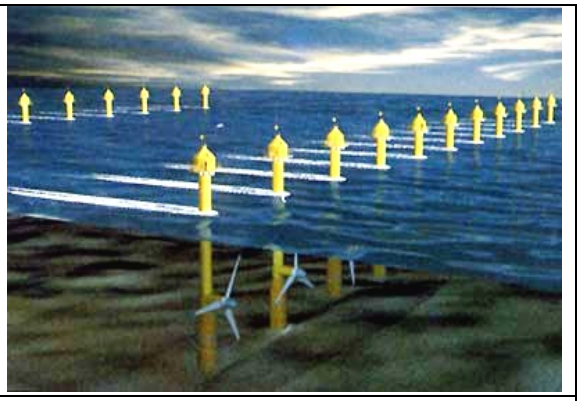

Figure 3.25. Tidal farm of Marine Current Turbines.

Turbine diameter	18.0 m
Length (Approx)	4.0 m
Breadth	46.0 m
Minimum water depth	38.0 m
Stand alone footprint volume	6,992 m^3

Table 3.12. Marine Current Turbine data.

Verdant Power: An axial-flow rotor turbine has been developed by Verdant Power to convert energy in the East Hudson river. The investigation of Axial-flow rotor turbine for the energy conversion started in 1998 and the company was formed in year 2000. The company started with small prototypes of their device in 1998 and began small scale testing. The devices that the company has made range in power output with planned models being 25 kW, 50 kW, and 100 kW thus far. Some relevant data are presented in Table 3.13.

Figure 3.26. Verdant turbine.

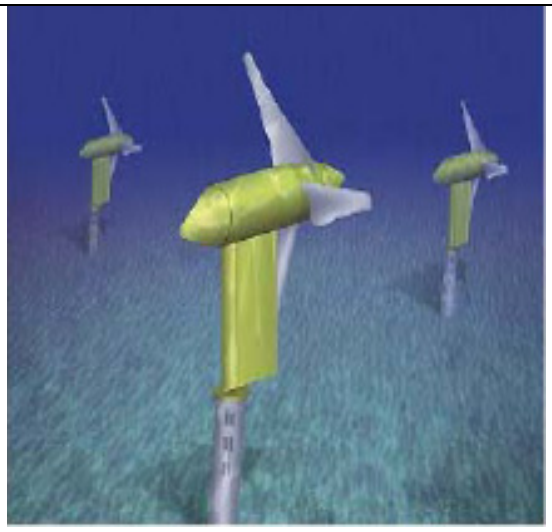

Figure 3.27. Conceptual model of Verdant turbine farm.

Turbine diameter	5.0 m
Length (Approx)	4.0 m
Breadth	5.0 m
Minimum water depth	15.0 m
Stand alone footprint volume	300 m^3

Table 3.13. Verdant data.

Lunar power: The Lunar power was first developed in U.K by Lunar Energy Limited. In this technology a venturi shaped duct is used to guide and accelerate the tidal stream toward the rotor. The duct allows the duct to redirect the water even if the water arrives at an angle of 40°, so it perpendicularly arrives to blades maximizing the efficiency.The first model and testing will be completed in 2007. Some relevant data are presented in Table 3.14.

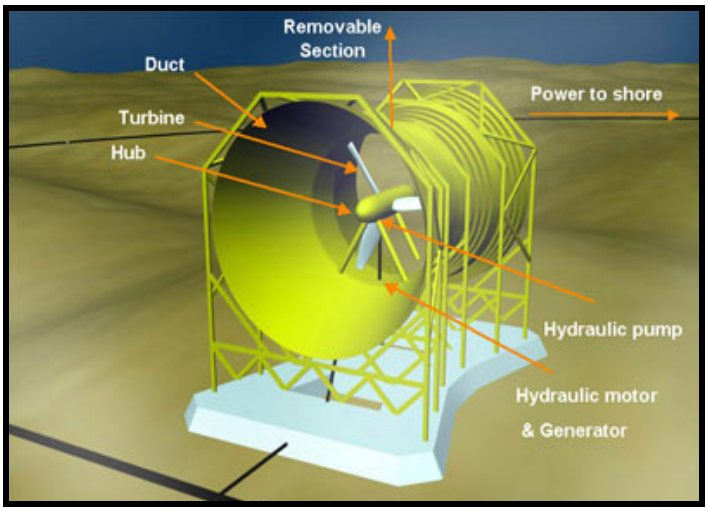

Figure 3.28. Conceptual model of Lunarpower venture duct turbine.

Length	27m
Diameter	21 m
Weight	1200 tons
Water depth	42 m
Current speed	6 knots
Life	10 Years
Rated Power	1500 kW
Volume of the device	9351 m^3
Foot print volume	23814 m^3

Table 3.14. Lunar power data.

The VIVACE Ocean/River Current Energy Converter: VIVACE was first developed in late 2003 (Bernitsas and Raghavan 2005b) and the first three models were completed and tested in the Marine Hydrodynamics Laboratory of the University of Michigan in 2004-05.

Since energy density data vary with the scale and configuration of the VIVACE Converter, a design comparable in scale to the three wave energy converters and the three current energy converters above is selected from Table 3.4 for benchmarking. This is the 100kWatt device labeled as small in Table 3.4. On the other hand, a single module of the mega-scale VIVACE in Table 3.4 is also comparable to the three wave energy converters

and the three current energy converters considered since it generates about 6.7kWatt of power. The availability of VIVACE has been estimated at 90%. The 10% down time represents maintenance and reversal time of tidal currents. Both are used in the comparison in Figure 3.30 and Figure 3.31. The small VIVACE Converter is not used in Figure 3.29 because it includes multiple module and space between them and consequently it's not comparable to single module wave energy converters. The relevant data for the small-scale (100kWatt) VIVACE Converter and the single module of the mega-scale VIVACE Converter are summarized in Tables 3.15 and 3.16, respectively.

Data for the three wave energy converters and the two VIVACE Converters are presented in Figure 3.29, Figure 3.30, and Figure 3.31. Typically, the following quantities are considered in comparing ocean energy converters.

Length	4 m
Diameter	0.2 m
Number of cylinders	328
Weight including struts and foundation	0.1 ktons
Water depth	5 m
Volume of Converter	1766 m^3
Footprint volume	1962 m^3
Life	20-30 years
U	1.5 m/s
P_{VIVACE}	$0.22\times\frac{1}{2}\rho U^3 DL$
Rated Power	100 kW
Actual Power (availability 90%)	90 kW

Table 3.15. VIVACE Converter: Data on the small-scale converter.

Length	20m
Diameter	1m
Number of cylinders	1
Weight including struts and foundation	8.675 tons
Volume of single module	23.56 m^3
Footprint volume	110 m^3
Life	20-30 years
U	1.5 m/s
P_{VIVACE}	$0.22\times\frac{1}{2}\rho U^3 DL$
Rated Power	7.6 kW
Actual Power (availability 90%)	6.84 kW

Table 3.16. VIVACE Converter: Data for a single module of the mega-scale converter.

(a) Volume Energy Density calculated as the actual energy generated over the volume physically occupied by a converter. The results for the devices considered are presented in Figure 3.29.

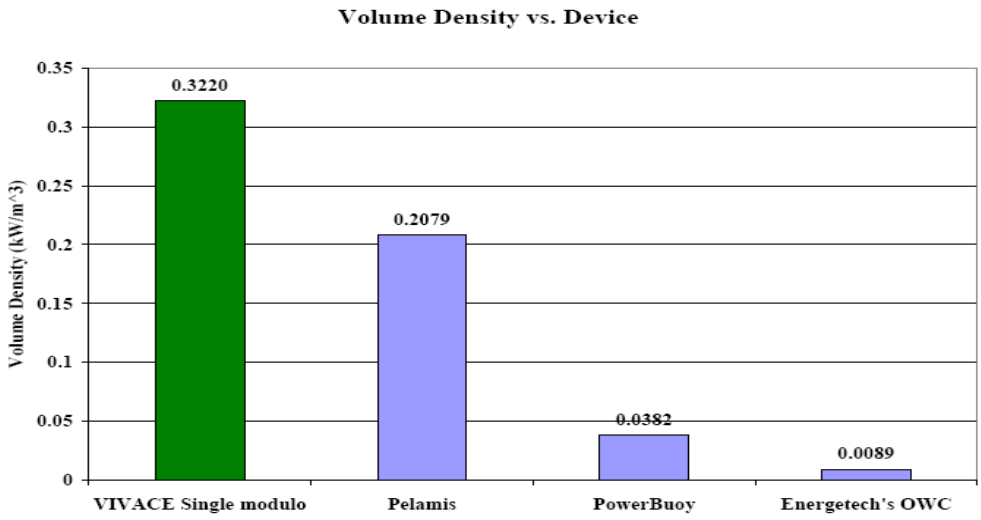

Figure 3.29. Volume energy density (Bernitsas et al. 2006b).

(b) Footprint Volume Energy Density calculated as the actual energy generated over the footprint volume blocked by a converter. For example, a surface converter has a footprint at the ocean bed and other use of the space between the footprint and the free surface is not possible. The results for the seven devices considered are presented in Figure 3.30.

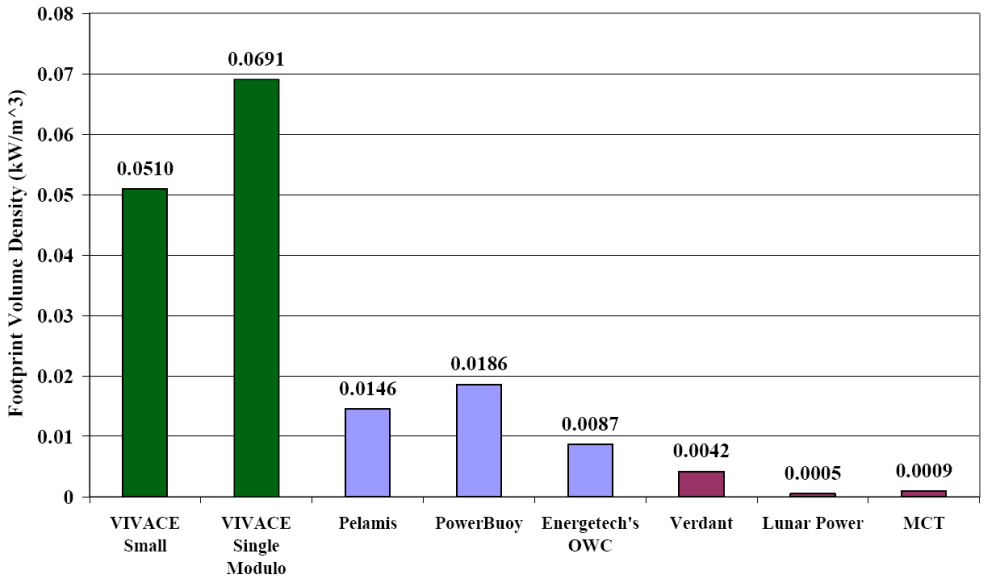

Figure 3.30. Footprint volume energy density including the turbines.

(c) Weight Energy Density calculated as the actual energy generated over the weight of the converter. The results for the five devices considered are presented in Figure 3.31.

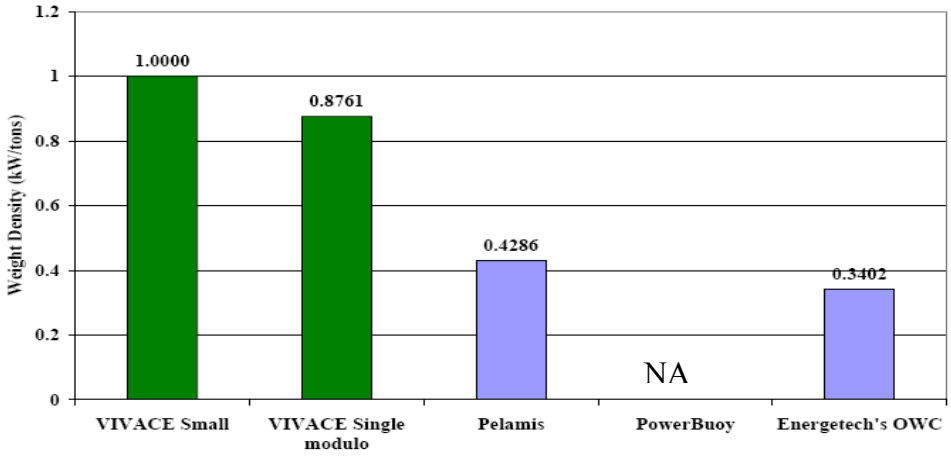

Figure 3.31. Weight energy density (Bernitsas et al. 2006b).

3.5.4. Advantages of VIVACE

Model tests and measurements on the VIVACE Converter provide preliminary data, which are satisfactory and promising. Specifically, VIVACE addresses the DOE and California Energy Commission requirement criteria as follows:

(1) Energy Density. Data presented in Section 3.4 show RMS harnessed power of $0.22\times\frac{1}{2}\rho U^3 DL$ and a peak harnessed power of $0.31\times\frac{1}{2}\rho U^3 DL$, even at this early development stage without any optimization of the design. Accordingly, the following preliminary benchmarking numbers were calculated for VIVACE using the data in Table 3.16: a) Energy of single module over displaced volume =0.3220kW/m^3, b) Energy of single module over foot print volume = 0.0691kW/m^3 c) Energy of single module over weight = 0.8761kW/ton. These values appear to be 2-10 times higher than the leading wave energy converters. Much higher energy densities can be achieved due to the modularity and scalability of VIVACE but at the expense of increased complexity.

(2) Navigation. The VIVACE Converter extracts energy from currents, which often run through the entire water body in shallow situations, not just at the water air interface like waves do. Accordingly, VIVACE whether it consists of one, a few, or thousands of oscillating cylinders remains submerged at all times, except for the time of maintenance.

(3) Coastal property. A lot of ocean energy in the form of wind, waves or currents is located along coasts. Coastal real estate is expensive and interference of any energy converter with the value of such property meets with public opposition as in the case of the wind farm off the coast of Massachusetts; a project that was cancelled in Spring 2005. VIVACE is submerged under the surface at the appropriate depth, and is therefore invisible from the surface. In addition, VIVACE is powered only by clean, renewable ocean currents, and thus is non-polluting.

(4) Marine life. The frequency of oscillation of VIVACE is slow and can be calculated approximately by using the Strouhal vortex shedding frequency for stationary cylinders. St is typically constant in each flow regime. St does not exist in only two transition regions where VIV is suppressed. In the laminar regime St=0.21; in the super-critical regime it varies around St=0.31; and in the post-super-critical regime it varies around St=0.46 (Zdravkovich 1997). Further, the mechanism that propels cylinders in

VIV transversely to the flow, that is of accumulating and shedding large vortices is similar to the way fish propel in water. Fish curve their bodies, accumulate large vortices, and then shed them by changing their body curvature (Liao et al. 2003a; Liao et al. 2003b). So, it is theorized that fish will not be affected by VIVACE motion.

(5) Maintenance. Offshore operations are expensive. Accordingly, low maintenance cost is mandatory. The VIVACE Converter has only plain cylinders exposed to the ocean environment. All other components of the Power Take-Off system such as hydraulics, transmission, and electronics will be housed in the support struts. The latter will be accessible through a hydraulic telescopic hatch, which can be raised above the free surface for easy access.

(6) Robustness. Robustness encompasses low maintenance, minimal exposure to damage, ability to take extreme environmental loads and resume operation quickly after such events, ability to extract energy with high energy density over broad ranges of excitation. Currents are steady and predictable. On the contrary, waves are available about 25% of the time and vary considerably. The VIVACE Converter is based on nonlinear resonance and consequently can operate in the range of synchronization over very broad ranges of current velocity variations. The low dependence of VIVACE on environmental conditions requires only slow time-scale controls. That is, we anticipate small variation of electrical damping for power extraction and slight spring stiffness adjustments to maintain VIVACE in nearly optimal operation.

(7) Life Cycle Cost. The installation cost of a 100MW VIVACE power plant is relatively high (Table 3.8) but the estimated electricity cost is competitive due to consistency of availability of the energy source, and low maintenance.

(8) Design Life. The VIVACE Converter design is comparable to low maintenance submerged offshore facilities with template foundation. Accordingly, its design life can easily be 20 years.

In addition to the DOE and CEC requirements VIVACE has the following advantages

- It is grid compatible
- It is scalable
- It can extract energy from low speed ocean/river currents and tides.

3.6. MAIN FINDINGS

A new concept for generation of clean and renewable energy from ocean/river currents has been introduced. An energy converter, nicknamed VIVACE (Vortex Induced Vibrations Aquatic Clean Energy) has been designed and tested. It extracts energy successfully and efficiently from fluid flow by enhancing rather than spoiling vortex shedding, utilizing rather than suppressing VIV, and harnessing rather than mitigating VIV energy for the first time. In its simplest form a VIVACE Converter module consists of a rigid circular cylinder mounted on linear springs. VIVACE models have been built and tested in the Low Turbulence Free Surface Water Channel of the University of Michigan. Based on the VIVACE design and tests, the following conclusions can be drawn. The VIVACE Converter satisfies all requirements set by the California Energy Commission and the US DOE: it is unobtrusive to navigation, the marine life, and coastal real estate; it is simple with all mechanical and electrical components sealed from the water environment; it is based on readily available offshore technology implying robustness and at least a 20 year life; it has high energy density; it generates energy with high energy density even at speeds as low as 0.5 knots. Additional advantages include consistency of current flow and its availability all year round; the broad range of synchronization, which allows efficient extraction of energy with minor and slow adjustment of basic design parameters such as the spring stiffness and induced damping; its ability to extract even more energy even in case of velocity surge to 5 knots and higher; its scalability, modularity, and design flexibility, which allow for a broad range of applications.

A single module of the VIVACE Converter was tested in the Low Turbulence Free Surface Water Channel of the Marine Hydrodynamics Laboratory of the University of Michigan. The following are the contributions in this chapter:

(i) Even though numerous experiments have been conducted in VIV since the early 1900's, the regime of applicability to the design of the VIVACE Converter had not been tested before. Specifically, for VIVACE to convert kinetic fluid flow energy to electricity, VIV has to be maintained under high damping.

(ii) In a realistic ocean environment, Reynolds number is high for energy generation, which proved to be beneficial as the amplitude of VIV at high damping condition increases significantly for high Re, a regime scarcely tested before.

(iii) The mathematical model proved that measurements were consistent and accurate by comparing the measured harnessed power to the power calculated using data also collected during a particular test.

(iv) The maximum peak harnessed power achieved for the tested VIVACE module was $P_{VIVACE} = 0.31 \times \frac{1}{2} \rho U^3 DL$. The corresponding integrated harnessed power in that particular test was $P_{VIVACE} = 0.22 \times \frac{1}{2} \rho U^3 DL$ with a theoretical upper limit based on measurements of $P_{UL\text{-}VIVACE} = 0.37 \times \frac{1}{2} \rho U^3 DL$. Test velocity was U = 0.840m/sec = 1.63 knots.

(v) The results show that the VIVACE Converter can convert kinetic energy to electricity with high energy density even at low speeds where watermills and turbines cannot operate efficiently.

Chapter 4

EFFECT OF REYNOLDS NUMBER ON VIVACE

4.1. BACKGROUND

VIVACE is scalable and can operate at both high and low Reynolds number. So, the effect of Reynolds number on the amplitude of VIV should be thoroughly understood. Vortex Induced Vibrations (VIV) of circular cylinders has been observed over the entire range of Reynolds numbers greater than 400, with the exception of the transition region from laminar to turbulent flow. The effect of Reynolds number on the amplitude and synchronization range of VIV hasn't been measured or documented well in laboratory or field tests. Previous studies at high Reynolds numbers (Re up to 10^7) were performed to measure the drag coefficient and the Strouhal number for a stationary cylinder in a steady uniform flow (Roshko 1954; Roshko 1961). To the author's knowledge experiments on VIV of cylinders at high Reynolds numbers ($Re>10^4$) are scarce and limited to studies by Moe et al.(1994) ($Re = 8.4\times10^3$), Vikestad (1998) ($Re = 10^5$), Ding et al. (2004) ($Re = 2.5\times10^5$), and Bernitsas et.al.(2006a; 2006b) ($Re = 1\times10^5$ to 2×10^5). Low Reynolds number studies on VIV have been done by numerous researchers (Williamson and Govardhan 2004). High Reynolds number (2×10^4- $4\times10^4 < Re < 3.5\times10^5$- 6×10^6) studies on VIV are very scarce because of facility limitations in achieving high Reynolds number flows. To the author's knowledge the previous high Reynolds (2×10^4- $4\times10^4 < Re < 3.5\times10^5$- 6×10^6) number study is the study done by Ding et al. (Ding et al. 2004) for the oil industry and by Bernitsas et al.(2006a; 2006b) for VIVACE.

The following conclusions have been published so far. An increase in Reynolds number increases the lift coefficient for Re in the range 5×10^3 to 8×10^3 (Khalak and Williamson 1997a). Up to two years ago, the maximum VIV amplitude reported for elastically supported cylinders in cross-flow motion was 1.13 times the diameter at a Reynolds number of 10^5 (Williamson and Govardhan 2004). Recently, research groups at Caltech and Cornell have been trying to corroborate that the VIV amplitude of oscillation is a function of Reynolds number around Re = 4.5×10^3. Recent experiments by Exxon/Mobil concluded that high amplitude oscillation (A/D = 2) is possible at high Reynolds numbers around 1.0×10^5 to 2.5×10^5 (Ding et al. 2004). In the VIV experiments performed for this dissertation, maximum amplitudes of about 2 diameters were measured routinely for Reynolds numbers in the range of 0.8×10^5 to 1.32×10^5 (Bernitsas et al. 2006b). This range of operation is near the critical Reynolds number for transition from laminar to turbulent flow. Low Reynolds number studies on VIV have been done by numerous researchers.

The design parameters for VIVACE are the cylinder diameter and the flow velocity. Selection of these two parameters controls the Reynolds number. For this reason, it is important to understand how Reynolds number affects VIVACE. The VIV amplitude directly affects the power generated by VIVACE as seen from the power equation (4.1).

$$P_{\text{VIVACE-Fluid}} = \frac{1}{2}\rho\pi C_y U^2 f_{osc} y_{\max} DL \sin(\phi) \tag{4.1}$$

The lift coefficient has an increasing trend for increasing Reynolds number as shown in Figure 4.18 (Khalak and Williamson 1999). The lift coefficient affects the power generated by VIVACE.

The vortex dynamics at different Reynolds number for flow around a stationary circular cylinder has been carefully and excellently reviewed by Williamson. Williamson and Govardhan (Williamson and Govardhan 2004) provided a good review on all the experiments conducted to study vortex induced vibrations of a bluff body. It is our understanding that VIV were never studied in the entire range of TrSL3 (Figure 4.1). In this chapter, the vortex induced vibration characteristics for the Reynolds number

regimes TrSL3 and TrBL0 are studied. Hereafter the term high Reynolds number means the TrSL3 and TrBL regimes (2×10^4- 4×10^4 < Re < 3.5×10^5- 6×10^6).

4.1.1. Classification of flow based on Reynolds number:

Previous researchers like Achenbach and Roshko have classified the regimes for the flow around a circular cylinder based on the visual observation and the changes in Strouhal number and the usual classification included six regimes.

Regime	Re range
Creeping or laminar flow	Re < 1
Steady separated region (closed near wake)	3-5 < Re < 30-40
Periodic laminar wake	30-40 < Re < 150-300
Subcritical regime	150-300< Re < 1.4×10^5
Critical regime	1.4×10^5 < Re < 1×10^6
Supercritical regime	1×10^6 < Re < 5×10^6
Transcritical regime	5×10^6 < Re

It has been observed by Schiller and Linke (1933) that the transition from laminar to turbulent boundary layer occurs in the shear layer emanating from the two sides of the cylinder after separation. In the above classification, the major changes associated with the transition in the shear layer and in turn on the base pressure, lift coefficient, correlation length, and velocity fluctuation in the subcritical regime have been masked by the constancy of the Strouhal number and the mean drag coefficient. According to the characteristics of the boundary layer over the cylinder surface and the separated shear layer, Zdravkovich (1990) subdivided the flow over a smooth cylinder into 15 character regimes as shown in Table 4.1 and Figure 4.1. In his classification, he further subdivided the subcritical regime into five more zones. Three divisions out of five are based on different aspects of the Transition of Shear Layer (TrSL). Based on the classification by Zdravkovich, the ranges of Reynolds number in which our experiments were conducted belongs to the TrSL3 and TrBL0 regime. The high amplitude of oscillation observed in

our experiments in comparison with previous experiments published in the open literature by other researchers, as shown in Figure 4.51, is attributed to the high Reynolds number.

To the author's knowledge most of the referenced previous experiments were conducted in TrSL1 and TrSL2 and the experiments conducted at the Low-Turbulence Free surface Water (LTFSW) Channel were conducted in the regimes TrSL2, TrSL3 and TrBL0. Compilation of the previous data from other investigators is shown in Table 4.2. Some of the data is taken from the review paper by Williamson and Govardhan (2004). To interpret the present results it becomes essential to understand the flow characteristic of these regimes and the near wake to understand why such a huge difference in response characteristic is observed. According to Roshko and Fiszdon (Roshko and Fiszdon 1969) near-wake is defined as the region in which interactions between the cylinder and the separated flow occur.

Reynolds number lower limit range < Re < upper limit range	Name of the regime	Characteristic feature	General properties
Re < 1		Creeping flow	**Laminar regime**
3-5 < Re < 30-40	L	Steady separation (recirculation bubble)	
30-40 < Re < 150-300	L	Periodic laminar shedding	
150-300< Re < 1×10^5 - 2×10^5	TrW and TrSL		**Subcritical regime** Laminar separation Transition in shear layer Turbulent wake
150 -200 < Re < 200 - 250	TrW1	Transition of laminar vortices in wake,	
200 - 250 < Re < 350 - 500	TrW2	Transition of irregular vortex during its formation	
350 - 500 < Re < 1×10^3- 2×10^3	TrSL1	Development of transition waves in free shear layer	
1×10^3- 2×10^3 < Re < 2×10^4- 4×10^4	TrSL2	Formation of transition vortices in free shear layer	
2×10^4- 4×10^4 < Re < 1×10^5- 2×10^5	TrSL3	Fully turbulent shear layer	
1×10^5 - 2×10^5< Re < 3.5×10^5- 6×10^6	TrBL		**Critical Regime** Laminar separation Turbulent reattachment Turbulent separation Turbulent wake
1×10^5 - 2×10^5< Re < 3×10^5- 3.1×10^5	TrS0 / TrBL0	Onset of transition at separation point	
3×10^5- 3.1×10^5 < Re < 3.3×10^5 - 3.4×10^5	TrS1/ TrBL1	Single separation bubble regime	
3.3×10^5- 3.4×10^5 < Re < 3.6×10^5 - 3.8×10^5		Unstable regime	
3.6×10^5- 3.8×10^5 < Re < 5×10^5- 1×10^6	TrS2/ TrBL2	Two-bubble regime	
5×10^5 – 1×10^6 < Re < 3.5×10^6- 6×10^6	TrS3/ TrBL3	Supercritical regime-fragmented separation bubble.	
3.5×10^6- 6×10^6 < Re < 6×10^6- 8×10^6	TrBL4	Transcritical regime – partal transition	
Re > 8×10^6	**T**	**Postcritical regime- complete transition**	

Table 4.1. Characteristic flow regimes in the wake of a circular cylinder based on Zdravkovich's classification.

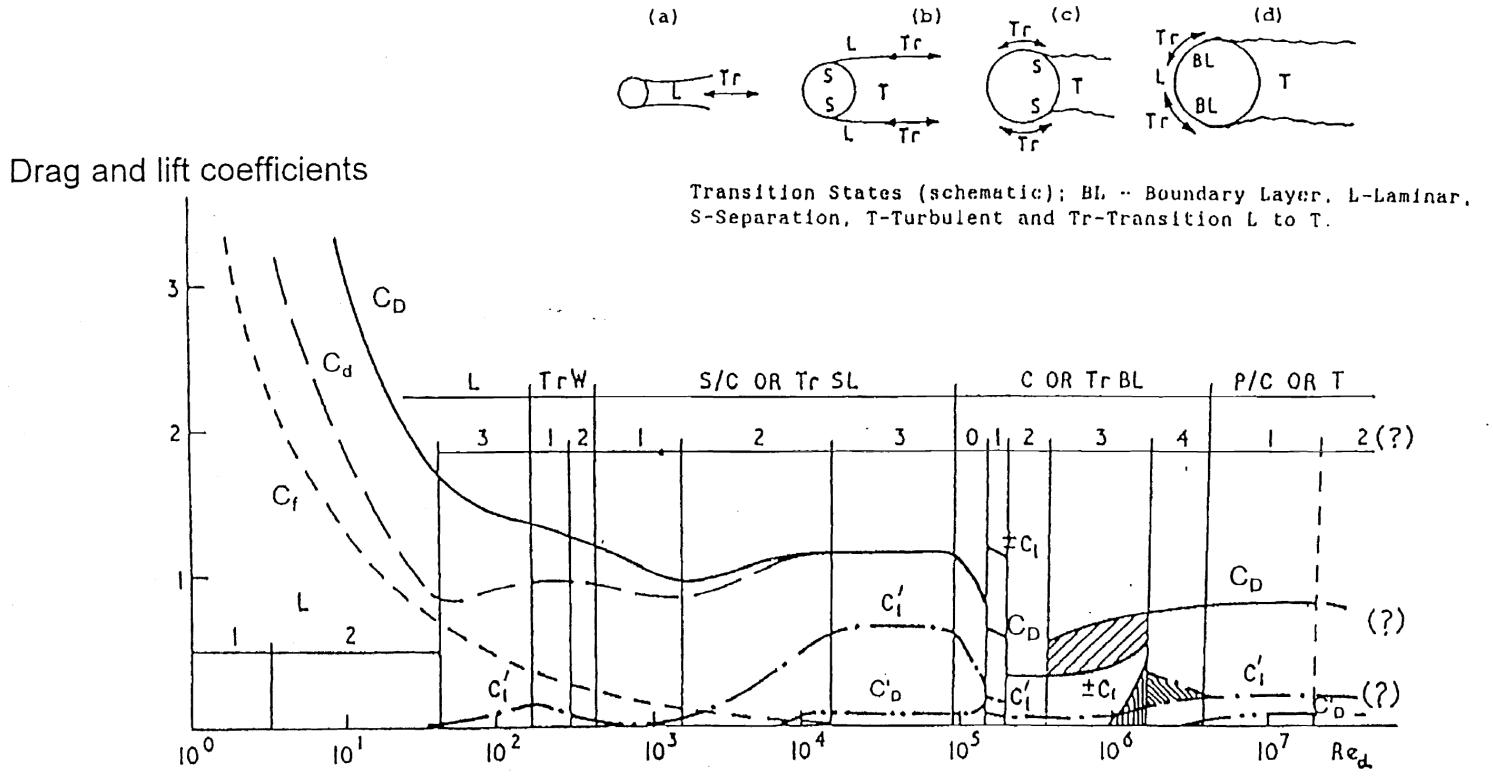

Figure 4.1. Drag and lift coefficients for a stationary circular cylinder for the whole spectrum of Reynolds number (Zdravkovich 1997).

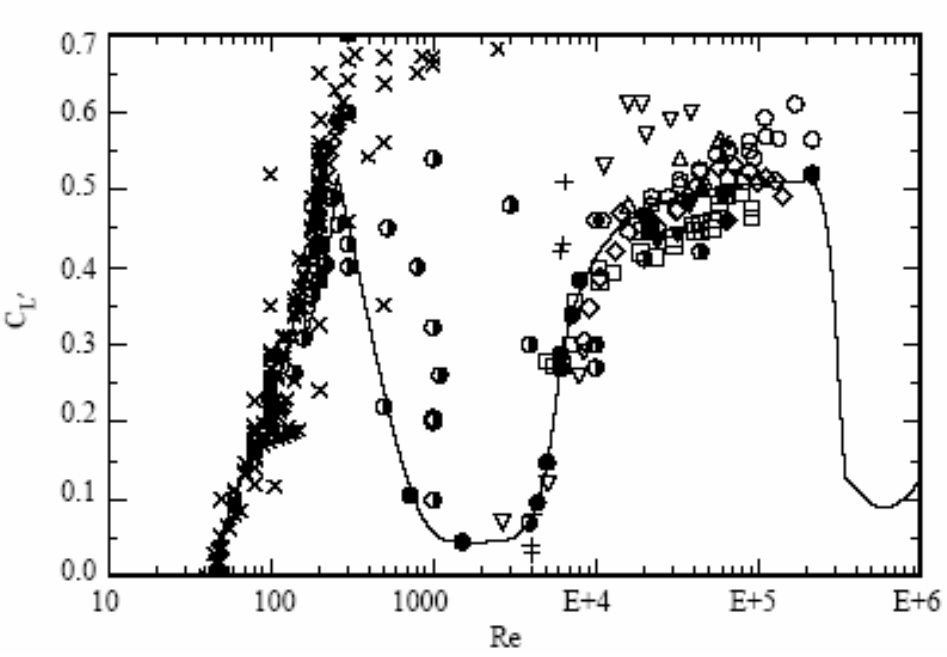

Figure 4.2. Fluctuating lift coefficient plotted versus Reynolds number. [Reproduced from Norberg (2003)].

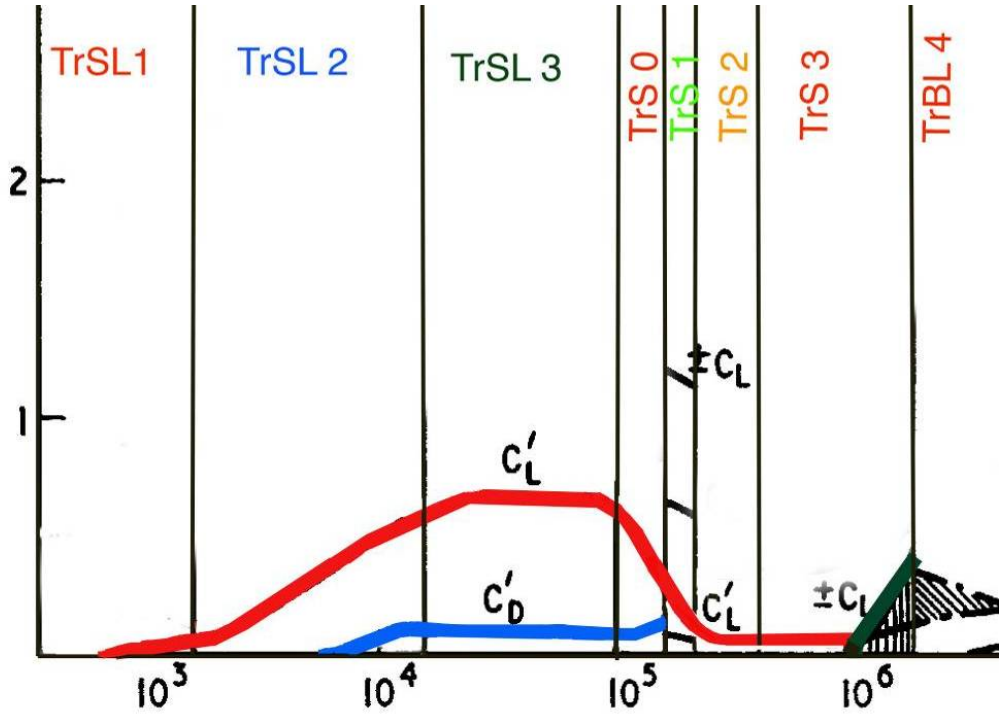

Figure 4.3. Zoomed in version emphasizing on the fluctuating lift and drag and mean lift coefficients belonging to the TrSL and TrBL regime.(Zdravkovich 1997).

Elastically-mounted rigid cylinders				
Investigators	Reynolds number	Regime	m*ζ	A* (maximum)
Klamo (2006)	4.59×10^2	TrW, TrSL1	0.665	0.23
Klamo (2006)	1.02×10^3	TrSL2	0.615	0.24
Klamo (2006)	2.48×10^3	TrSL2	0.4381	0.43
Angrilli et al. (1972)	2.50×10^3 –7.00×10^3	TrSL2	0.049	0.54
Klamo (2006)	5.18×10^2	TrSL1	0.039	0.55
Klamo (2006)	9.95×10^2	TrSL2	0.03	0.66
Klamo (2006)	2.64×10^3	TrSL2	0.006	0.75
Hover et al. (1998)	3.80×10^3	TrSL2	0.04	0.8
Gharib (1999)	1.10×10^4-4.00×10^4	TrSL2	0.094	0.84
Owen et al. (2001)	1.65×10^3 -7.50×10^3	TrSL2	0.036	0.84
Dean et al. (1977)	2.80×10^3 -1.02×10^4	TrSL2	0.0055	0.94
Sarpkaya(1995)	6.00×10^3 -3.50×10^4	TrSL2	0.052	0.95
Fujarra et al. (1998)	1.44×10^4-5.04×10^4	TrSL2	0.036	1.01
Anand and Torum (1985)	6.50×10^3 -3.50×10^4	TrSL2	0.013	1.07
Moe and Overvik (1982)	6.00×10^3 -3.00×10^4	TrSL2	0.013	1.09
Vikestad et al. (2000).	1.40×10^4-6.50×10^4	TrSL2, **TrSL3**	0.012	1.13
Jauvtis and Williamson (2003)	5.00×10^3 -1.30×10^4	TrSL2	0.0048	1.13
Khalak and Williamson (1999)	5.00×10^3 -1.60×10^4	TrSL2	0.0047	1.18
Govardhan and Williamson (2002)	2.90×10^3 -1.90×10^4	TrSL2	0.0027	1.19
Brankovic and Bearman (2006)	3.00×10^3 -2.10×10^4	TrSL2	0.00012	1.2
Jauvtis and Williamson (2004)	7.20×10^3 -1.54×10^4	TrSL2	0.0064	1.5
Present experiments	8.00×10^3 -1.50×10^5	TrSL2, **TrSL3,TrBL**	0.251	1.97
Bernitsas et al. (2006b)	8×10^4 -1.32×10^5	TrSL2, **TrSL3,TrBL**	0.251	1.97
Ding et al. (2004)	7.00×10^4-2.50×10^5	**TrSL3, TrBL**	N.A	2.0

Table 4.2. Vortex induced vibration maximum amplitude ratio data.

4.1.2. Characteristics of TrSL2 and TrSL3 regime

Most of the previous investigations of VIV have focused on relatively low Reynolds numbers less than 3×10^4, and the present study is concerned with a range of Reynolds numbers extending up to Re = 2×10^5. The referenced experiments conducted previously mostly lie in the TrSL2 regime (1×10^3- 2×10^3 < Re < 2×10^4- 4×10^4). Within this regime the transition in the shear layer from laminar to turbulent is initiated and

complete transition of the shear layer occurs at the end of the regime. In the TrSL3 regime the shear layer is fully turbulent. In the TrSL2 regime, the Strouhal number is nearly constant and the variation is minimal. Also, the base pressure coefficient C_{Pb}, reaches the lowest limit of the whole TrSL regime as shown in Figure 4.4, followed by a substantial increase in its value. In the TrSL3 regime, the base pressure coefficient C_{Pb}, reaches the highest limit in the whole TrSL regime and keeps increasing throughout the whole regime as shown in Figure 4.6. Unal and Rockwell (1988b) observed that the variation of C_{Pb} and C_L are related to the magnitude of the velocity fluctuation in the shear layer. The above statement is clearly depicted in Figure 4.4. Unal and Rockwell (1988a) also observed that reducing the velocity fluctuation by using a splitter plate can reduce the lift force on the cylinder. The variation of lift and drag forces for these regimes are reproduced from review papers of Norberg (2003) and Zdravkovich (1997) (Figure 4.1-Figure 4.3). In Figure 4.3 the zoomed version of the fluctuating lift coefficient is reproduced.

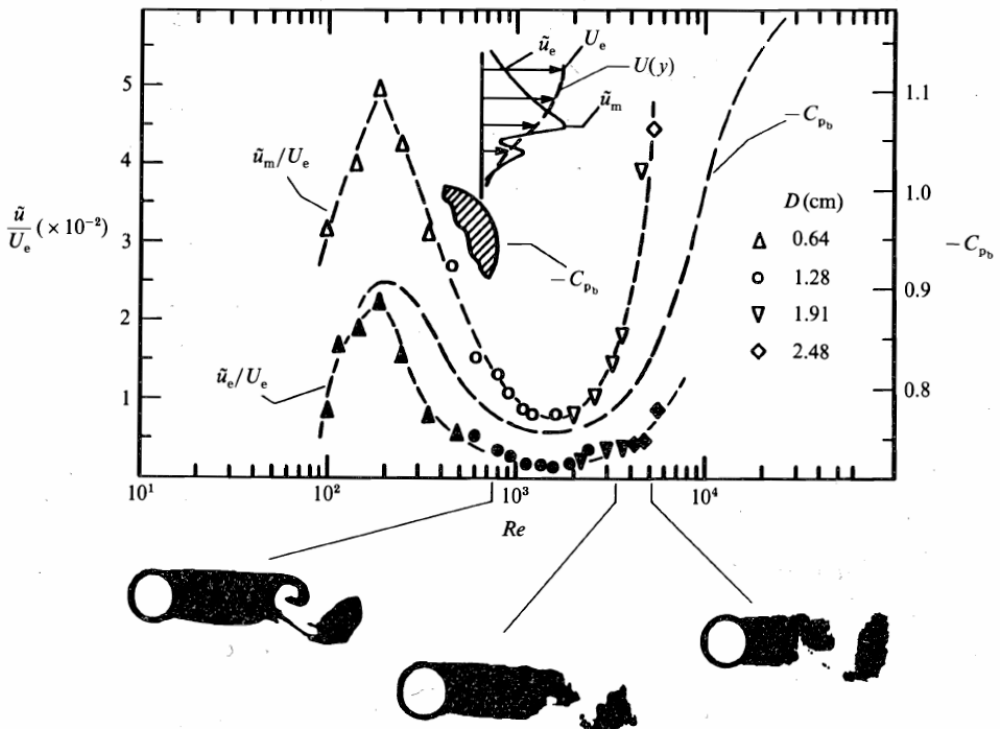

Figure 4.4. Variation with Reynolds number Re of mean base pressure coefficient C_{Pb} and velocity fluctuation amplitudes measured at edge of ($\tilde{\theta}_e/U_e$) and at maximum amplitude location within ($\tilde{\theta}_m/U_m$) the shear layer at x/D = 0.5. [Reproduced from Unal and Rockwell (1988b)].

Recently Huang et al. (2006) reported that the boundary layer showed significantly different flow patterns in two subranges of Reynolds number: $Re < 5.5\times10^4$ and $Re > 5.5\times10^4$. It was noted that in the low-Reynolds-number subrange (TrSL2 regime), the laminar separation mode existed. In the high-Reynolds-number subrange (TrSL3 regime), the separation bubble mode (secondary recirculation bubbles caused by the reattachment of separated boundary layers) existed, which was previously thought to exist only in the critical regime (3×10^5- $3.1\times10^5 < Re < 3.5\times10^6$- 6×10^6).

One other major characteristic difference between the TrSL2 and TrSL3 regimes is the fluctuating and mean pressure difference. In Figure 4.5, the fluctuating pressure distribution plot is shown. The fluctuating pressure increases with the Reynolds number and a major change is observed above $Re > 5\times10^3$. For $Re > 2\times10^4$ there is another sharp jump. There are few experimental results for this high Reynolds number. Additionally, they were at the end of synchronization rather than in the middle of it.

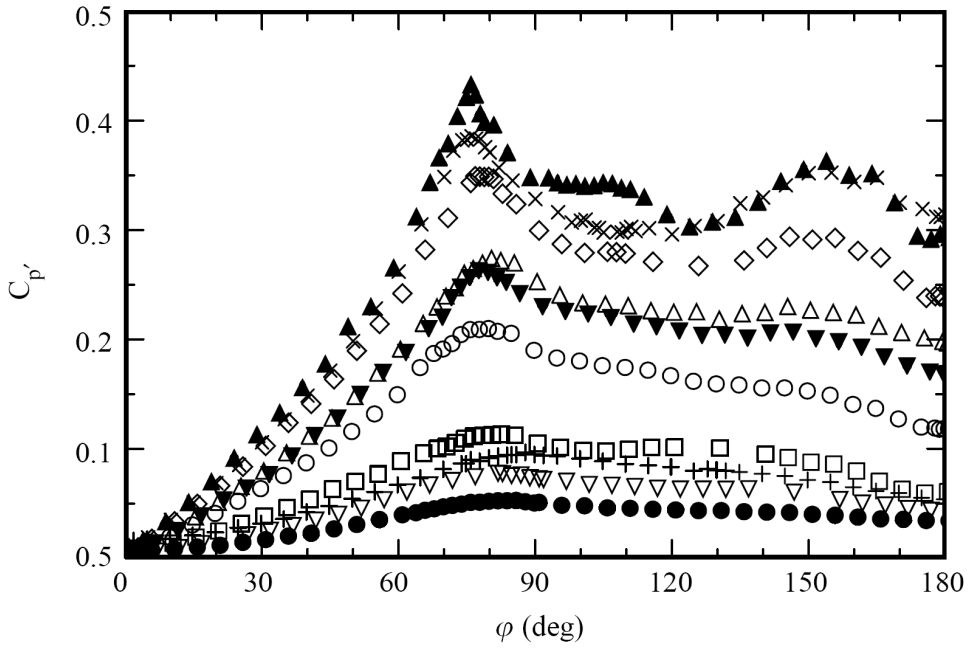

Figure 4.5. R.m.s. of fluctuating pressure distributions, C_p; for Re: +; 7.2×10^2; ●; 1.5×10^3; ▽; 4.4×10^3; □; 5.0×10^3; ○; 6.1×10^3; ▼; 7.2×10^3; △; 8.1×10^3; ◊; 2.0×10^4; x; 6.1×10^4; ▲; 2.1×10^5. [Reproduced from Norberg (1987)].

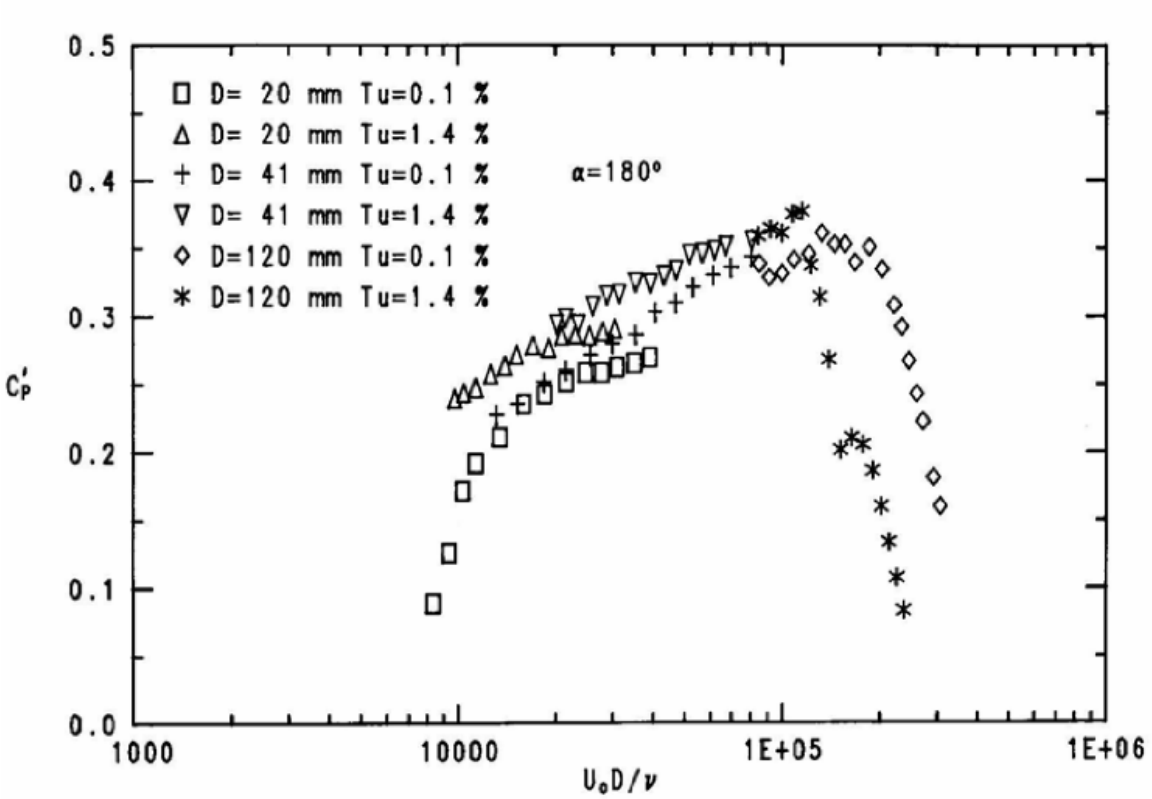

Figure 4.6. RMS base pressure coefficient vs Reynolds number for Tu = 0.1% and 1.4%. [Reproduced from Norberg (1987)].

4.1.3. Vortex formation length

According to Gerrard (1966) the vortex formation lengths were determined from the points closest to the cylinder at which irrotational fluid crosses the wake center line. When Reynolds number is increased, the vortex formation length (L_F), starts decreasing at the end of the TrSL2 regime (Nakamura and Igarashi 2004; Norberg 1987; Schiller and Linke 1933). Figure 4.7 suggests that the vortex formation length has a minimum in the TrSL3 regime. The formation length has a higher value throughout the majority of the TrSL2 regime and reaches a maximum of 3 diameters at a Reynolds number slightly above 10^3 (see Figure 4.7). It is shown in Figure 4.7 that at the end of the TrSL2 regime the formation length decreases rapidly up to about Re = 10^4 and then it stagnates for the TrSL3 regime to a value of 1.2 diameters. In Figure 4.7, it is seen that the effect of the higher turbulence intensity accelerates the reduction of the formation length in the TrSL2 regime and it doesn't have any effect in the TrSL3 regime.

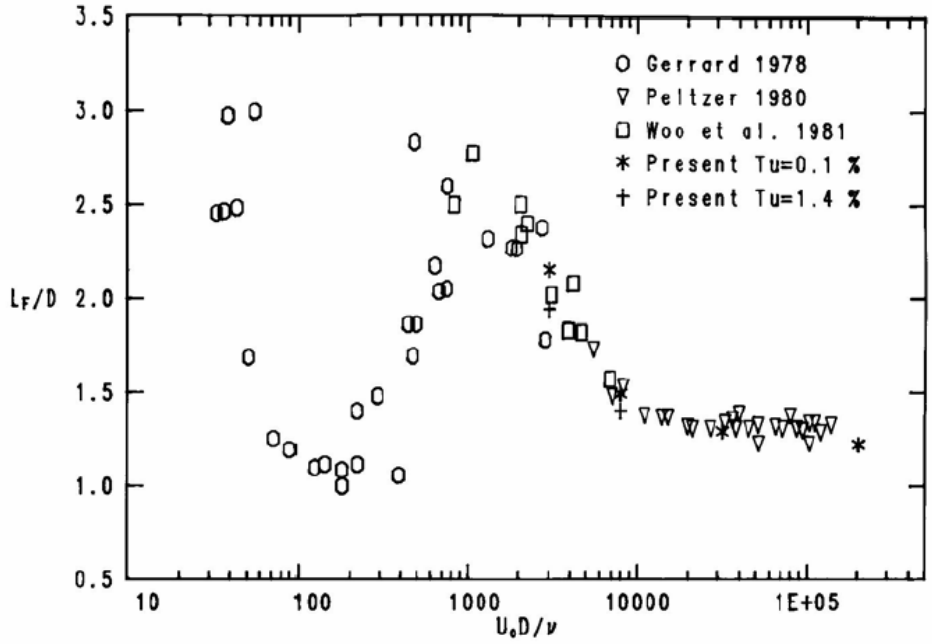

Figure 4.7. Vortex formation length as a function of Reynolds number. [Reproduced from Norberg (1987)].

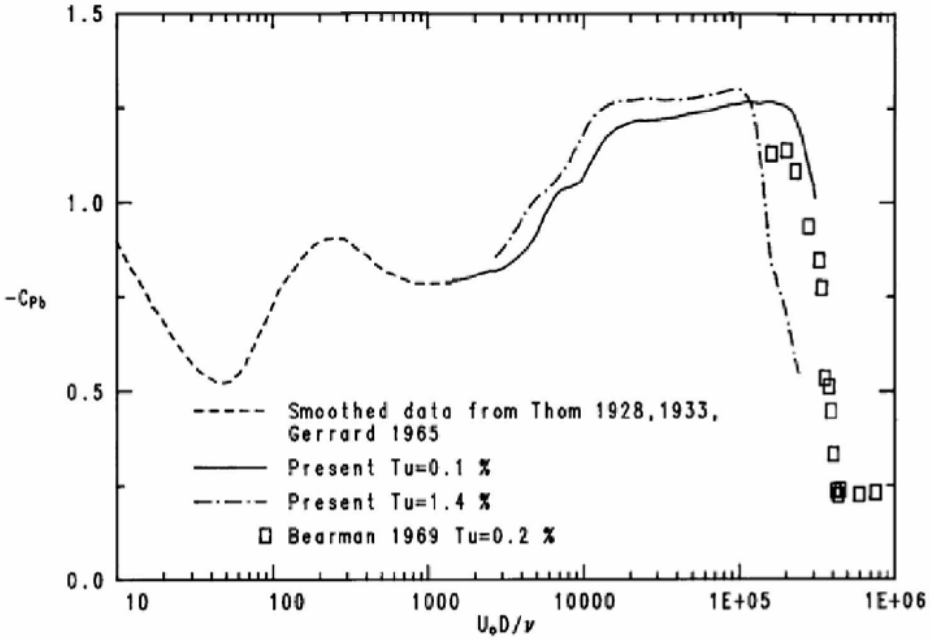

Figure 4.8. Variation of the mean base pressure coefficient as a function of Reynolds number range. [Reproduced from Norberg (1987)].

In the TrSL2 regime the reduction of the formation region after it reached its maximum is associated with the upstream movement of the position of transition in the

shear layers (Gerrard 1966). Since the complete transition of shear layer has occurred in the TrSL3 regime, the formation length stagnates. In Figure 4.7 and Figure 4.6, it is observed that the vortex formation length (L_F) is very closely related to the base pressure coefficient C_{Pb}. Norberg attributes this observed relation to the increase in the curvature of the streamlines associated with vortex formation to a decrease in L_F which results in a decrease of the base pressure. Unal and Rockwell (1988b) observed that the decrease/increase in formation length was associated with the increase/decrease in the velocity fluctuations. They observed when a splitter plate was used for suppression which resulted in the increase in the formation length and it was associated with the decrease in velocity fluctuation. The decrease in L_F/D could only partly explain the observed changes in the R.M.S lift coefficient (Gerrard 1966).

The reduction in the formation length with increase in Reynolds number is shown in Figure 4.9 as PIV images from experiments conducted at Lehigh University (Lin et al. 1995; Saelim 2003). In the PIV images of Figure 4.9, the important feature of the near-wake above a critical value of Reynolds number is the coexistence of the large-scale Kármán vortices, and the small-scale shear layer vortices also called Kelvin-Helmholtz vortices or secondary vortices. These two classes of vortices belong to two different length and time scales. These vortices are formed due to a Kelvin-Helmholtz instability (Williamson 1996). The shear layer vortices are referred to as secondary vortices in few other literatures.

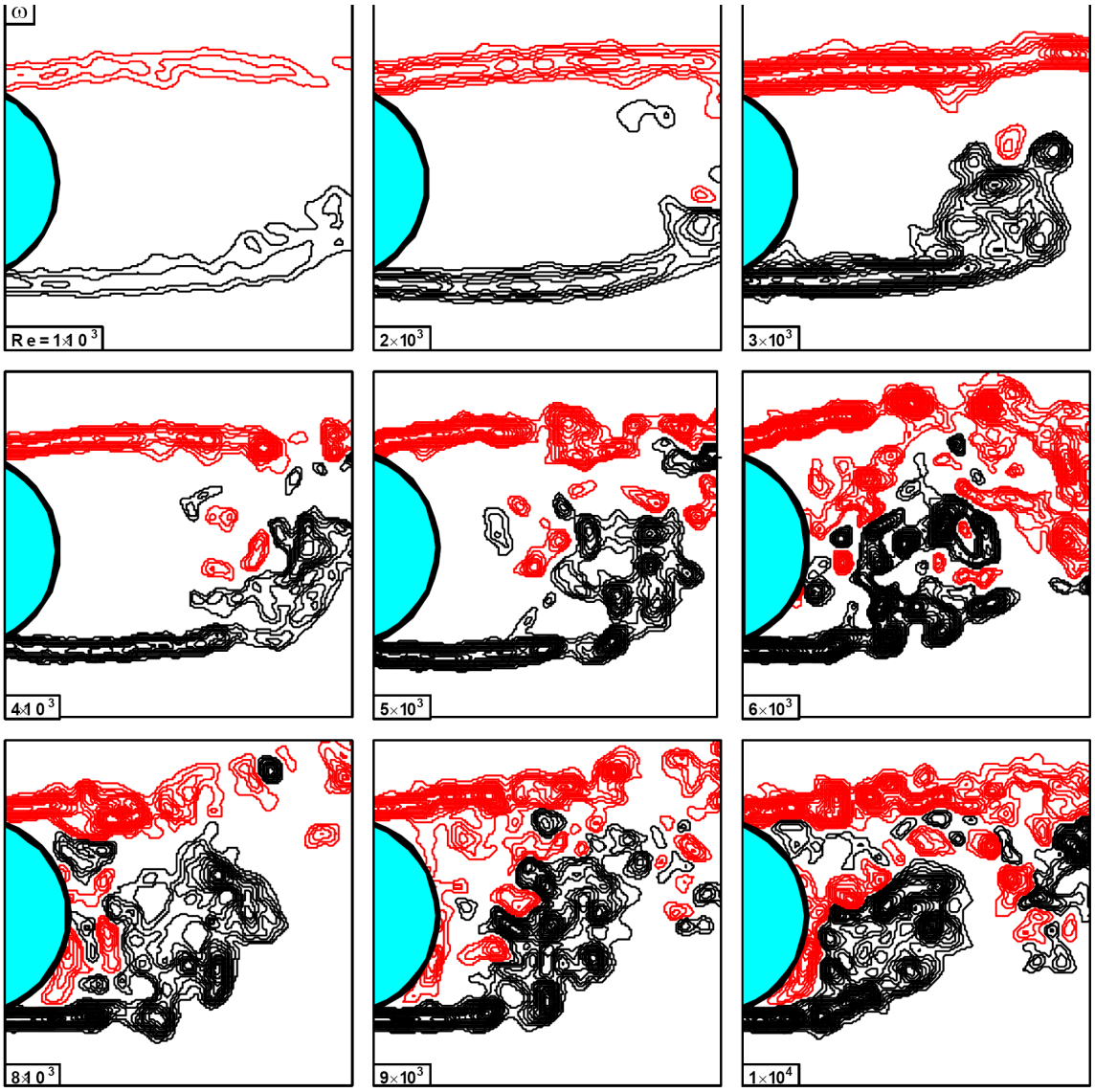

Figure 4.9. Instantaneous vorticity distributions showing the topological change in the near-wake structure as the Reynolds number is increased. At higher Reynolds number the shear layer vortices amalgamate into the Kármán vortices in the near wake producing stronger Kármán voritces. PIV measurements by Saelim (2003).

In his dissertation, Saelim (2003) found significant values of Reynolds stress correlation occurring in the separating shear layer by using PIV for his experiments, Reynolds numbers corresponds to the end of the TrSL2 regime and close to the beginning of the TrSL3 regime. In turn, the increase in Reynolds stress increases the entrainment demand of the separating shear layers (Chyu and Rockwell 1996b). An increase in Reynolds stress is attributed to the increase in the velocity fluctuations (Chyu and

Rockwell 1996b). He found that both the rms (root-mean-square) of the streamwise velocity fluctuation u_{rms}/U and the fluctuating vorticity rms indicate enhanced levels along the separating shear layer for the Reynolds number corresponding to the end of TrSL2 regime. The increased entrainment results in the increase in the negative base pressure coefficient (Chyu and Rockwell 1996b). In turn, the negative base pressure coefficient correlates with the decreased formation length of large-scale Kármán vortices.

4.1.4. Vortex dynamics: formation and character of secondary vortices

In recent years, the emphasis of study in the near wake of circular cylinder has been on two concepts. One is the interaction and development of three dimensional secondary vortex structures in the wake, such as the A- or B-mode for streamwise vortices (Figure 4.13-Figure 4.16). The other concept is the shear layer vortices due to Kelvin-Helmholtz instability (Figure 4.17) occurring for relatively high Reynolds numbers with the primary Kármán vortices (Brede et al. 1996; Chyu et al. 1995; Chyu and Rockwell 1996a; Chyu and Rockwell 1996b; Lin et al. 1995; Wei and Smith 1986; Williamson 1996) .

Vortex dynamics can be classified on the basis of the Reynolds number range (Williamson 1996). For higher Reynolds number (Re > 350), transition from laminar to turbulent can happen in the separating shear layer or in the boundary layer. Zdravkovich has classified three subregimes within the transition from laminar to trubulent in the Shear Layer (TrSL) and they are TrSL1 ($350 \leq Re \leq 1\times10^3–2\times10^3$), TrSL2 ($1\times10^3–2\times10^3 \leq Re \leq 2–4\times10^4$) and TrSL3 ($2–4\times10^4 \leq Re \leq 1–2\times10^5$). The fluctuating lift coefficient shows a different characteristic in each regime which can be seen in the Figure 4.1 and Figure 4.3.

In previous VIV experiments, most of the laboratory measurements correspond to the TrSL1 and TrSL2 regime and in these two regimes the magnitude of fluctuating lift force is lower in comparison to the fluctuating lift in TrSL3 regime and this is one of the reasons why VIV amplitude ratios as high as the one we measured has not been observed earlier.

The formation of the small Kelvin-Helmholtz vortices (K-H vortices) in the separated shear layer was first observed as a fluctuation in a hot-wire signal by Bloor

(1964) for $Re>1.3\times10^3$. Wei and Smith (1986) hypothesized that the initial development of the Kelvin-Helmholtz vortices is due to the amplification of a free-shear instability in the separated boundary layer right before the formation of primary Strouhal vortices. This results in three-dimensional distortion of an initially straight line vortex filament as shown in Figure 4.10 and Figure 4.11. They found that the ratio of frequency of the shear-layer vortices with respect to the Strouhal frequency from hot-wire anemometry data and from flow visualization to be $Re^{0.77}$ and $Re^{0.87}$, respectively.

Prasad and Williamson (1997) found that the ratio of frequency of the shear-layer vortices with respect to the Strouhal frequency can be represented by a power law of $Re^{0.67}$. In their experiments, they showed that the end conditions can significantly affect the critical Reynolds number for the onset of the shear-layer instability.

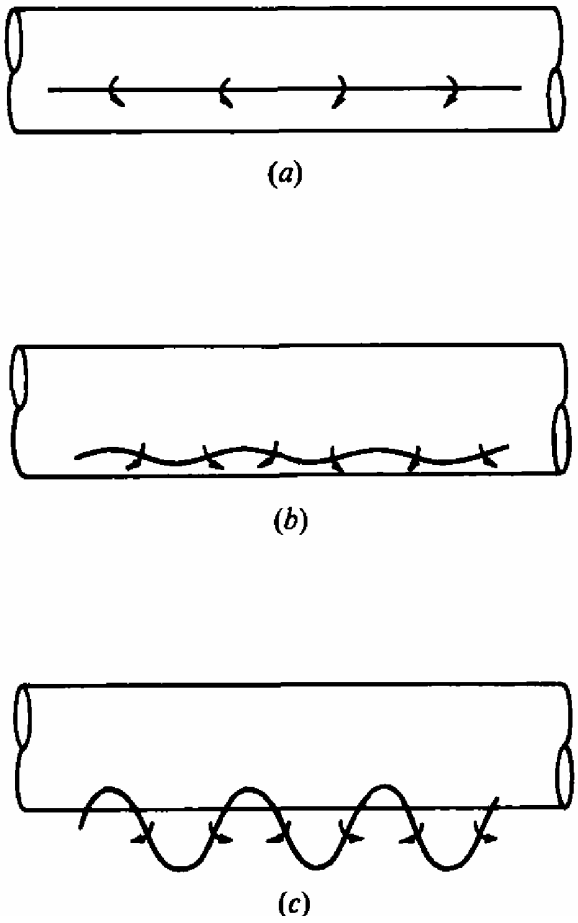

Figure 4.10. Schematic sequence of the growth of spanwise waviness in secondary vortices. [Reproduced from Wei and Smith (1986)].

There is a lot of variation in the Reynolds number data at which the shear layer vortices appear. Bloor (1964) detected the shear layer vortices for $Re > 1.3\times10^3$. Based on flow visualization Unal and Rockwell (1988b) observed the development of shear layer vortices only for Reynolds numbers greater than 1.9×10^3. It was later observed that the onset of the Kelvin-Helmholtz instability depends upon the background disturbances and free stream turbulence and this instability distinctively occurs in the range of $Re \approx 600$ to 1.9×10^3 (Lin et al. 1995; Wu et al. 1996). Braza et al. (1986) observed that the Kelvin-Helmholtz instability of the shear layers is primarily two-dimensional and it leads to the rise of two-dimensional Reynolds stresses and successively increases base suction.

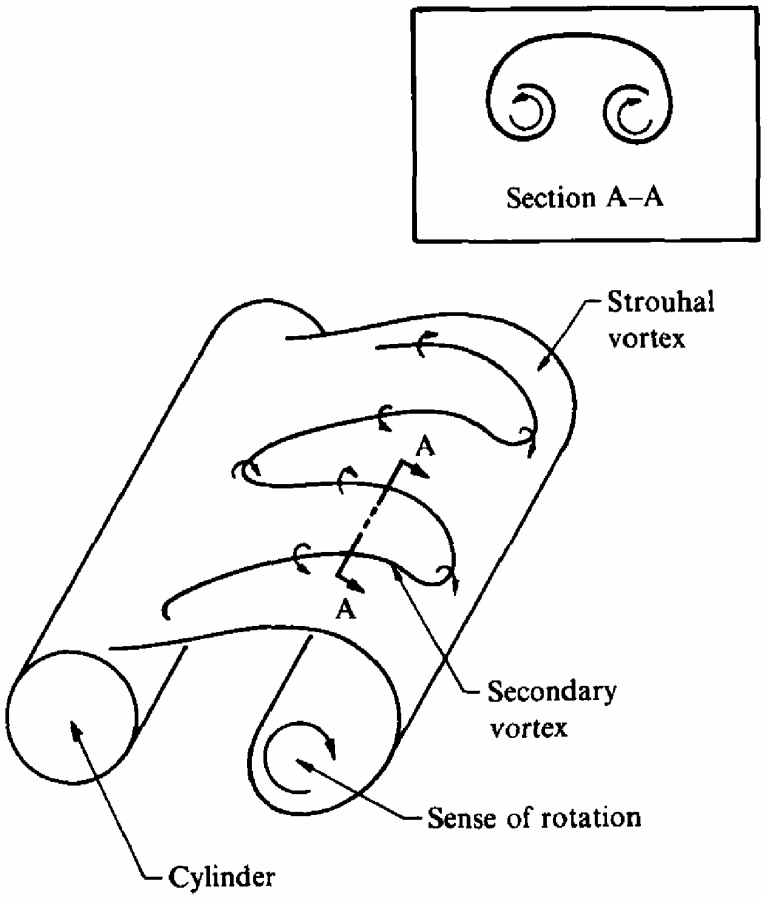

Figure 4.11. Interaction between secondary vortices and Kármán vortex. [Reproduced from Wei and Smith (1986)].

Chyu et al. (1995) and Chyu and Rockwell (1996b) found that the formation length of the primary Kármán vortices can be shortened when the cylinder oscillation is

perturbed at the instability frequency of the shear layer and its subharmonics. The application of small amplitude perturbations at the instability frequency of the shear layer and its subharmonics for a low Reynolds number (5×10^3) case can emulate the high Reynolds number effect (Re =10^4) (Chyu et al. 1995; Chyu and Rockwell 1996b).

Lo and Ko (2001) observed in the regime, $7\times10^3<Re<2\times10^4$, pairing of small scale secondary vortices and which in turn play crucial roles in the formation of the large-scale primary vortices. That is the onset of small scale vortices in the shear layer makeup the large scale Kármán vortex formation, resulting in higher vorticity strength of the Kármán vortices.

The smaller scale turbulence intensity generated by the shear layer vortices at higher Reynolds number due to reduction in scale of the shed shear layer vortices interacts with the boundary layer and constantly feeds the vortex formation region. This results in stronger and better correlated vortex shedding and consequently VIV.

In Figure 4.12, using the relation by Prasad and Williamson (1997), the ratio of the frequency of shedding of shear layer vortices to that of the frequency of Kármán vortices in the Reynolds number range of the present experiments is plotted. In Figure 4.12, as the Reynolds number increases the ratio between the frequencies of the secondary and Strouhal vortices also increases. In addition, it means that the relative size or strength of the secondary vortices reduces considerably in comparison to the Strouhal vortices.

The scale and the size of the shear layer vortices in comparison with primary Kármán vortices at different Reynolds number may be the reason for the variation in the base pressure. Interaction between two different scales of vortices are not the same, they could result in agglomeration of vortices or no interaction.

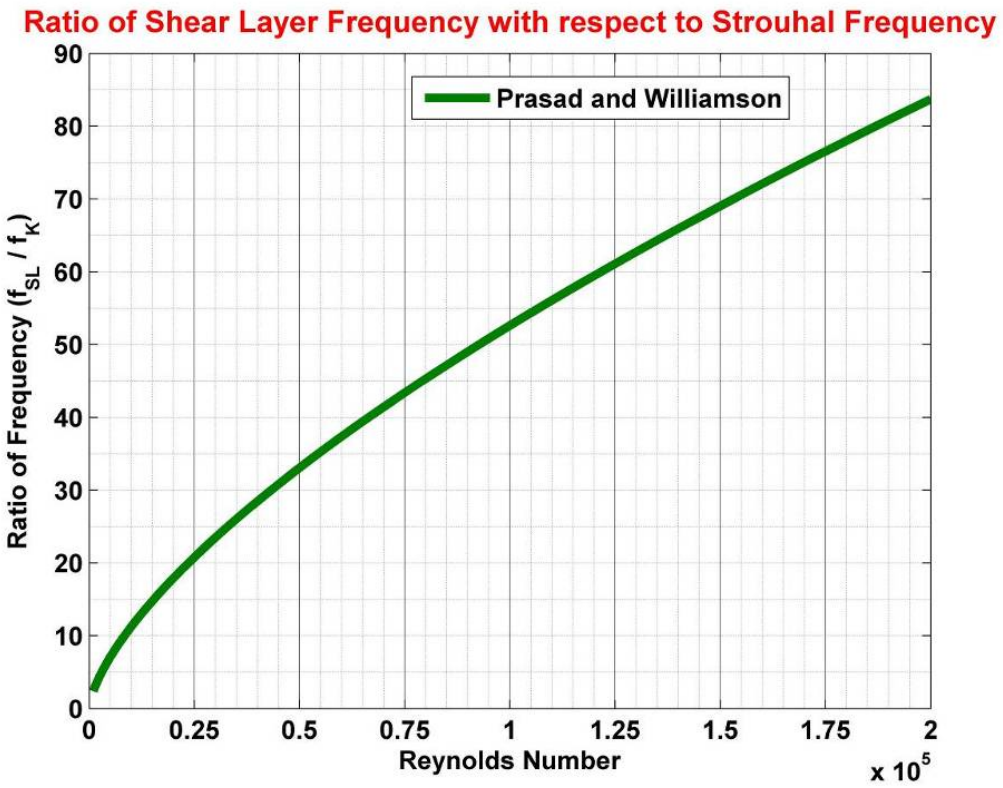

Figure 4.12. Ratio of the frequency of shedding of shear layer vortices to that of Kármán vortices for Reynolds number encountered in our experiments are plotted using the relation by Prasad and Williamson (1997).

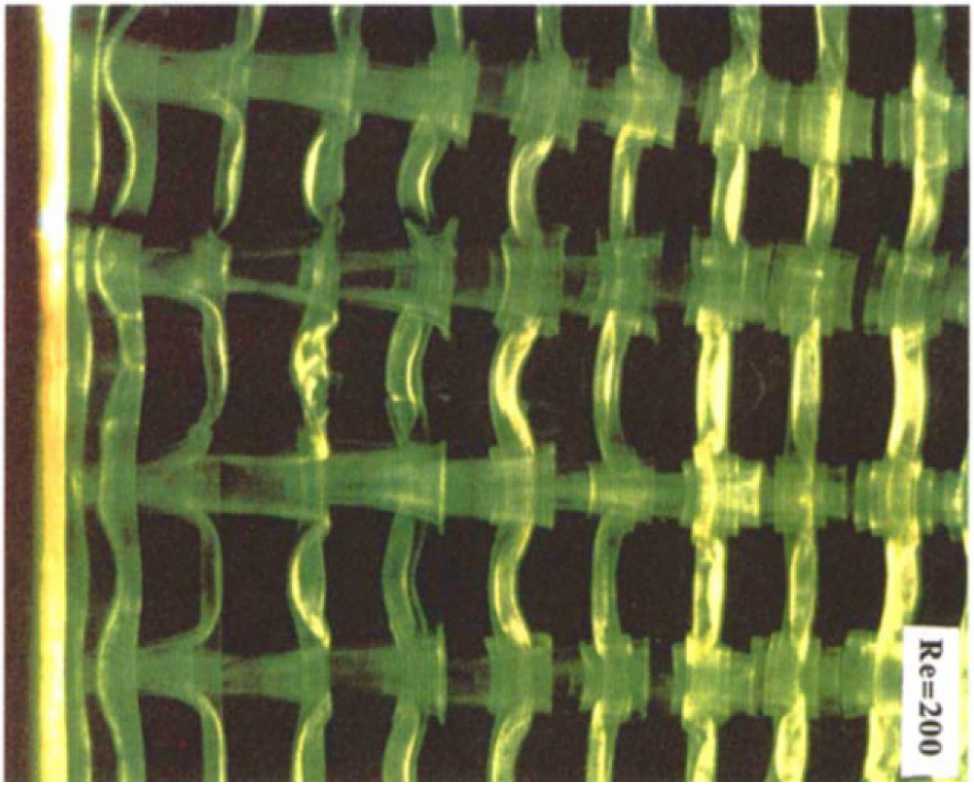

Figure 4.13. Visualization by Williamson of the Mode A instability at Re =200. [Reproduced from Williamson (1996)].

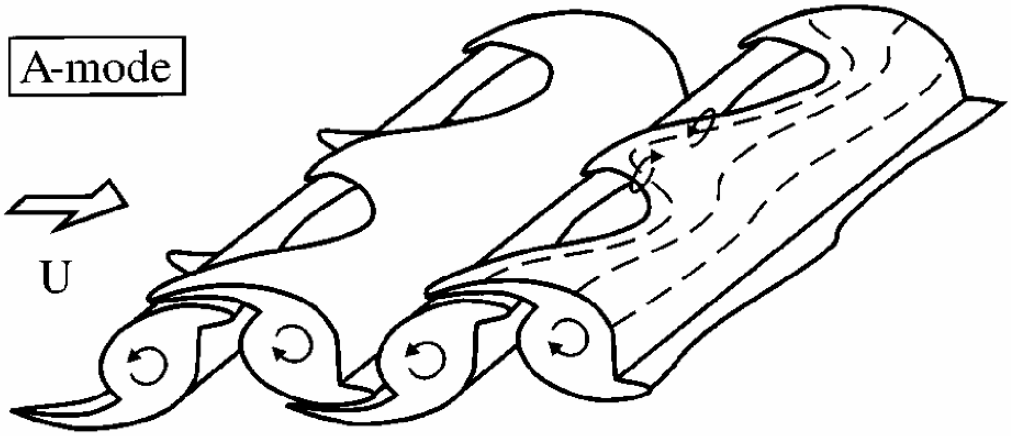

Figure 4.14. Schematics of the primary and secondary vortices in the transitional wake of the cylinder for the shedding mode A. Arrows denote the sense of rotation and dashed lines represent vortex lines. [Reproduced from Brede et al. (1996)].

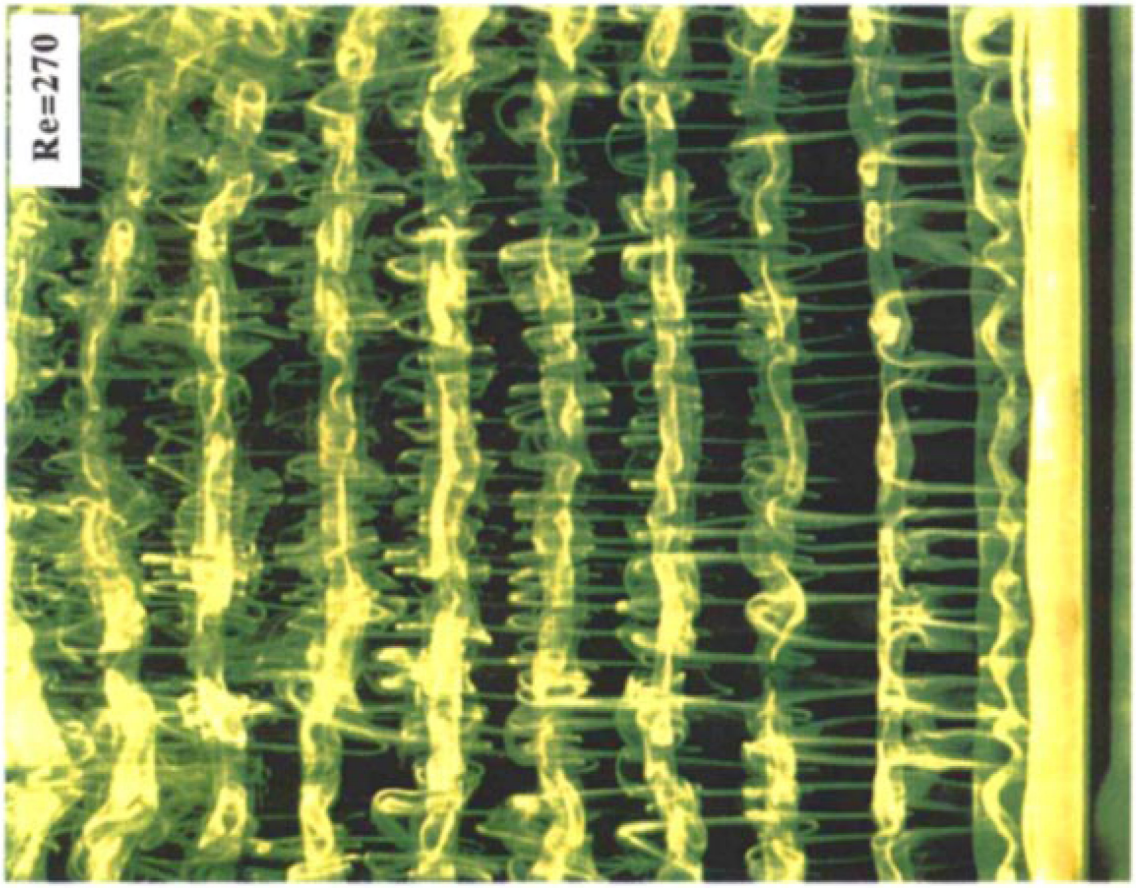

Figure 4.15. Visualization by Williamson of the Mode B instability at Re =270. [Reproduced from Williamson (1996)].

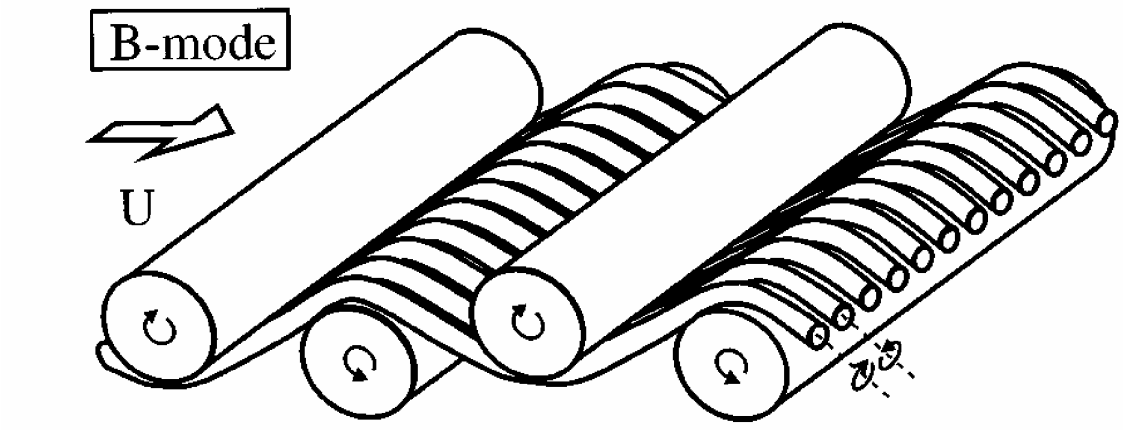

Figure 4.16. Schematics of the primary and secondary vortices in the transitional wake of the cylinder for the shedding mode B. Arrows denote the sense of rotation and dashed lines represent vortex lines. [Reproduced from Brede et al. (1996)].

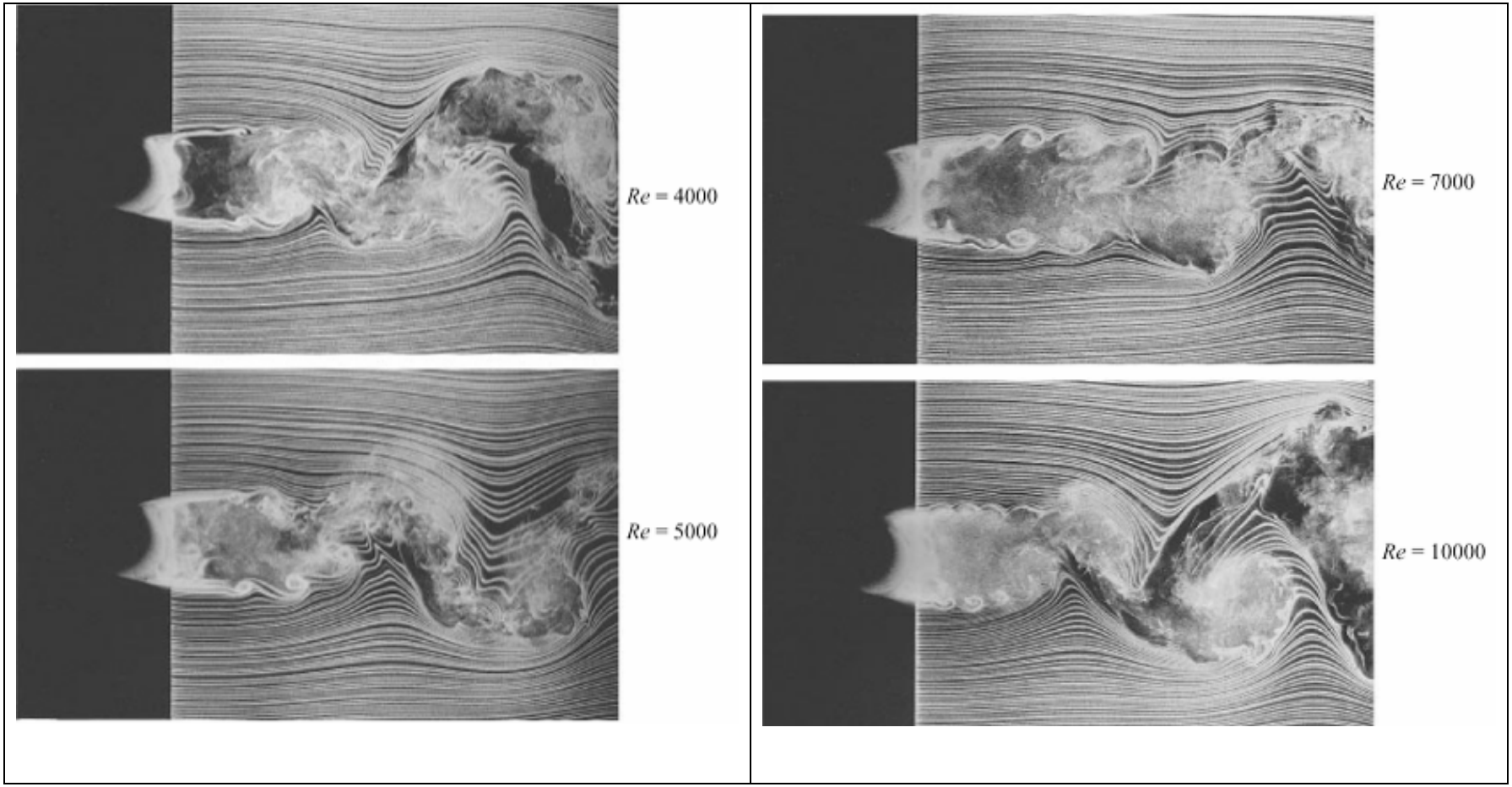

Figure 4.17. Near wake behind a circular cylinder at various Reynolds numbers [Reproduced from Prasad and Williamson (1997)]. The number of vortices is observed to increase and the shear-layer instability intensifies as Reynolds number increases.

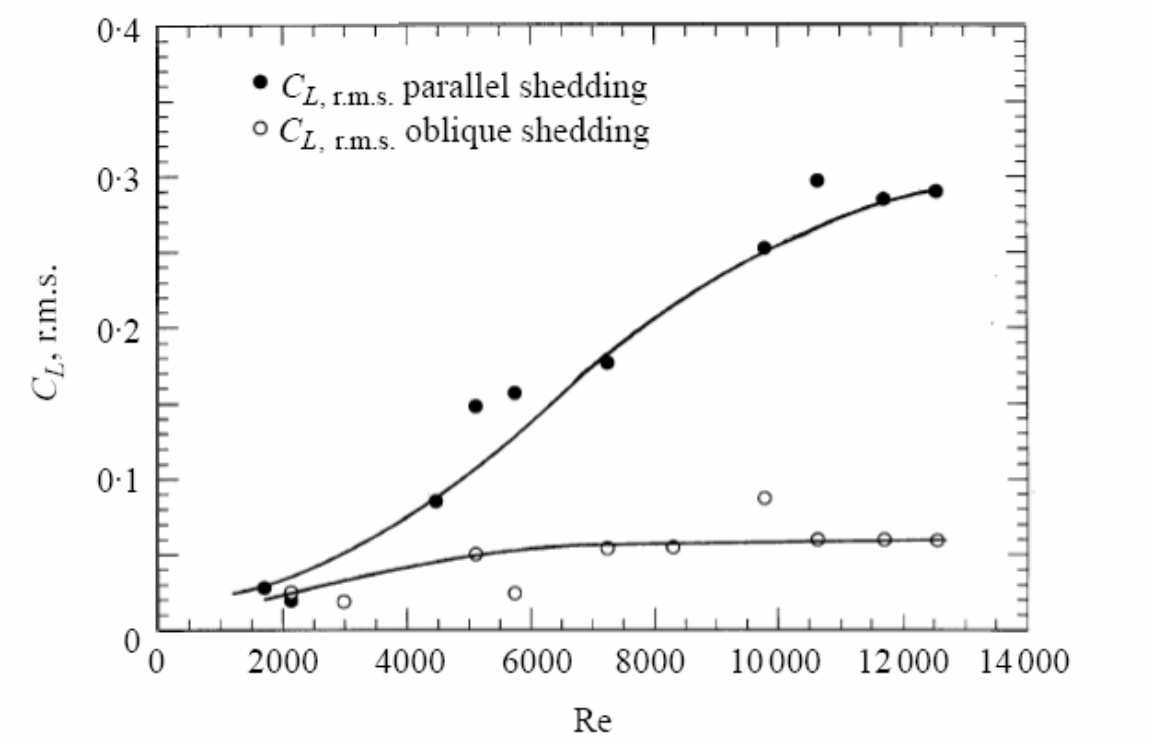

Figure 4.18. R.M.S lift coefficient plotted as a function of Reynolds number for a static cylinder, comparing conditions of parallel and oblique shedding from the body. [Reproduced from Khalak and Williamson (1996)].

4.2. PROBLEM DEFINITION

The goal is to study the effect of higher Reynolds numbers ($Re>10^4$, TrSL3 regime) on Vortex Induced Vibrations. Particulars of VIV that should be studied experimentally include amplitude, range of synchronization, branches of response within the synchronization range, vortex structures, hysteresis, etc. High Reynolds numbers represent realistic conditions at which VIV occur in practical ocean engineering applications.

4.3. SOLUTION APPROACH

To study the effect of Reynolds number on VIV, experiments were conducted in the Low-Turbulence Free Surface Water (LTFSW) Channel, in the Marine Hydrodynamics Laboratory (MHL) of the University of Michigan. All cylinders are 36" long and are made of aluminum coated with polymer paint for surface smoothness and protection. Model diameters are 2.5", 3", 3.5", 5", and 6". Aspect ratio varies from 14.4 to

6. The blockage ratio in the test section of the LTFSW Channel ranges from 7.14% to 17.14%, where the bigger diameter cylinders are used for studying the proximity to critical regime of Reynolds number. Models are suspended via two compression coil-springs attached to the end-plates of the cylinders. The cylinder is constrained to oscillate transversely to the flow freely using linear bearings sliding on shafts.

4.4. RESULTS, OBSERVATIONS, AND DISCUSSION

4.4.1. Effect of Reynolds number on VIV response

Vortex induced vibration is nonlinear in character and one of its attributes is the range of synchronization of the forcing frequency and the natural frequency in water. For synchronized vibration the forcing frequency from the shedding of vortices need not lock-in with the primary natural frequency in water it can lock-in with the sub and superharmonic components of the natural frequency (Govardhan and Williamson 2002; Sumer and Fredsoe 1997). The strength of the vortices shed increases as the amplitude of oscillation increases (Bearman 1984) or the vortex structure changes resulting in more vortices per cycle. The total circulation of these vortices increases with the amplitude. The oscillation of the cylinder enhances the correlation of the wake structure along the span as shown in Figure 4.19 and intensifies the forcing and in turn the amplitude (Bearman 1984). Koopman (1967) experimentally observed that the significant growth in correlation length occurs for vibration amplitude ratios as small as y/D = 0.1.

The magnitude of the self limiting of the oscillation amplitude is associated with the vortex structure that the system can support, which are related to the damping, mass ratio, and Reynolds number. In the experiments conducted by Williamson and Roshko (1988), they found that distinctive wake structures were stable for different combination of the amplitude ratio and reduced velocity based on the oscillation frequency in the parameteric space of the amplitude ratio and reduced velocity based on the oscillation frequency (Figure 4.26). In Chapter 7, it is shown that the increase in amplitude is not self limited if the cylinder surface is modified.

Recently Hover et al. (2004) have shown that there is loss of end-force correlation during the jump from the upper branch to the lower branch and then a steady decrease in

correlation of the force and velocity at the end of synchronization as shown in Figure 4.20 and Figure 4.21. They attributed the notch in the end force correlation, observed near $U^*_{fn,air}$ = 6-7.5, to the coexistence of 2S and 2P wake structure along the span of the cylinder and the stability of their coexistence has been verified by Techet et al. (1998) using a tapered cylinder. In their experiments they observed, after the transition from the 2S to 2P wake structure, the end-force correlation becomes one again for a reduced velocity in air $U^*_{fn,air}$ =7.5 – 8.5. The notch in the end force correlation observed near the jump is strongly affected by the mass and damping ratio as shown in Figure 4.22. As the reduced velocity increases above $U^*_{fn,air}$ > 8.5 the amplitude of oscillation decreases steadily and the decrease is associated to the gradual loss in end force correlation. In Figure 4.20 and Figure 4.21, at higher reduced velocity ($U^*_{fn,air}$ > 8.5), there is a loss of synchronization of the wake velocity frequency and the primary natural frequency of the structure and this results in the loss of lock-in between the forcing and the primary natural frequency of the structure and ultimately resulted in the end of synchronization. In his thesis, Davis (2001) too attributes the loss of lock-in of the wake velocity at the end of synchronization with the transition in wake structure from 2P to P+S.

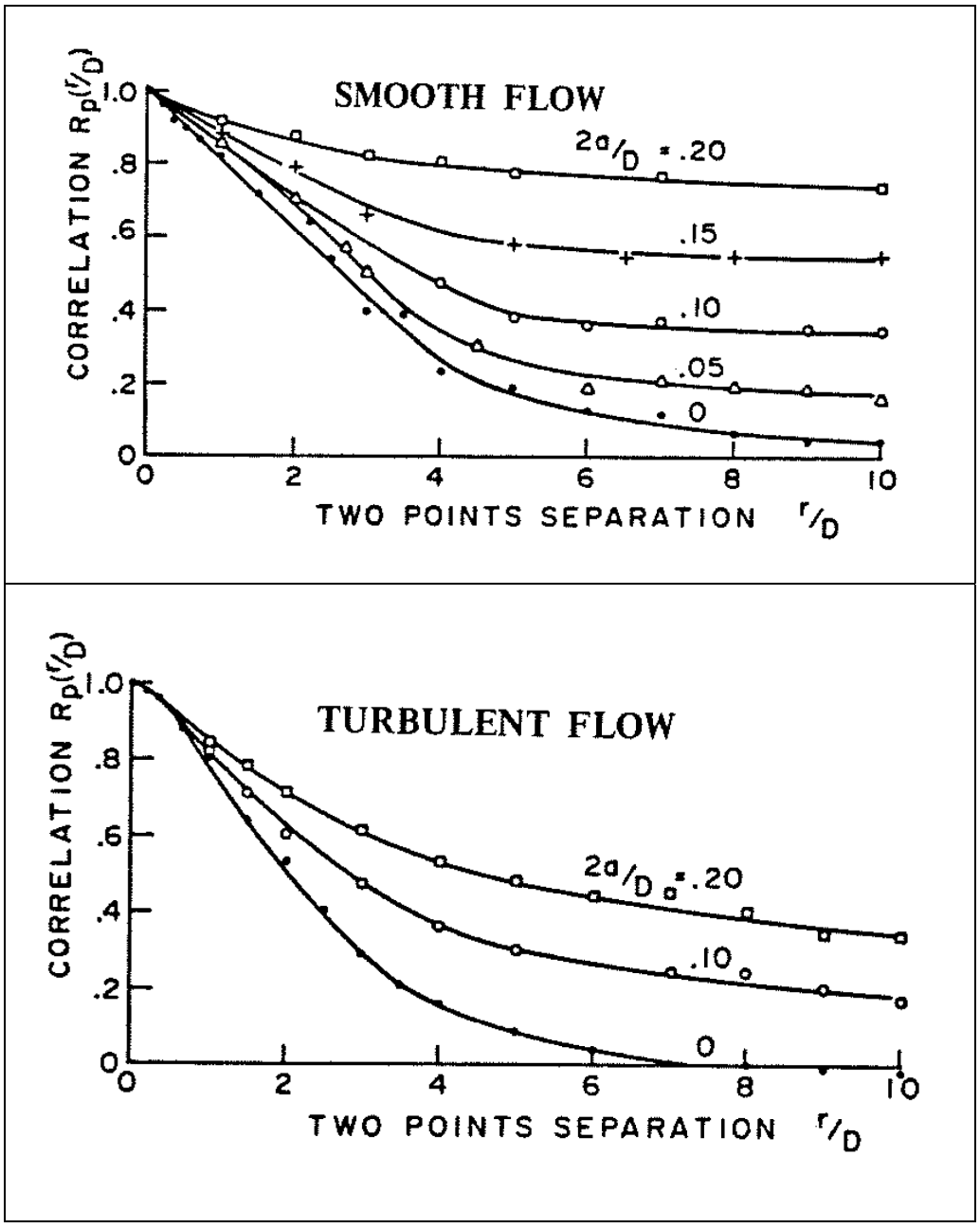

Figure 4.19. Spanwise distribution of correlation coefficient between pressures measured on a cylinder forced to oscillate cross flow as functions of amplitude (Novak and Tanaka 1975).

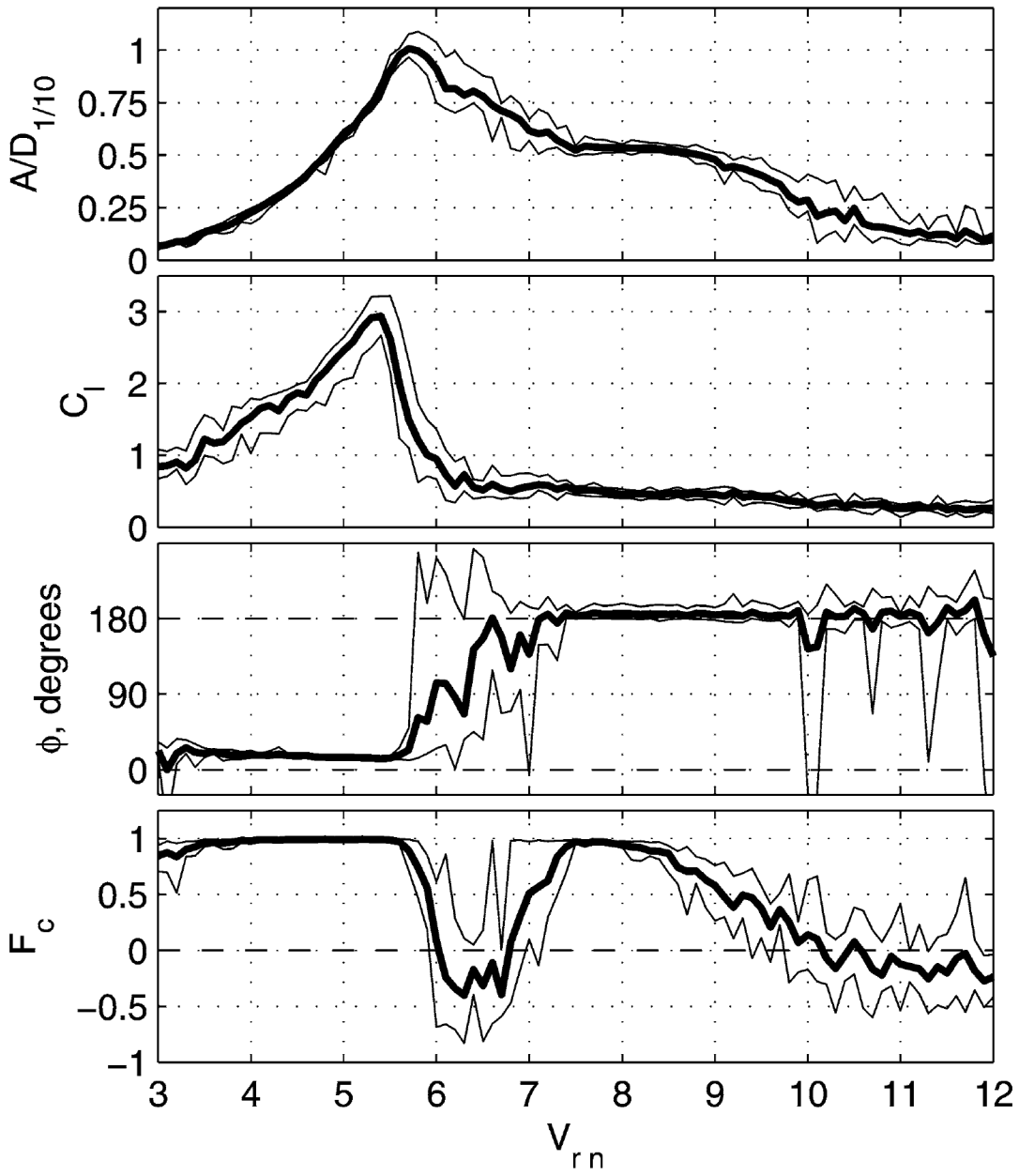

Figure 4.20. The trend of correlation of the end lift force is shown for a freely vibrating cylinder as a function of reduced velocity in air (V_{rn}) where C_l is the lift coefficient; φ (degrees) is the phase angle between lift force and cylinder displacement; and F_c is the correlation coefficient of end lift forces. [Reproduced from Hover et al. (2004)].

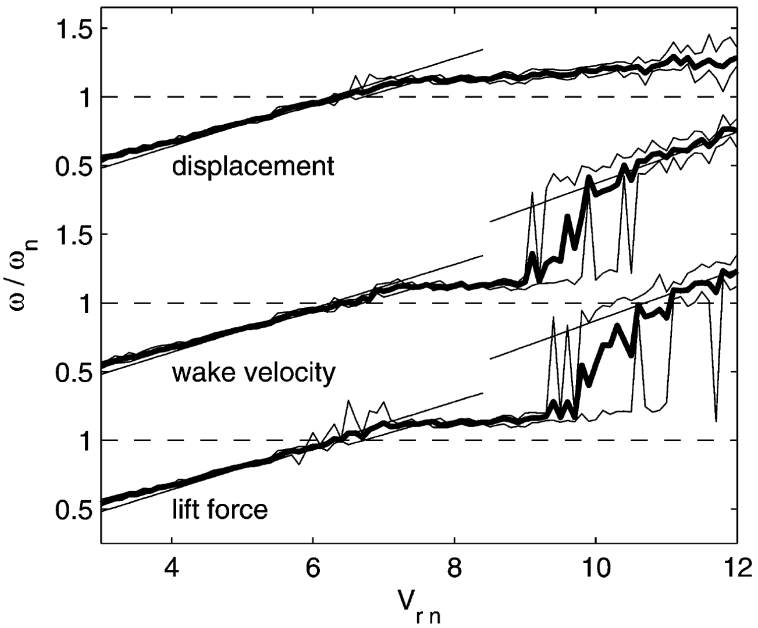

Figure 4.21. Loss in lock-in of the wake velocity and the lift force at the end of synchronization. [Reproduced from Hover et al. (2004)].

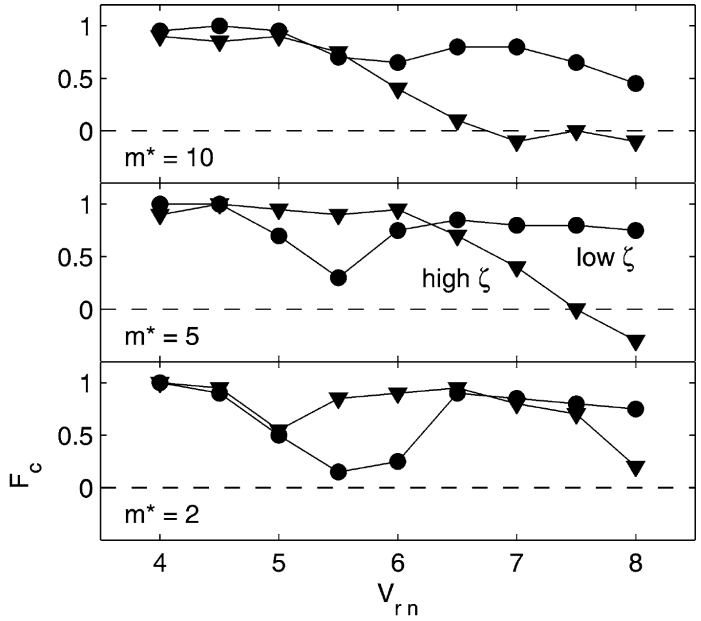

Figure 4.22. End force correlation (F_c) dependence on mass and damping parameters where low damping cases correspond with $\zeta \approx 0.01$, and high damping cases have $\zeta \approx 0.10$. [Reproduced from Hover et al. (2004)].

In Figure 4.23, and later in Figure 4.50, and Figure 4.51, it is clearly noticed that the high amplitude upper branch increases as we increase the Reynolds number. In Figure 4.51, the VIV response from the experiments done by Khalak and Williamson(1999),

Govardhan and Williamson (2000), Feng (1968), and one of the cases from our experiments are plotted to show the effect of Reynolds number. The cases of Khalak and Williamson, Govardhan and Williamson, and Feng tests fall in the TrSL2 regime and the case from our experiments fall in the TrSL3 regime.

The whole range of synchronization observed in the experiments done by Khalak and Williamson are nearly the same as our experiments, though the product of mass ratio and damping ratio is about 20 times more in our experiments. In our experiments, the width of the upper branch is nearly the same as the total width of Khalak and Williamson case, which includes the lower branch. The above observation is attributed to the high fluctuating lift coefficient associated with the TrSL3 regime where our experiments were conducted.

In the case of Govardhan and Williamson, the mass ratio is less than our experiments and the product of mass ratio and damping ratio is nearly 23 times more than in our experiments. Even with such high $(m^*+C_a)\zeta$, the ratio of amplitude of oscillation in our experiment is 1.8 times more than the Govardhan and Williamson case and for both experiments the width of the upper branch is nearly the same. In the present experiments the lower branch didn't have much range of synchronization owing to the high damping introduced in our experiments.

In the case of Feng's experiment the mass ratio was very high and the product of mass ratio and damping ratio is higher than the case from our experiments. The effect of damping and low Reynolds number attributed to their lower magnitude of response. The maximum amplitude ratio that was observed in the Feng's case was nearly 0.55.

In Figure 4.23, and later in Figure 4.24, and Figure 4.50, the effect of Reynolds number on VIV response is shown by comparing among the results from our experiments, this is to avoid the discrepancy in the experimental conditions. In Figure 4.50, the VIV response of a 2.5″ cylinder operating in different Reynolds number regimes is plotted. This is achieved by using two sets of different spring stiffness, which resulted in two VIV systems with different natural frequencies. The difference in natural frequencies between the two systems shifted the operational range of synchronization to higher and lower Reynolds number. The shift to higher operational Reynolds number

increased the amplitude of oscillation and the range of synchronization as shown in Figure 4.23, Figure 4.24, and Figure 4.50.

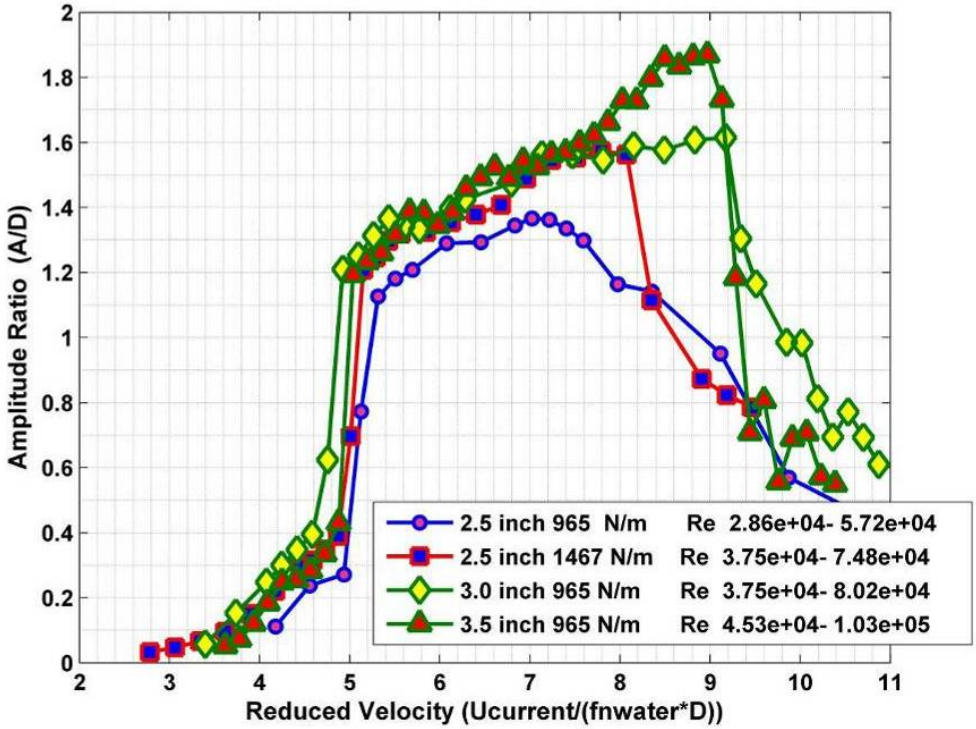

Figure 4.23. Comparison of VIV data from our experiments conducted at different Reynolds number plotted with respect to reduced velocity in water, demonstrating the dependence of VIV response with Reynolds number.

In Figure 4.23, the difference in the amplitude response character occurs above U* >7.2. Below U* < 7.2, the amplitude response collapsed together, independent of the Reynolds number. For U* >7.2, a major difference in the response character is observed. In Figure 4.23, as the operational Reynolds number shifts to the right the response amplitude increases and the range of high amplitude vibration also increases, proving a strong Reynolds number dependence. For Re $>5.5\times10^4$, the range of synchronization is nearly the same but the ratio of amplitude of oscillation is higher. It is observed that there is a linear character between the amplitude response and reduced velocity in the range of upper branch and it can be linearly fitted as,

$$A^*=0.175U^*+0.325 \quad (4.1)$$

In Figure 4.23, for the case of the 2.5″ cylinder with a lower natural frequency, there is a decrease in the ratio of amplitude of oscillation for U* >7.2 and it is attributed to the loss in lock-in of the primary frequency with the wake velocity and spanwise correlation (Hover et al. 2004). For the case of 2.5″ cylinder with higher natural frequency, the high amplitude oscillation extended further. In the case of 3.0″ cylinder, the operation Reynolds number increased due to the increase in diameter and this resulted in increase of the amplitude of oscillation. The range of synchronization extended further for the case of 3.0″ cylinder in comparison to 2.5″ cylinder. The increase in amplitude of oscillation for the 3.0″ cylinder plateaus at the end of synchronization without any further increase.

In Figure 4.23, for the case of 3.5″ cylinder the increase in amplitude of oscillation was steady along the upper branch and the ratio of amplitude of oscillation reached a maximum of 1.8. In the case of 3.5″ cylinder the growth in the increase of amplitude didn't plateau as in the case of 3.0″ cylinder.

The author hypothesizes that the increase in amplitude is due to the increase in turbulence in the near wake at high Reynolds number due to the smaller scale shear layer vortices and the shortening of the formation length. The increase in turbulence increases velocity fluctuations and the Reynolds stress, thus, increasing entrainment (Saelim 2003; Unal and Rockwell 1988b) and the lift coefficient and base pressure. In the high Reynolds number regime (TrSL3 regime), the secondary vortices formed are highly energized and the vorticity content of these vortices keeps increasing with the Reynolds number (Lo and Ko 2001). In the high Reynolds number regime, the higher vorticity of the secondary vortices favor pairing among themselves and this results in highly energized interaction between the excited small-scale secondary vortices and the large-scale primary vortex sheet occurs (Lo and Ko 2001)

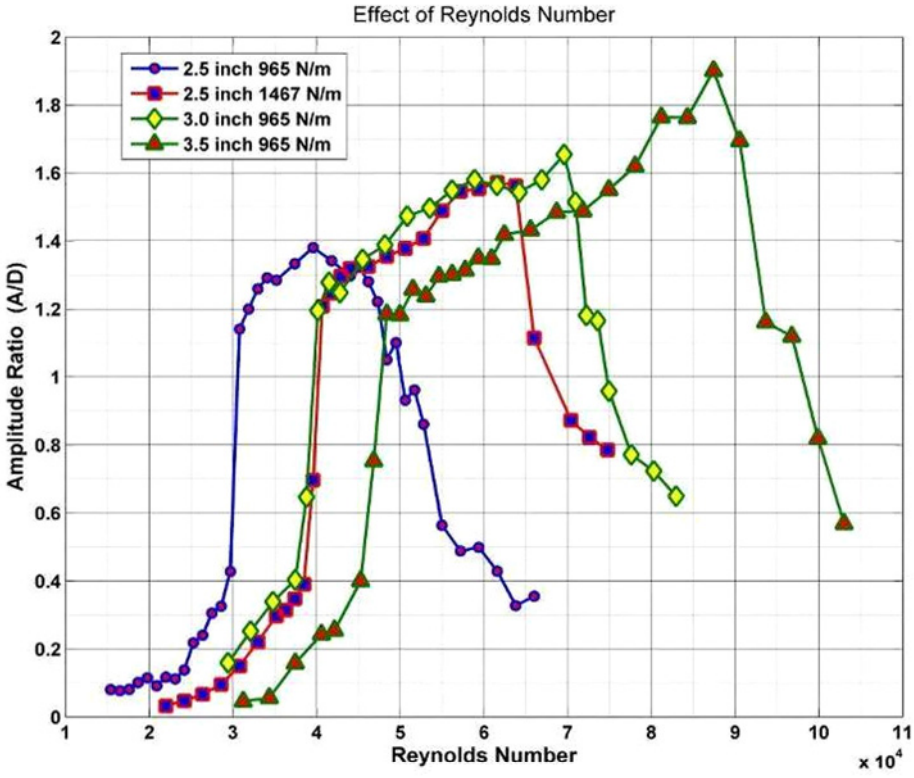

Figure 4.24. VIV data from our experiments plotted against Reynolds number, demonstrating the dependence of VIV response with Reynolds number.

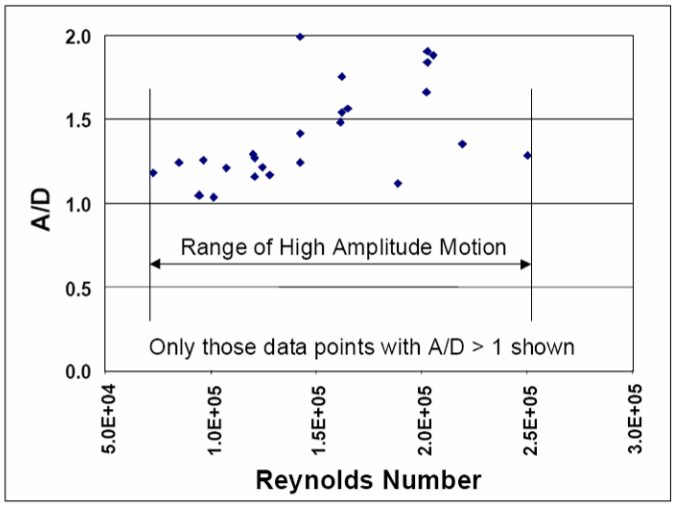

Figure 4.25. Range of high amplitude vibration obtained by Exxon Mobil research team for a smooth cylinder in the Reynolds number range 7×10^4 – 2.5×10^5. [Reproduced from Ding (2004)].

4.4.2. Predicting the vortex modes using the Williamson and Roshko map

Williamson and Roshko (1988) extensively mapped different wake states to the parameter space of amplitude ratio and the true reduced velocity using the forced oscillation of cylinder as shown in Figure 4.26. In Figure 4.26, the response data for a low $(m^*+C_a)\zeta$ system collapses well when the "true" normalized velocity $\left(\frac{U}{f_{osc}D}St\right)$ is used. A good agreement between the mode predicted by the Williamson and Roshko map and the vortex shedding mode of the different response branches for a low $(m^*+C_a)\zeta$ system were confirmed by flow visualization (Govardhan and Williamson 2000).

In Figure 4.27, both the case of low damping and low Reynolds number and the case of high damping and high Reynolds number are plotted. For high Reynolds number and high damping experiment, the synchronization started at a higher "true normalized reduced velocity" in comparison to the low Reynolds number and low $(m^*+C_a)\zeta$ experiment. According to the Williamson and Roshko's plot, in the case of low Reynolds number the response curve traverses through the 2S mode in the initial branch regime.

In our experiments, in the case of high Reynolds number and high damping, the wake state starts with a 2P mode in the initial branch. The presence of the 2P mode in the initial branch could characterize the huge jump in amplitude observed in the high Reynolds number cases. In the case of high Reynolds number and high damping experiments, the wake state for most of the upper branch is 2P. At higher reduced velocity in the case of high Reynolds number experiments, the high amplitude vibration continues further into the regime where no synchronized patterns were observed (Figure 4.27) and continued to have high amplitude vibration. To extend the VIV synchronization further the VIV character either have to collapse into the stable regime (as Williamson and his group achieved in the case of low mass ratio and damping) or sustain VIV in the region where synchronized pattern is not observed.

In Chapter 7, it is shown that a synchronized pattern can be achieved by correlating the separation along the span.

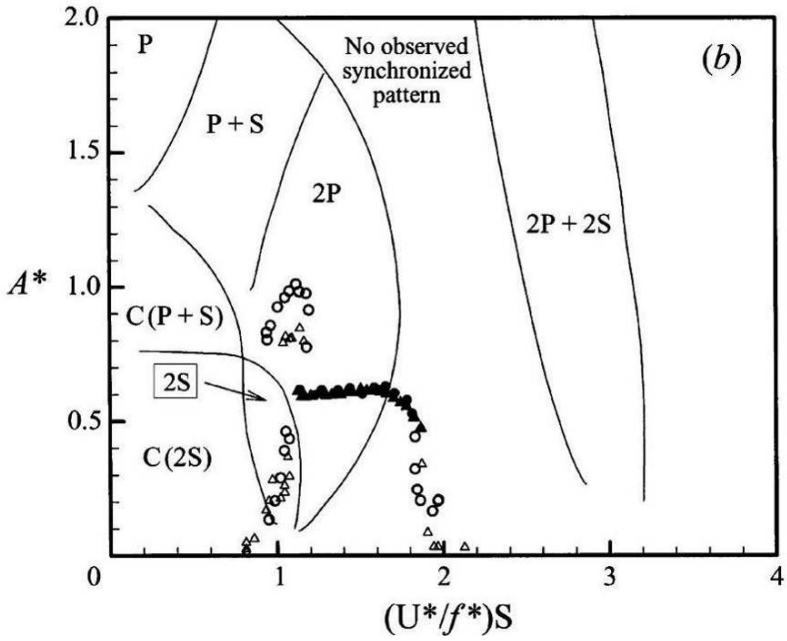

Figure 4.26. Response of VIV systems with low $(m^*+C_a)\zeta$ plotted over Williamson and Roshko map. (Williamson and Govardhan (2004)).

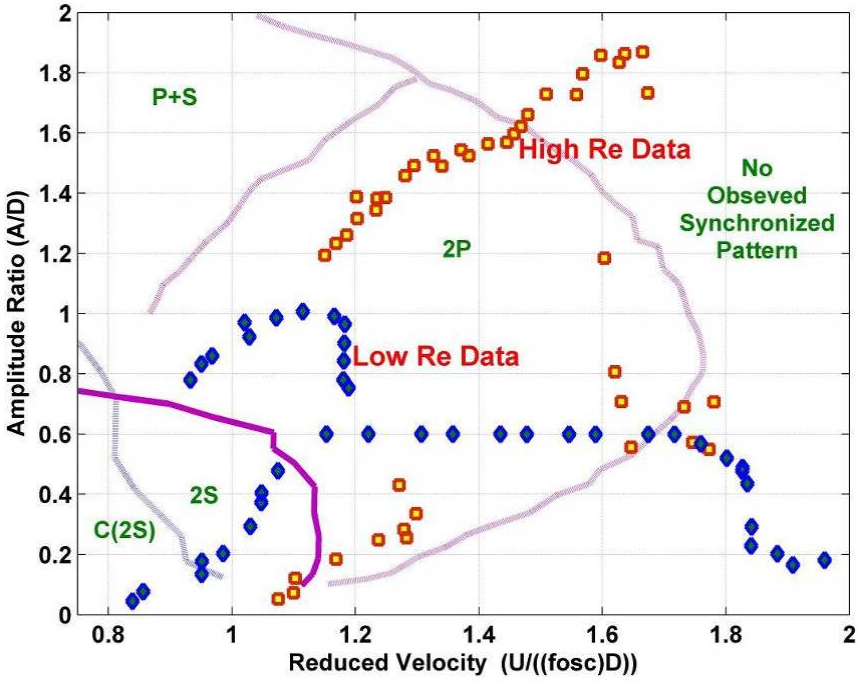

Figure 4.27. Comparison of response of low $(m^*+C_a)\zeta$ and low Reynolds numbers VIV system with the response of VIV system from our experiments at high Reynolds numbers and high damping, plotted over Williamson and Roshko map.

4.4.3. Analysis of spectral content

The spectral contents of the displacements were studied for systems operating in two different Reynolds number regimes. This study throws more light into understanding the change in the wake as the Reynolds number increases. In our experiments, the wake velocity was not measured. So the analyses were done on the displacement time traces. The influence of the higher harmonic components is less in the displacement spectrum in comparison to the velocity spectrum, so logarithmic spectrums of the displacements were plotted. It is harder for the wake character to manifest in the displacement spectrum unless it is strong. This would surface clearly in the force spectrum due to the direct influence of the wake structure on the forcing of the cylinder. In the present measurements prominent higher harmonics are observed for higher Reynolds number cases suggesting that the wake structure is reorganizing itself to maintain the high amplitude observed in the experiments.

In Figure 4.23, the effect of Reynolds number was studied. To understand the difference in response more clearly, the spectral responses were studied in more detail. Two extreme cases corresponding to 3.5″ (Re = 4.53×10^4 – 1.03×10^5) and 2.5″ (Re =2.86×10^4 – 5.72×10^4) in Figure 4.23 were chosen. The spectral components corresponding to reduced velocity for the whole range of experiments are plotted from Figure 4.28 through Figure 4.46 to study the power, distribution, and growth of the harmonic components. In both cases for reduced velocity less than 5 the spectral components had the same characteristics as shown in Figure 4.28 through Figure 4.32. The above reduced velocity refers to the range before the jump from initial branch to upper branch. For the 2.5″ cylinder case, the spectral components for the reduced velocity between 5 and 7.2 are shown in Figure 4.34, Figure 4.36, and Figure 4.38. In the above three figures, the spectrum has a small peak at the third harmonic component of the oscillation frequency. For the 3.5″ cylinder case, the spectral components for the reduced velocity between 5 and 7.2 are shown in Figure 4.33, Figure 4.35, and Figure 4.37. In these three figures, the spectra have more prominent peaks at the second and third harmonic components of the oscillation frequency.

As the reduced velocity increases above reduced velocity of 7.2, there is a steady increase in amplitude ratio for the 3.5″ cylinder and there is a steady drop in amplitude ratio for the 2.5″ cylinder case. For reduced velocity above 7.2, the power spectrum of the displacement show major differences in the higher harmonics for both cases. For the 3.5″ cylinder case, the spectral components for the reduced velocity above 7.2 are shown in Figure 4.37, Figure 4.39, Figure 4.41, Figure 4.43, and Figure 4.45. In these figures the spectra have more prominent peaks at the second harmonic components of the oscillation frequency. For the 2.5″ cylinder case, the spectral components for the reduced velocity above 7.2 are shown in Figure 4.38, Figure 4.40, Figure 4.42, and Figure 4.44. In the above figures, the spectra have no conspicuous peaks at the second harmonic or third harmonic components of the oscillation frequency. It can be hypothesized from the spectral character observed that initial range of synchronization that is for reduced velocity less than 5, there is the usual 2S mode of vortex shedding (Figure 4.26). For reduced velocity above 5 and less than 7.2 the lower Reynolds number case (2.5″ cylinder) shows the 2S and P+S type of character along the span with the peaks in the third harmonic of oscillation frequency and for the high Reynolds number (3.5″ cylinder) there is both the 2P and P+S or 2P and 2S along the span. These two hypotheses by the author are corroborated by the observations made by Hover et al. (2004) and Davis (2001) in their work on the three dimensionality in the vortex shedding process.

For the case of low Reynolds number and when the reduced velocity > 7.2, the higher harmonic peaks are lost and the only conspicuous peaks are at the primary oscillating frequency. In the case of high Reynolds number, the peak at the second harmonic is still pertinent and it becomes more prominent as the Reynolds number increased and the third harmonic peak is lost with increase in Reynolds number. It can be hypothesized that, at high Reynolds numbers, due to the higher level of velocity fluctuations, the 2P mode becomes more stable and stronger and thus leading to a stronger forcing and larger amplitude of oscillation.

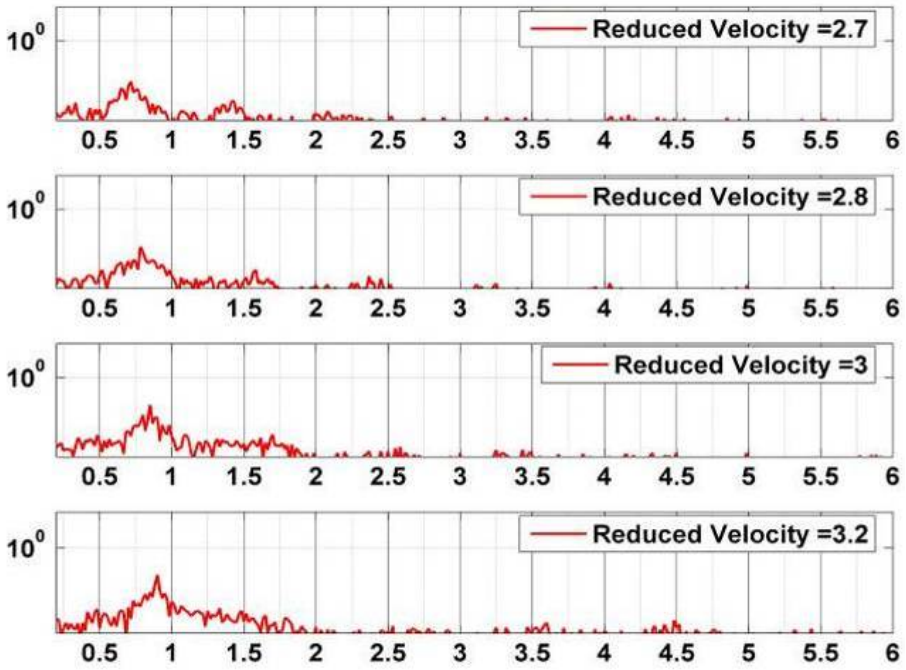

Figure 4.28. Spectra of displacement time series for a 2.5″ smooth cylinder operating in Re = 2.9×10^4 – 5.7×10^4 for reduced velocity, 2.7 – 3.2.

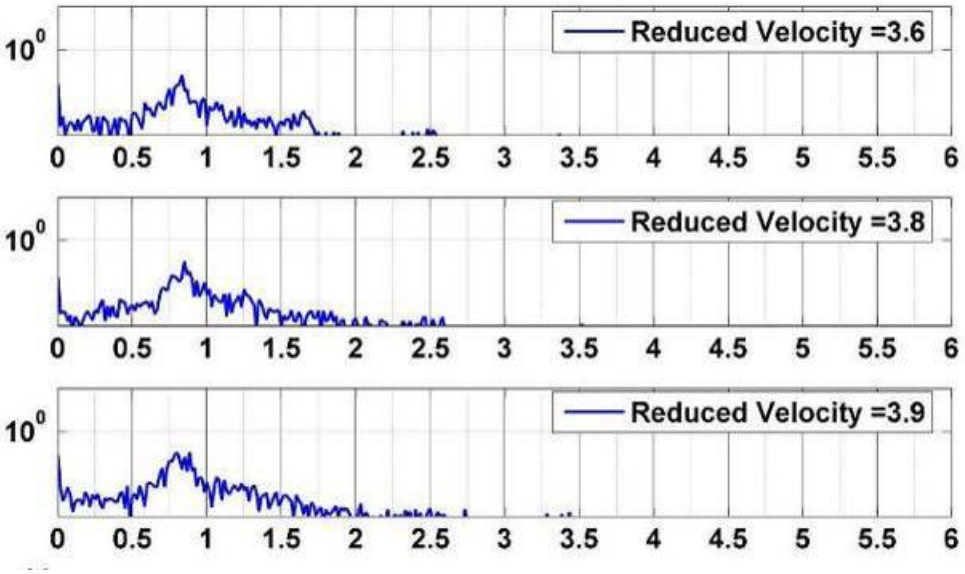

Figure 4.29. Spectra of displacement time series for a 3.5″ smooth cylinder operating in Re = 4.5×10^4 – 1×10^5 for reduced velocity, 3.6 - 4.1.

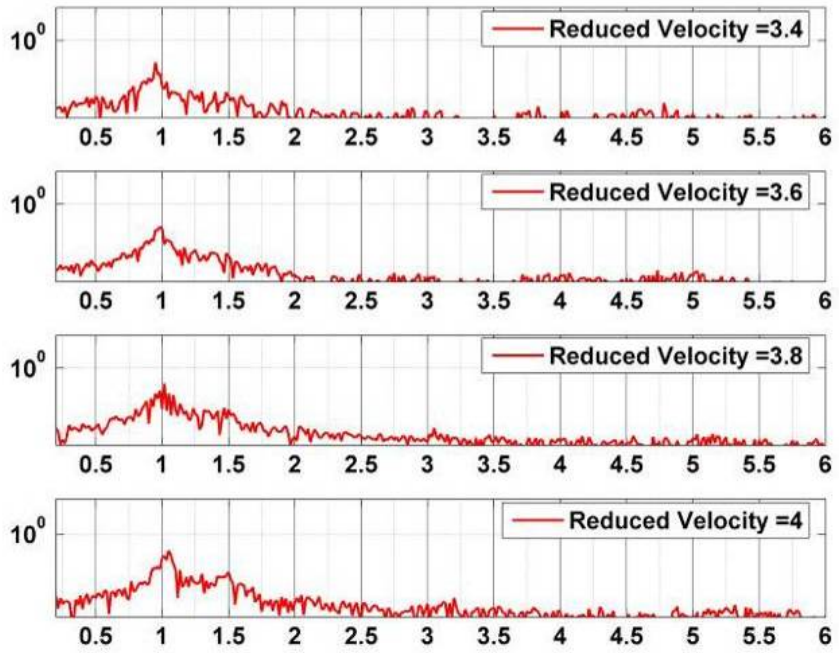

Figure 4.30. Spectra of displacement time series for a 2.5″ smooth cylinder operating in Re = 2.9×10^4 – 5.7×10^4 for reduced velocity, 3.4 – 4.

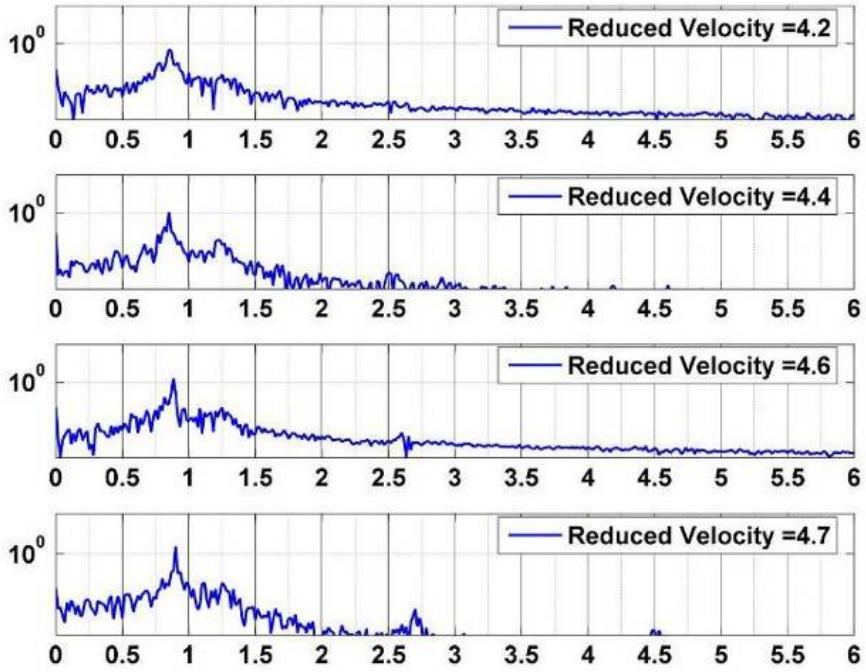

Figure 4.31. Spectra of displacement time series for a 3.5″ smooth cylinder operating in Re = 4.5×10^4 – 1×10^5 for reduced velocity, 4.2- 4.7.

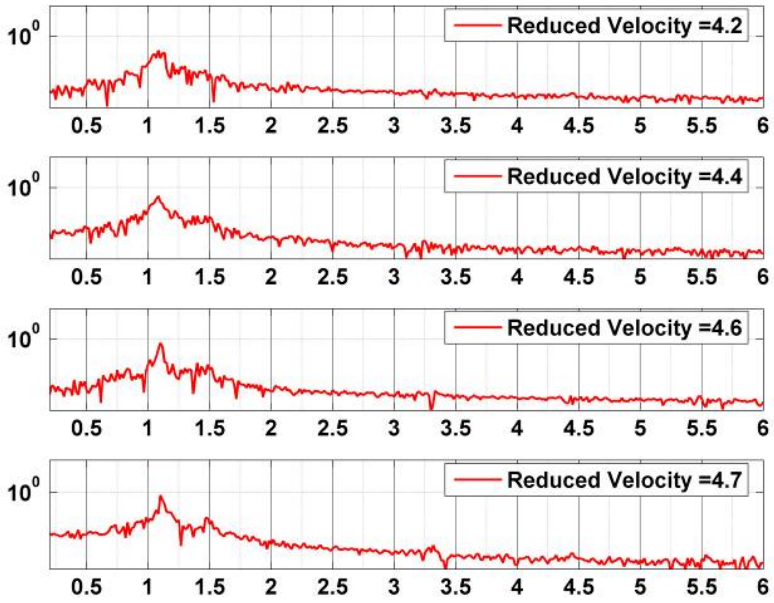

Figure 4.32. Spectra of displacement time series for a 2.5″ smooth cylinder operating in Re = 2.9×10^4 – 5.7×10^4 for reduced velocity, 4.2 – 4.7.

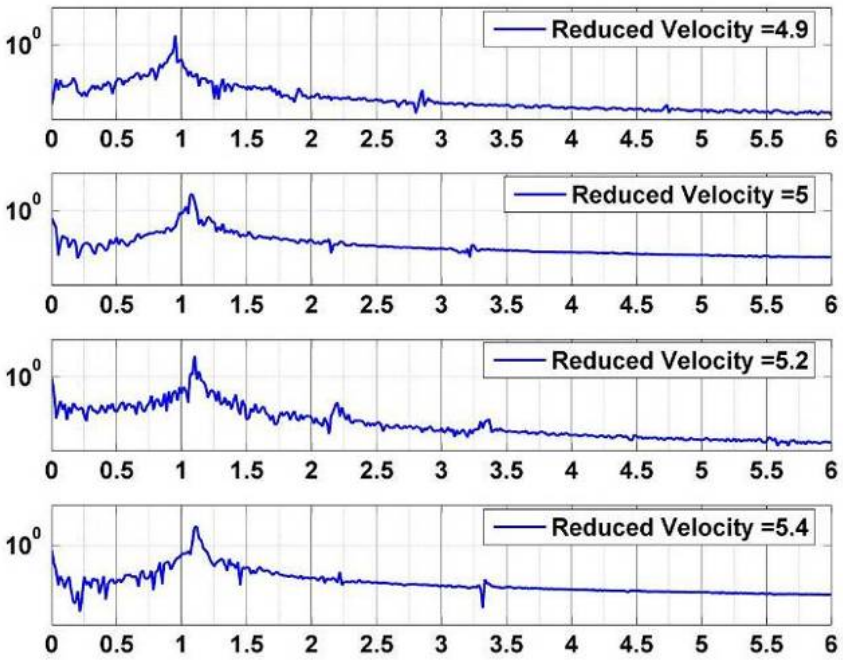

Figure 4.33. Spectra of displacement time series for a 3.5″ smooth cylinder operating in Re = 4.5×10^4 – 1×10^5 for reduced velocity, 4.9 – 5.4.

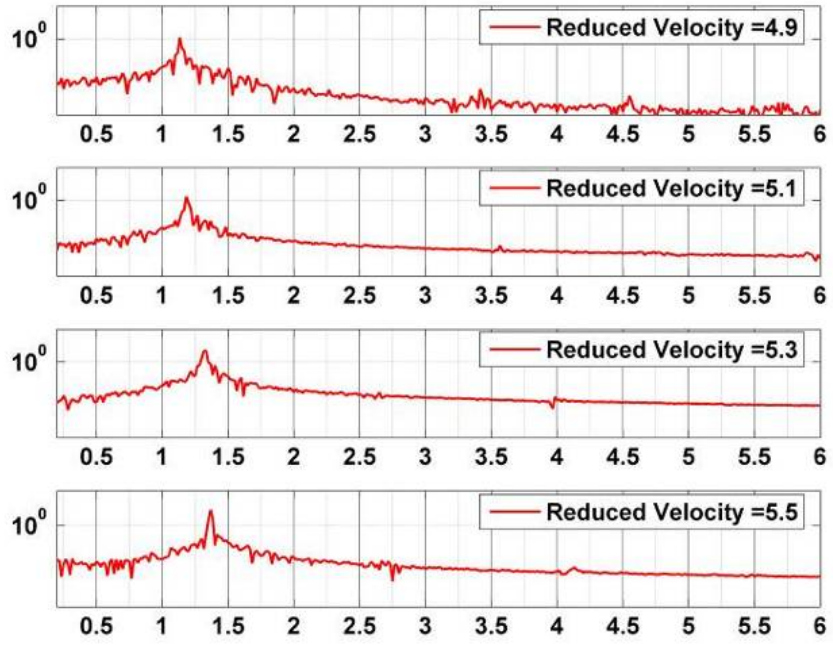

Figure 4.34. Spectra of displacement time series for a 2.5″ smooth cylinder operating in Re = 2.9×10^4 – 5.7×10^4 for reduced velocity, 4.9 – 5.5.

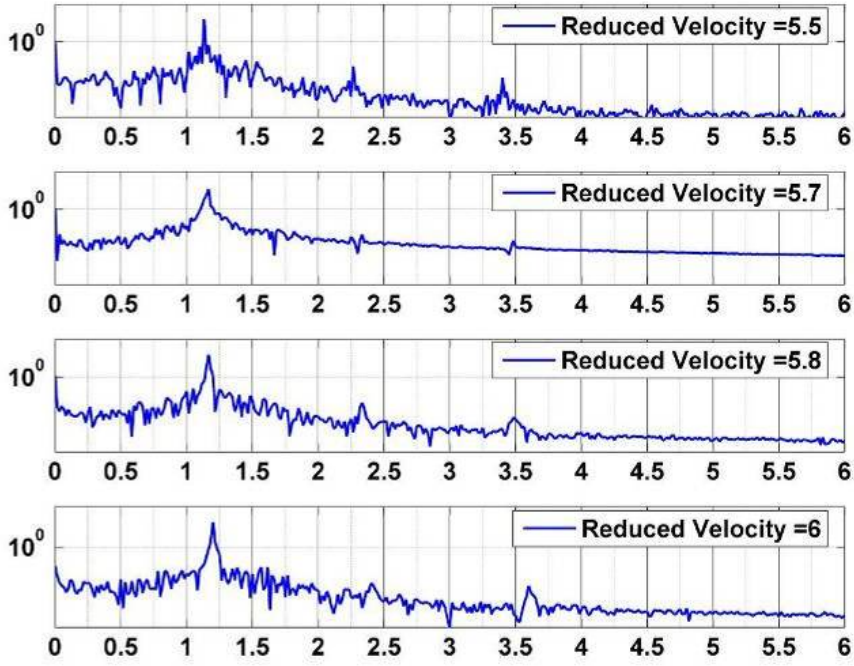

Figure 4.35. Spectra of displacement time series for a 3.5″ smooth cylinder operating in Re = 4.5×10^4 – 1×10^5 for reduced velocity, 5.5 – 6.

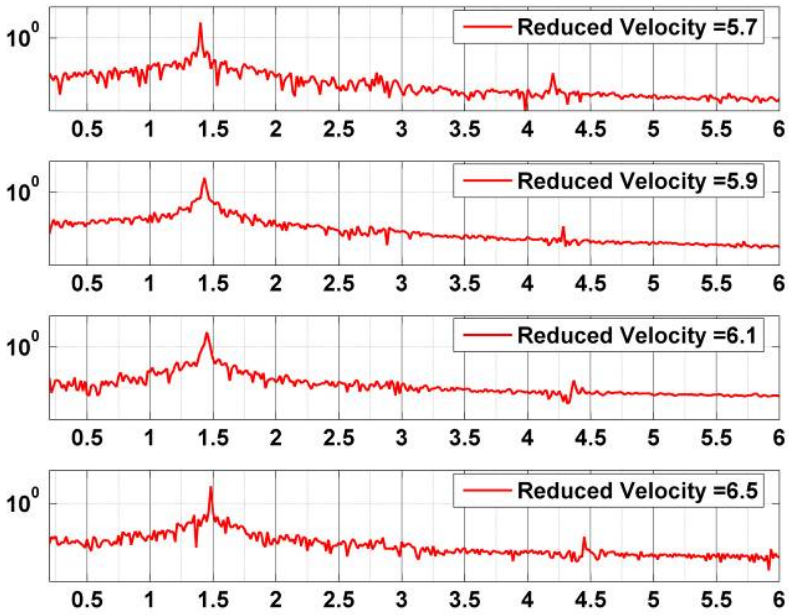

Figure 4.36. Spectra of displacement time series for a 2.5″ smooth cylinder operating in Re = 2.9×10^4 – 5.7×10^4 for reduced velocity, 5.7 – 6.5.

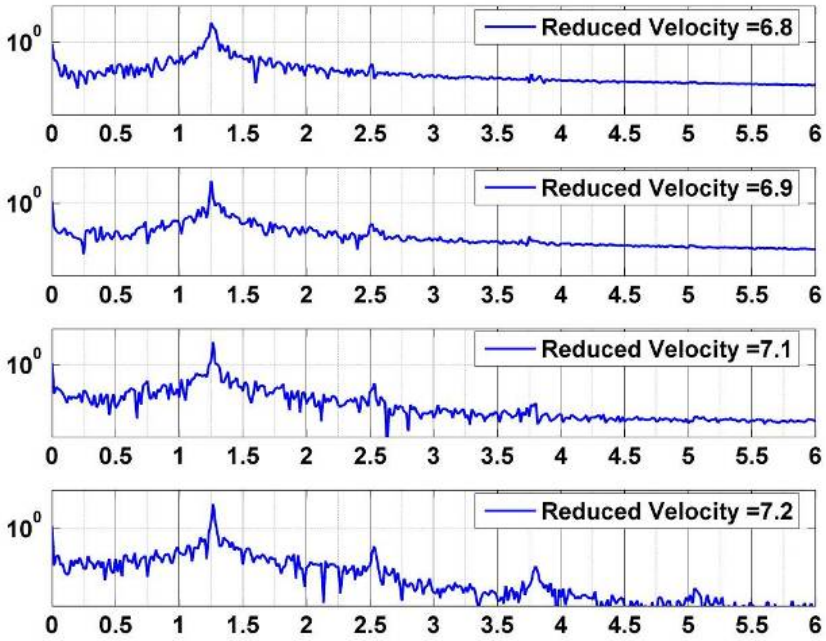

Figure 4.37. Spectra of displacement time series for a 3.5″ smooth cylinder operating in Re = 4.5×10^4 – 1×10^5 for reduced velocity, 6.8 – 7.2.

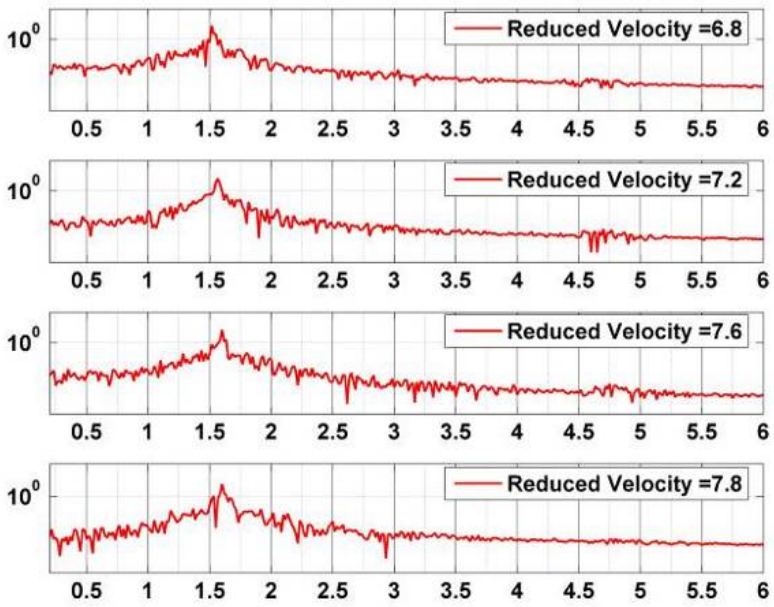

Figure 4.38. Spectra of displacement time series for a 2.5″ smooth cylinder operating in Re = 2.9×10^4 – 5.7×10^4 for reduced velocity, 6.8 – 7.8.

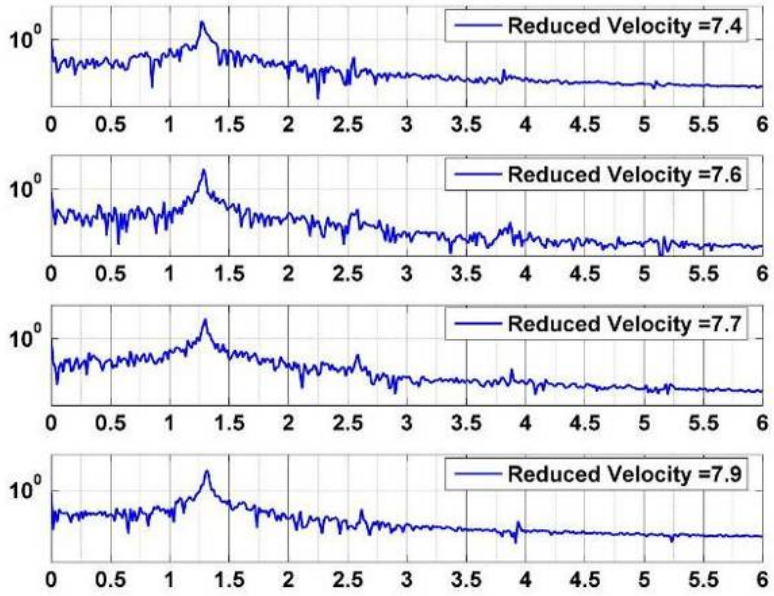

Figure 4.39. Spectra of displacement time series for a 3.5″ smooth cylinder operating in Re = 4.5×10^4 – 1×10^5 for reduced velocity, 7.4 – 7.9.

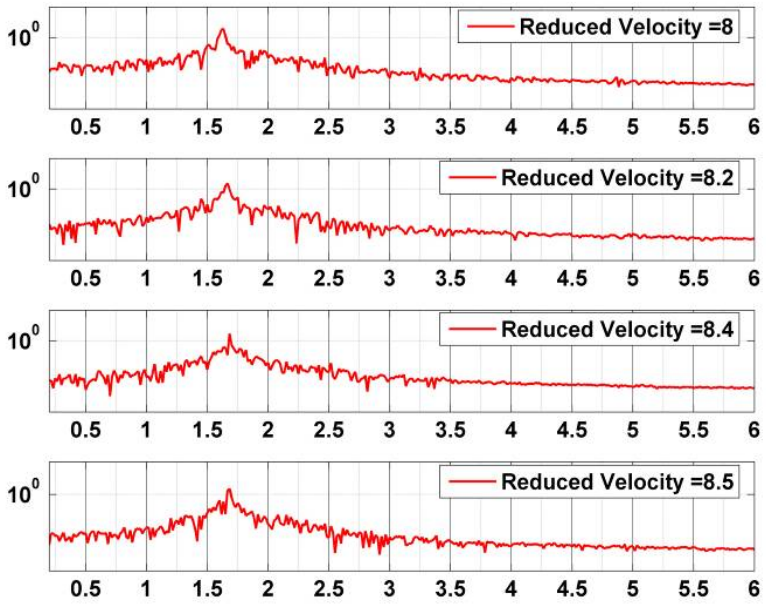

Figure 4.40. Spectra of displacement time series for a 2.5″ smooth cylinder operating in Re = 2.9×10^4 – 5.7×10^4 for reduced velocity, 8.0 – 8.5.

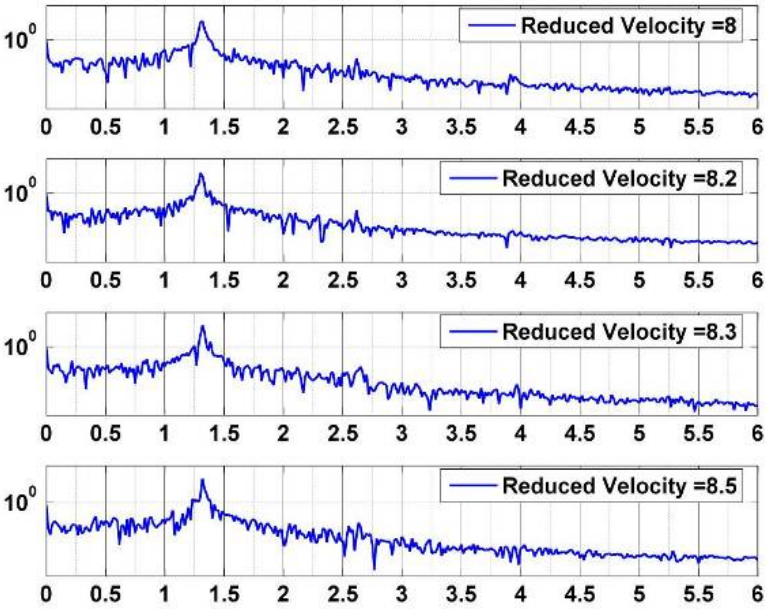

Figure 4.41. Spectra of displacement time series for a 3.5″ smooth cylinder operating in Re = 4.5×10^4 – 1×10^5 for reduced velocity, 8.0 – 8.5.

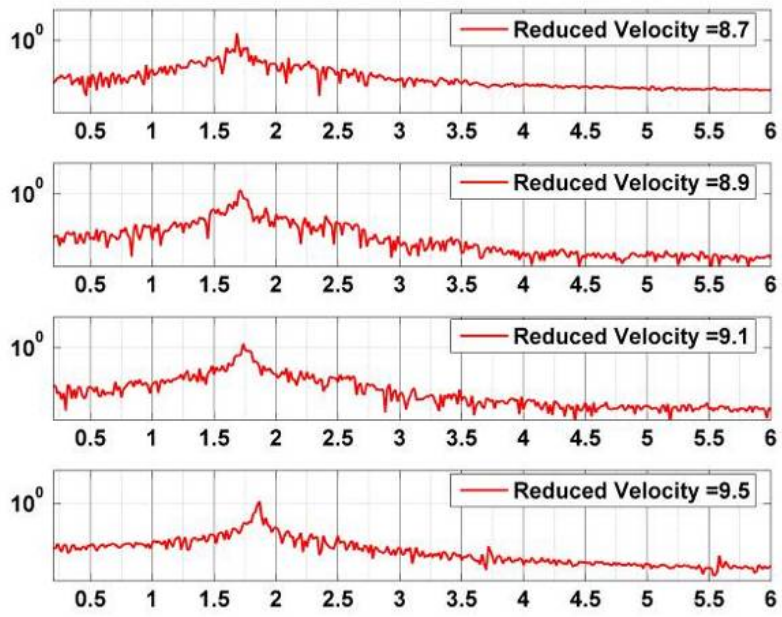

Figure 4.42. Spectra of displacement time series for a 2.5″ smooth cylinder operating in Re = 2.9×10^4 – 5.7×10^4 for reduced velocity, 8.7 – 9.5.

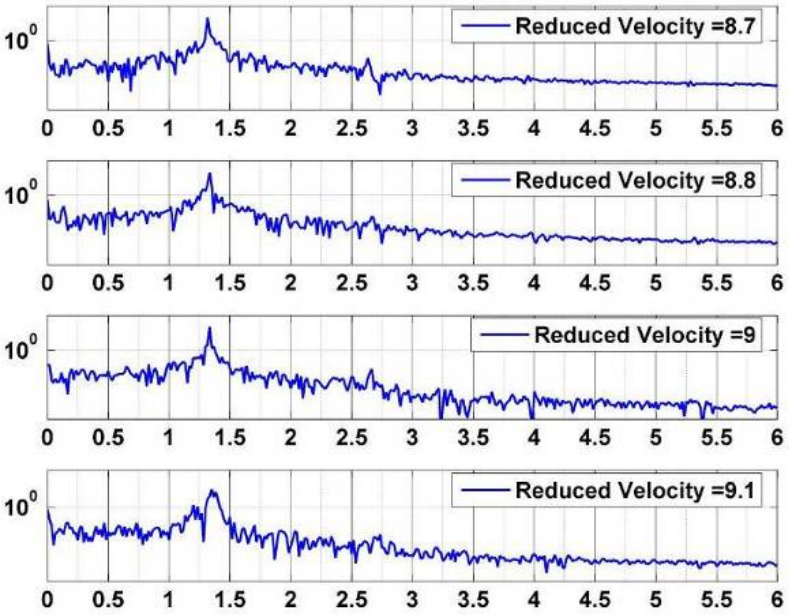

Figure 4.43. Spectra of displacement time series for a 3.5″ smooth cylinder operating in Re = 4.5×10^4 – 1×10^5 for reduced velocity, 8.7 – 9.1.

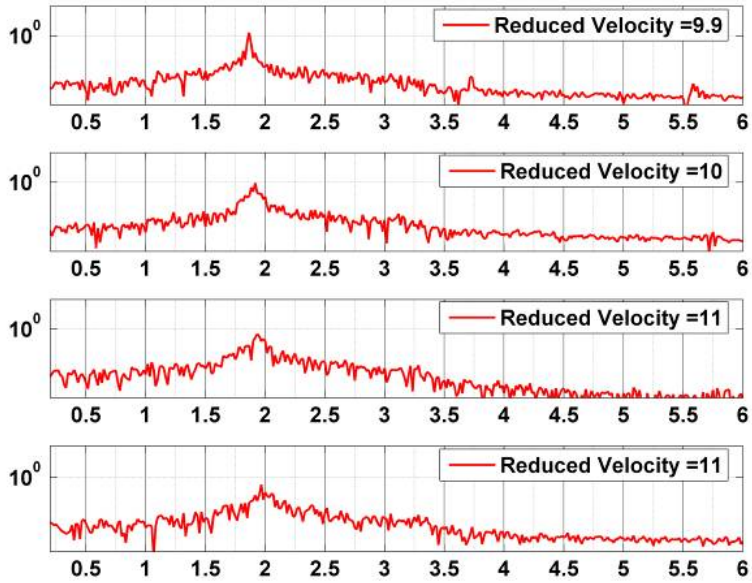

Figure 4.44. Spectra of displacement time series for a 2.5″ smooth cylinder operating in Re = 2.9×10^4 – 5.7×10^4 for reduced velocity, 9.9 – 11.9.

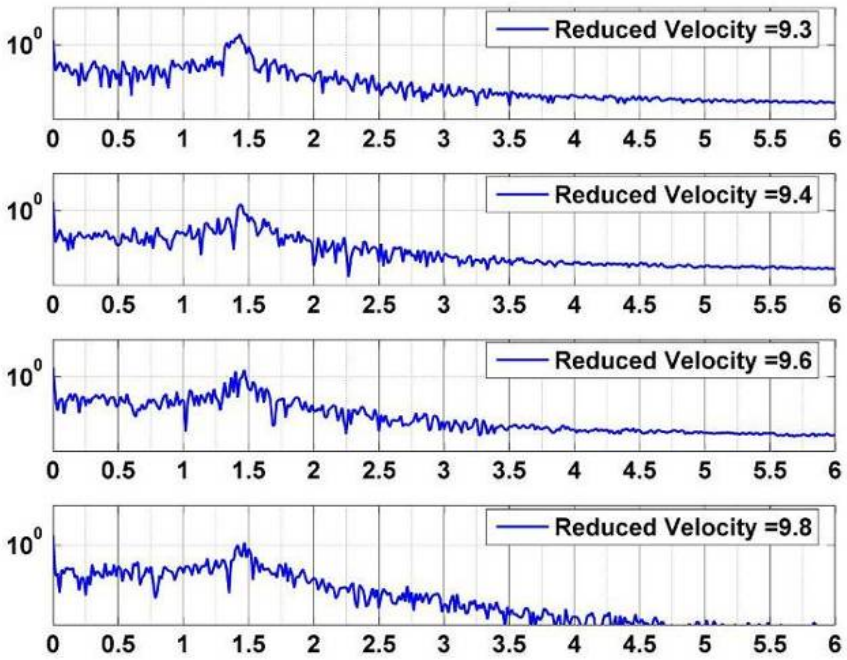

Figure 4.45. Spectra of displacement time series for a 3.5″ smooth cylinder operating in Re = 4.5×10^4 – 1×10^5 for reduced velocity, 9.3 – 9.8.

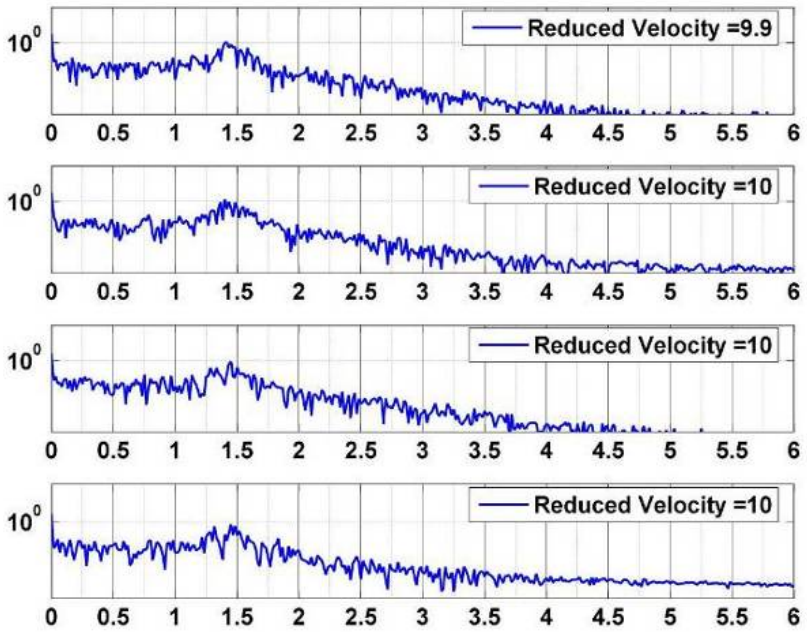

Figure 4.46. Spectra of displacement time series for a 3.5″ smooth cylinder operating in Re = 4.5×10^4 – 1×10^5 for reduced velocity, 9.9 – 10.8.

4.4.4. The lower branch is lost due to high damping.

In our experiments the VIV response characteristics throughout the synchronization range was observed to have only two branch response (see Figure 4.47). In Figure 4.47 the branches that are identified are the initial and upper branch as per the definition of Khalak and Williamson (1997b).

Khalak and Williamson (1997b), observed that the VIV response was either two branch or three branch depending on the product of mass ratio and damping ratio. The two branch response constituted of the initial and lower branch and the three branch response constituted of initial, upper and lower branch as shown in Figure 4.48. Recently, Govardhan and Williamson (2006) claimed that the number of response branches is a function of Reynolds number in addition to $(m^*+C_a)\zeta$. In their experiments they also found that the demarcation line for the three branch response is $A^*=0.6$ as shown in Figure 4.49. According to their demarcation, the present experiments should be in the three branch response as shown in Figure 4.49.

In our experiments we see predominantly two branch response, the initial branch and upper branch as shown in Figure 4.47. In Figure 4.47, the lower branch was nearly eliminated. This is not the common VIV character that has been observed for high $(m^*+C_a)\zeta$ experiments. In the earlier experiments with high $(m^*+C_a)\zeta$ experiments conducted by Feng (1968), the amplitude ratio gradually increases with the reduced velocity along the initial branch till a reduced velocity value of 5. At reduced velocity of value 5 the amplitude response undergoes a jump from initial branch to lower branch. The magnitude of the amplitude response for the previous high $(m^*+C_a)\zeta$ experiments is smaller for nearly the same $(m^*+C_a)\zeta$ that is used in the present experiments. In our experiments, the jump from the initial branch to upper branch is similar to a low $(m^*+C_a)\zeta$ type of experiments.

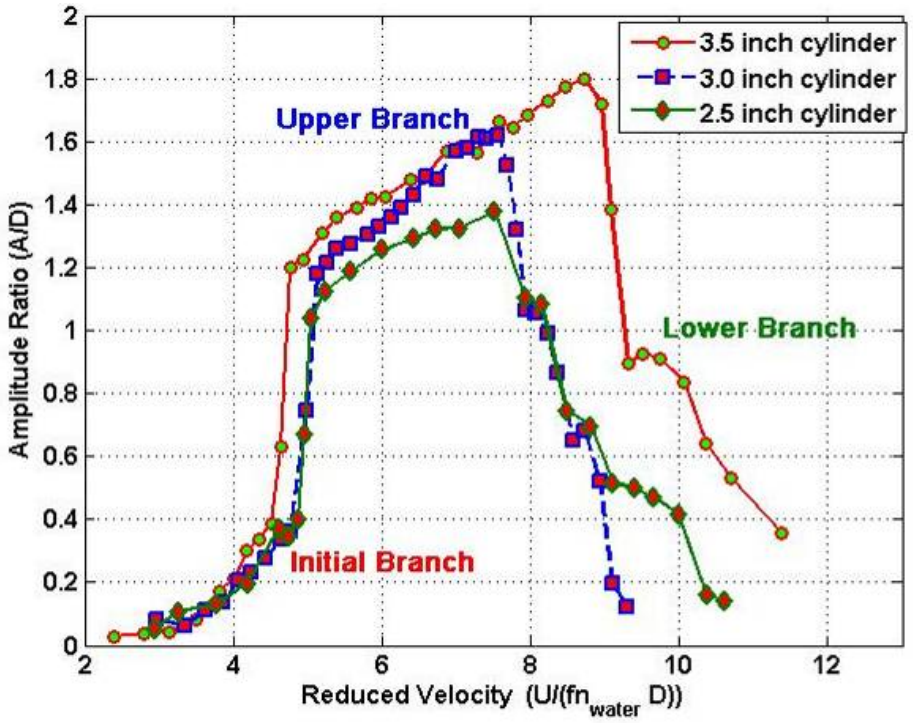

Figure 4.47. Lower branch is lost in the VIV response of the present experiments due to high damping. Three different cases have been compiled.

In our experiments, the upper branch is maintained for longer synchronization range and the width of the lower branch in comparison to the upper branch is narrow. In some cases at the end of the synchronization range, the upper branch jumps to a lower value of amplitude ratio and a small hump is created which could be considered as lower branch. In other cases, the jump is from synchronization to desynchronization and no

hump is created. In our experiments, the reduction in the width of the lower branch can be related to the high $(m^*+C_a)\zeta$ values present in the experiments. As the $(m^*+C_a)\zeta$ increases, the end force correlation reduces at a faster rate in the lower branch regime as shown in Figure 4.22. In the lower branch, there is a steady reduction in the correlation length (Hover et al. 2004; Hover et al. 1998). At the beginning of the synchronization, higher damping values tend to correlate the end force better (Hover et al. 2004).

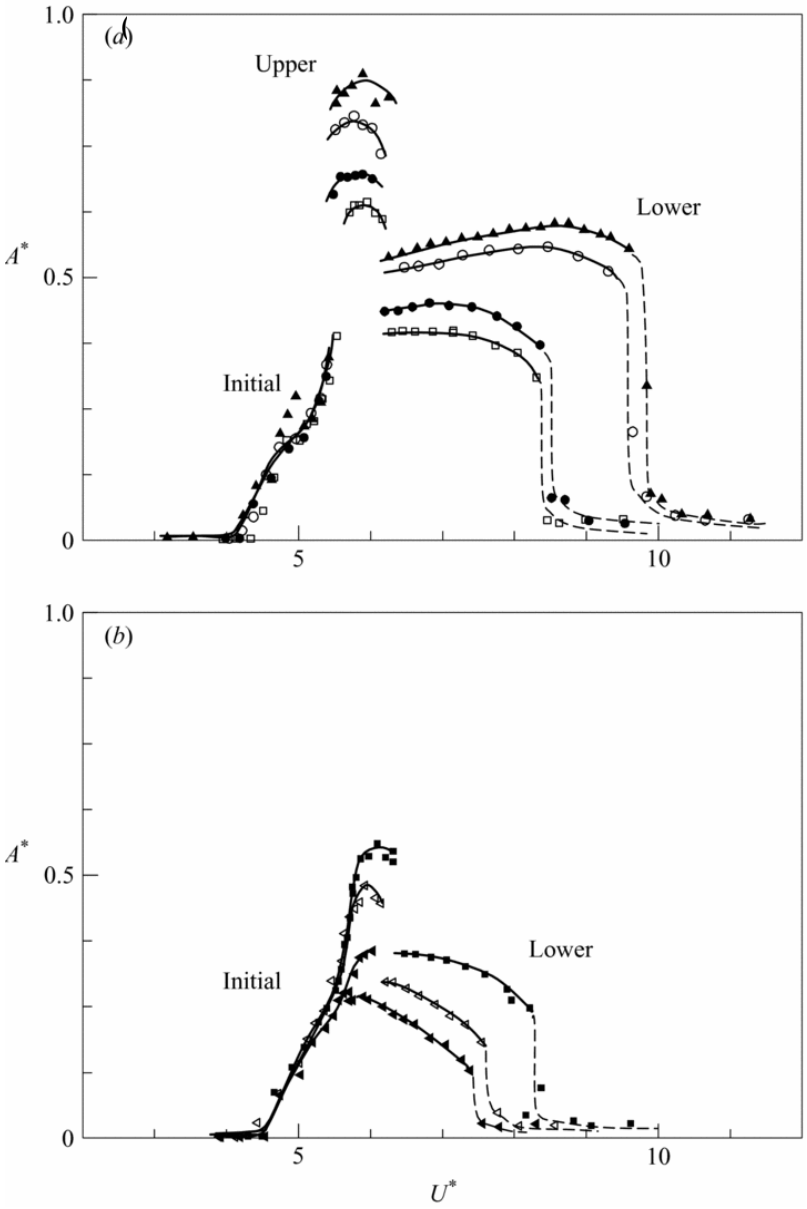

Figure 4.48. Amplitude response plots for increasing mass–damping values (α), Re ≈4000). (a) Three-branch amplitude responses; α= 0.000-0.252; (b) two-branch amplitude responses. α = 0.340-0.585. [Reproduced from Govardhan and Williamson (2006)].

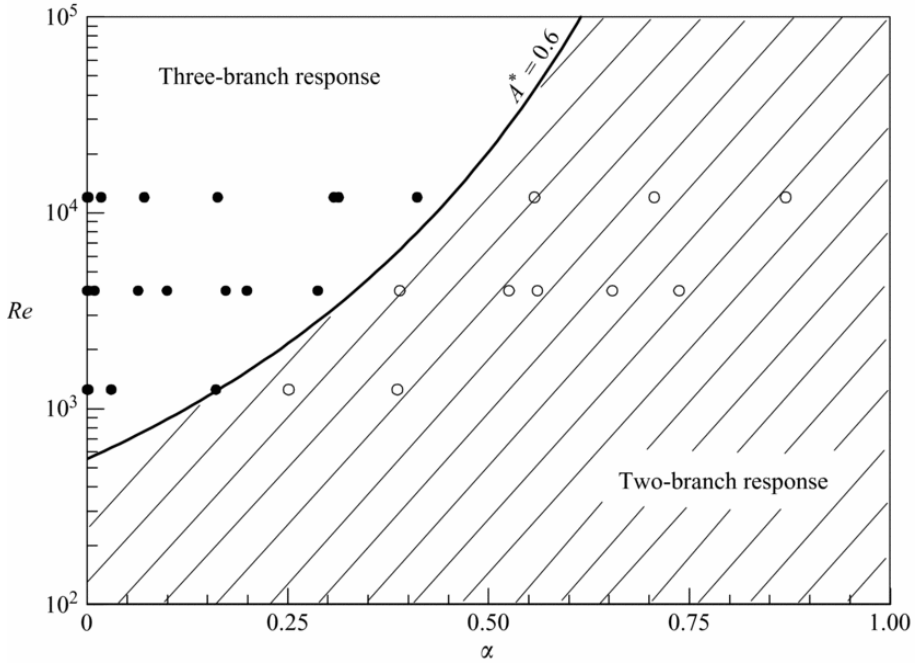

Figure 4.49. The region of the three-branch and the two-branch response in the parameter space of mass–damping parameter and Re (Govardhan and Williamson 2006).

4.4.5. Reynolds number has a stronger influence than m* and m*ζ on A/D

In our experiments, it was found that the dependence of high amplitude VIV response is more dictated by the Reynolds number than mass ratio and $(m^*+C_a)\zeta$. Experiments were conducted for the same mass ratio and nearly same $(m^*+C_a)\zeta$ but at different Reynolds number by shifting the natural frequency of the system. The response is plotted in Figure 4.50. In this plot, the VIV response for higher Reynolds number had a higher amplitude ratio of oscillation and the range of the upper branch also increased. It seems that there is a critical combination of Reynolds number and reduced velocity above which a linear and steadily increasing upper branch is observed rather than a curving upper branch seen for low Reynolds number cases (Figure 4.23 and Figure 4.24).

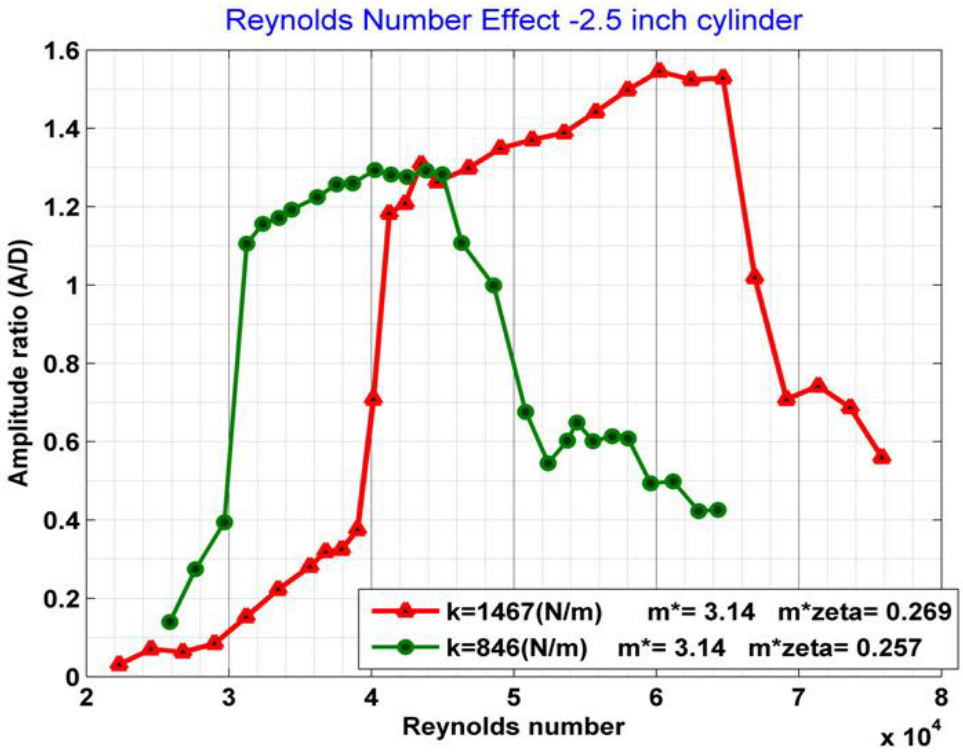

Figure 4.50. The VIV response data of 2.5″ cylinder with the same mass ratio and nearly same damping operating in two different range of Reynolds number which was achieved by varying the natural frequency of the system, demonstrating the dependence of VIV response with Reynolds number.

4.4.6. High amplitude VIV is achieved in spite of high damping.

In Figure 4.51, the effect of $(m^*+C_a)\zeta$ and mass ratio for experiments conducted at different regimes of Reynolds number is considered. In Figure 4.51, the present experiment is compared to the experiments done by Khalak and Williamson ($Re \approx 5.00\times10^3$-$1.60\times10^4$), Govardhan and Williamson ($Re \approx 2.90\times10^3$-$1.90\times10^4$), and Feng ($Re \approx 6.05\times10^3$-$2.30\times10^4$). The maximum amplitude ratio for the present experiments and Khalak and Williamson are nearly 1.8 times even though the product of mass ratio and damping ratio is about 20 times higher in our experiments. In the case of Govardhan and Williamson, the mass ratio is less than our experiments and the product of mass ratio and damping ratio is about 23 times larger than in our experiments. Still, the ratio of amplitude of oscillation is 1.8 times higher in our experiments. The range of upper branch for both the experiments is the same. In the case of Feng's experiments, the mass ratio was 170 times higher and the product of mass ratio and damping ratio is about 1.4 times

higher than our experiments. The resulting ratio of amplitude of oscillation of our experiments is about 3.3 times higher than Feng's experiments.

In our experiments, the high amplitude ratio of A/D =1.8 was achieved in spite of the high $(m^*+C_a)\zeta$. The effect of high damping has been offset by the character of the Reynolds number of the present experiment which falls in the TrSL3 regime. The high lift coefficient in the TrSL3 regime and other factors discussed in the Section 4.1.2 enabled the VIV systems in the TrSL3 regime to achieve high amplitude vibration despite of high damping. In Figure 4.51, our experiment plot might look like an amplification of the Feng's data, but they both are characteristically different from each other. In our data, upper branch is the dominant branch and in Feng's case, lower branch is the dominant one.

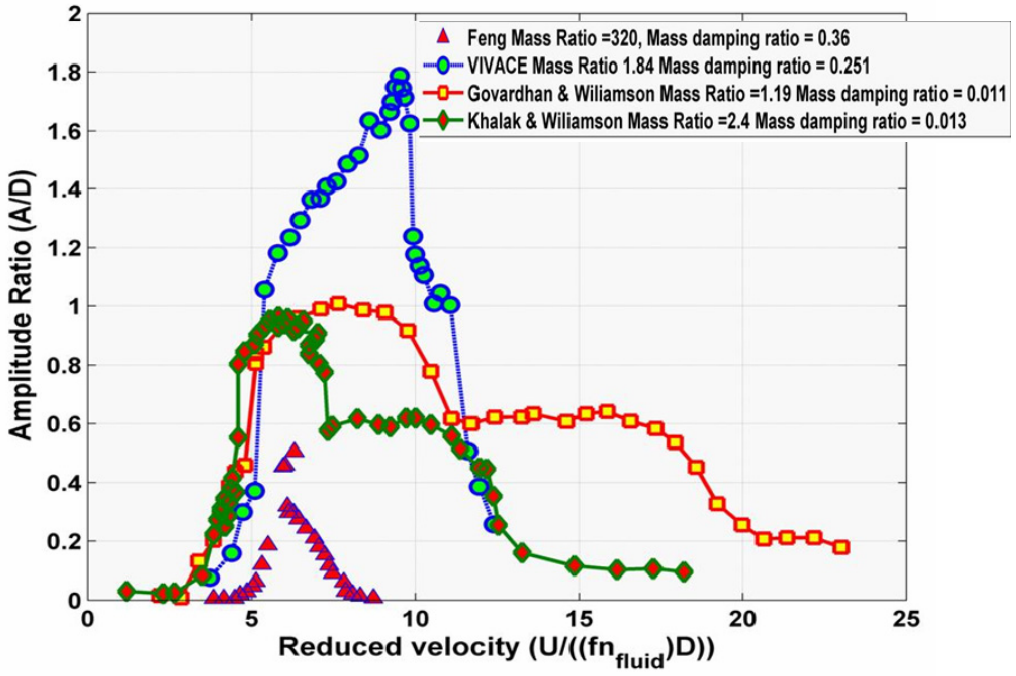

Figure 4.51. Comparison of high $(m^*+C_a)\zeta$ and high Reynolds number VIV data from our experiments with experiments conducted by other researchers with low and high $(m^*+C_a)\zeta$ but at lower Reynolds number experiments.

4.4.7. Disappearance of hysterisis

In our experiments, no hysteretic response was found between the initial and upper branch as in the case low $(m^*+C_a)\zeta$ experiment as shown in Figure 4.53 and Figure 4.54. In Figure 4.53, the response amplitude is plotted for the forward reduced velocity

and the backward reduced velocity and there was no hysterisis in the response observed. The experiments were conducted very carefully to detect any hysterisis phenomena. In Figure 4.54, the ratio of the response frequency to the natural frequency in water is plotted for the forward reduced velocity and the backward reduced velocity and there were no hysterisis was observed in the frequency response. In our experiments, hysterisis was not observed between upper branch and lower branch as in high $(m^*+C_a)\zeta$ experiment. In the case of low $(m^*+C_a)\zeta$ experiments a hysteretic response was found between initial and upper branch (Williamson and Govardhan 2004). The loss in hysteresis in the present experiments is attributed to the high damping conditions. In VIV experiments the hysteretic character and the size of the hysteretic region depend on the level of damping in the system (Klamo et al. 2006). Our experiments are conducted at high $(m^*+C_a)\zeta$ values ($\alpha > 0.2$). The high damping experiments are conducted to model VIVACE. In low Reynolds number cases, a hysteretic region was observed between the lower branch and the desynchronized region (Klamo et al. 2006; Singh and Mittal 2005), Klamo et al.'s results are reproduced in Figure 4.56. The hysteretic character shows a marked difference for low $(m^*+C_a)\zeta$ and high $(m^*+C_a)\zeta$ experiments as seen in Figure 4.54 and Figure 4.55. In the experiments done at Cornell by Williamson's group, the hysterisis character observed between the initial and upper branches is attributed to the low mass ratio cases.

The hysteresis observed in VIV is associated with the different vortex-shedding modes associated with different branches (Williamson and Govardhan 2004). It can be hypothesized that the correlation of the end-force associated with different branches might be the reason for hysterisis from the experimental results of Hover et al. (2004). The correlation of the end-force might be the reason for the hysteretic character, because it is associated with the transition of the vortex shedding modes along the cylinder for a particular reduced velocity. As the reduced velocity is increased, the jump between the initial branch and the upper branch would result in only in a partial transition from the 2S to 2P mode along the cylinder span (Hover et al. 2004). When the reduced velocity is approached backward from a higher reduced velocity value, the cylinder span would have a stable 2P state and the transition from 2P to 2S mode might extend to lower reduced velocity for a low mass and damping system. This latent effect of transition might result

in hysterisis. In Figure 4.52, a schematic representation of hysterisis in the lock-in region of a freely vibrating circular cylinder with low $(m^*+C_a)\zeta$ and high $(m^*+C_a)\zeta$ is shown.

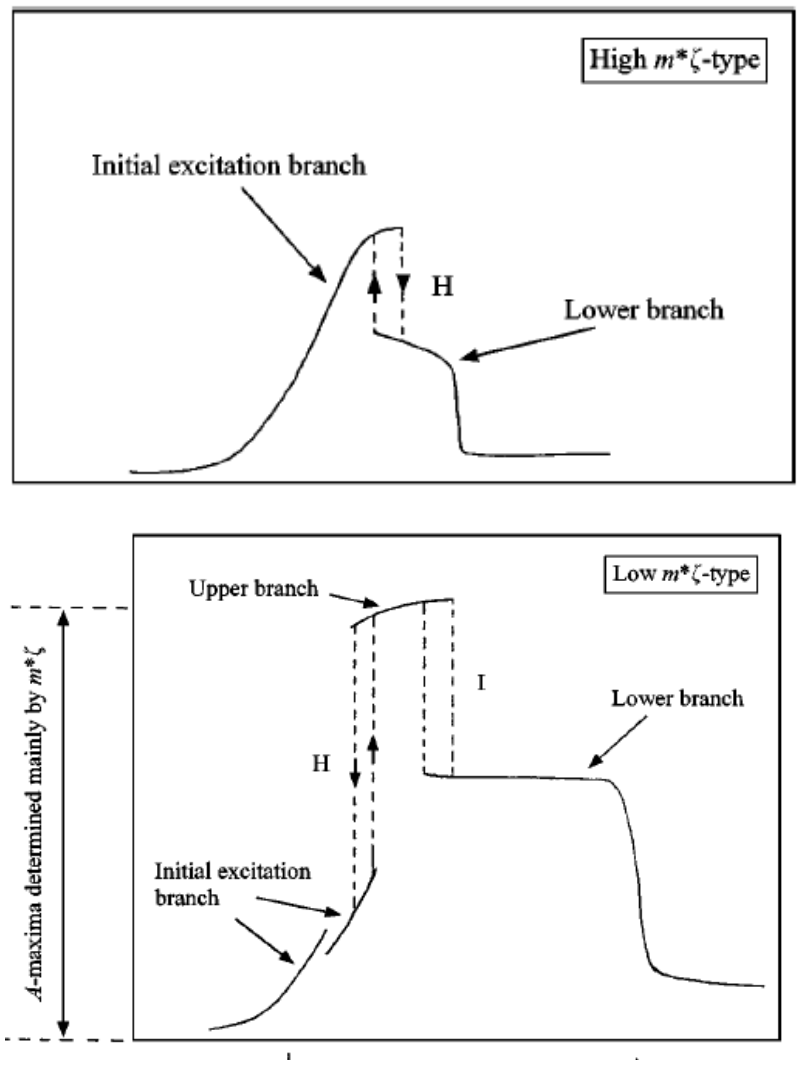

Figure 4.52. Schematic representation of hysterisis in the lock-in region of a freely vibrating circular cylinder with low $(m^*+C_a)\zeta$ and high $(m^*+C_a)\zeta$. [Reproduced from Williamson and Govardhan (2004)].

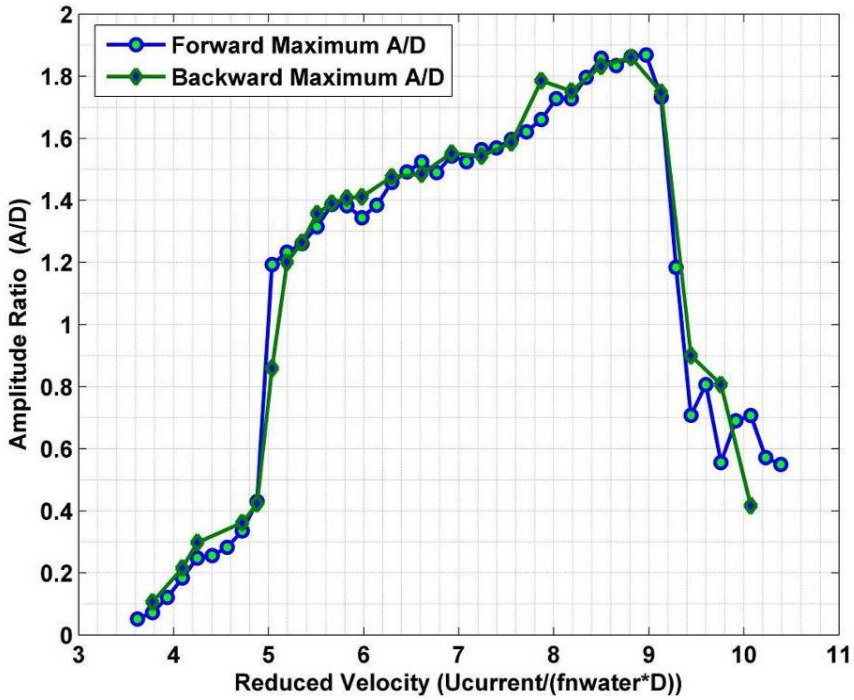

Figure 4.53 The amplitude of VIV response of a 3.5″ cylinder in the present experiments for the forward and backward reduced velocity, demonstrating no hysterisis.

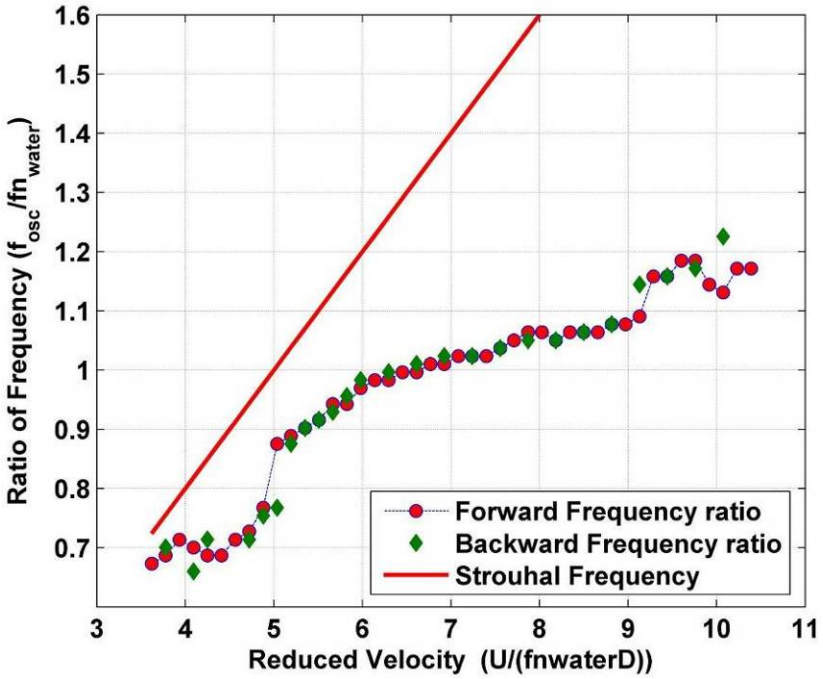

Figure 4.54. The frequency ratio of VIV response of a 3.5″ cylinder in the present experiments for the forward and backward reduced velocity, demonstrating no hysterisis.

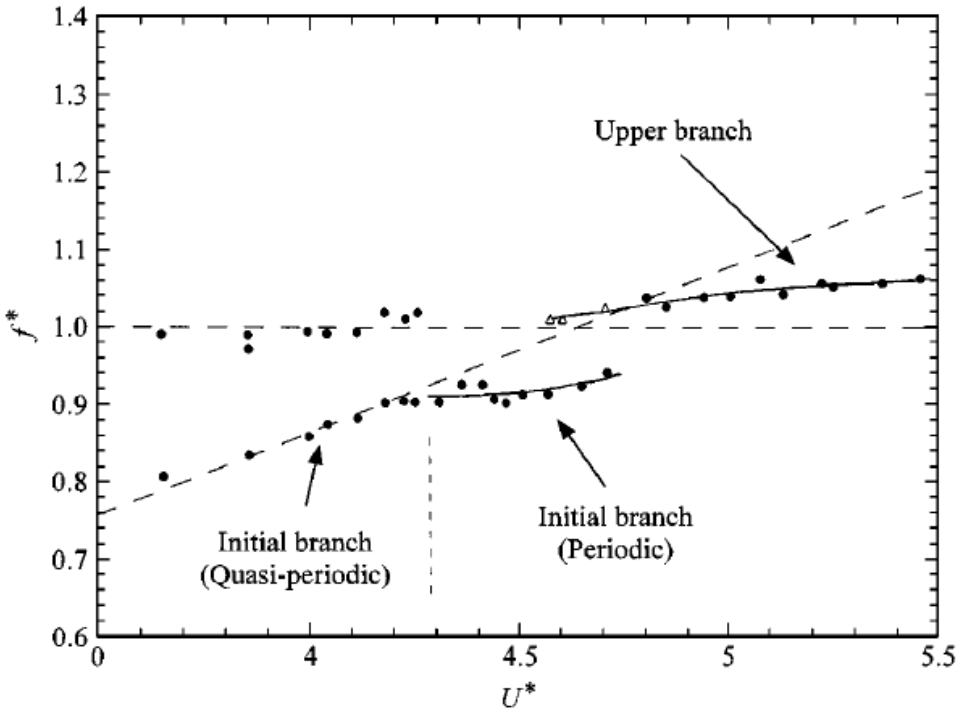

Figure 4.55. The frequency ratio of VIV response of the low mass and damping experiments conducted at low Reynolds number for the forward and backward reduced velocity, demonstrating hysterisis (Khalak and Williamson 1999).

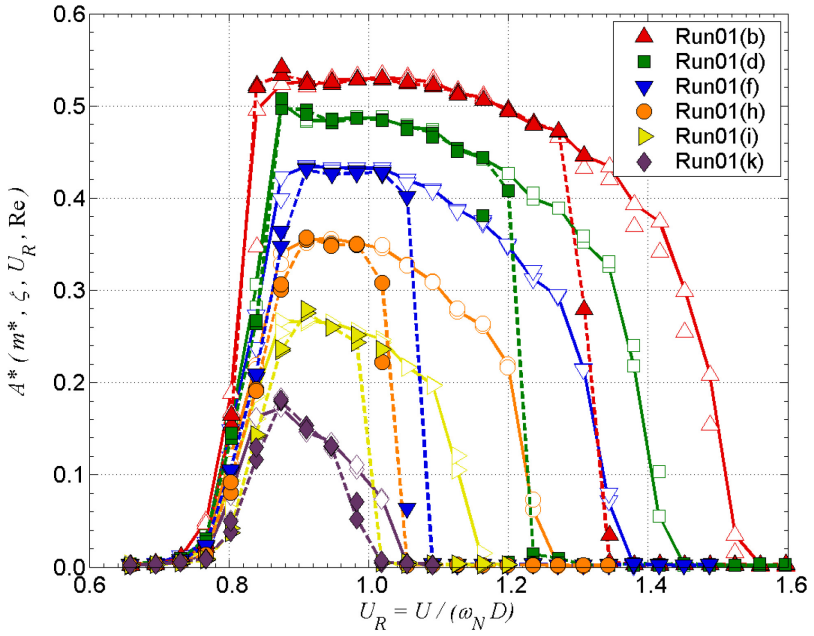

Figure 4.56. Hysteretic response observed between the lower branch to desynchronized state. Solid lines and white data points show increasing tunnel velocities and dashed lines and colored data points show decreasing tunnel velocities. [Reproduced from Klamo (2006)].

4.4.8. Mass damping plots in TrSL3 regime

The reigning two plots that exist for the prediction of peak amplitude ratio based on the mass ratio and damping are the Griffin plot and Sarpkaya's plot. They plot the peak-amplitude data with respect to, the product of mass ratio with damping coefficient $m^*\zeta$, and Skop Griffin parameter S_G ($=2\pi^3 St^2 \zeta \rho_m/\rho_f$). In this Section, we look at the Griffin-plot that is modified by Govardhan and Williamson (2006). The peak amplitude when plotted with respect to the product of mass ratio and damping has a lot of scatter due to the variation in the experimental variables and the density and viscosity of the fluid in which the experiments were conducted. There has been continuous effort to find an effective relation between the peak amplitude with respect to the product of mass ratio and damping. Sarpkaya (2004) in his review paper, mentions about his attempt to plot amplitude ratio with an exponential relation to the Skop-Griffin parameter. In his method he doesn't recognize the effect of Reynolds number. It was recently identified by researchers at Caltech and Cornell that peak amplitude is a function of Reynolds number for low Reynolds number. In our experiments we proved the dependence of VIV response on Reynolds number. Recently, Govardhan and Williamson (2006) redefined the Griffin plot, the peak VIV amplitude as a function of $(m^*+C_a)\zeta$ variable with Reynolds number as parameter (see Figure 4.57).

Govardhan and Williamson (2006) came up with a better fit for the peak amplitude in terms of the mass-damping parameter for the experiments that have been conducted in the TrSL2 regime. In their fit, the values didn't include the value from Ding et al. (2004) which belonged to TrSL3 regime. The expression that they used for fitting the peak amplitude in terms of mass-damping ratio and Reynolds number is

$$A^* = (1 - 1.12\,\alpha + 0.30\,\alpha^2)\,\log_{10}(0.41\,Re^{0.36}), \qquad (4.2)$$

where $\alpha = (m^*+C_a)\zeta$.

The data used by Govardhan and Williamson (2006) for the modified Griffin expression and the plot belongs to the experiments conducted in the TrSL2 regime. In Figure 4.57, our experimental data are plotted over the extrapolated curves derived by solving the equation (4.2) with respect to the $(m^*+C_a)\zeta$ parameter and the Reynolds number as defined by Govardhan and Williamson (2006). The data from the present experiments overshoot the extrapolated values from the modified Griffin expression. This

helps in concluding that even when the damping is increased (for power generation) higher amplitude of oscillation can be attained and maintained if the operational Reynolds number is chosen appropriately.

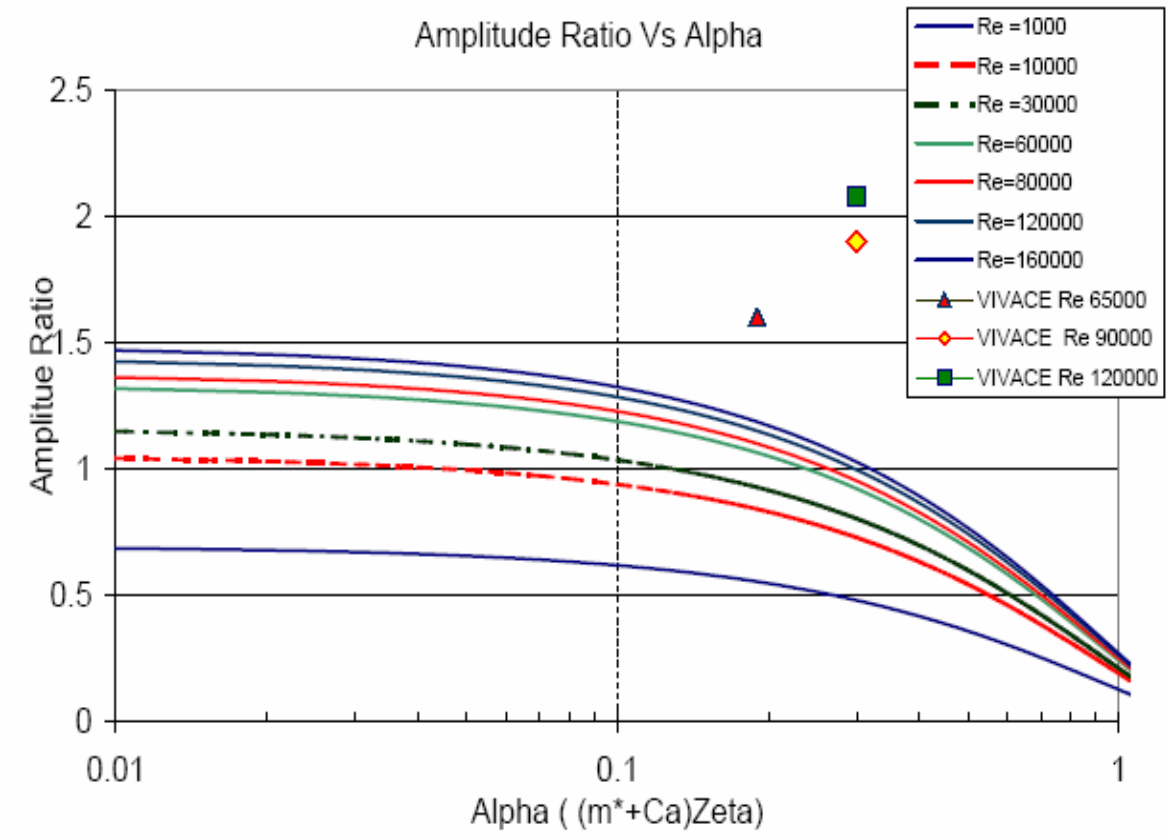

Figure 4.57. The effect of high Reynolds number is demonstrated by overlapping our experimental data on the modified Griffin plot based on the equation from Govardhan and Williamson (2006).

4.5. MAIN FINDINGS

The VIVACE experiments were performed in the TrSL2 and TrSL3 regime of Reynolds number. The TrSL3 regime was not explored before and predictions were based on the TrSL2 regime. From our experiments it can be concluded that there is a strong dependence of VIV response and character on Reynolds number. VIV is significantly different between the TrSL2 and TrSL3 regime. In the TrSL3 regime the high amplitude of oscillation was sustained even at high value of damping, which proves TrSL3 to be one of the optimal regimes for VIVACE operation. An amplitude ratio of 1.9

was achieved for a smooth cylinder in VIV even with high damping imposed. It is attributed to the TrSL3 regime of Reynolds number in which VIVACE was operating. This is of particular interest to the present line of research since the goal is to improve the design of the VIVACE Converter which extracts energy from ocean/river currents. It is obvious that higher Reynolds number operation of VIVACE will generate higher energy levels and energy density. The following statements can be made on the basis of author's findings:

- The range of synchronization of the upper branch of VIV increases with increasing Reynolds number in the TrSL2 and TrSL3 regimes.
- The amplitude ratio (A/D) increases with Reynolds number within the upper branch.
- The lower branch is lost due to high damping.
- The VIV response in TrSL3 regime takes a different path in the Williamson-Roshko map.
- In the present range of Reynolds number, A/D of 1.9 was achieved for a smooth cylinder in spite of high damping.
- The hysteresis phenomenon was not observed in our experiments due to the high damping in the experiments.
- Reynolds number has a stronger influence than m* on A/D in this range of Reynolds number.
- In our experiments, the VIVACE VIV system falls in the tail end of Griffin plot with its high $(m^*+C_a)\zeta$ but still high amplitude was achieved and maintained due to the effect of Reynolds number.

Chapter 5

EFFECT OF FREE SURFACE ON VIVACE

5.1. BACKGROUND

When VIVACE Converter operates in shallow waters, such as rivers and streams, it will be affected by proximity to the free surface. The Froude number plays an important role and its effect on VIV has to be studied.

Proximity to free surface of VIVACE cylinders in VIV needs to be studied for three reasons: (i) Energy is lost as vortices disturb the free surface and thus are not available to be harnessed. (ii) Surfacing vortices disturb the fish-food film at the free surface possibly creating environmental problems. (iii) Very close proximity to free surface may even suppress VIV completely.

Proximity to free surface of offshore pipelines, structures, and underwater vehicles with a bluff body like a submarine is a concern to industry. To the authors' knowledge, the closest relevant data on flows past cylinders near a free surface are limited to studies by Sheridan et al. (1995; 1997) on experiments on a fixed cylinder in a steady flow and, by Reichl et al. (2005; 2001) on numerical simulations of flow past a fixed cylinder. The effect of free surface on VIV has been studied only for forced vibration (Carberry 2002; Carberry et al. 2004; Lin and Rockwell 1999; Lin et al. 1996; Zhu et al. 2000). A VIV study in proximity to free surface has not been undertaken before. This study contributed toward designing a VIVACE Converter and specifying design parameters like the distance of the cylinder away from the free surface, and the

Froude number based on diameter $\left(Fr_D = \frac{U}{\sqrt{gD}}\right)$ and gap $\left(Fr_h = \frac{U}{\sqrt{gh}}\right)$ at which the system can operate. Hereafter, the term Froude number denotes the Froude number based on diameter and wherever the Froude number based on gap is used it will be stated explicitly.

The following conclusions have been published so far. At Fr_D in excess of 0.3–0.4 and gap ratio h/D < 0.55, where h is the distance from the undisturbed free surface to the top of the cylinder, free surface deformation becomes substantial. Data is available for Fr_D up to 0.72 and h/D as low as -0.13 (Reichl 2001). Transition from subcritical (Fr_h<1) to supercritical (Fr_h>1) results in localized free surface sharpening and wave breaking in the near wake (Sheridan et al. 1995; Sheridan et al. 1997). Since surface vorticity is directly related to surface curvature (Rood 1995), such high surface deformation results in significant surface vorticity. The latter diffuses and then convects into the main flow altering the development of Strouhal vortices from the top shear layer, affecting wake skewness and suppressing the absolute instability. The variations of flow particulars such as Strouhal number and vortex formation length have been published for Fr_D up to 0.5 and h/D as low as 0.1 (Reichl et al. 2003a).

5.2. INTRODUCTION

Proximity of a circular cylinder near a free surface in a steady flow past a cylinder is not only a concern for VIVACE, it represents a generic problem of importance in the area of offshore engineering in the design of offshore structures and pipelines. In naval architecture, the problem arises in underwater vehicles such as submarines and in ship design. An elastically supported cylinder in a fluid flow and in close proximity to a free surface undergoes a drastic change in vortex generation and interaction in the near-wake of the cylinder and, under appropriate conditions, it may result in revival of the recirculation bubble and no alternate shedding (Sheridan et al. 1995; Sheridan et al. 1997). This results in the stability characteristic changing from absolute to convective instability. Stability alteration from absolute instability to convective instability behind the cylinder results in cessation of vortex shedding and ultimately suppressing Vortex Induced Vibrations (VIV).

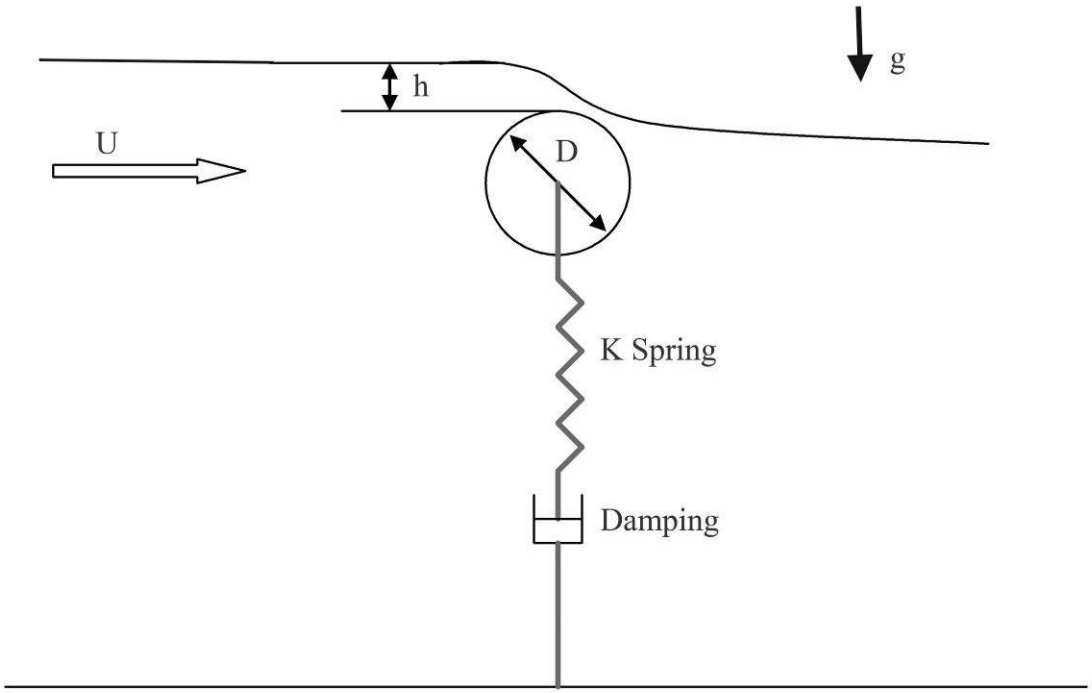

Figure 5.1. Schematic representation of cylinder in close proximity to the free surface.

Bearman et al. (1978) were some of the earliest investigators to study the effect of a cylinder in a close proximity to a plane rigid boundary. Comparing the effect of a free surface with a plane rigid boundary would not be appropriate for Fr_h and Fr_D >0.16 on account of the following reasons:

a. For Froude number > 0.16, appreciable surface deformation is noticed (Carberry et al. 2004).

b. Deformation of the free surface occurs in response to pressure fluctuations below the surface and the shear stress is zero for a clean free surface (no surfactants). In contrast, along a plane rigid boundary, the shear stress is not zero and vorticity is generated with no surface deformation.

c. Free surface deformation and resulting curved boundary condition will result in the generation of vorticity for a free surface (Rood 1995) or non-zero surface shear due to surface contamination or by surfactants.

Qualitative visualization and numerical simulation of flow around a translating stationary cylinder beneath a free surface have been studied by Miyata et al. (1990).

Sheridan et al. (1997) systematically observed the wake behind a circular cylinder close to a free surface at a Reynolds number 5.99×10^3-9.32×10^3 using PIV. They found that the wake states behind the cylinder in close proximity to the free surface strongly depend on the variation of Froude number and the gap ratio. Sheridan et al. (1997) found that vorticity from the free surface adjacent to the cylinder surface forms a jet-like flow in the near wake for low gap ratio and/or at higher Froude number for moderate gap ratio. For moderate and higher value of Froude number, the near-wake behind a circular cylinder shows different wake structures as the gap between cylinder and the free surface is varied (Hoyt and Sellin 2000; Sheridan et al. 1995; Sheridan et al. 1997). Reichl (Reichl et al. 2005; 2001) did a thorough numerical simulation of the experimental results of Sheridan et al. (1997). At a very low Reynolds number of 180, he was able to reproduce the general nature of the flow around the circular cylinder near a free surface irrespective of the Reynolds number effect. Forced oscillations beneath a free surface were studied by Carberry et al. (2004). She observed that there was an alteration of wake state and cessation of vortex shedding, but found no critical depth or Froude number which resulted in complete cessation of vortex shedding. The reason attributed to this observation was the variation of the gap between the cylinder and the free surface due to the oscillation of the cylinder. This results in the variation of Froude number based on the gap (Fr_h).

Sheridan et al. (1997) and Reichl et al. (2005; 2001) have studied in detail the effect of close proximity of the free surface on the development of the Kármán mode of instability for a stationary cylinder and possible generation of new classes of the near-wake structure. Triantafyllou and Dimas (1989) demonstrated analytically that the near wake can exhibit a convective, as opposed to a global (or absolute) instability when the cylinder is piercing a free surface and thus resulting in cessation of vortex shedding.

There has been a strong impetus from a few researchers to link vortex shedding and stability theory. Later researchers attributed the vortex shedding process to absolute instability (Triantafyllou and Dimas 1989; Triantafyllou et al. 1986). Absolute instability is defined for a flow for which an impulsively generated, small-amplitude transient grows exponentially at the location of its generation and affects flow both upstream and downstream and the group velocity is nonzero. Convective instability is the case in which

the transient or wave packet is convected downstream and the location of generation of the impulse is unaffected (Huerre and Monkewitz 1990). Convective instability can be suppressed if the point where the perturbations originate is controlled. In the case of absolute instability, the local response to an initial impulse grows in time due to the nonzero group velocity character. This results in the disturbances traveling back upstream and disrupting the flow even after the initial disturbance is neutralized. This is attributed as a reason why the bluff body wakes, which are absolute instabilities, are more difficult to control and vortex induced vibration still remains untamed.

For the flow around a circular cylinder (Re >350), the boundary layer after separation transforms into free shear layers downstream. Depending on the range of Reynolds number, the shear layers have definite lift and drag and Strouhal frequency characteristic (Zdravkovich 1997). A near-wake region with a static pressure lower than the undisturbed stream is enclosed by the free shear layers developed around the circular cylinder. For the Reynolds number range studied ($8\times10^3 \le \mathrm{Re} \le 1.5\times10^5$), the near-wake comprises of two modes that coexist: the shear layer mode and the Kármán mode (Bloor 1964; Chyu et al. 1995; Reichl 2001). The shear layer mode is associated with the onset of Kelvin–Helmholtz instability in the free shear layer formed from the surface of the cylinder. This instability eventually leads to small-scale vortices that may interact with large-scale ones (Lo and Ko 2001). The Kármán mode is described as self-excited oscillation that is caused by the hydrodynamic instability of time averaged flow produced by the absolute instability and convective instability (Huerre and Monkewitz 1990). At very low Reynolds number (Re < 47), the flow around a circular cylinder separates from the body and forms a "separation bubble" engulfing the wake, initially into a steady region of re-circulating flow behind the cylinder. The flow is convectively unstable, which means that the instability propagates, amplifies and disturbances are carried outside the separation bubble leaving the bubble unaffected. As the Reynolds number increases and exceeds a value of about 47, it results in Hopf bifurcation (Mathis et al.) and the flow in the bubble becomes absolutely unstable. This means that transient waves or any disturbances inside the bubble are amplified exponentially and the steady flow that is observed at Re < 47 becomes unsteady resulting in a periodic solution (Kármán instability) creating a vortex street by breaking the separation bubble. The use of base

bleed and base suction are methods which apply this phenomenon to control and ultimately suppress vortex shedding.

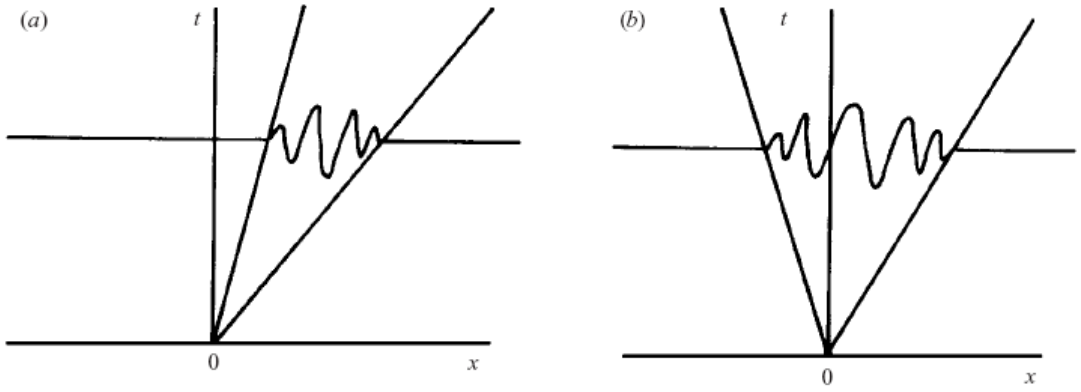

Figure 5.2. Schematic sketches of traveling wave generated by an impulse (a) Convective instability, (b) Absolute instability. [Reproduced from Huerre and Monkewitz (1990)].

5.3. PROBLEM DEFINITION

Study the effect of proximity of free surface on Vortex Induced Vibrations of a circular cylinder in a steady flow, which is parallel to the free surface. The cylinder axis is perpendicular to the horizontal flow and parallel to the free surface. In this chapter, a cylinder in VIV beneath a free surface is considered. VIV particulars such as amplitude, range of synchronization, branches of response within the synchronization range, vortex structures, and hysteresis, are determined experimentally for various gap ratios.

5.4. SOLUTION APPROACH

The effect of free surface on VIVACE was studied in the Low-Turbulence Free Surface Water (LTFSW) Channel, in the Marine Hydrodynamics Laboratory (MHL) of the University of Michigan.

The parameters varied in the model tests are the cylinder diameter D, the flow speed U, and the equilibrium position of the cylinder below the free surface h. In turn, these parameters determine the Froude number based on diameter, gap, and Reynolds number for a specific water depth. These tests are very important for the development of the VIVACE Converter.

Six models are used in the tests. All cylinders have length L=36” (914mm) and are made of aluminum coated with polymer paint for surface smoothness and protection.

Model diameters are 1″ (25.4mm), 2.5″ (63.5mm), 3″ (76.2mm), 3.5″ (88.9 mm), 5″ (127mm), 6″ (152.4mm). The blockage ratio in the test section of the (LTFSW) Channel ranges from 2.33% to 31.3%. Models are suspended via two compression coil-springs attached to the end-plates of the cylinders. The cylinder is constrained to oscillate transversely to the flow freely using linear bearings sliding on shafts. There are narrow gaps of about 10 mm between the walls of the (LTFSW) Channel and the end-plates of the model.

Using the six models described above, VIV tests are performed in the (LTFSW) Channel spanning the following ranges of parameters: Re $\in[8\times10^3 - 1.5\times10^5]$, m* $\in$[1.0 - 3.14], U $\in$[0.35 m/s - 1.15 m/s], L/D $\in$[6 – 36], distance of free surface from equilibrium position of the cylinder (h/D) $\in$[4-0.196], m*ζ $\in$[0.14 - 0.26].

5.5. RESULTS, OBSERVATIONS, AND DISCUSSION

5.5.1. Effect of free surface on range of synchronization

The range of synchronization of the upper branch of VIV decreases with increasing proximity to the free surface (Figure 5.4, Figure 5.6, and Figure 5.8). In Figure 5.20 - Figure 5.29, both the positive amplitude and negative amplitude ratios are plotted, to understand the effect of asymmetry in the boundary conditions. The positive and negative amplitude ratio plotted are the maximum and minimum value about the mean position of the oscillation at a particular velocity rather than the equilibrium position of the cylinder before the experiment started. This is a better representation of the amplitude of oscillation because of the shift in the mean position of the oscillation due to the increase in the mean downward lift force as the cylinder gets closer to the free surface and/or as the velocity increases (see Figure 5.12). In the unbounded higher Reynolds number experiments, the amplitude of oscillation versus reduced velocity shows an increasing slope along the upper branch (Figure 4.24). As the distance between the cylinder and the free surface reduces, the amplitude of oscillation reaches a plateau at a lower value. For low values of gap ratios the plateau reduces to a point as seen in Figure 5.4 and Figure 5.6. In our experiments, it is found that there is a strong relation on the range of synchronization and the gap ratio. In Figure 5.4 and Figure 5.6 it is observed that the range of synchronization reduces drastically as the gap ratio reduces. In the

synchronization range, for lower gap ratio, the increase in amplitude of oscillation between initial and upper branch is characterized by a steady increase rather than the jump observed from initial to upper branch in the fully submerged cylinder VIV at a reduced velocity of 5 as shown in Figure 5.4 and Figure 5.6. In the cases of cylinder closer to a free surface, the synchronization range starts earlier as the cylinder gets closer to the free surface.

Reichl compiled his numerical simulation for the case of a stationary cylinder in close proximity to the free surface results based on Froude number and gap ratio at Re = 180 as shown in Figure 5.3. In Figure 5.3, it is observed that no shedding of vortices was observed for the cases where the gap ratios were less than 0.2 and Fr > 0.3. In the experiments conducted at the LTFSW Channel with the 2.5″ cylinder, no range of synchronization was observed for the gap ratio of 0.2 as seen in Figure 5.6 but synchronization and VIV was observed in the case of 5″ cylinder for a gap ratio of 0.2 as shown in Figure 5.8 and the reasons for this are elucidated in the forthcoming Section.

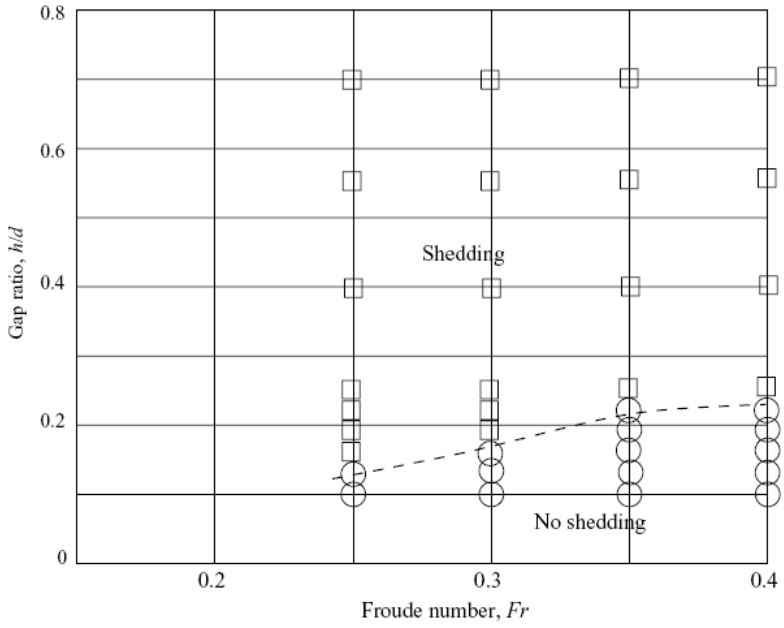

Figure 5.3. Existence or non-existence of shedding as a function of Froude number and gap ratio for a stationary cylinder. [Reproduced from Reichl (2001)].

The decrease in the range of synchronization is attributed to the strong skewing of the wake as the gap ratio decreases and the Froude number increases. This results in affecting the separation. The position of the top separation point was observed to be time

varying even at a Reynolds number as low as 180 in the case of a stationary cylinder closer to the free surface (Reichl 2001). The variation of the separation point was due to the time varying free surface curvature. For a cylinder in VIV close to a free surface, the oscillation of the cylinder strongly modulates the free surface because the local Froude number changes with time. The VIV of a cylinder strongly alters the amount of mass influx for the growing vortices on the top side of the cylinder and the period of the shedding of vortices. This results in a level of feedback between the free surface and the shedding of vortices from the cylinder. Due to the delayed separation at the top of the cylinder, the size of the wake decreases with increasing Froude number (Reichl 2001) and so the strength of the vortices. The flow between the free surface and the cylinder controls the separation and, in turn, the frequency of shedding. This results in a considerable reduction in the bandwidth of lock-in between the frequency of shedding, the frequency of oscillation and the natural frequency. Thus, VIV becomes difficult to maintain for a larger range of synchronization.

The effect of free surface on the range of synchronization, become more apparent when the range of synchronization is plotted in terms of Froude number rather than the reduced velocity as seen in Figure 5.4 through Figure 5.6. At higher flow speeds, Froude number provides more insight on the modification of the free surface in relation to the gap ratio. When the Froude number is in the range of 0.3-0.4, it results in significant surface distortion, and hence an appreciable flow modification around the vibrating cylinder at the top of the cylinder. This results in change in the position of both the stagnation and separation points. As the Froude number increases, the position of the top separation point is affected more.

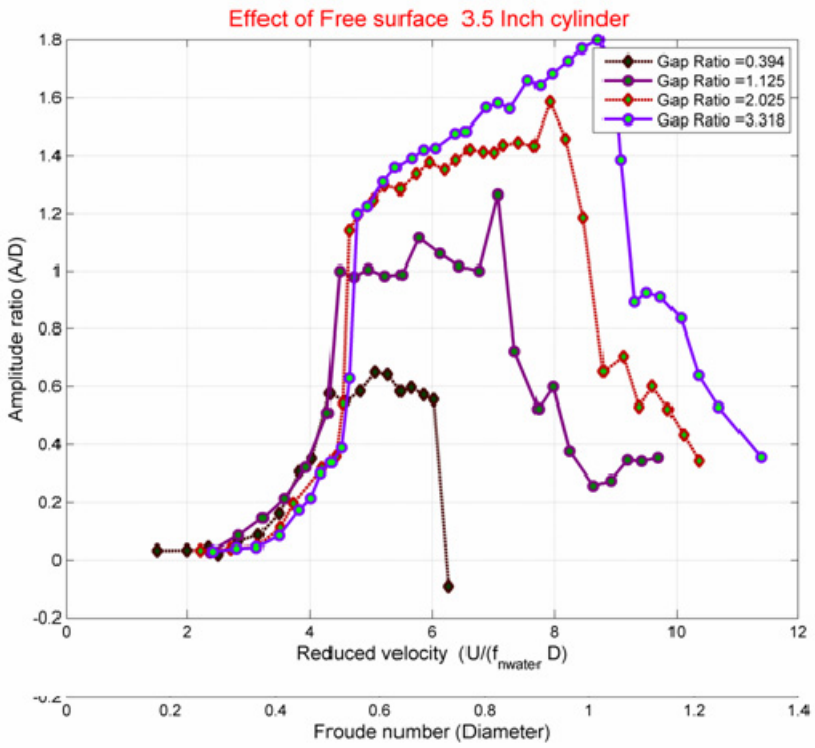

Figure 5.4. For a 3.5″ cylinder in VIV, variation in the amplitude response versus the reduced velocity and Froude number based on diameter for different gap ratio is plotted.

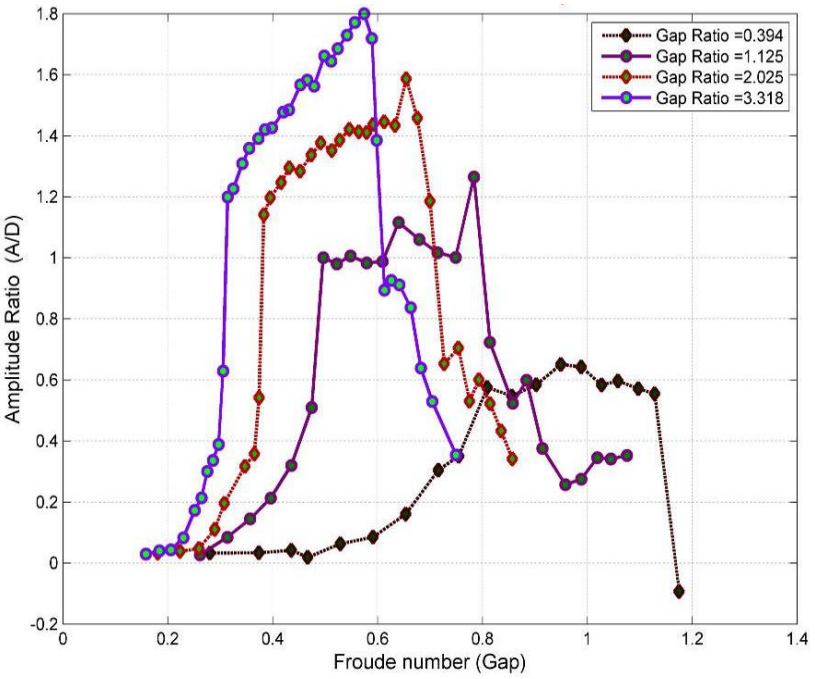

Figure 5.5. For a 3.5″ cylinder in VIV, variation in the amplitude response versus the Froude number based on gap height for different gap ratio is plotted.

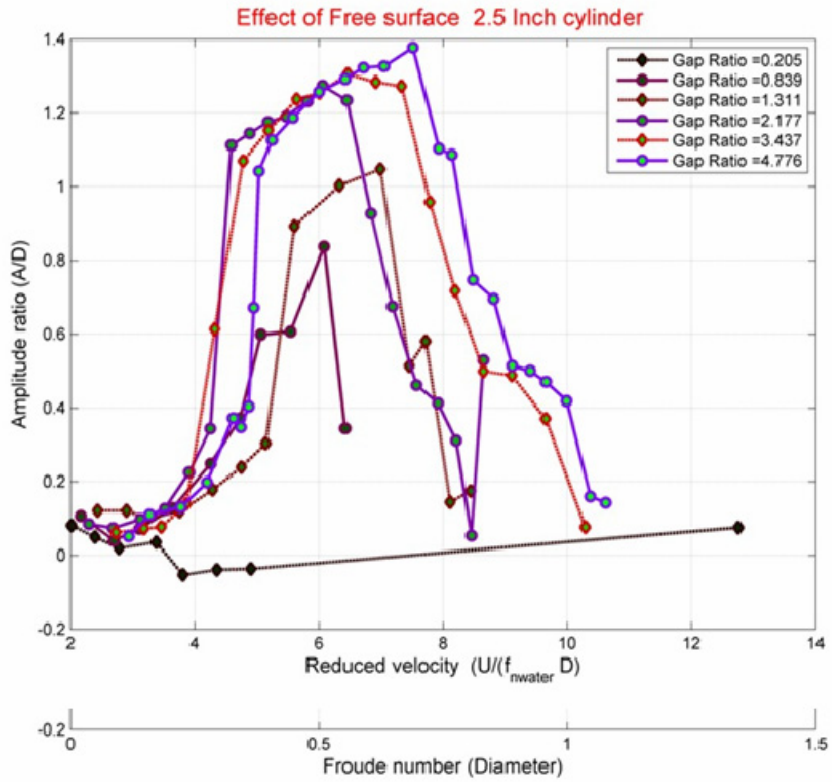

Figure 5.6. For a 2.5″ cylinder in VIV, variation in the amplitude response versus the reduced velocity and Froude number based on diameter for different gap ratio is plotted.

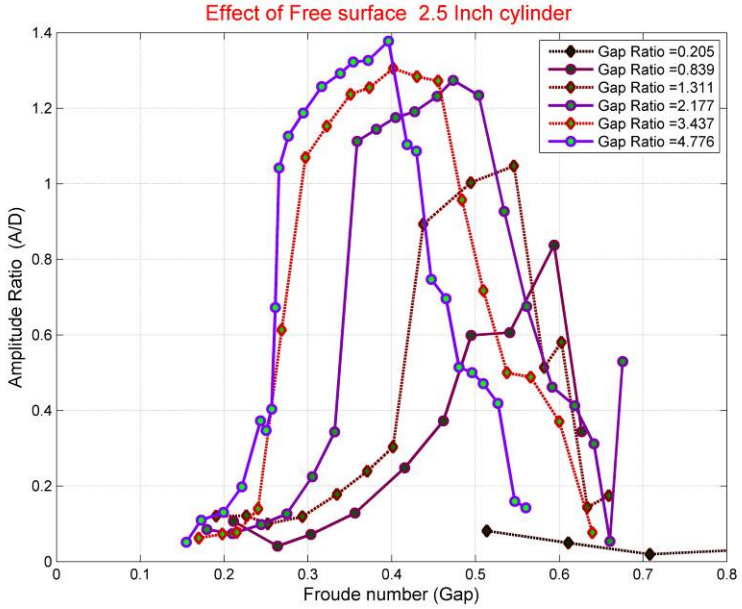

Figure 5.7. For a 2.5″ cylinder in VIV, variation in the amplitude response versus the Froude number based on gap height for different gap ratio is plotted.

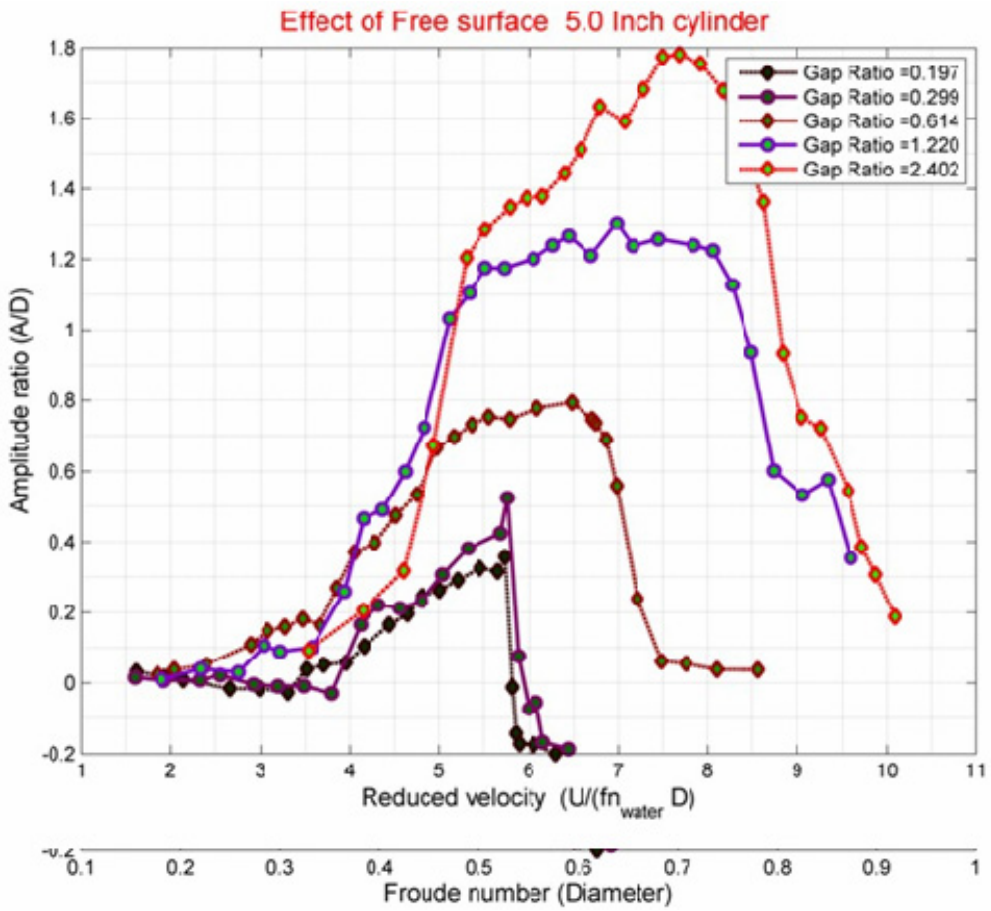

Figure 5.8. For a 5″ cylinder in VIV, variation in the amplitude response versus the reduced velocity and Froude number based on diameter for different gap ratio is plotted.

5.5.2. Effect of free surface on the amplitude of oscillation

The amplitude of oscillation shows a decreasing trend as the cylinder approaches the free surface as shown in Figure 5.4 through Figure 5.8. The increasing trend of the upper branch as we have seen for cylinder far away from the free surface h/D >3.0 is not observed for lower gap ratios. The slope of the increase in amplitude of oscillation reduces and it plateaus as the cylinder approaches the free surface. VIV ultimately ceases as the gap ratio between the cylinder and the free surface diminishes. Our tests show that this may occur at a particular Froude number for a particular gap ratio and a particular cylinder. Random VIM motion was observed when the gap ratio was h/D < 0.2 in the case of 2.5″ cylinder Figure 5.6. The cease of vortex shedding may be attributed to the increased fluid momentum in the form of a jet through the gap between the cylinder and the free surface and diffusion of opposite signs of the free surface vorticity from the

deformed free surface due to the proximity of the cylinder to the free surface with the vortices generated from the upper shear layer of the cylinder.

The below formulation (equation (5.1)) is by Lighthill (1986). He relates the time rate of change of moment of vorticity to the vector force acting on a body, where D is drag and L is lift, $\hat{x}$ is the position vector from the center of the cylinder to the location of vorticity $\hat{\omega}$ and v is the volume of interest.

$$D\,\hat{i} + L\,\hat{j} = -\frac{d}{dt}\left[\frac{1}{2}\rho\int_{v}\hat{x}\times\hat{\omega}\,dv\right] \tag{5.1}$$

Lift force is a direct consequence of the vorticity shed in the flow from the cylinder in VIV. The vortices present in the flow comprise of vortices created from the free surface deformation and the alternating vortices shed from the oscillating cylinder. The vortices shed due to the free surface deformation has vorticity of opposite rotation in relation to the vorticity of the vortices shed from the top of the cylinder and this leads to partial cancellation of the vortices shed from the top. The vortices shed from the top of the cylinder are also affected by the skewing of the wake due to the free surface distortion and reduction in the mass influx into the shear layer. In turn, they all affect the vorticity distribution around the cylinder. The above changes in the behavior of the wake and the vorticity strength of the vortices alter significantly the lift force acting upon the cylinder.

The fluctuating lift force shows a decreasing trend as shown in Figure 5.12 - Figure 5.14 and the frequency spectrum of forcing becomes broad banded as the gap ratio reduces and Froude number increases Figure 5.9.

Further tests need to be conducted to determine the critical Froude number in a parameter space of gap ratio, Froude number, and cylinder diameter.

5.5.3. Mechanism for the cessation of vortex shedding

In the design of VIVACE, it is important to understand the effect of proximity of the free surface to the range of synchronization and in this Section more light is shed on the trend of range of synchronization. It is noticed that, in the cases with low gap ratio and moderate gap ratio at high Froude number, the range of synchronization has a sudden termination and VIV ceases. Tests show that this may occur at a particular Froude number. VIV completely ceases at very small gap ratios irrespective of the Froude number unless the flow is completely modified by the hydraulic jump. To the author's

knowledge the reasons for the sudden termination and reduction of the synchronization range were never explored. In our experiments for smaller gap ratios, it was noticed that at the end of synchronization or at higher Froude numbers, the VIV amplitude jumped from a high amplitude vibration to zero amplitude vibration rather than a gradual decrease as seen for higher gap ratios. This phenomenon can be attributed to the jet-like flow with higher momentum through the gap between the cylinder and the deformed free surface. This result in an abrupt change in wake-state behind the oscillating cylinder, diffusion of vorticity from the free surface deformation due to the proximity of the cylinder to the free surface, and the opposite signs of the free surface vorticity and the vorticity generated from the upper shear layer of the cylinder.

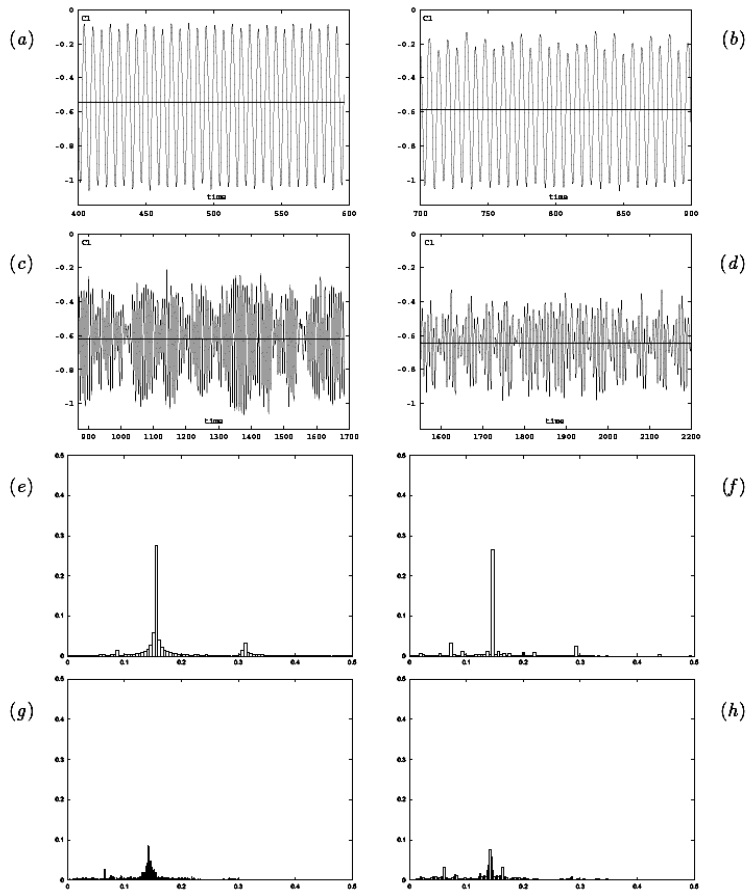

Figure 5.9. Numerical simulations of lift traces and spectra for a gap ratio of 0.25 for Froude numbers 0.25 (a,e), 0.30 (b,f), 0.35 (c,g) and 0.40 (d,h) for a stationary cylinder. The Reynolds number for each case is 180. [Reproduced from Reichl (2001)].

In the case of lower Froude numbers at lower gap ratio, the level of surface deformation and hence the level of skew in the wake is significantly different from that of higher Froude number cases (Reichl et al. 2005; Sheridan et al. 1997). For higher Froude numbers, larger scale surface deformation occurs and, in some instances, the flow separates from the free surface and attaches to the cylinder. This is called Coanda effect Sheridan et al. (1995; 1997). The wake state for a low gap ratio depends on the Froude number and have been categorized by Sheridan et al. (1995; 1997).

At lower gap ratios and high Froude numbers, there has been considerable amount of experimental work done for stationary cylinders by Sheridan et al. (1998; 1995; 1997) and Hoyt & Sellin (2000) lying within the parameter range considered within this Section. Numerical simulations were done by Reichl (2001) to explore more thoroughly the flow pattern for the above cases.

All of the above mentioned authors observed significant changes in the wake behavior in the case of stationary cylinder for the Froude numbers considered here. Carberry et al. (2004) reported a change in wake-structure for a forced oscillating cylinder as the gap ratio was reduced. According to Sheridan et al. (1997), the nature of the flow can be divided crudely into three basic wake states. The classification of the wake states is based on the characteristic of the flow between the upper surface of the cylinder and the free surface that Sheridan et al. (1997) terms as a 'Jet'.

1. The 'Jet' follows the free surface and remains attached to it resulting in a long wave distortion of the surface.

2. The 'Jet' separates from the free surface, and it is inclined at an angle of approximately 10° and it follows the wake and skews the wake. The 'Jet' exists in between the wake of the cylinder and the free surface.

3. The 'Jet' separates from the free surface and it stays attached to the rear of the cylinder and it delays separation and only separates near the underside of the cylinder. This phenomenon is observed in the aerospace industry. It is known as Coanda effect named after Coanda who used this phenomenon in his invention.

In the first pattern of the wake structure, regular vortex shedding and VIV is still prevalent. In the second pattern of the wake structure, limited vortex shedding still exists (Reichl et al. 2003a). In the third wake state, the vortex shedding completely ceases.

In the second state, the skewing of the wake by the jet results in the formation of a large recirculation bubble. Consequently, the flow around the cylinder has the same topology as a lower Reynolds number flow. The formation of a recirculation bubble from alternate vortex shedding is the character of the wake becoming convectively unstable from absolute instability. The skewing angle of the wake increases as the surface deformation increases by the increase in Froude number and decrease in gap ratio.

In Figure 5.6 through Figure 5.8, for lower gap ratios, it is observed that the amplitude of oscillation at the end of synchronization jumps to a near zero value at a critical value of Froude number. The nature of this behavior is a strong suggestion of bifurcation of stability character of the flow. In the case of 5″ cylinder for the gap ratios h/D< 0.3, the jump occurred at Froude number Fr = 0.57 (Figure 5.8). The jump in the amplitude ratio to a near zero value occurred at Fr = 0.71 for a gap ratio 0.394 (Figure 5.4). In the case of 2.5″ cylinder, there was no oscillation at gap ratio of 0.205. But in contrast, for the 5″ cylinder, VIV was still prevalent for gap ratio values less than 0.2. The above observation can be attributed to the closer proximity of the 2.5″ cylinder to the skewed wake than for the 5″ cylinder case. In Figure 5.10, a schematic diagram of two cylinders near a free surface with different diameter but same gap ratio with no surface deformation is shown. In Figure 5.10, a straight line is drawn at an angle of 10° to emulate the skewing of the wake (Reichl 2001) to the undisturbed free surface. It is obvious that the jet is closer to the 2.5″ body that could favor the wake to adhere to the body and result in the Coanda effect. That results in suppressing the vortex shedding and VIV rather than attach to the free surface.

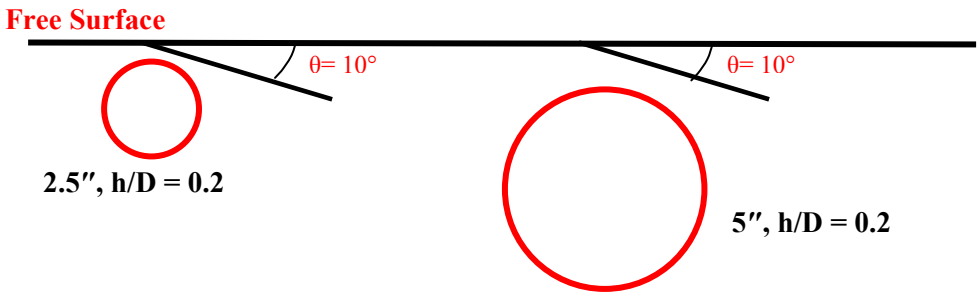

Figure 5.10. Schematic diagram of cylinders of diameter 2.5″ and 5″ near a free surface with gap ratio (h/D) = 0.2.

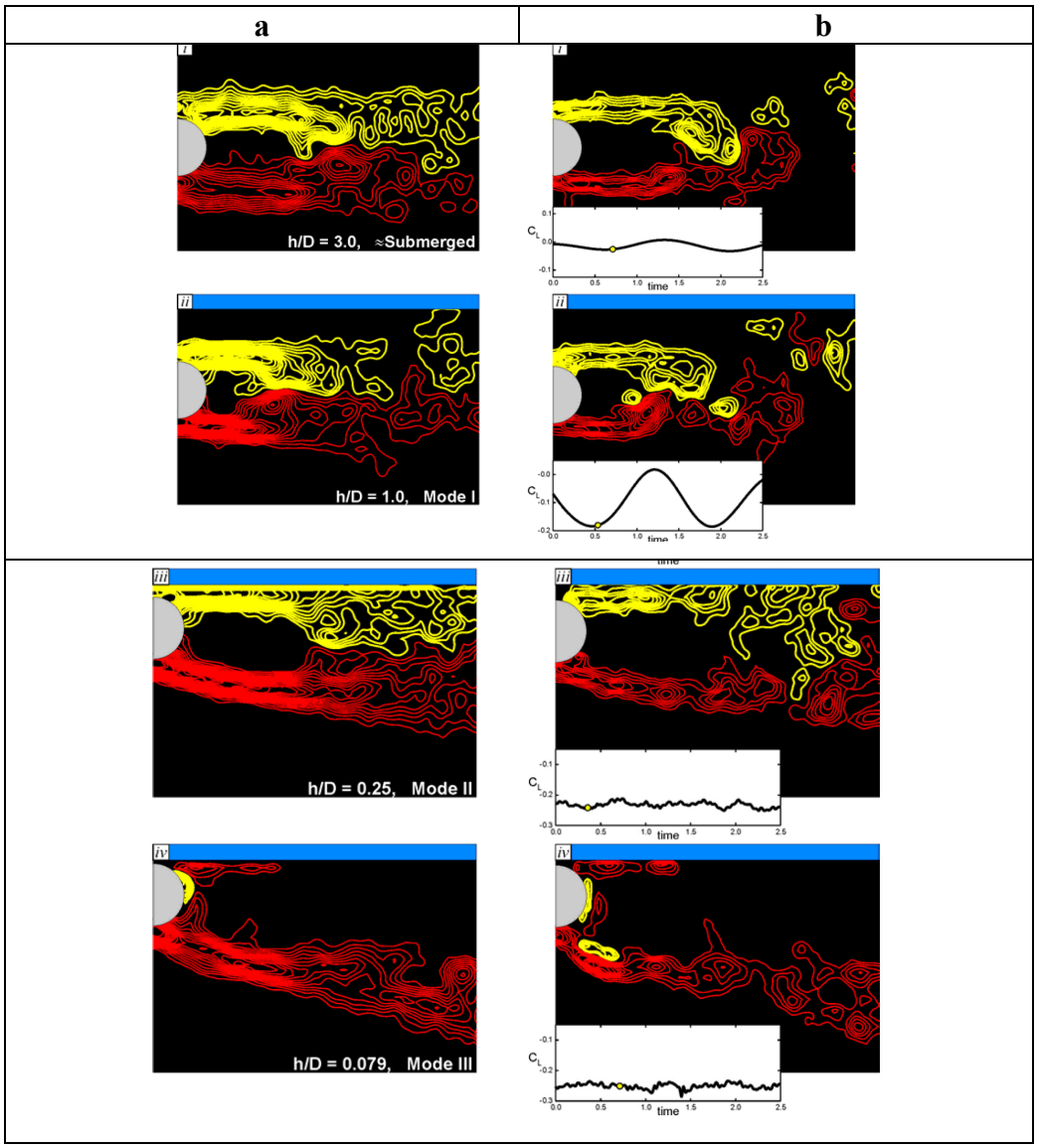

Figure 5.11. a) Mean vorticity fields, and b) instantaneous vorticity fields, at h/D = i) 3.0, ii) 1.0, iii) 0.25 and iv) 0.079. [Reproduced from Carberry (2002)].

In the experiments done by Zhu (2000) with a forced oscillation of circular cylinder near a free surface, they found that vorticity at lower gap ratio is significantly redistributed from the higher gap ratio cases. The lift coefficient curve changed phase by about 90 degrees and results in a substantially larger magnitude of negative lift coefficient (see Figure 5.13).

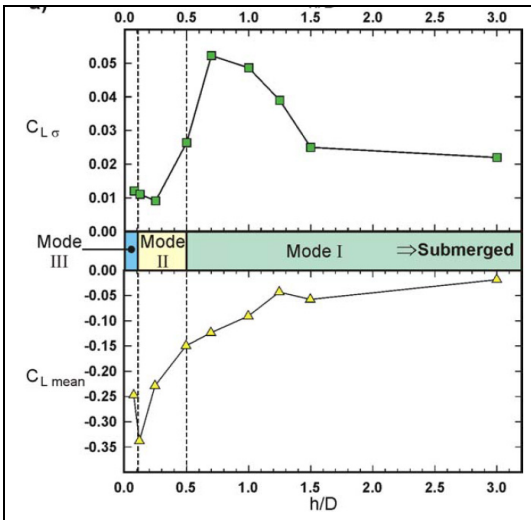

Figure 5.12. Variation of the mean and standard deviation of the lift force coefficient. [Reproduced from Carberry (2002)].

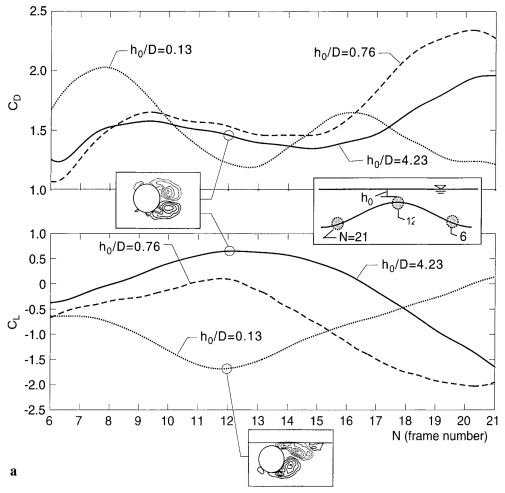

Figure 5.13. Values of drag and lift coefficients C_D and C_L as a function of frame number N of the PIV cinema sequence for three values of submergence, h/D = 0.13, 0.76, and 4.23. [Reproduced from Zhu et al. (2000)].

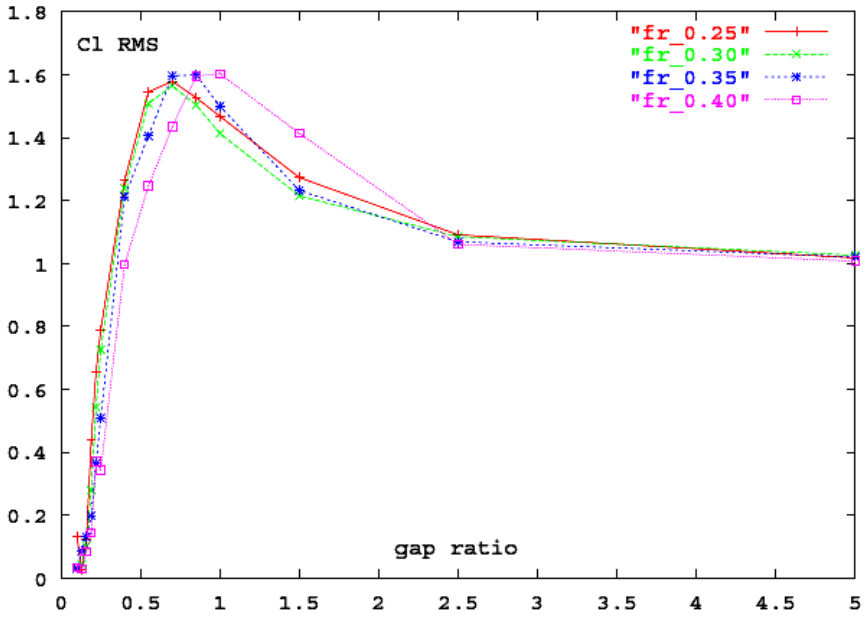

Figure 5.14. Variation of the normalized RMS lift coefficient with gap ratio for Froude numbers of 0.25, 0.30, 0.35 and 0.40 from numerical simulations at a Reynolds number of 180. [Reproduced from Reichl (2001)].

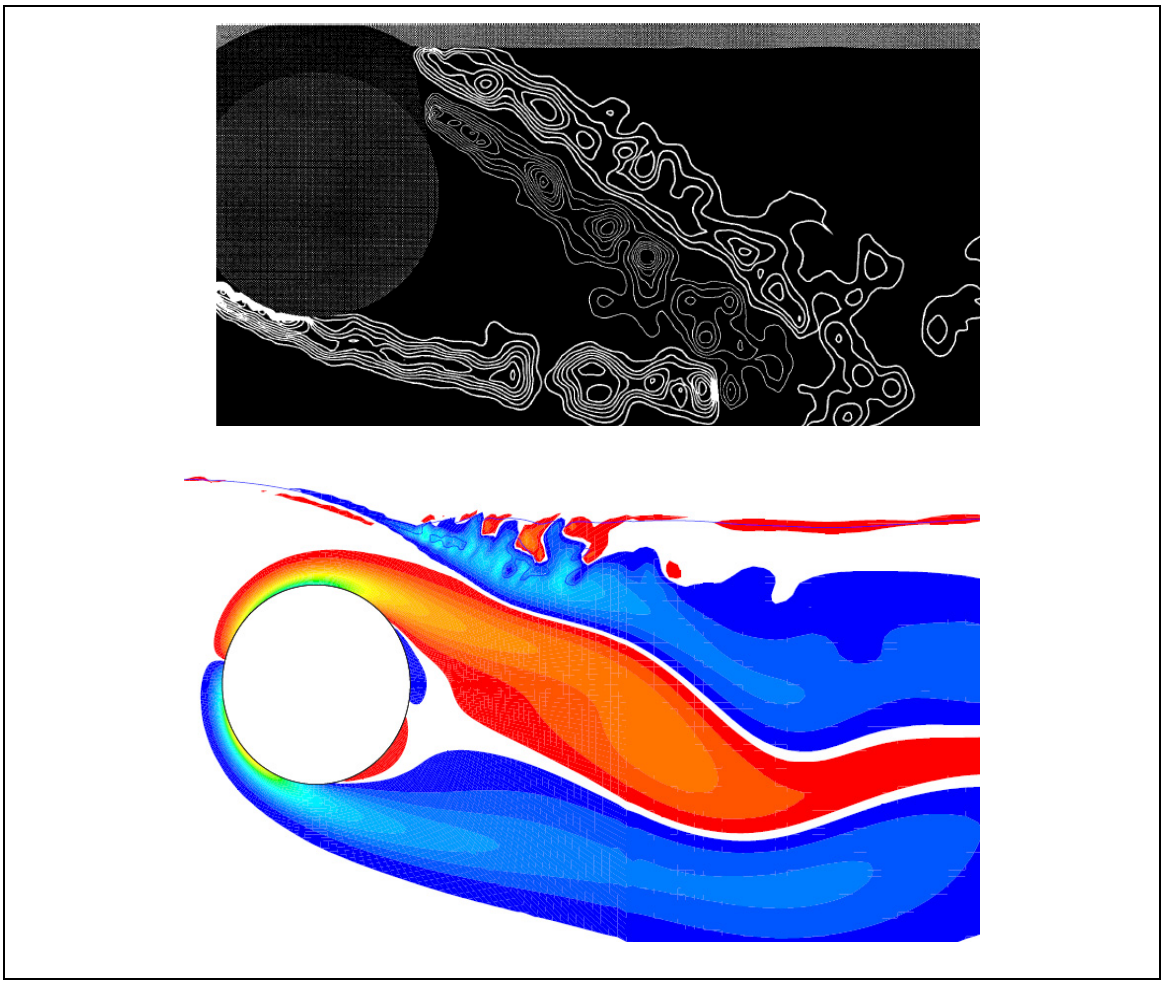

Figure 5.15. Experimental vorticity field for a Reynolds number in between 5990 and 9120 for a gap ratio of 0.43, a Froude number 0.60 (Sheridan et al. 1997) (top), and the numerically predicted vorticity field for a Reynolds number of 180 at a gap ratio of 0.40, a Froude number of 0.60 (Reichl 2001) (bottom).

In the study conducted by Reichl (2001), he observed that the front stagnation point is not affected by the Froude number but it is affected by the gap ratio. In his study, he observed that for small gap ratios at which shedding were not observed, the stagnation and separation points oscillated in an erratic way.

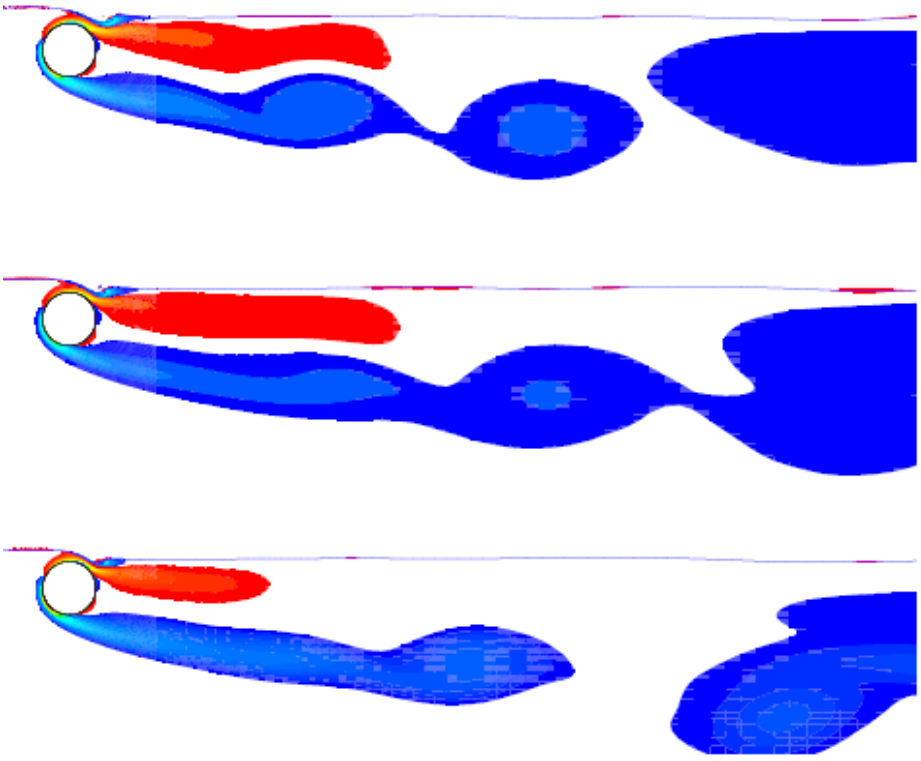

Figure 5.16. Vorticity fields at a Froude number of 0:50 for gap ratios of 0:16, 0:13 and 0:10 (top to bottom) from numerical simulations at a Reynolds number of 180. [Reproduced from Reichl (2001)].

In the operation of VIVACE, it is of interest to know the gap ratio and Froude number combination at which vortex shedding gets suppressed. Even though the boundary layer is close to the free surface at very low gap ratios, the author believes that the suppression of vortex shedding at a critical gap ratio by the effect of free surface is not due to the gap reducing to the order of the boundary layer thickness. Instead the boundary layer can be influenced by the significant skewing of the wake due to the free surface curvature in relation to the gap between the cylinder and free surface. In the case of a smaller diameter cylinder the wake skewed at 10° is closer to the cylinder surface than in the case of larger diameter cylinder (Figure 5.10) and this result in an earlier Coanda effect for the same gap ratio as seen in Figure 5.10. The author has calculated the boundary layer and displacement thickness using Pohlhausen's method for different Reynolds numbers and compiled it in Table 5.1. The angles 60 and 80 degrees were chosen for the calculation because in most of the cases the separation point lies within this range.

$\frac{\delta^*}{D} = 0.4085\left(\frac{1}{\mathrm{Re}^{1/2}}\right)$ Displacement thickness at 60 degree (Polhausen's method)

$\frac{\delta}{D} = 1.1784\left(\frac{1}{\mathrm{Re}^{1/2}}\right)$ Boundary layer thickness at 60 degree (Polhausen's method)

$\frac{\delta^*}{D} = 0.5096\left(\frac{1}{\mathrm{Re}^{1/2}}\right)$ Displacement thickness at 80 degree (Polhausen's method)

$\frac{\delta}{D} = 1.4012\left(\frac{1}{\mathrm{Re}^{1/2}}\right)$ Boundary layer thickness at 60 degree (Polhausen's method)

	Displacement thickness ratio $\left(\frac{\delta^*}{D}\right)$		**Boundary layer thickness ratio** $\left(\frac{\delta}{D}\right)$	
Re	**60°**	**80°**	**60°**	**80°**
180	0.031	0.038	0.088	0.104
1.0E+04	0.004	0.005	0.012	0.014
4.0E+04	0.002	0.003	0.006	0.007
7.0E+04	0.002	0.002	0.004	0.005
1.0E+05	0.001	0.002	0.004	0.004
1.3E+05	0.001	0.001	0.003	0.004
1.6E+05	0.001	0.001	0.003	0.004
1.9E+05	0.001	0.001	0.003	0.003
2.2E+05	0.001	0.001	0.003	0.003
2.5E+05	0.001	0.001	0.002	0.003

Table 5.1. Boundary layer and displacement thickness calculated using Pohlhausen's method for different Reynolds number.

5.5.4. Hysteresis due to metastable wake states

For low gap ratio experiments, a strong hysteresis character was observed. The hysteresis observed is different from the hysteresis in the unbounded VIV. In the unbounded VIV for low $(m^*+C_a)\zeta$, hysteresis occurs between the initial branch and upper branch with intermittency between upper and lower branch and for high $(m^*+C_a)\zeta$ hysteresis occurs between the initial branch and lower branch. In the case of a cylinder oscillating close to a free surface, the hysteresis is observed at the end of the synchronization regime. For intermediate gap ratios, it occurred at the beginning of the synchronization. The hysteresis in most of the cases of the present experiments was observed in the relatively high Froude number range between 0.4-0.6 depending on the gap ratio and the radius of curvature of the cylinder. The hysteresis observed is attributed

to the wake states that are metastable. Sheridan et al. (1995; 1997) found in their experiments that two characteristically different wake states can exist and flip between each other at a given point in a parameter space defined by gap ratio and Froude number. Later, the same phenomena was observed by Hoyt et al. (2000) in their experiments (Re $=2.7\times10^4$) and by Reichl (2001) in his numerical simulations (Re=180). The existence of these two wake states occurred for low gap ratio and was found to have limiting stability. The existence of these wake states was a function of several variables like surface curvature, speed of the flow, gap ratio, diameter, Froude number diameter and Froude number gap ratio. Even though the variables are interconnected, the effect of each variable is significant when a single variable is varied keeping others constant. For example, as velocity changes, it will influence the Froude number and it will alter the curvature and the reduced velocity and, in turn, the vorticity dynamics of the wake.

Sheridan et al. (1995) found that flipping between the wake states can be induced by external disturbances in the region downstream. In the case of an elastically mounted cylinder close to a free surface, the wake states are hysteretic which is in contrast to the case of a stationary cylinder close to a free surface for which the wake states are metastable. When the cylinder is in VIV, the amplitude of oscillation is a strong enough disturbance to induce the flipping of wake states. And in addition, when the cylinder is in VIV, the gap between the cylinder and the free surface modulates. These two reasons in conjuction modifies the character of the wake behind a cylinder in VIV to be hysteretic instead of metastable.

In the case of very small gap ratios, it is likely that the more significant skew caused by the wake would result in the Coanda effect. As the jet gets closer to the body surface, it has higher tendency to attach to the body resulting in the cessation of alternate vortex shedding.

In the study by Reichl, Sheridan et al. (1995), Sheridan et al. (1997) and Hoyt and Sellin (2000), the case with gap ratio 0.25 and Froude number was studied in greater detail. Reichl and Sheridan et al. reported that at this gap ratio and Froude number, the wake states change characteristically. They concluded that it is the precursor of altered wake states.

The metastable behavior has a clear impact upon the lift with the separation of the 'jet' from the free surface resulting in a decrease in the lift force acting upon the stationary cylinder. Carberry (2001) and Reichl (2001) had plotted the lift coefficient corresponding to the different wake states and gap ratios in their dissertation (see Figure 5.12 and Figure 5.14). Zhu et al. (2000) plotted the time variation of the lift coefficient (see Figure 5.13). In all these plots, a dramatic decrease in the lift coefficient is observed.

The hysteresis observed in our experiments can be attributed to the metastable wake states observed by Reichl (2003b; 2001), and Sheridan et al. (1995; 1997). Sheridan et al. (1997) observed metastable wake state for certain ranges of flow parameters and depths of submergence of the cylinder. He observed that the pattern of shedding flipped between the two states. Sheridan et al. (1997) also observed that the external disturbance can be a precursor for the metastable wake states. In our experiments, it is observed that due to VIV, a particular state among the metastable wake states becomes stable depending on the initial conditions, whether the velocity is increasing or decreasing. This dependence of the wake states on the initial condition results in the strong hysteretic character that was observed.

A schematic approach of the transition between wake states using the images of Sheridan et al. (1997) are shown in Figure 5.19. In Figure 5.19, Step 1 represents the jet attached to the free surface, Step 2 represents the jet existing between the free surface and the cylinder and Step 3 is the state where the wake state is same as Step 2 but the angle of skew is increased by the increase in velocity, increase in Froude number based on gap ratio and/or the decrease in gap ratio. Step 4 represents the jet attached to the body surface, which is due to the Coanda effect. Steps 1 and 2 can coexist in the same parameter space. For low Froude number cases they exist for both high and low gap ratios (Sheridan et al. 1995; Sheridan et al. 1997). Steps 3 and 4 can coexist in the same parameter space for low gap ratio cases (Sheridan et al. 1995; Sheridan et al. 1997)

In the case of 3.5″ cylinder and gap ratio of 0.3937, the forward range of synchronization started at a reduced velocity of 3.1 and the amplitude of oscillation kept increasing with the forward reduced velocity and at a reduced velocity of 6.0 the amplitude ratio suddenly jumped from a value of 0.85 to nearly zero (Figure 5.22). To further understand the bifurcation effect, the time series is plotted where the amplitude of

oscillation decreases for the same velocity (Figure 5.18). The abrupt jump in the amplitude takes place at a Froude number of 0.72 (Figure 5.20). But when the velocity is reduced or when we come backward, the amplitude of oscillation is zero until a reduced velocity of 4.7 is reached and where the corresponding Froude number value was 0.55 (Figure 5.20). The hysteresis observed at the end of the synchronization is due to the flipping between Step 3 and Step 4 as shown in Figure 5.19 This case showed a strong hysteresis character at the end of synchronization range. The value of gap ratio of 0.3937 ≈ 0.4 and the Froude number 0.55 is similar to the cases of Sheridan et al. (Sheridan et al. 1995; Sheridan et al. 1997) and Reichl (2001) where they noticed a change in wake states and cessation of vortex shedding.

The wake state and definition of critical Froude number is more complicated in the case of VIV because of the coexistence of the fluid induced excitation, the motion induced excitation, and the feedback between them. In the case of VIV of a cylinder close to a free surface, the skewing of the wake occurs due to the free surface and the motion of cylinder.

In the 5″ cylinder case and gap ratio of 0.3, the forward range of synchronization started at a reduced velocity of 3.45 and the amplitude of oscillation keep increasing with the forward reduced velocity as shown in Figure 5.25. At a reduced velocity of 5.25, the amplitude ratio plummeted from a value of 0.75 to a nearly zero amplitude ratio as shown in Figure 5.25. The abrupt jump in the amplitude takes place at a Froude number of 0.57 as shown in Figure 5.23. But when we approach rearward the end of synchronization by reducing the velocity, the amplitude of oscillation is zero until a reduced velocity of 4.3 for Froude number of 0.475 (see Figure 5.23 and Figure 5.25). The hysteresis observed at the end of the synchronization is due to the flipping between Step 3 and Step 4 as shown in Figure 5.19. These observations prove a strong hysteretic character. The synchronization continues rearward until a reduced velocity of 3.0 and corresponding Froude number of 0.325 (see Figure 5.23 and Figure 5.25). In this case, the hysteresis character is seen both at the start and end of the synchronization range. The hysteresis observed at the start of the synchronization is due to the flipping between Step 1 and Step 2 as shown in Figure 5.19. In the 5″ cylinder case and gap ratio of 0.3, strong hysteritic character is observed at both the beginning and the end of synchronization range.

In the case of 5″ cylinder and gap ratio of 0.197, the forward range of synchronization started at a reduced velocity of 3.0 and the amplitude of oscillation keeps increasing with the forward reduced velocity and at a reduced velocity of 5.2, the amplitude ratio of oscillation suddenly jumped from a value of 0.58 to nearly zero amplitude ratio of oscillation (see Figure 5.28). The abrupt jump in the amplitude takes place at a Froude number of 0.57 (see Figure 5.25). The value of the critical Reynolds number at which the amplitude of oscillation jumps to nearly zero amplitude varies with the diameter of the cylinder. This corroborates that the surface curvature in relation to the cylinder diameter (see Figure 5.10) is important as discussed in Section 5.5.3. But when we approach rearward by reducing the velocity, the amplitude of oscillation is zero until a reduced velocity of 4.3 and the corresponding Froude number was 0.375. The measurements prove a stronger hysteresis character (see Figure 5.28 and Figure 5.25). The amplitude of oscillation, even though less in magnitude, continued rearward until a reduced velocity of 2.0 and the Froude number was 0.2 (see Figure 5.28 and Figure 5.25). In this case, the hysteritic character is observed both at the start and end of the synchronization but at the start of synchronization, it is not as strong as in the previous case.

In the 2.5″ cylinder case and gap ratio of 0.197, the vortex induced vibration was completely suppressed as shown in Figure 5.6 and Figure 5.7. For lower Froude number, it was suppressed due to the Coanda effect. At higher Froude numbers, it was suppressed due to strong skewing of the wake by the standing waves generated. This was observed by Sheridan et al. (1995; 1997) and by Reichl (2001) in his numerical simulations . In the case shown by Reichl (2001), there was no entrainment between the opposite sign vortices and they form a long recirculation bubble transforming from an absolute instability to convective instability.

The early start of synchronization and the non-existence of the jump can be attributed to the skewing of the wake. In Section 5.5.5, the hysteretic effect on the frequency of oscillation will be discussed in detail.

In the case of VIV near free surface, based on the findings of Sheridan et al. (Sheridan et al. 1995; Sheridan et al. 1997) and the observation made in our experiments, the following hypotheses can be made for a cylinder in VIV near a free surface.

- Steps 1 and 2 can coexist in the same parameter space:
  (i) At higher gap ratios (h/D > 0.4) and Fr < 0.6.
  (ii) At low gap ratios (0.2 <h/D < 0.4) for low Froude number (Fr < 0.4).
- Steps 3 and 4 can coexist in the same parameter space:
  (i) At higher gap ratios (h/D > 0.4) and high Froude number (Fr > 0.6).
  (ii) At low gap ratios (h/D < 0.4) for low and moderate Froude number

Our experiments resolve that, contingent on which metastable wake states are present, the fluid instability can alter from an absolute to a convective instability. The level of surface deformation and hence skew at any particular instant determines the wake behavior. Lashkov et al. (1992) prevented the Coanda effect by microribbing of curved surfaces. In our experiments the Coanda effect was prevented by using roughness strips as it will be discussed in detail in Chapter 7.

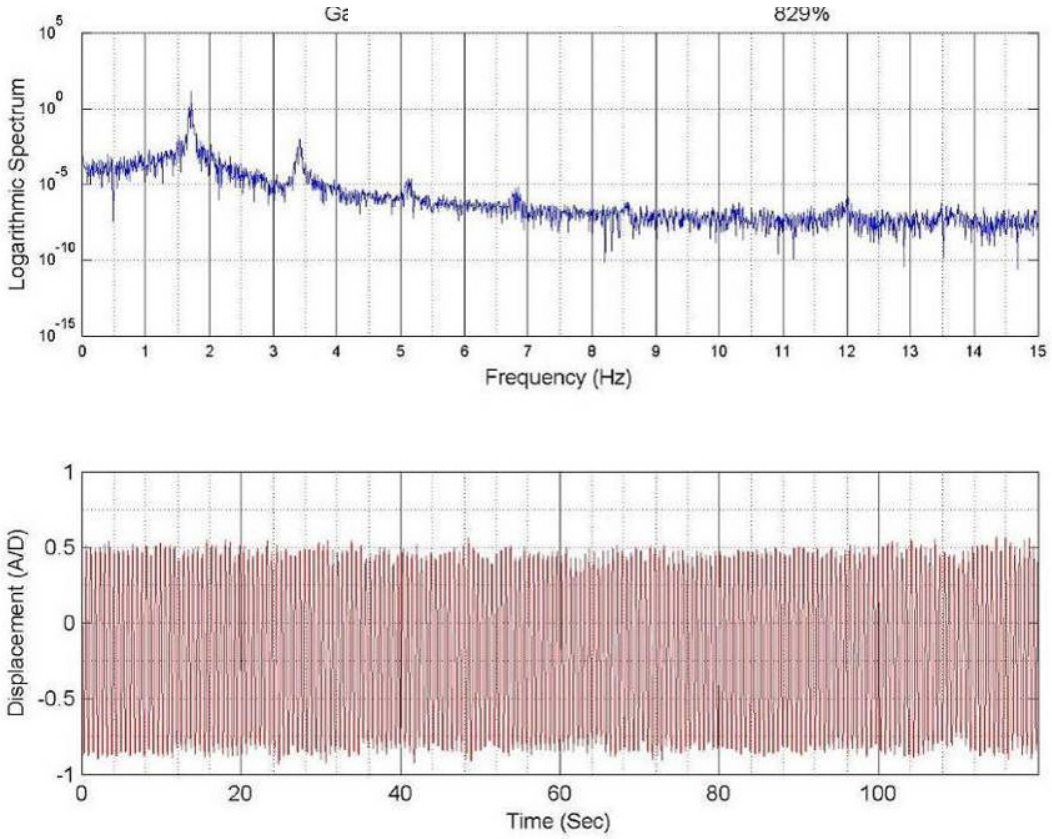

Figure 5.17. Stable high amplitude VIV response for h/D = 0.3937 at U = 0.643 m/s.

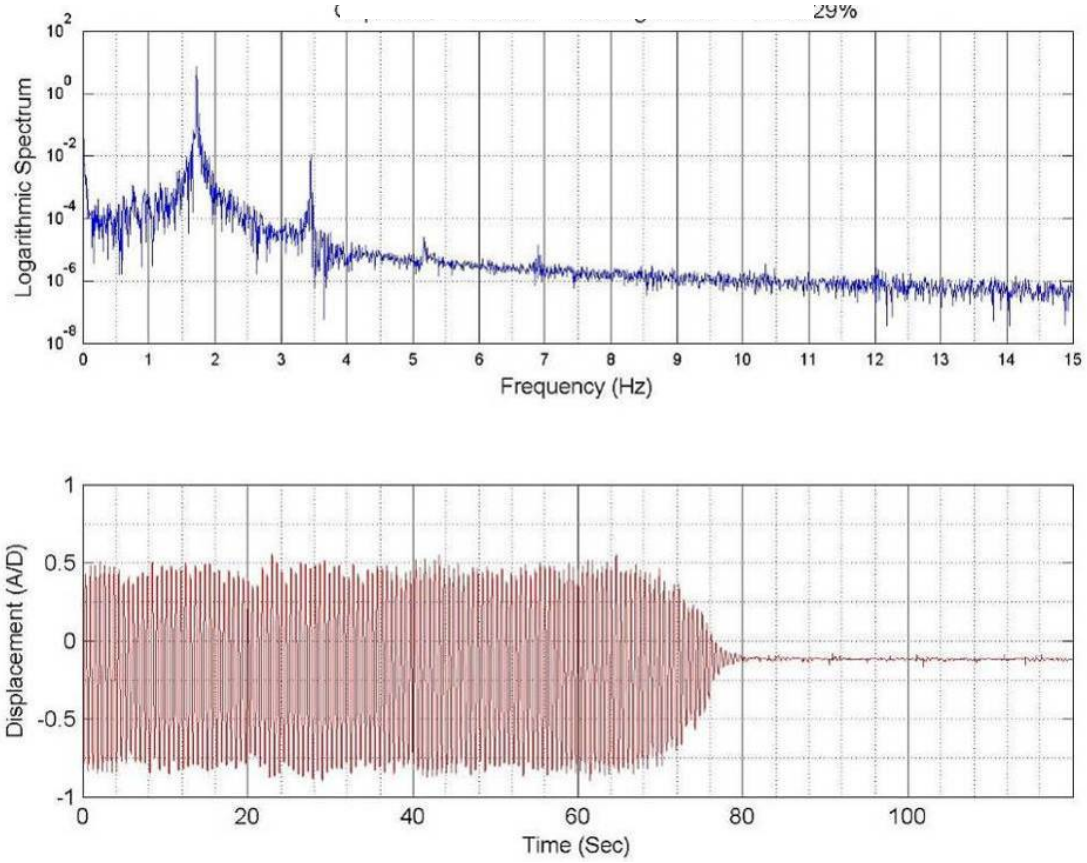

Figure 5.18. Abrupt change in the stability of VIV response for h/D = 0.3937 at U = 0.662m/s.

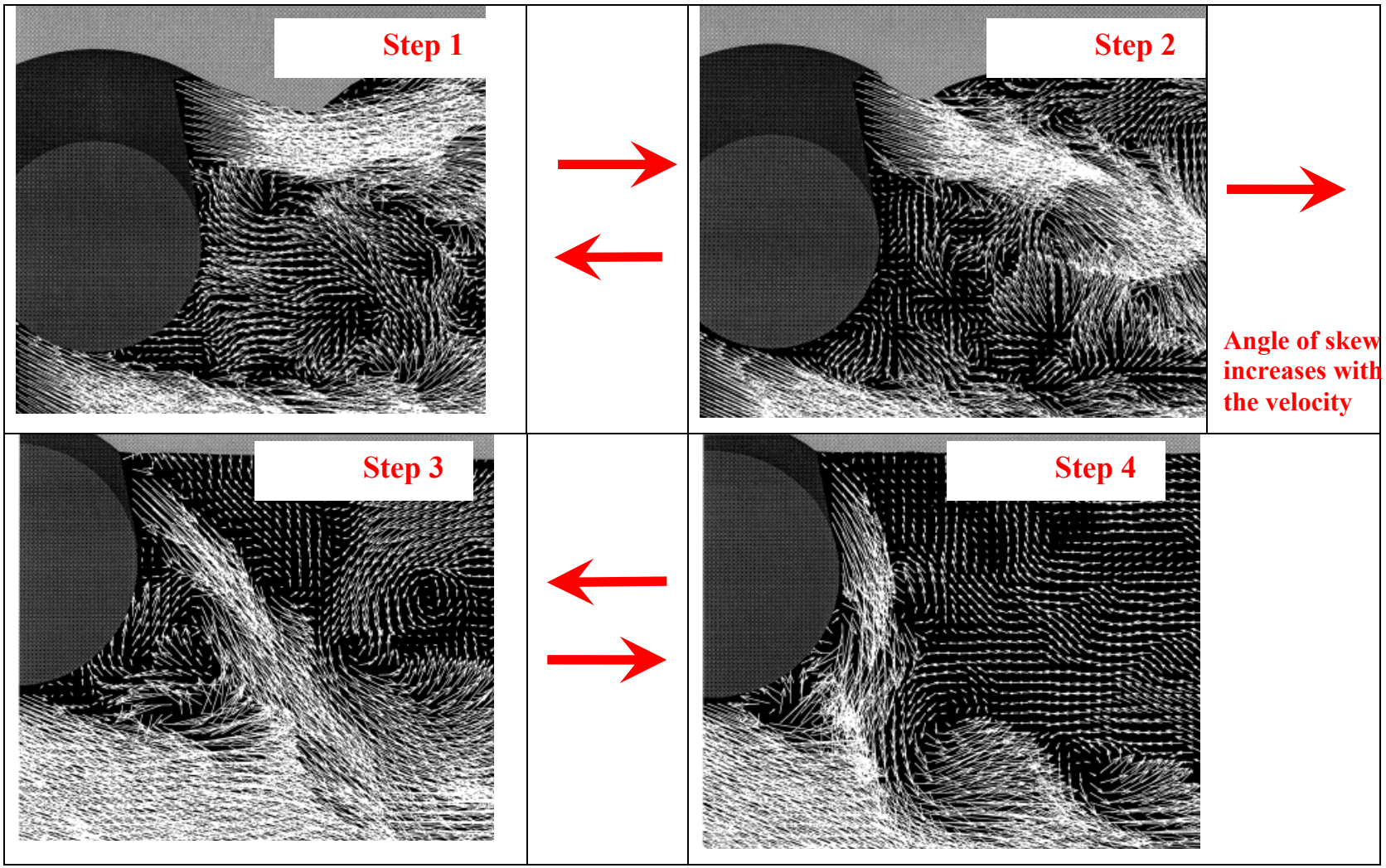

Figure 5.19. The schematic version of the steps occurring in the near wake behind the cylinder close to a free surface as the Froude number and gap ratio are varied. The images are reproduced from Sheridan et al. (1997).

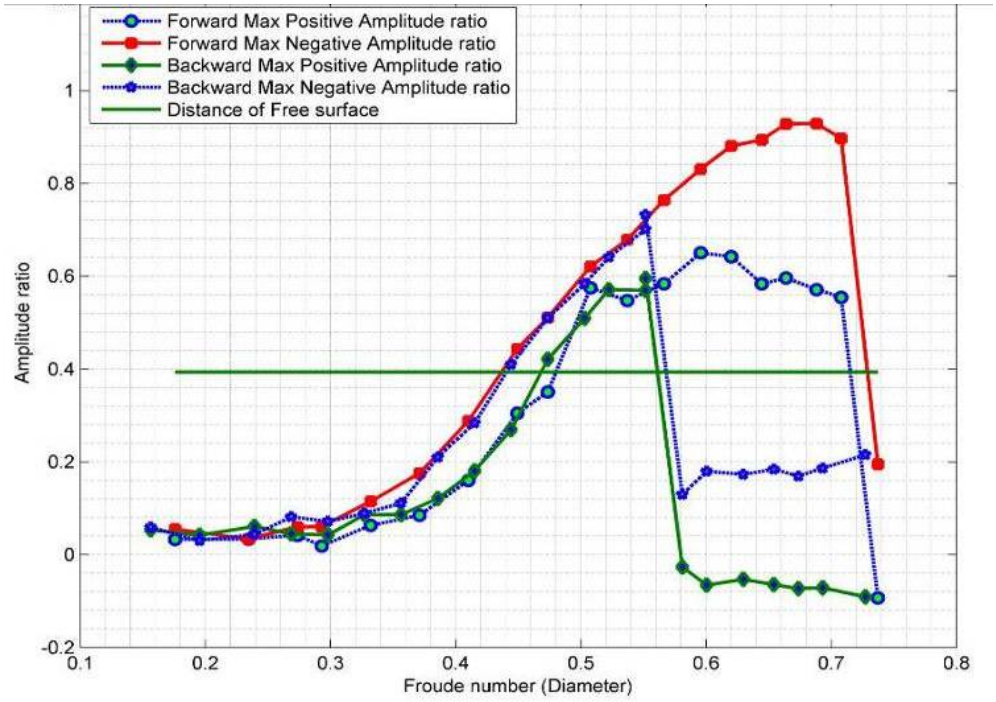

Figure 5.20. Forward and backward VIV response versus Froude number (Diameter) of a 3.5″ cylinder for a gap ratio of 0.394.

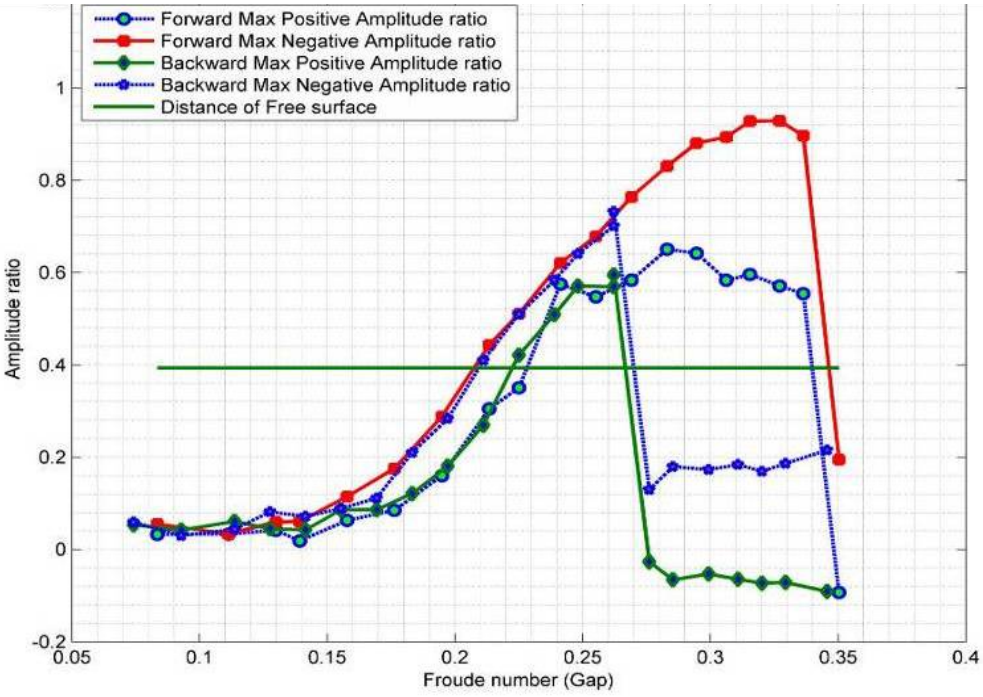

Figure 5.21. Forward and backward VIV response versus Froude number (gap) of a 3.5″ cylinder for a gap ratio of 0.394.

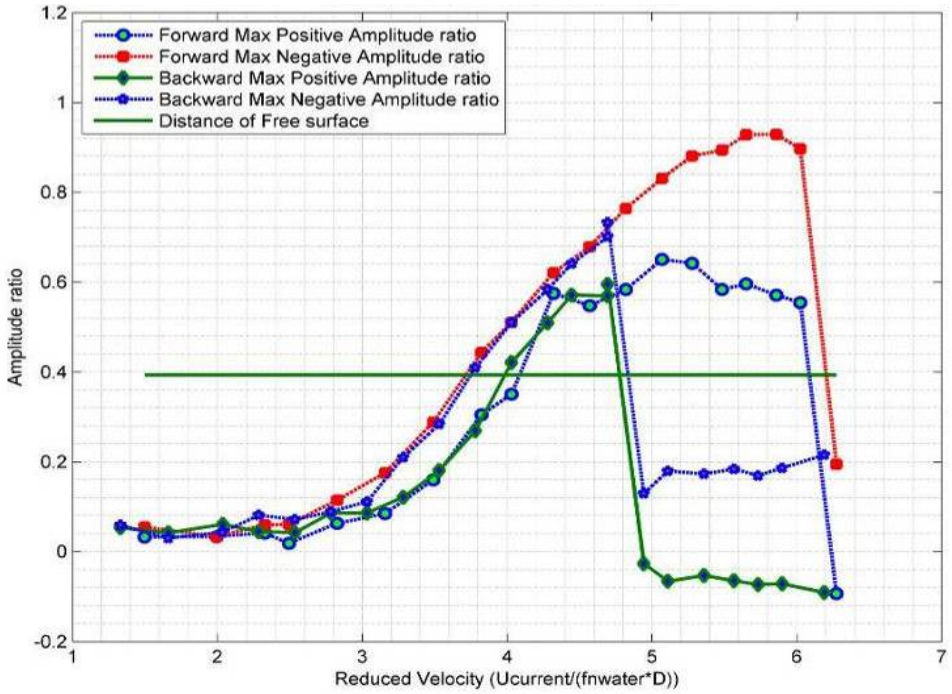

Figure 5.22. Forward and backward VIV response versus reduced velocity of a 3.5″ cylinder for a gap ratio of 0.394.

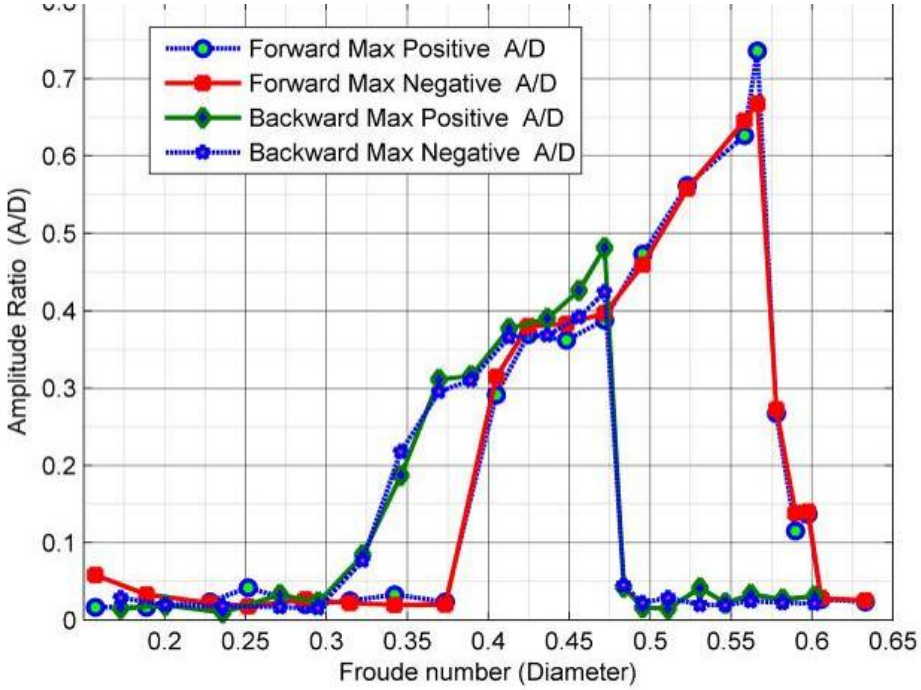

Figure 5.23. Forward and backward VIV response versus Froude number (Diameter) of a 5″ cylinder for a gap ratio of 0.299.

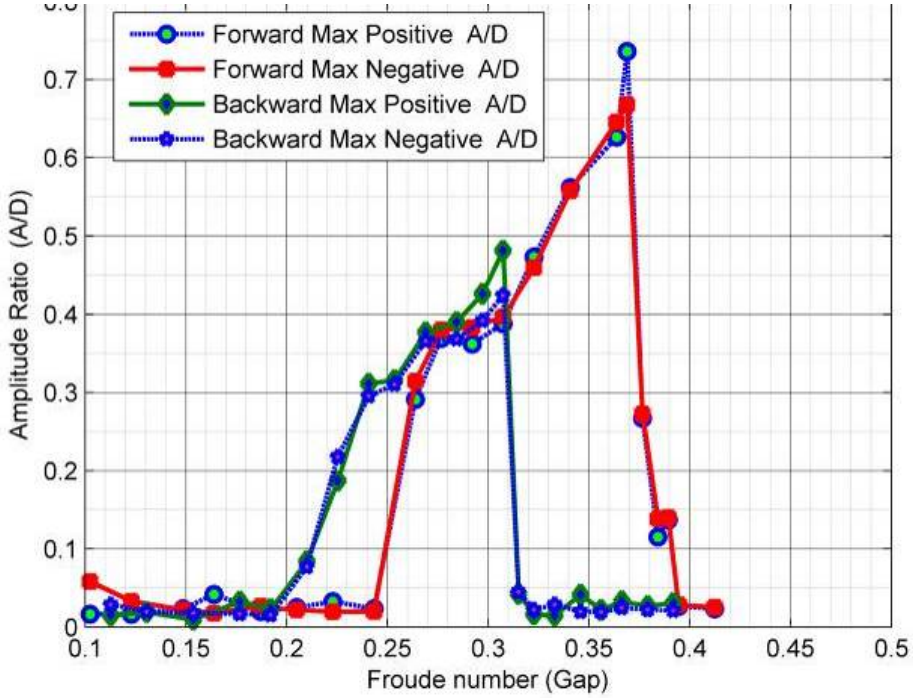

Figure 5.24. Forward and backward VIV response versus Froude number (gap) of a 5″ cylinder for a gap ratio of 0.299.

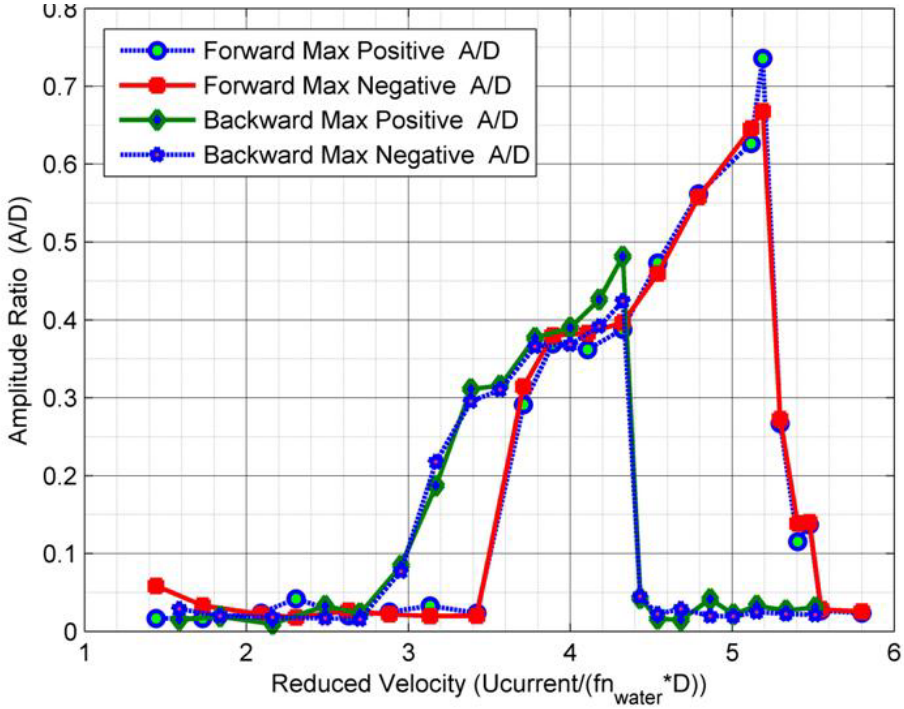

Figure 5.25. Forward and backward VIV response versus reduced velocity of a 5″ cylinder for a gap ratio of 0.196.

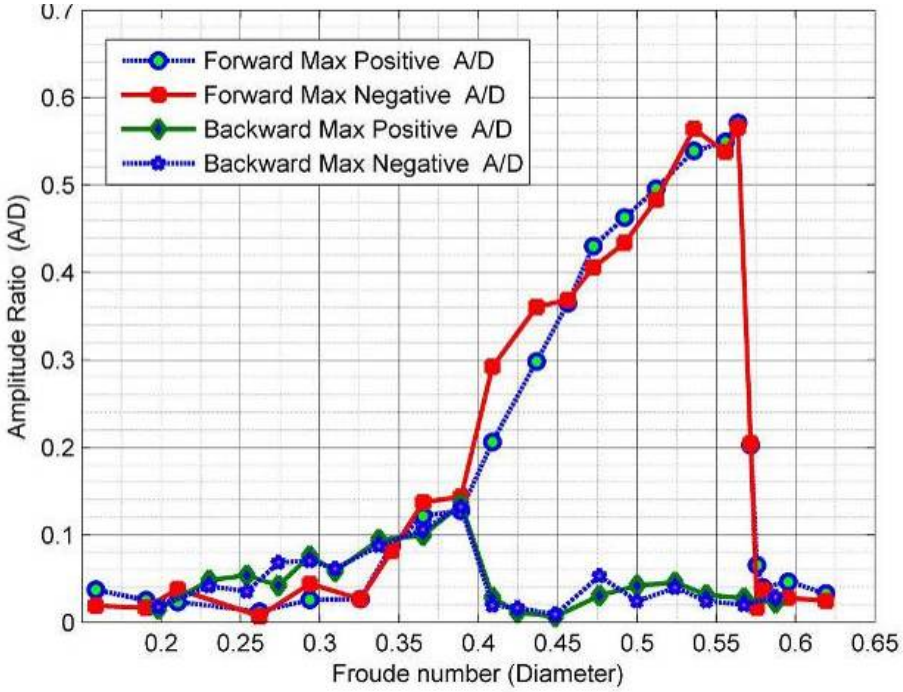

Figure 5.26. Forward and backward VIV response versus Froude number (Diameter) of a 5″ cylinder for a gap ratio of 0.196.

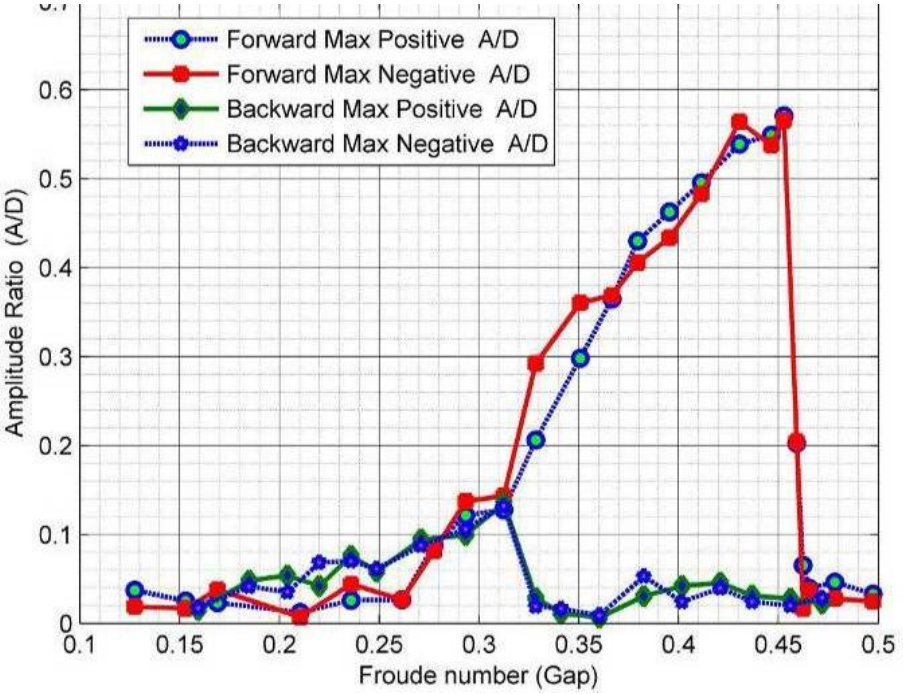

Figure 5.27. Forward and backward VIV response versus Froude number (gap) of a 5″ cylinder for a gap ratio of 0.196.

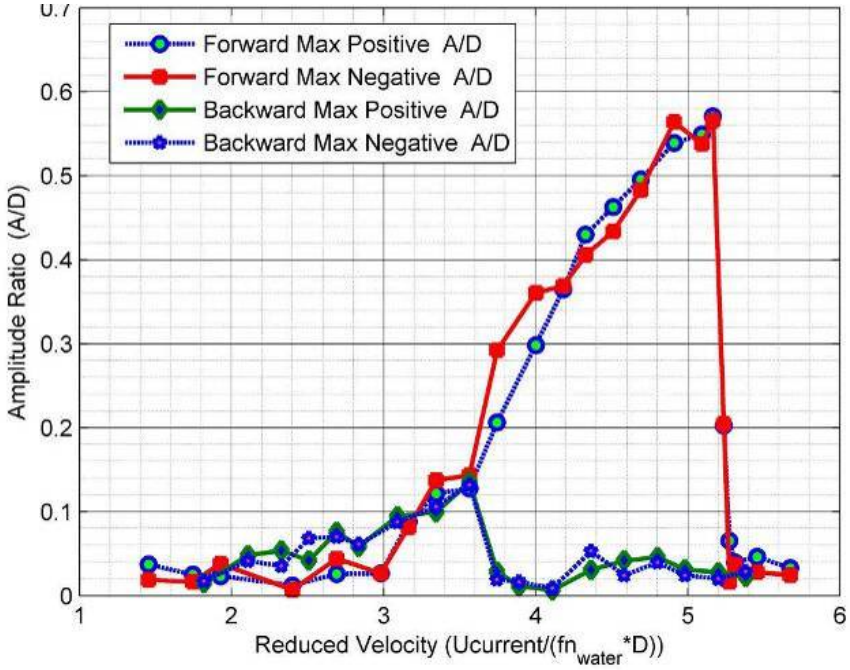

Figure 5.28. Forward and backward VIV response versus reduced velocity of a 5″ cylinder for a gap ratio of 0.196.

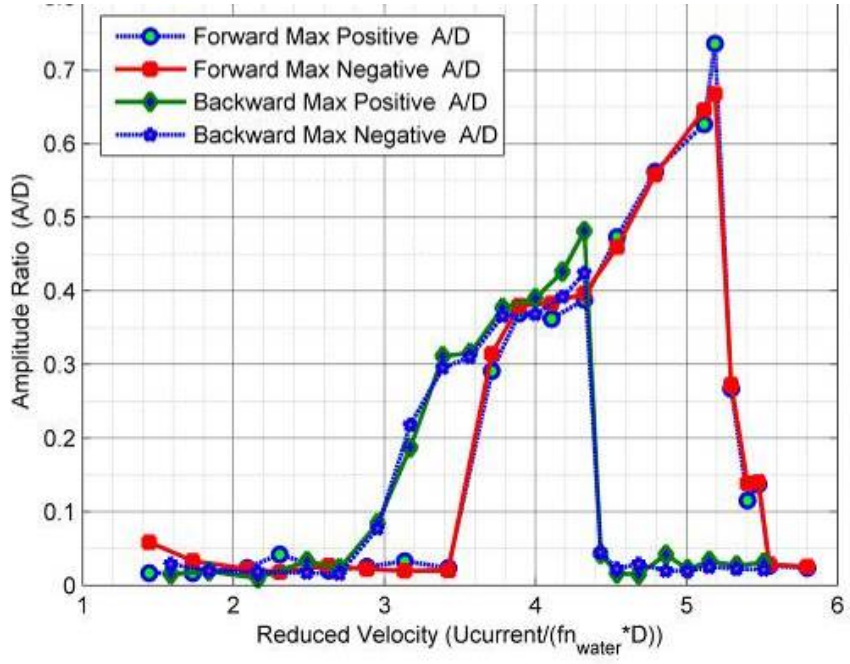

Figure 5.29. Forward and backward VIV response versus reduced velocity of a 5″ cylinder for a gap ratio of 0.299.

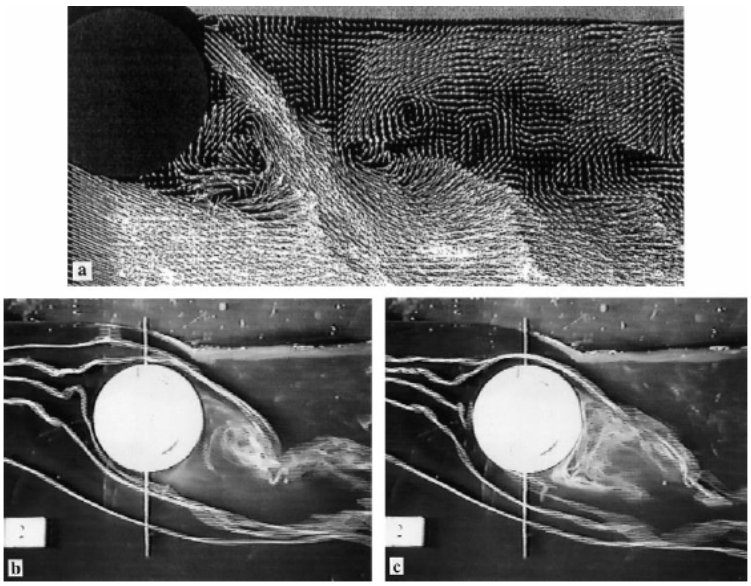

Figure 5.30. The experimental results of Sheridan et al. (1997) (top) for a gap of 0.31, a Froude number 0.60 and a Reynolds number between 5990 and 9120, and experimental results of Hoyt et al. (2000) (bottom) at a gap ratio of 0:31, a Froude number of 0.53 and a Reynolds number of 2.7×10^4. [Reproduced from Hoyt et al. (2000)].

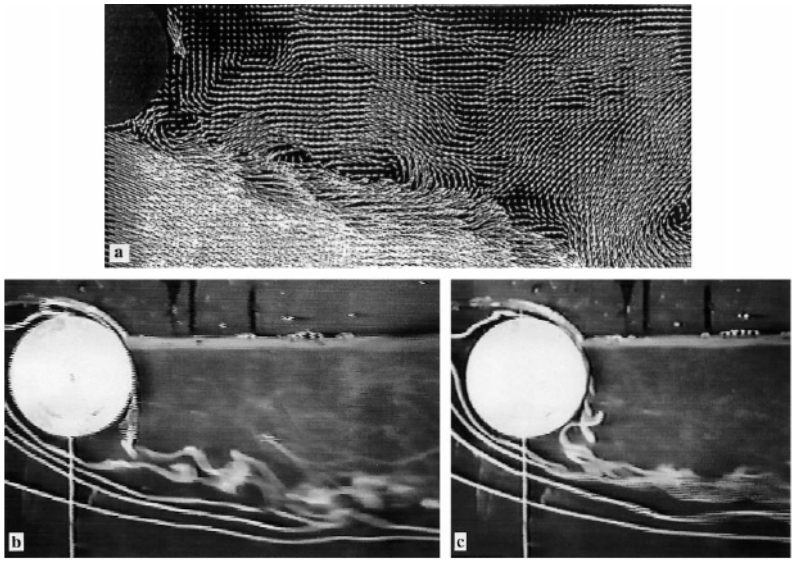

Figure 5.31. The experimental results of Sheridan et al. (1997) (top) for a gap of h/D=0, and a Reynolds number between 5990 and 9120, and experimental results of Hoyt et al. (2000) (bottom) at a gap ratio of 0, and a Reynolds number of 2.7×10^4. [Reproduced from Hoyt et al. (2000)].

5.5.5. Frequency content

In the previous section, the hysteresis in the response of the cylinder was observed and the hysteretic character was attributed to changes in the character of the wake in response to the variation in gap ratio and Froude number. In turn, this alteration in the wake state should in turn affect the response of the oscillation frequency of the system. In the numerical study on stationary cylinder by Reichl, he observed that the Strouhal number gradually increases for intermediate gap ratio and for lower gap ratios it reduced considerably Figure 5.32. According to the author's knowledge, the shedding frequency associated to the different wake structure (see Figure 5.19) is not known. The character of the wake structure depends on gap ratio and Froude number.

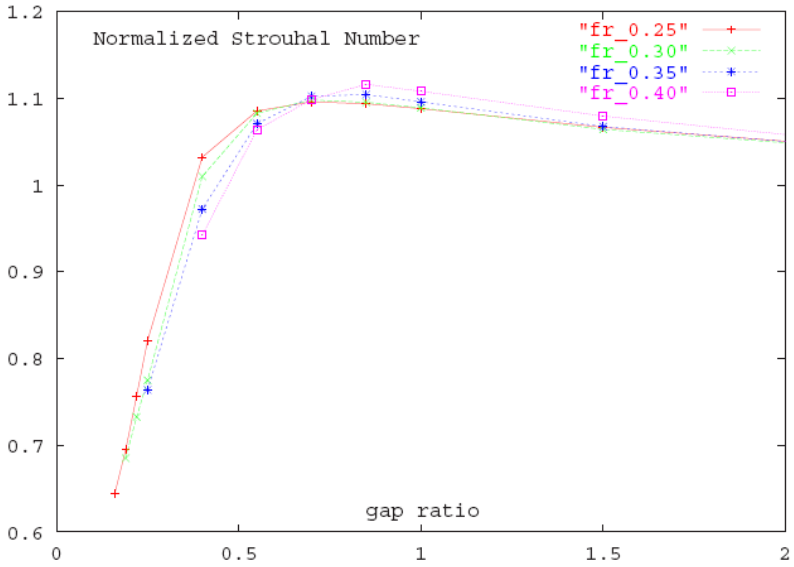

Figure 5.32. Variation of Strouhal number (normalized with respect to Strouhal number of the reference cylinder (i.e. St/St_0)) with gap ratio for Froude numbers of 0.25, 0.30, 0.35, and 0.40. from numerical simulations at a Reynolds number of 180. [Reproduced from Reichl (2001)].

Different metastable wake states have different topology in their near wake structure. In our experiments we observe that wake states corresponding to various combinations of gap ratio and Froude number are associated with different frequency of shedding. The skewing of wake by the jet lying between the free surface and the cylinder would result in faster shedding of the vortices and hence higher shedding frequency. In the case where the wake state is due to the Coanda effect, the frequency of shedding is nearly suppressed and so the frequency is considerably reduced as shown in Figure 5.38,

Figure 5.39, Figure 5.40, Figure 5.41, and Figure 5.42. Inset of the wake structure from Sheridan et al's (1997) experiment corresponding to different range of gap ratio and Froude number has been attached to Figure 5.41, and Figure 5.42. In Figure 5.41, and Figure 5.42, it is observed that the frequency character changes as the wake structure flips. In the above frequency plots mentioned, there is an alteration in the frequency character as the reduced velocity was increased and it is hypothesized to be associated with` the modification in the near wake state.

The frequency character for low gap ratio is different from the fully submerged case because the frequency of oscillation has a strong tendency to synchronize with the shedding frequency rather than the natural frequency as shown in Figure 5.33, Figure 5.34, Figure 5.35, Figure 5.36, and Figure 5.37.

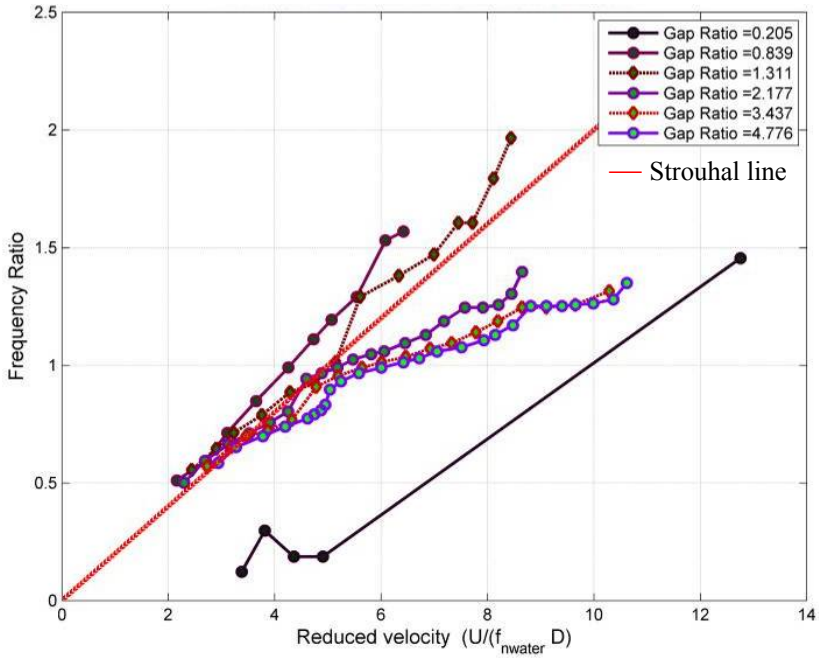

Figure 5.33. Forward frequency of VIV response versus reduced velocity of a 2.5″ cylinder for gap ratios 0.2, 0.84, 1.3, 2.18, 3.44, and 4.78.

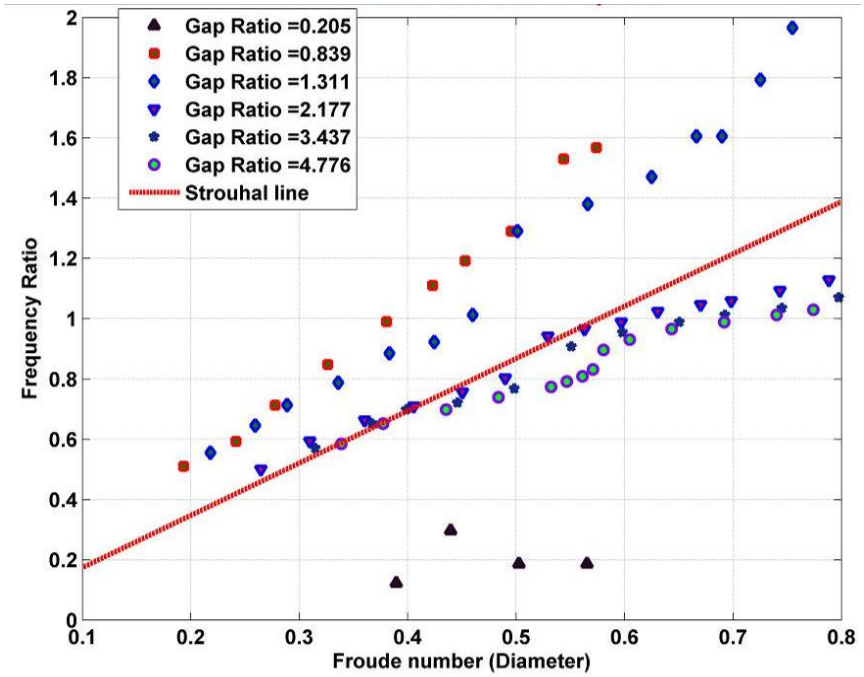

Figure 5.34. Forward frequency of VIV response versus Froude number (diameter) of a 2.5″ cylinder for gap ratios 0.2, 0.84, 1.3, 2.18, 3.44, and 4.78.

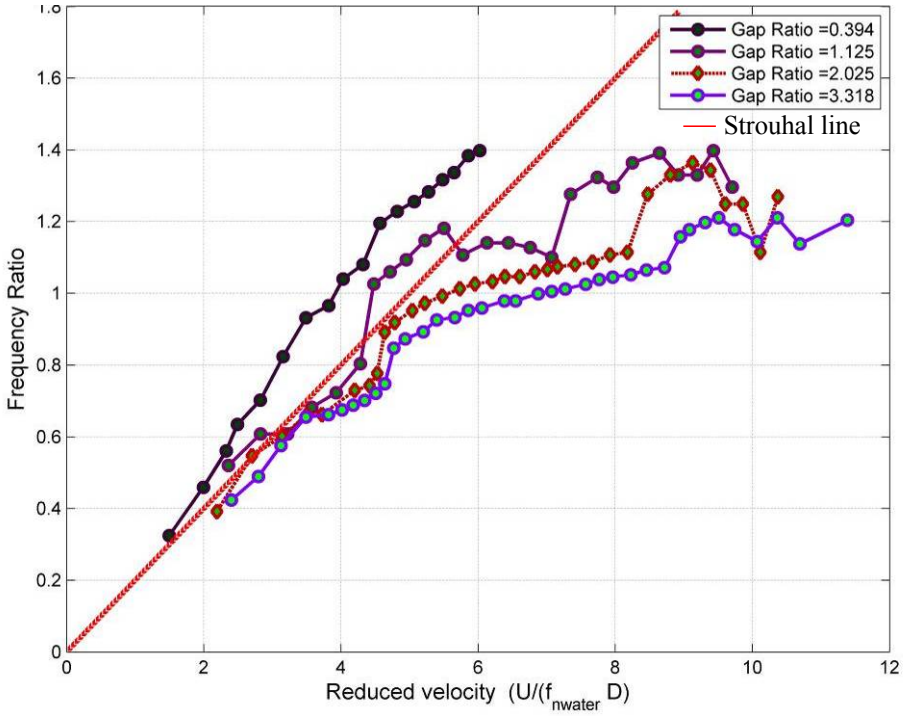

Figure 5.35. Forward frequency of VIV response versus reduced velocity of a 3.5″ cylinder for gap ratios 0.39, 1.13, 2.03, and 3.32.

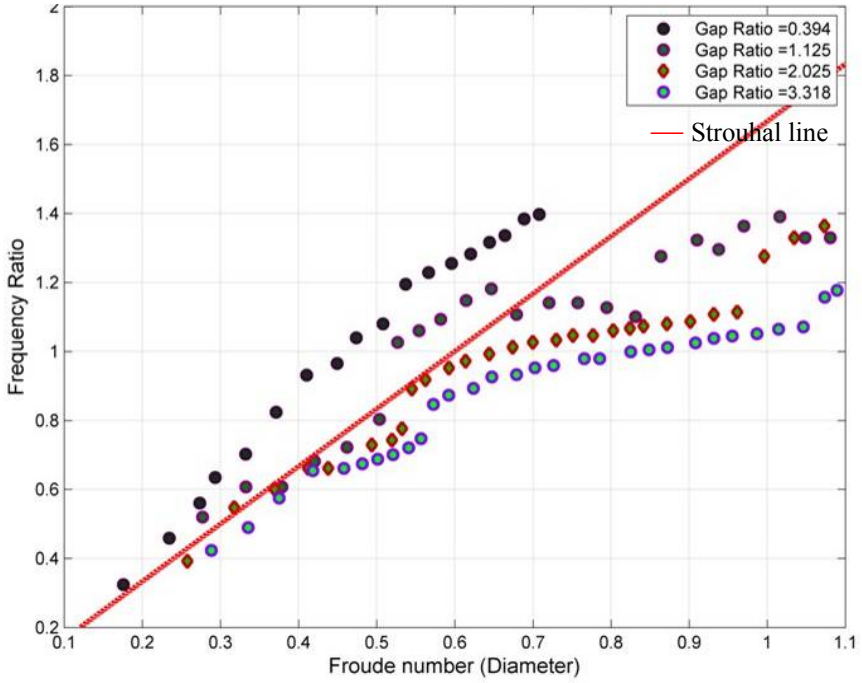

Figure 5.36. Forward frequency of VIV response versus Froude number (diameter) of a 3.5″ cylinder for gap ratios 0.39, 1.13, 2.03, and 3.32.

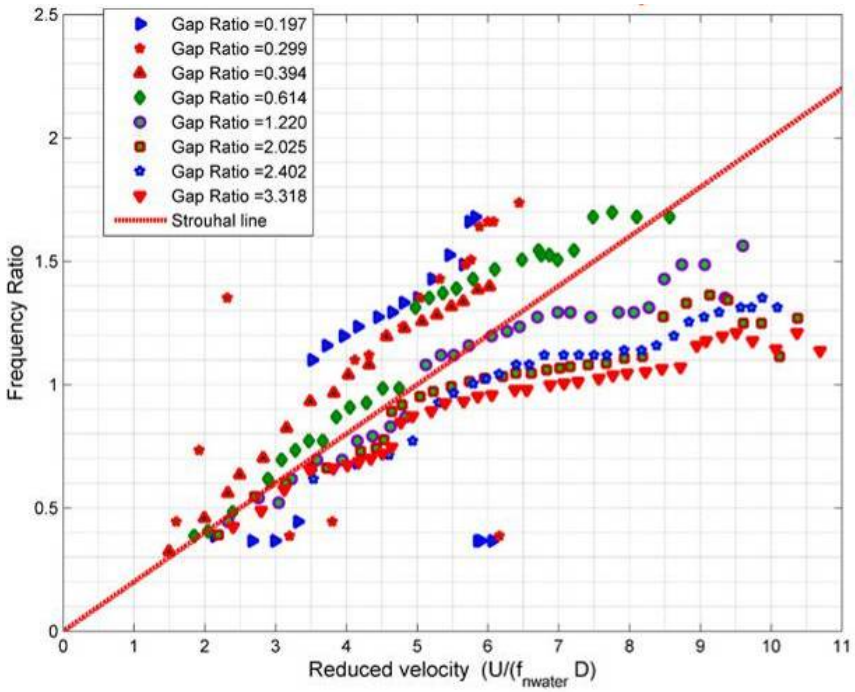

Figure 5.37. Compiled forward frequency of VIV response versus reduced velocity of a 3.5 and 5″ cylinder for gap ratios denoted in the figure.

In Figure 5.38, Figure 5.39, Figure 5.40, Figure 5.41, and Figure 5.42, there is flipping between different wake states observed for low gap ratio as the velocity is increased. This switching between the wake states can be attributed to the stability of different wake states which is affected by the surface curvature and the modification of the wake by the cylinder being submerged further than its original gap ratio because of the increasing mean lift force and the formation of the standing wave behind the cylinder as the velocity increases.

In Figure 5.41, the forward and backward frequencies are plotted for a 5″ cylinder with a gap ratio of 0.19 and there is switching between the dominant frequencies of oscillation as the velocity increases. This switching is manifested in the amplitude plot where the amplitude is switching between higher amplitude of oscillations and the lower amplitude with a strong hysteresis character.

In Figure 5.34, the forward frequency is plotted for a 2.5″ cylinder with a gap ratio of 0.2 and the dominant frequency of oscillation is a very low value. The low value of the frequency of oscillation is associated with the cessation of alternate vortex shedding due to either Coanda effect or the extreme skewing of wake.

In Figure 5.38, Figure 5.39, and Figure 5.40 strong hysterisis is observed in the frequency content. The hysterisis character is observed and it becomes stronger as the Froude number increases and the gap ratio decreases. The hysterisis is associated with the wake structure. As the wake structure transforms due to Coanda effect or the extreme skewing of the wake, the frequency of oscillation jumps to a very low value as shown in Figure 5.38, Figure 5.39, and Figure 5.40.

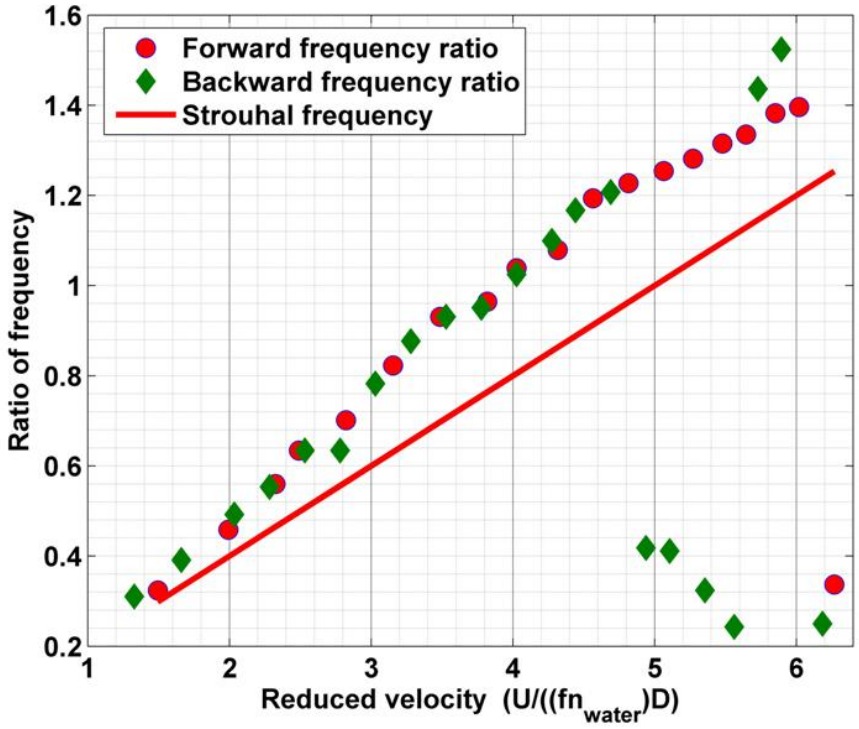

Figure 5.38. Forward and backward frequency ratio of VIV response versus reduced velocity of a 3.5″ cylinder for a gap ratio of 0.394.

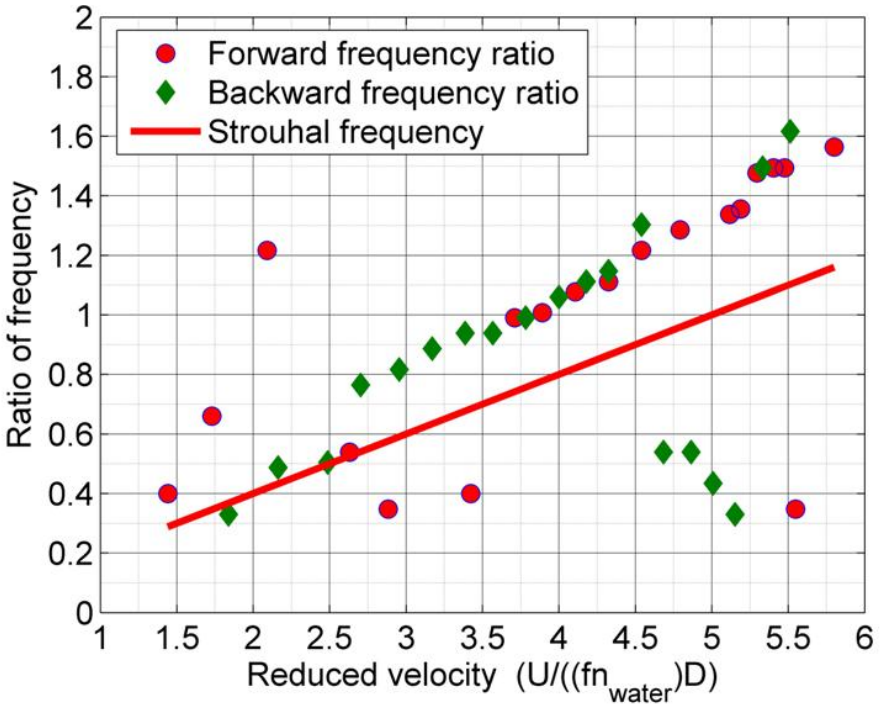

Figure 5.39. Forward and backward frequency ratio of VIV response versus reduced velocity of a 5″ cylinder for a gap ratio of 0.299.

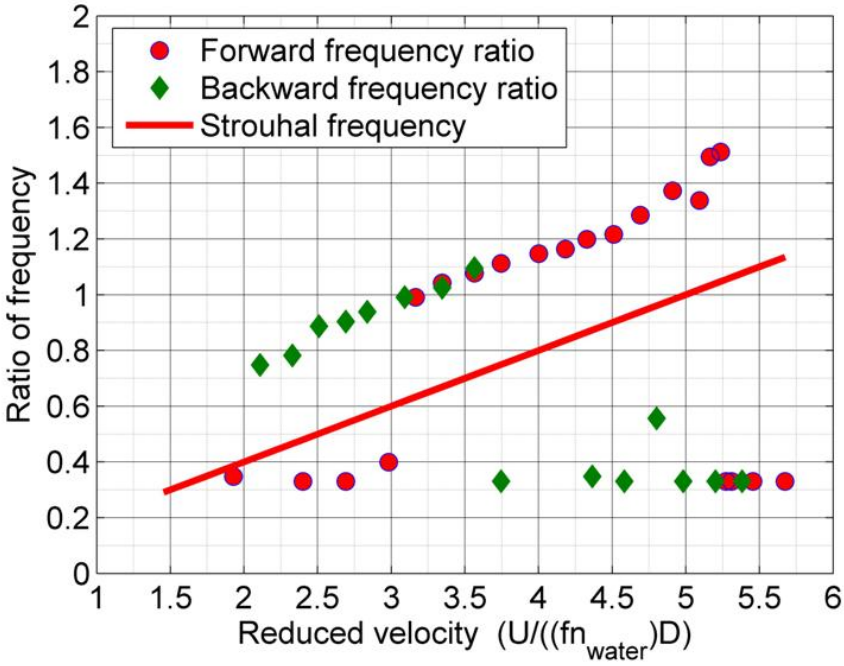

Figure 5.40. Forward and backward frequency ratio of VIV response versus reduced velocity of a 5″ cylinder for a gap ratio of 0.197.

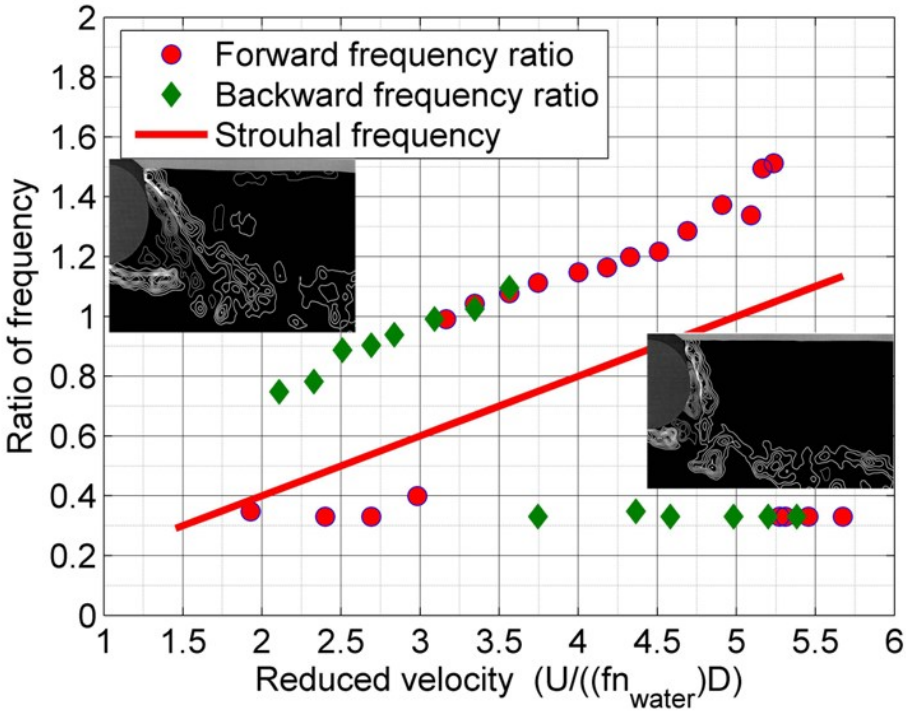

Figure 5.41. Forward frequency of VIV response versus reduced velocity of a 5″ cylinder for gap ratios of 0.197 with inset of wake states from Sheridan et al's (1997), corresponding to the frequency character.

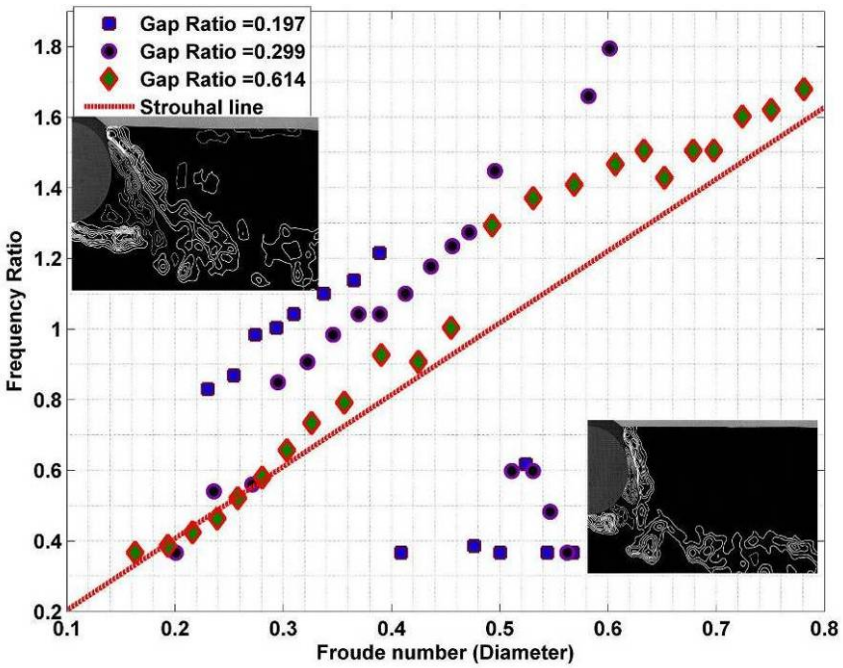

Figure 5.42. Forward frequency of VIV response versus Froude number (diameter) of a 5″ cylinder for gap ratios of 0.197, 0.299, and 0.614 with inset of wake states from Sheridan et al's (1997), corresponding to the frequency character.

5.6. MAIN FINDINGS

VIV tests in the LTFSW Channel of the University of Michigan for Reynolds number in the range of $[8\times10^3 - 1.5\times10^5]$ have shown unmistakably the strong dependence of VIV on the proximity to the free surface. This is of particular interest to the present line of research since the goal is to improve the design of the VIVACE Converter, which extracts energy from ocean/river currents. It is of interest in other bluff body applications which are closer to the free surface. The results of this chapter can be summarized as follows:

For a cylinder in VIV,

- Proximity to the free surface reduces range of synchronization of VIV.
- Proximity to the free surface reduces the amplitude ratio (A/D).
- In the unbounded case, lock-in occurs in the classical sense where $f_{v,mode} = f_{osc} \approx f_{n,water}$. In the case near to the free surface, the lock-in/synchronization of the frequencies occurs between $f_{osc} = f_{v,mode} > f_{St}$.

- Approaching closer to the free surface does not suppress VIV but lock-in results in $f_{v,mode} = f_{osc}$; and the natural frequency ($f_{n,water}$) does not play a role in lock-in.
- Near to the free surface, at the onset of VIV, A/D increases slowly, not in a jump as in VIV away from FS.
- Proximity to free surface introduces hysteresis at the end of synchronization and the beginning of the synchronization due to the flipping between the wake states.
- Hysteresis at the end of synchronization can be attributed to the wake structure bifurcation at $Fr_{Dcritical}$, which is a function of the gap ratio and the gap.
- At $Fr_{Dcritical}$, A/D goes to zero. This is attributed to the transition of the alternate vortex shedding behind a bluff body to the formation of recirculation bubble. In other words, the instability behind the cylinder alters from absolute to convective instability.

Chapter 6

EFFECT OF BOTTOM BOUNDARY ON VIVACE

6.1. BACKGROUND

Few studies on vortex-induced vibrations of a stationary or elastically mounted cylinder close to a rigid bottom boundary have been conducted in the past. Their objective was to understand the influence of a rigid seabed boundary on the dynamics of a pipeline in ocean currents near the seabed. In the present study, even though the application of it is to maximize VIV under high damping, there is a similar need to understand the effect of proximity to bottom boundary(Raghavan et al. 2007a). This study explores the effect of the proximity of the bottom boundary to a cylinder at high Reynolds number (TrSL3 regime) and complement published data for underwater pipelines at low Reynolds number (TrSL2 regime, beginning of TrSL3 regime).

In this chapter, proximity to a bottom boundary is studied for three reasons.

(i) Energy is lost as vortices disturb the bottom boundary and, thus, is not available to be harnessed.

(ii) Very close proximity to bottom boundary affects vortex shedding and may even suppress VIV.

(iii) Vorticity near a bottom boundary may disturb contaminated soft sediments or marine life habitats possibly raising environmental concerns.

The physics of cross-flow around a cylinder near a plane boundary changes depending on whether the cylinder is stationary or in vortex induced vibration. Below is a review of published data to understand the modification of the flow around a cylinder due

to proximity to a rigid bottom boundary. The review is divided into two, based on whether the rigid cylinder is stationary or elastically supported.

6.1.1. Stationary cylinder

In the case of a stationary cylinder, one of the earliest investigations was carried out by Taneda (1965). In his investigation, he towed a circular cylinder close to a stationary wall through a water basin at a very low Reynolds number in order to eliminate the boundary layer effect. In his investigation, he visualized the flow behind the cylinder at two gap ratios, G/D =0.6 and G/D = 0.1, at a Reynolds number value of 170, and he observed that regular Kármán vortex shedding took place at G/D = 0.6 as shown in Figure 6.1 (a). However, at a gap ratio of 0.1, only a weak single row of vortices were observed to shed as shown in Figure 6.1 (b).

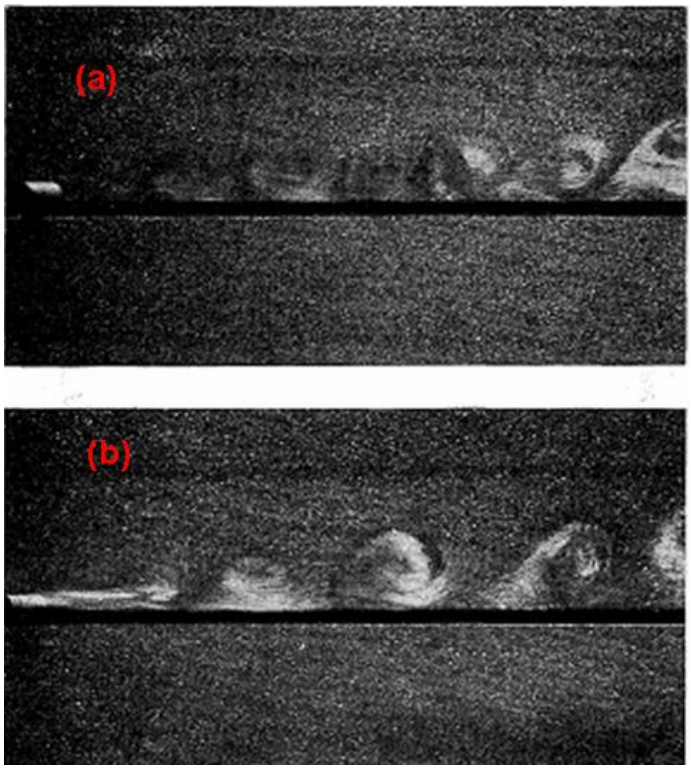

Figure 6.1. The wall effect on the vortex street at a gap ratio (a) G/D =0.6, (b) G/D = 0.1 at Re =170. [Reproduced from Taneda (1965)].

Roshko et al. (1975) measured the drag and lift forces for a circular cylinder located near a plane bottom boundary at Re = 2.0×10^4, which lies in the upper subcritical (TrSL3) flow regime. They investigated for gap ratios between 0 and 6 and observed that the drag coefficient (C_D) decreases and lift coefficient (C_L) increases (Figure 6.2) as the gap ratio decreases. Zdravkovich (1985) observed cessation of regular vortex shedding behind a towed cylinder below a critical values of G/D ≈ 0.3.

The variation of the forces with boundary layer thickness were investigated by Grass et al. (1984) and Taniguchi and Miyakoshi (1990). They found that the variation of lift and drag forces are significantly influenced by the boundary layer at small gap ratios where the boundary layer thickness is comparable to the gap ratio.

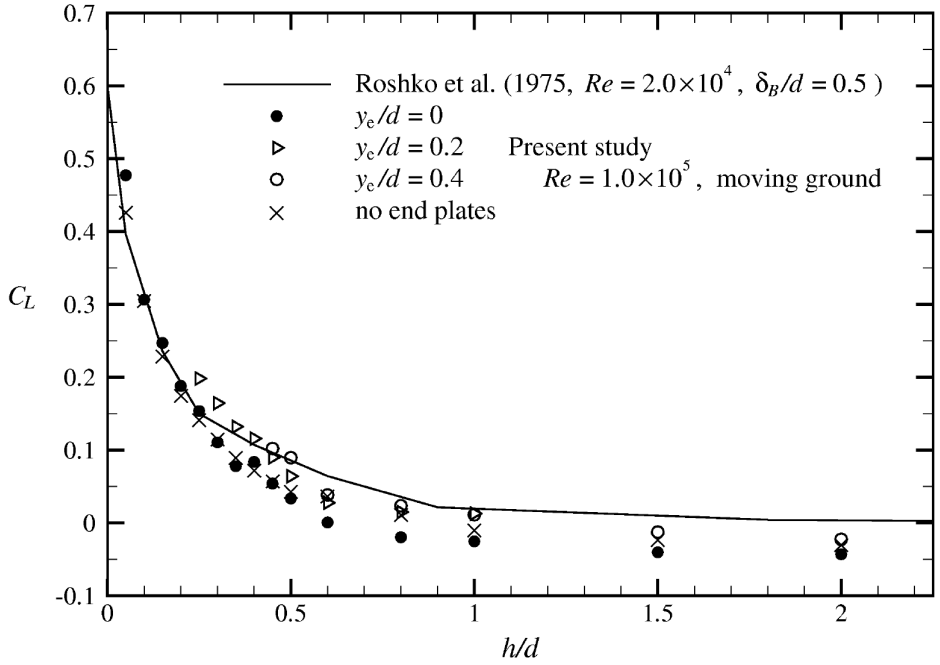

Figure 6.2 Time averaged lift coefficient versus gap ratio (h/d same as G/D). [Reproduced from Nishino et al. (2007)].

Grass et al. (1984) observed that, for small gap ratios, separation zones form on the rigid bottom boundary both upstream and downstream. They also found that for small gap ratios < 0.5, the regular Kármán vortex shedding was sporadic and less energetic. For small gap ratios, Grass et al. (1984) suggested that the fluid flowing in the gap between the cylinder and the wall was deflected to form a free jet by the downstream separation

zone and the rolling up of vortices at the bottom side of the cylinder was prevented. They also observed that the gap ratio again varied depending on the boundary layer thickness.

Zdravkovich (1985) observed that for Re between 4.8×10^4 and 3.0×10^5, the lift coefficient (C_L) is affected by the boundary layer state and not by the thickness of the boundary layer whereas the variation of drag coefficient was dominated by G/δ_B rather than by the gap ratio G/D.

Bearman and Zdravkovich (1978) carried out investigations in the Re range 2.5×10^4–4.8×10^4 (TrSL3 regime) and the characteristic change in drag and lift forces with various gap ratios were explained by interpreting the measured time-averaged C_p distributions. They attributed the positive lift for small gap ratio (G/D) to an asymmetric pressure distribution around the cylinder. The pressure distribution became symmetric as the gap ratio between the cylinder and the bottom boundary increased above 0.4. Bearman and Zdravkovich (1978) determined the critical gap ratio at which cessation of regular Kármán vortices occurs and they based it on the measured velocity fluctuations in the near wake of the cylinder. In their measurements for all gap ratios (G/D) greater than 0.3, the peak of the power spectra of velocity fluctuations was at the Strouhal value 0.2. For (G/D) less than 0.3, the peak of the power spectra of velocity fluctuations disappeared.

Price et al. (2002) investigated the flow around a stationary cylinder near a plane boundary at Reynolds number in the range of 1200-4960 in combination with flow visualization using PIV. They found that for gap ratios $b/D \leq 0.125$, the vortex shedding is either suppressed or extremely weak and is random. Regular vortex shedding starts at gap ratios $0.5 \leq b/D \leq 0.75$. Price et al. (2002) observed that there was pairing between the shear-layer vortices from the rigid bottom boundary due to the gap flow and the vortices that are shed from the bottom side of the cylinder, since they are of opposite sign vorticity. Price et al. (2002) also observed that even for lower gap ratios, the shear layer curls up on the top of the cylinder in a periodic manner. In their frequency content analysis of the wake for G/D = 0.25, the dominant wake periodicity or the shedding frequency (St) was dependent on Re, as shown in Figure 6.3. They observed that the Strouhal number was dependent on the gap ratio for Reynolds number values less than

2600. For gap ratio 0.125 the wake frequency had two dominant peaks as shown in Figure 6.3 (a).

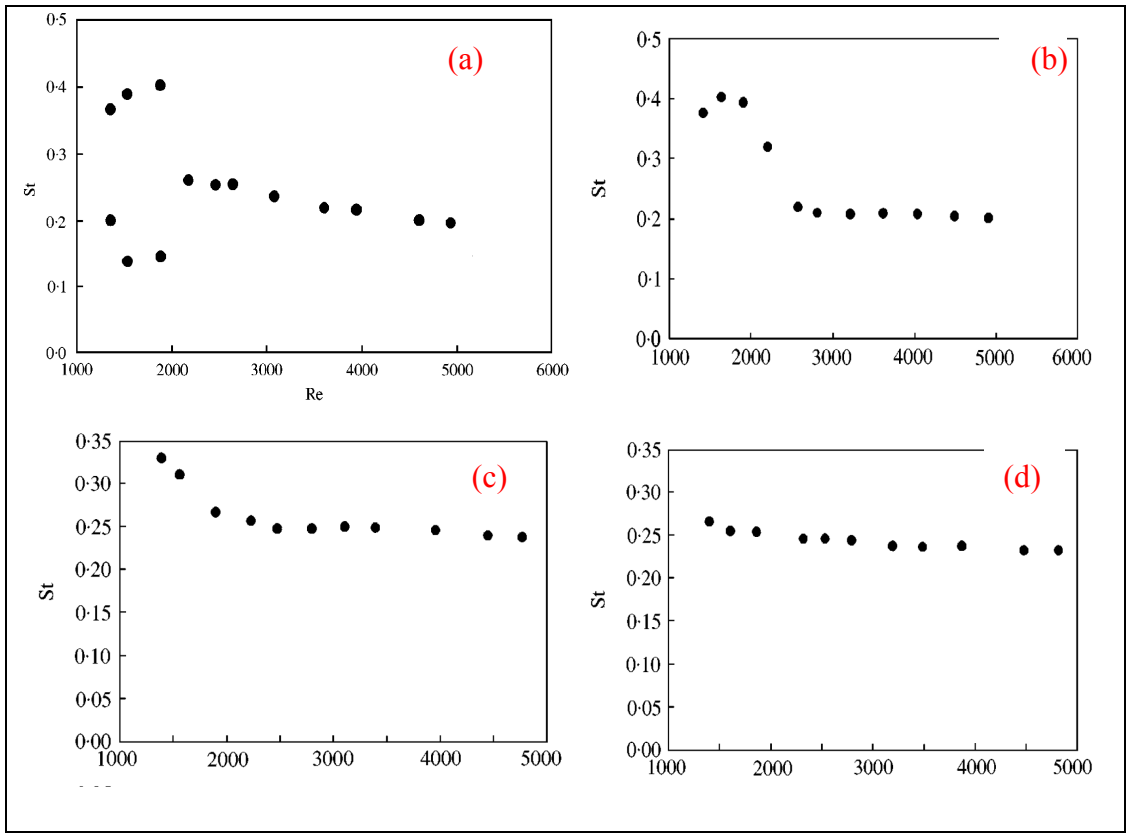

Figure 6.3. Variation of dominant wake Strouhal number, as a function of Re: (a) G/D = 0.125; (b) G/D = 0.25; (c) G/D = 0.5; (d) G/D = 1.0. [Reproduced from Price et al. (2002)].

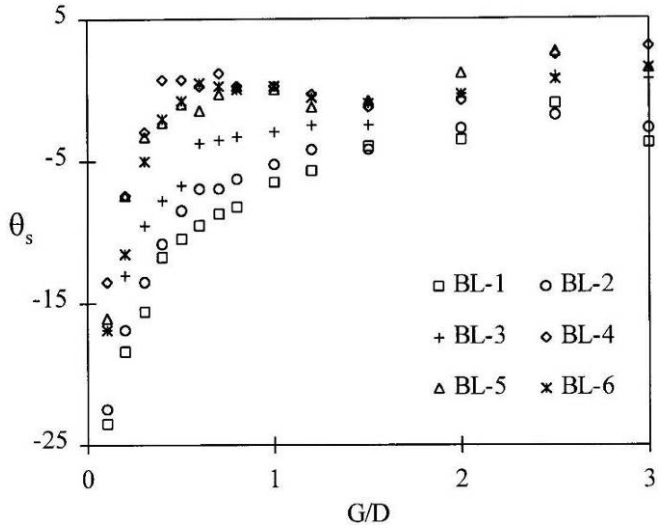

Figure 6.4. Variation of the stagnation point., where, BL-1, δ_B/D = 0.14; BL-2, δ_B/D = 0.25; BL-3, δ_B/D = 0.48; BL-4, δ_B/D = 1.06; BL-5, δ_B/D = 1.64; BL-6, δ_B/D = 2.89; (Lei et al. 1999).

Lei et al. (1999) re-examined the influence of both the gap ratio and the boundary layer for the flow around a circular cylinder. They observed displacement of the stagnation point and a decrease of the base pressure with the increase in gap ratio (see Figure 6.4). They observed that with an increase of the boundary layer thickness along the rigid boundary, an increase of the base pressure results with an upward displacement of the stagnation point. In turn, these changes in the stagnation point (see Figure 6.4) and the base pressure affect the variations of the lift force on the cylinder as shown in Figure 6.5 and Figure 6.6.

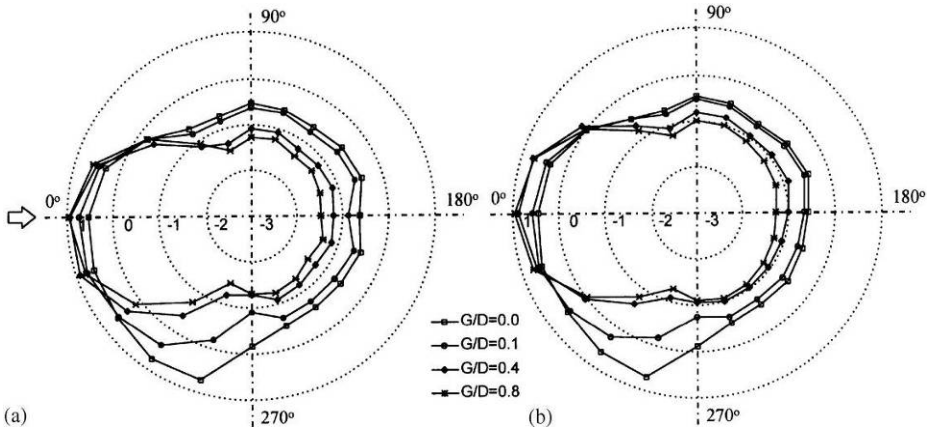

Figure 6.5. Pressure distributions around the cylinder – effect of the gap ratio. (a) $\delta_B/D = 0.48$ (b) $\delta_B/D = 1.06$. (Lei et al. 1999).

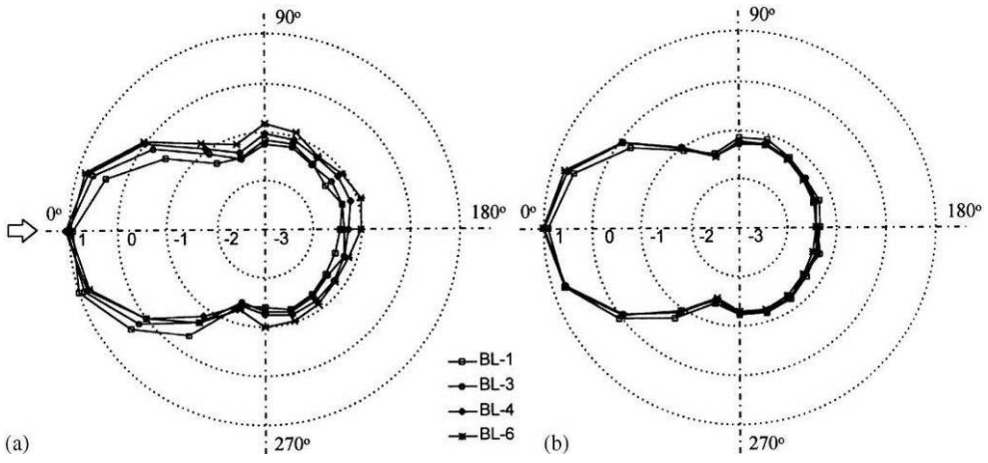

Figure 6.6. Pressure distributions around the cylinder – effect of the boundary layer. (a) G/D=0.6. (b) G/D=2.0. , where, BL-1, $\delta_B/D = 0.14$; BL-3, $\delta_B/D = 0.48$; BL-4, $\delta_B/D = 1.06$; BL-6, $\delta_B/D = 2.89$. (Lei et al. 1999).

Lei et al. (1999) observed that the gap ratio at which regular Kármán vortex shedding was suppressed decreased as the thickness of the boundary layer increased. Lei et al. (1999) also observed that the effect of the plane bottom boundary on vortex induced forcing and vortex shedding behavior is negligible for gap ratios greater than 2.0

6.1.2. Cylinder on elastic supports

Unlike most previous studies on vortex shedding past a stationary cylinder in close proximity to a boundary, this chapter focuses on the influences of VIV when the cylinder is in close proximity to a boundary. Publications on the effect of a plane boundary on an elastically supported cylinder are scarce. Evidence of change for a flow around a cylinder on an elastic support in close proximity to the boundary includes such properties as position of the stagnation point, position of the separation point, shedding frequency, and topology of the wake as observed by Fredsoe et al. (1987).

Investigators	Reynolds number	Regime	$(A/D)_{max}$ for G/D< 0.5	G/D analyzed
Anand (1985)	6.5×10^3-3.5×10^4	TrSL2	0.65	0.5-1.0
Fredsoe et al. (1987)	10^4-3×10^4	TrSL2	1.5	0.1-1.0
Yang et al. (2006)	1.6×10^4	TrSL2	1.5	0.1-1.45
Present experiments	8×10^3-1.5×10^5	TrSL3	1.9	0.16-3.2

The study of the effect of proximity of plane boundary on VIV is limited to the studies by Anand (1985), Fredsoe et al. (1987), Tsahalis and Jones (1981), Jacobsen et. al (1984), and Yang et al. (2006). In the study by Fredsoe et al. (1987), the effect of proximity of a plane boundary was assessed based on the amplitude and range of synchronization of VIV at Reynolds number of 2×10^4. The amplitude of oscillation away from the bottom boundary positive A/D increased as the gap ratio decreased (Fredsoee et al. 1987). Specifically, they found that positive A/D = 1.4 and negative A/D = 0.2 for a gap ratio of 0.2; and positive A/D = 0.95 and negative A/D = 0.6 for a gap ratio of 0.7.

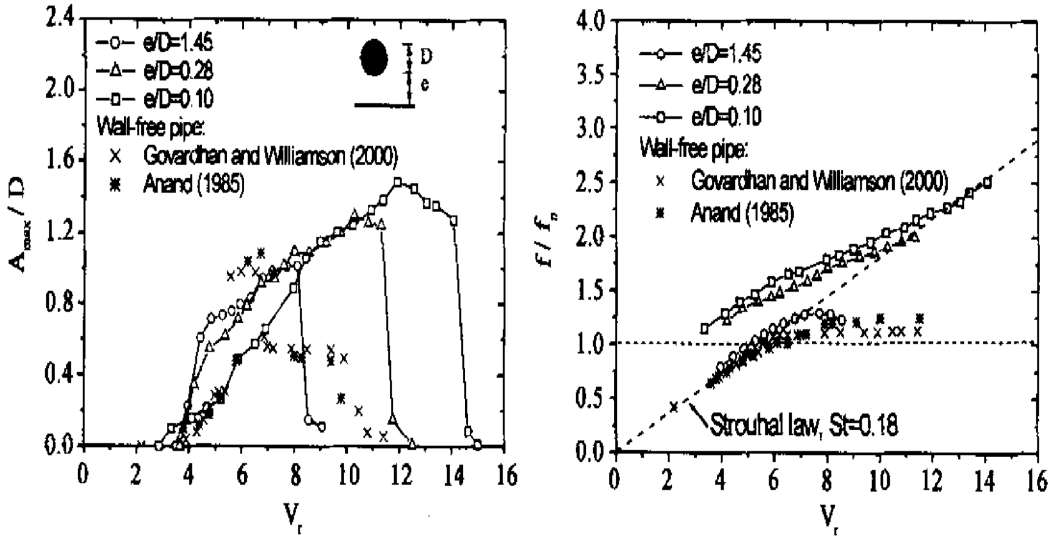

Figure 6.7 Compilation of plots of the experiments done by Anand (1985) and Yang et al. (2006). [Reproduced from Yang et al. (2006)].

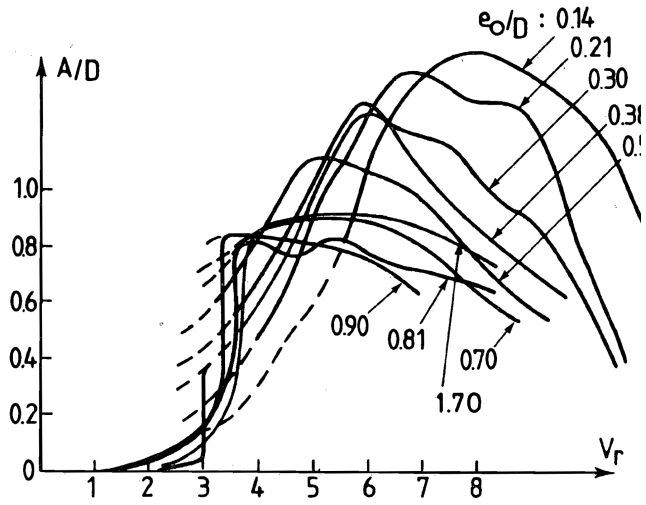

Figure 6.8 Amplitude ratio plotted as a function of reduced velocity for different gap ratios. [Reproduced from Fredsoe et al. (1987)].

Fredsoe et al. (1987)and Yang et al. (2006) found that with the decrease in gap ratio, both the synchronization width, in terms of reduced velocity, and the amplitude ratio increased as shown in Figure 6.7 and Figure 6.8. The vortex induced vibration started earlier (at a lower reduced velocity) in comparison to the cylinder in unbounded fluid.

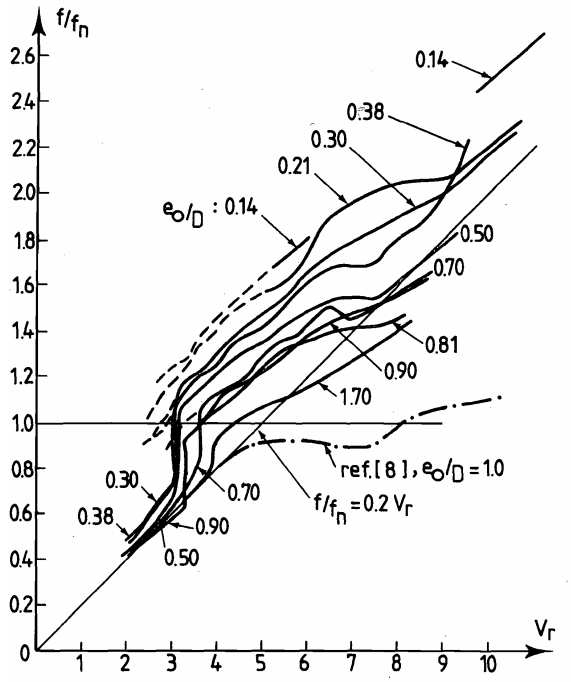

Figure 6.9 Variation in frequencies with gap ratio. [Reproduced from Fredsoe et al. (1987).

Fredsoe et al. (1987) and Yang et al. (2006) found that with the decrease in gap, ratio the dimensionless frequencies f_{osc}/ fn_{water} moved away from the Strouhal line during the synchronization but the constant St they used were different. Fredsoe et al. used 0.2 and Yang et al. used 0.18 as shown in Figure 6.7 and Figure 6.9. At the end of synchronization, dimensionless frequencies f_{osc}/ fn_{water} come closer to the Strouhal line.

6.2. PROBLEM DEFINITION

The goal is to study the effect of proximity of bottom boundary on Vortex Induced Vibrations. This investigation considers particulars of VIV that include amplitude, range of synchronization, branches of response within the synchronization range, vortex structures, hysteresis, etc. of a cylinder in VIV in proximity to a bottom boundary at $8\times10^3 – 1.5\times10^5$ under high damping.

6.3. SOLUTION APPROACH

In our experiments, VIV tests were conducted in the Low-Turbulence Free Surface Water (LTFSW) Channel, in the Marine Hydrodynamics Laboratory (MHL) of the University of Michigan.

Six models were used in the tests. All cylinders have length L=36" (914mm) and are made of aluminum coated with polymer paint for surface smoothness and protection. Model diameters are 2.5" (63.5mm), 3" (76.2mm), 3.5" (88.9 mm). The blockage ratio in the test-section of the (LTFSW) Channel ranges from 6.9% to 9.7%. Models are suspended via two compression coil-springs attached to the end-plates of the cylinders. The cylinder is constrained to oscillate transversely to the flow using linear bearings sliding on shafts. There are narrow gaps of about 10 mm between the walls of the (LTFSW) Channel and the end-plates of the model.

Using the six models described above, VIV tests were performed in the (LTFSW) Channel spanning the following ranges of parameters: Re $\in[8\times10^3 - 1.5\times10^5]$, m* $\in$[1.8 - 3.14], U $\in$[0.35 m/s - 1.15 m/s], L/D $\in$[10.3 - 14.4], closest distance to bottom boundary (G/D) $\in$[4 - 0.16], m*ζ $\in$[0.14 - 0.26].

6.4. RESULTS, OBSERVATIONS, AND DISCUSSION

6.4.1. Effect of bottom boundary on the range of synchronization

The range of synchronization and response of a cylinder in VIV at different gap ratios away from the bottom boundary is compiled in Figure 6.10. In moderate gap ratios, the range of synchronization is wider than the unbounded case. As the cylinder gets closer to the boundary layer of the rigid bottom boundary, however, the range of synchronization does not show a definite trend (increasing or decreasing) as in the case of Yang et al. (2006), and Fredsoe et al. (1987). This difference can be attributed to the different regime of Reynolds number in which the present experiments are conducted. In Figure 6.10, for gap ratio greater than 3.0, the bottom boundary effect becomes negligible. For gap ratio 0.65<G/D<3.0, the range of synchronization is wider; synchronization starts earlier and ends later in terms of reduced velocity and with respect to the cases of gap ratio greater than 3.0, as shown in Figure 6.10 and Figure 6.38. For

gap ratio < 0.65, in comparison to gap ratio G/D > 3.0, it is observed that the onset of synchronization is more gradual than for G/D>3.0, where synchronization starts with a jump in A/D as shown in Figure 6.10 and Figure 6.38. The high amplitude oscillation in the range of synchronization shifts to higher reduced velocities (U*) as shown in Figure 6.10. In all cases, the range of synchronization extended to reduced velocity as high as 12. In some cases, the range of synchronization extended beyond the capacity of the LTFSW Channel and it wasn't possible to determine the end of synchronization.

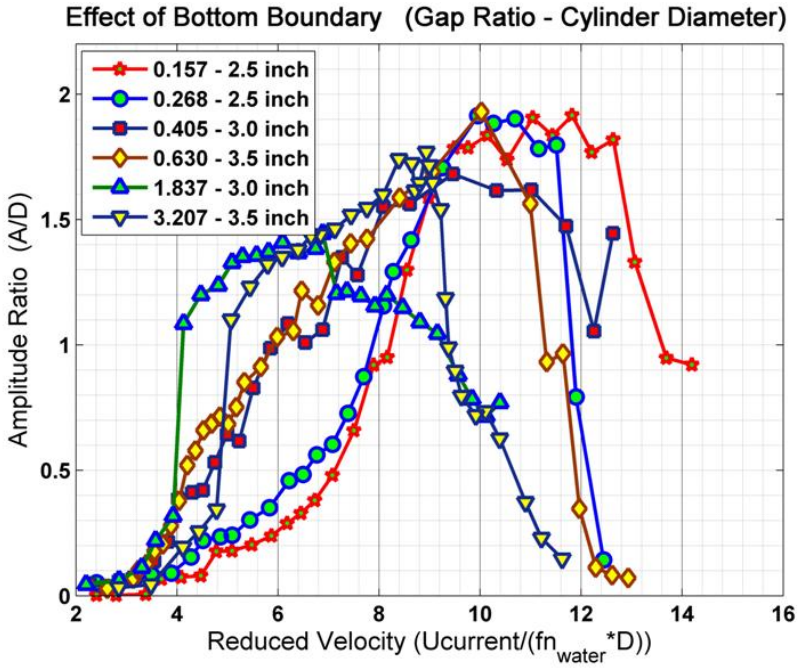

Figure 6.10 Amplitude ratio plotted as a function of reduced velocity for gap ratios G/D = 0.157-3.207.

The synchronization range exhibits an abrupt end (A/D jumps from very high values of oscillation to nearly zero value) for G/D = 0.63 and 0.268. In the case of unbounded VIV systems (G/D >3.0), the end of synchronization exhibits a gradual reduction, manifesting loss in correlation and detuning of frequency (see Figure 6.10). In our experiments for low gap ratios, the abrupt jump at the end of synchronization indicates a jump in the phase between vortex shedding forcing and displacement. A similar phase shift was observed at the beginning of the synchronization for unbounded cases (Williamson and Govardhan 2004). In our experiments, the lift force was not recorded to validate the above statement. In Figure 6.38 and Figure 6.30, the range of

synchronization didn't end for the cases where the gap ratio G/D was 0.157 and 0.405. For the other two cases, where gap ratio was 0.268 and 0.630, the synchronization regime ended abruptly.

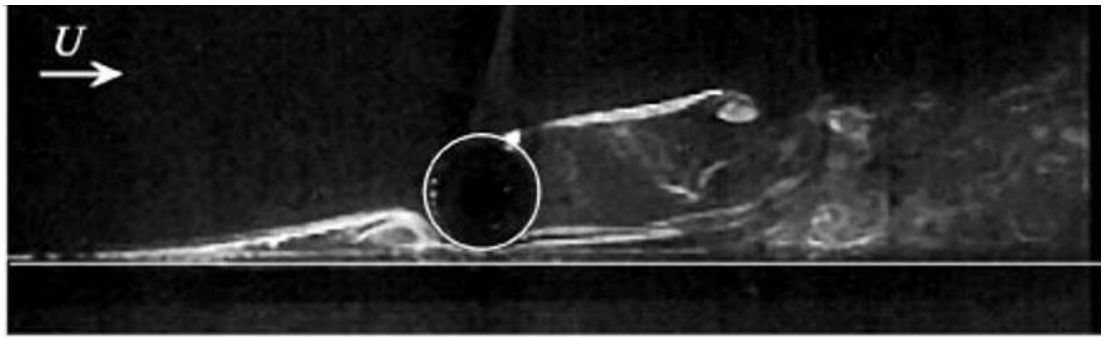

Figure 6.11. Flow visualization and PIV results for G/D = 0.125. [Reproduced from Price et al. (2002)].

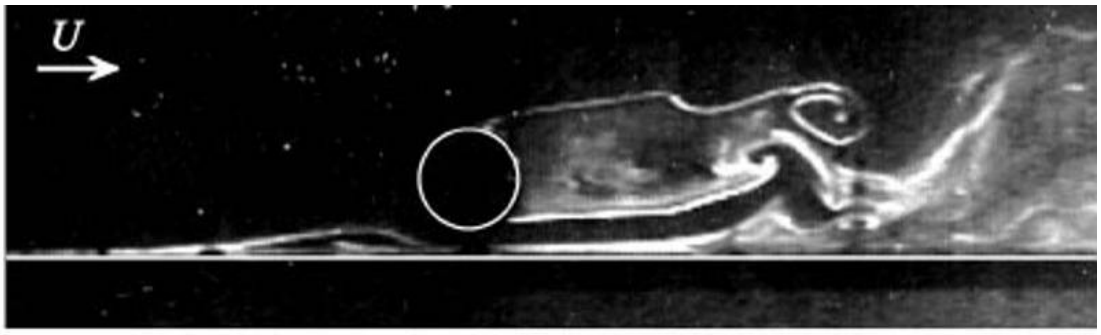

Figure 6.12. Flow visualization and PIV results for G/D = 0.25. [Reproduced from Price et al. (2002)].

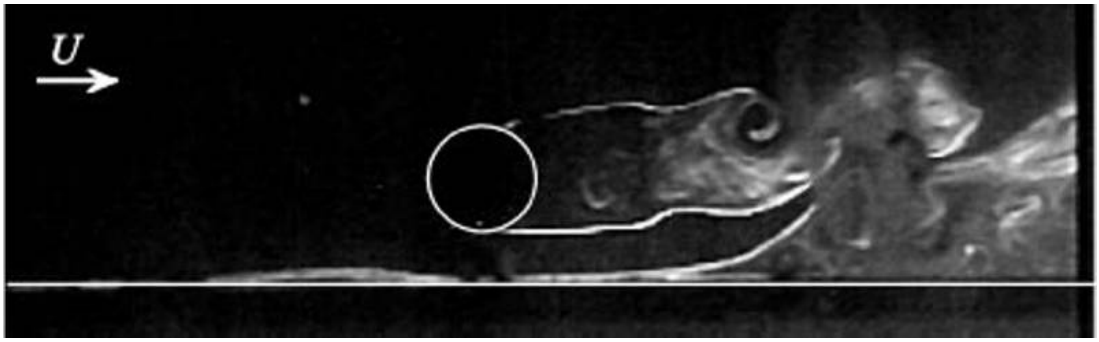

Figure 6.13. Flow visualization and PIV results for G/D = 0.5. [Reproduced from Price et al. (2002)].

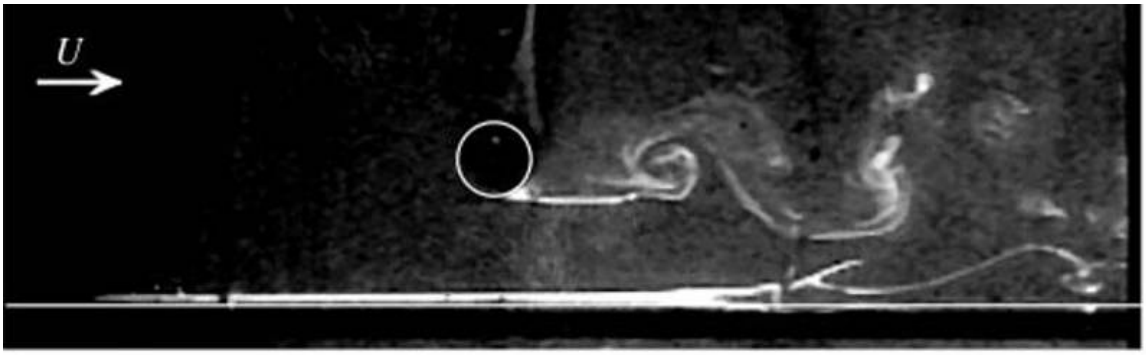

Figure 6.14. Flow visualization and PIV results for G/D= 1.5. [Reproduced from Price et al. (2002)].

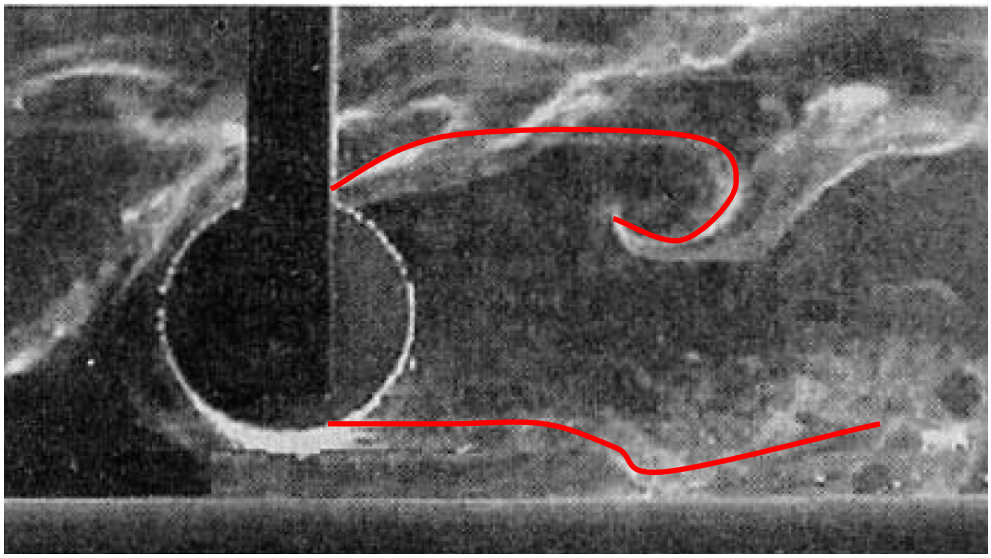

Figure 6.15. Vortex shedding at G/D =0.28, Re= 1.2×10^3. [Reproduced from Yang et al. (2006)].

6.4.2. Effect of bottom boundary on the amplitude of oscillation

The amplitude response of a cylinder in VIV at different gap ratios away from the bottom boundary is plotted in Figure 6.10. Typical time traces of A/D in the three regimes considered are shown in Figure 6.19, Figure 6.20, and Figure 6.21. In Figure 6.10 and Figure 6.19, it is observed that for gap ratio G/D > 3.0, the bottom boundary effect becomes negligible. For gap ratio 0.65<G/D<3.0, the amplitude of oscillation is reduced in magnitude but the positive and the negative amplitudes are symmetrical (see Figure 6.16) and the response is very similar to the cases where G/D > 3.0, as shown in Figure 6.10, Figure 6.17 and Figure 6.20. The reduction in the amplitude can be

attributed to the reduction in lift because of the partial development of the bottom vortex due to interference with the boundary layer of the bottom boundary, which interacts with the growth of vortices formed at the bottom of the cylinder, resulting in only partial circulation generation.

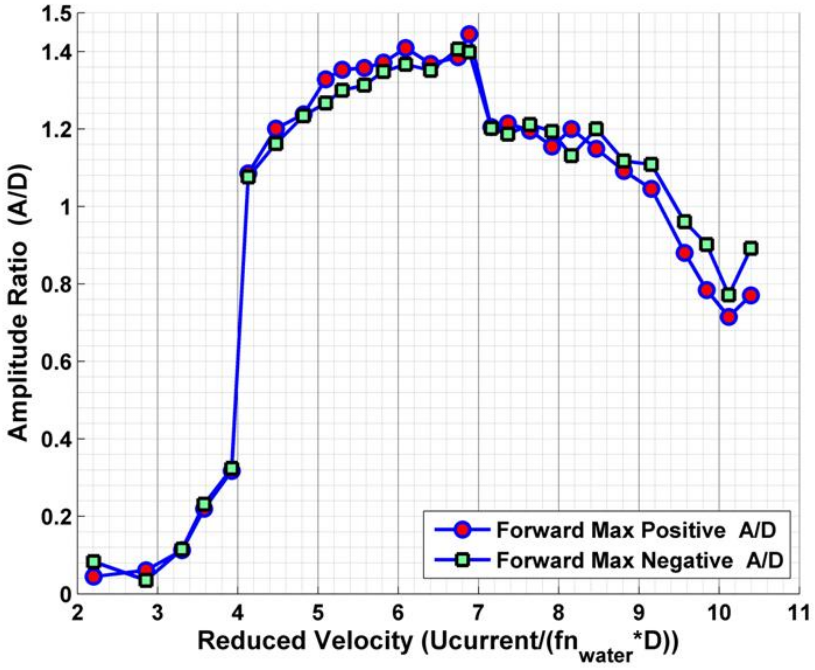

Figure 6.16. Both positive and negative maximum amplitude ratio plot versus the reduced velocity for gap ratio 1.873.

For gap ratio < 0.65, in comparison to gap ratio > 3.0, it is observed that the amplitude of oscillation grows gradually at the onset of synchronization and not with a jump as shown in Figure 6.10 and Figure 6.38. The ratio of amplitude of oscillation A/D at the top side reaches (positive amplitude) nearly 2 and it is higher than the values that observed for the unbounded cases. Such a high value of amplitude of oscillation can be argued to be due to the incomplete or non-generation of bottom vortices. Since the top vortex is less partially diffused by the opposite sign vorticity from the bottom vortex, the loss of vorticity is reduced (Bearman 1984; Gerrard 1966). This result in an increase in the strength of the top vortices compared to unbounded cases. The time series corresponding to G/D = 0.268 is shown in Figure 6.21. In Figure 6.21, the time series weren't

symmetrical as observed for the other two regimes of gap ratio G/D >3.0 and 0.65<G/D<3.0.

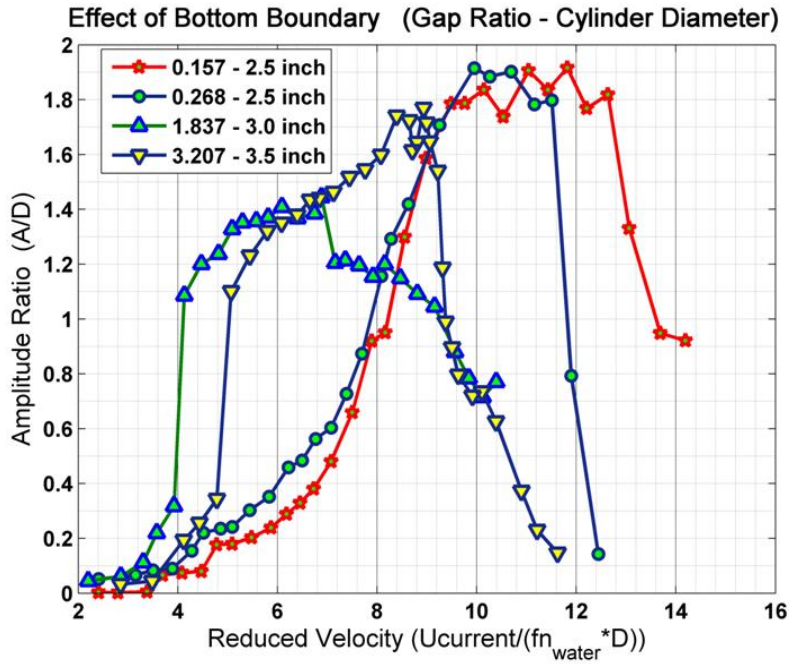

Figure 6.17. Amplitude ratio plotted as a function of reduced velocity for gap ratios 0.157, 0.268, 1.837, and 3.207.

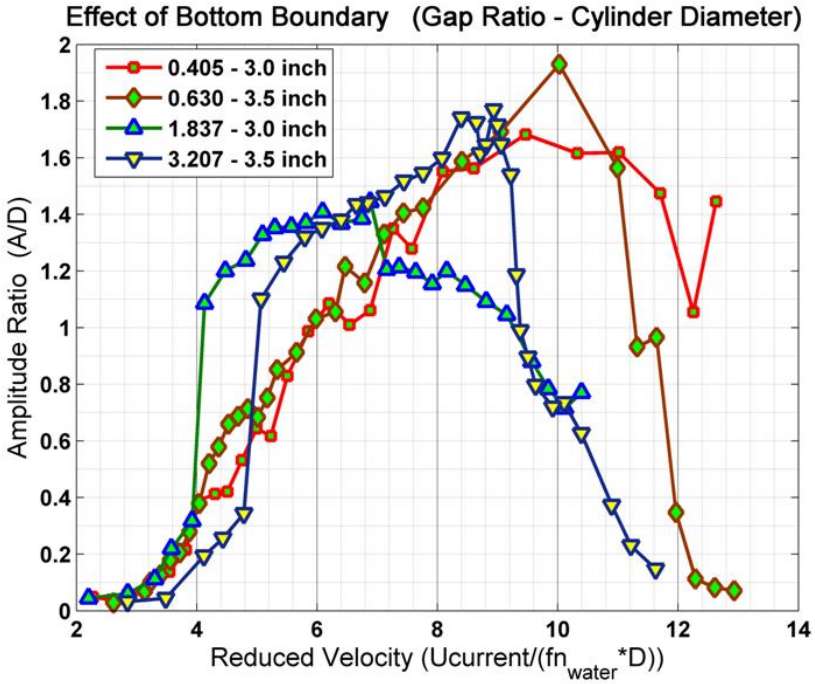

Figure 6.18. Amplitude ratio plotted as a function of reduced velocity for gap ratios 0.405, 0.630, 1.837, and 3.207.

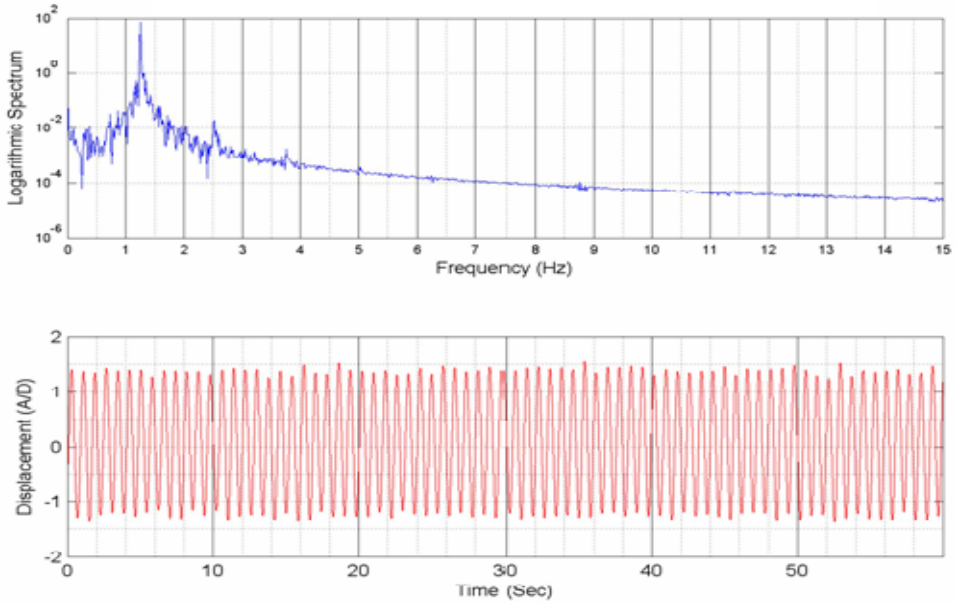

Figure 6.19. Frequency spectrum and time series plot of the displacement ratio at velocity 0.76 m/s (maximum amplitude achieved), for a gap ratio G/D = 4.18.

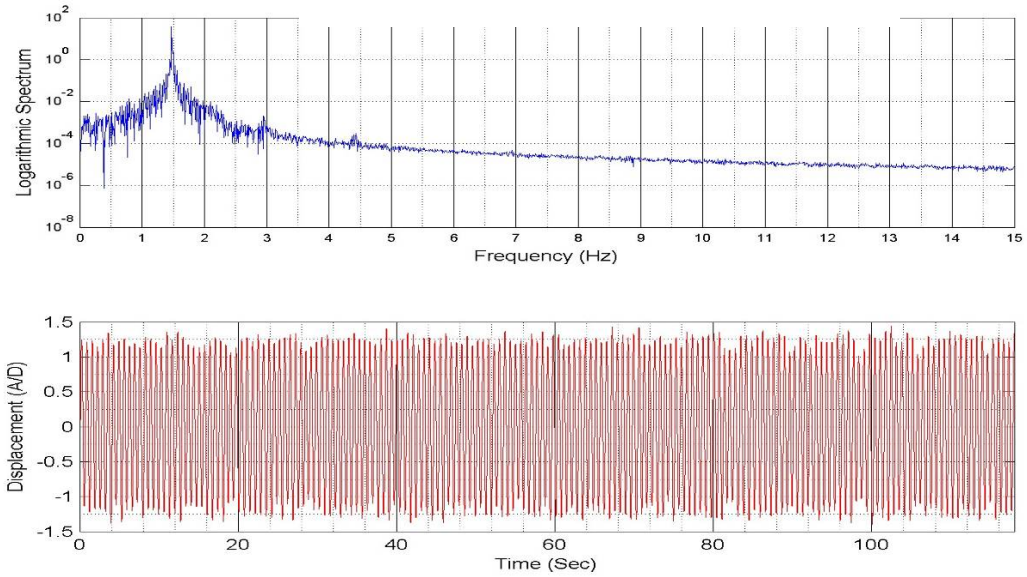

Figure 6.20. Frequency spectrum and time series plot of the displacement ratio at velocity 0.76 m/s (maximum amplitude achieved), for a gap ratio G/D = 1.84.

For gap ratio < 0.65, it is observed that the amplitude of oscillation has two kinds of response. In Figure 6.38, the growth A/D versus reduced velocity is concave for G/D = 0.405 and 0.63 and convex for G/D =0.157 and 0.268 and this is discussed later in Section 6.4.6.

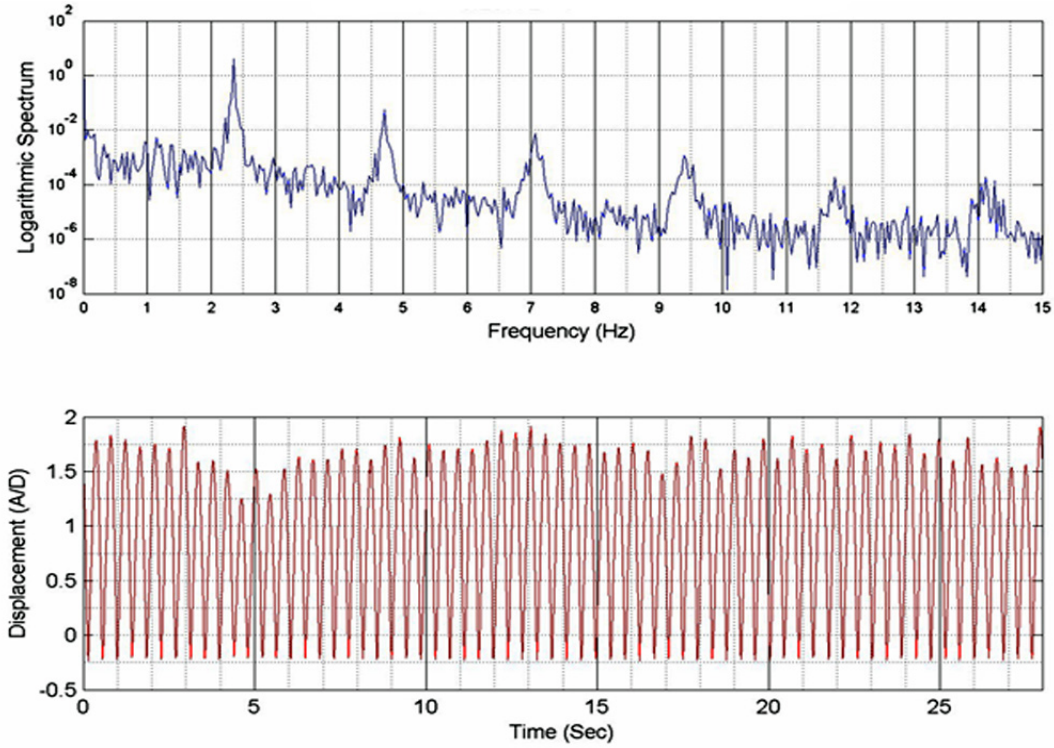

Figure 6.21. Frequency spectrum and time series plot of the displacement ratio at velocity 0.9 m/s, for a gap ratio G/D = 0.268.

6.4.3. Transition from initial branch to upper branch

Beginning of lock-in for a VIV system in unbounded fluid is associated with a jump in the phase between the vortex forcing and the cylinder cross-flow displacement (Bearman and Currie 1979; Bishop and Hassan 1964; Brika and Laneville 1993; Tanida et al. 1973). Ongoren and Rockwell (1988a), in their flow visualization experiment, observed that when a cylinder is forced to oscillate near or at $\frac{f_{excitation}}{f_{vs}} = 1$, the phase of the shed vortex jumps approximately by an angle π with respect to the cylinder displacement. Khalak and Williamson (1997a) later validated for free vibration experiments. When the cylinder vibrates in a flow, vortex shedding occurs at the outside of the cylinder at its maximum positions when $\frac{f_{vs}}{f_{n,water}} < 1$ (for a cylinder on an elastic support) during the initial part of lock-in illustrated in Figure 6.23. In this case, the lift forcing due to alternate shedding is in-phase with the cylinder motion. With further

increase of the flow velocity, the value of $\frac{f_{vs}}{f_{n,water}} \geq 1$ and it results in an abrupt change in the vortex shedding. This change manifests itself as the vortices shedding from the bottom part of the cylinder at its extreme positions. This is shown in Figure 6.22 and illustrated in Figure 6.23. Hence, an abrupt phase shift and the lift that ultimately becomes out-of-phase with the cylinder motion during lock-in is associated with VIV. Ongoren and Rockwell in their experiments observed that the phase jump does not occur if the cylinder has significant afterbody. This is because the jump in phase of the initially formed vortex can be prevented if the vortex formation length is increased, which can be achieved by a cylinder which has a significant afterbody length

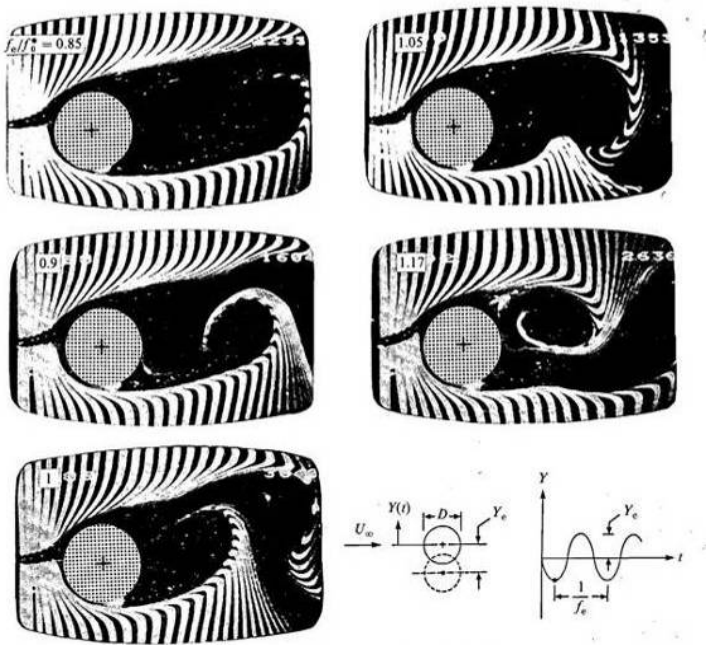

Figure 6.22. The switch in timing or phase of vortex shedding as vibration frequency increases with the body, at the top of its vertical motion (Ongoren and Rockwell 1988a).

For the cases of VIV of cylinder in close proximity to a boundary, the jump from initial branch to upper branch was not present as shown in Figure 6.10, Figure 6.38, Figure 6.17, and Figure 6.18. The slope of increase in amplitude is steady with an increase in velocity or reduced velocity as shown in Figure 6.38 and Figure 6.17. In the present case, the absence of the jump can be explained to be due to the absence of vortex

on the bottom side of the cylinder. At closer proximity to the rigid bottom boundary, the vortices are formed only at the top of the cylinder and are not formed at the bottom of the cylinder as shown in Figure 6.1, Figure 6.11, and Figure 6.12, The vortex formation length increases considerably when the cylinder in VIV approached the bottom boundary because there is no entrainment of flow due to the absence of the bottom vortices as shown in Figure 6.1, Figure 6.11, and Figure 6.12. This result in an increase in vortex formation length above the minimum value of the length required for the phase shift in the vortex shedding process in lock-in.

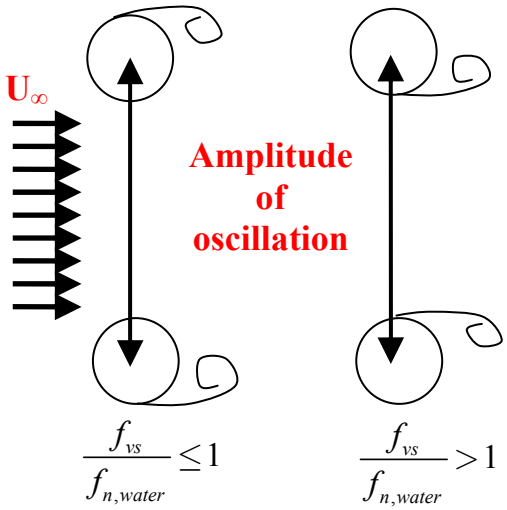

Figure 6.23. Schematic representation of the shift in the timing of vortex shedding, with the body at the top of its vertical motion.

6.4.4. Frequency spectrum

In our experiments, frequency spectral analysis of the cross-flow displacement of the cylinder in VIV reveals higher frequency components (Figure 6.21). The frequency components can be due to the chopping of the negative displacement due to the bottom boundary. In Figure 6.24, a sinusoidal function with snipped negative displacement is plotted. The Fourier spectrum for that time history gave higher harmonic components which were not present in the time trace. In Figure 6.25, the Fourier spectrum of the previous time trace (Figure 6.24) was superimposed with second harmonic time trace. It also shows higher harmonic components with more power. This difference in power,

however, doesnot help in establishing the presence of a vortex mode with a larger number of vortices. Conclusive result can be achieved through flow visualization only.

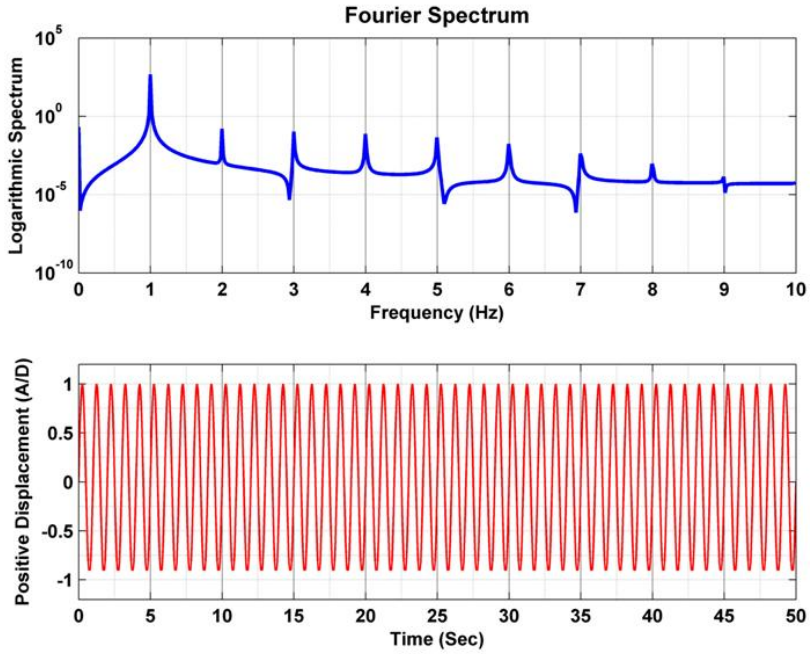

Figure 6.24. Frequency spectrum and time series plot where positive displacement is.sin(2πt) for sin(2πt)>-0.9 and zero for sin(2πt)≤ -0.9.

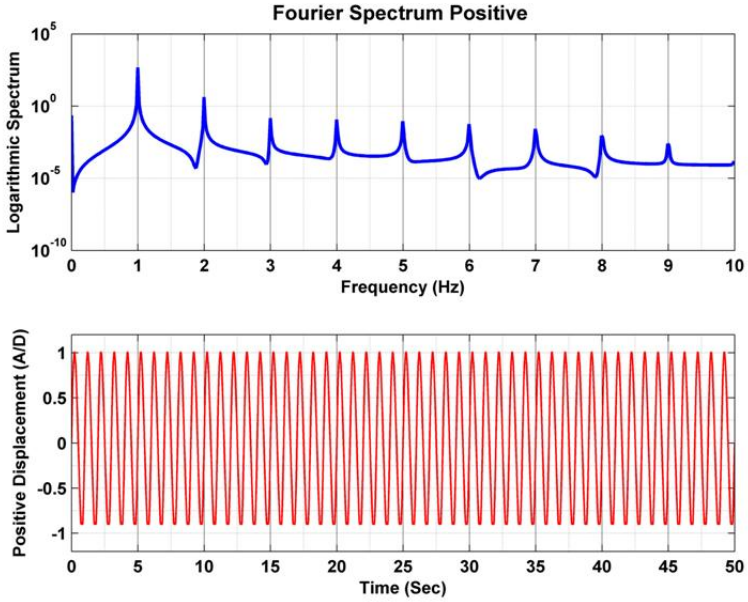

Figure 6.25. Frequency spectrum and time series plot where positive displacement is.sin(2πt)+ 0.1×sin(4πt) for sin(2πt)>-0.9 and zero for sin(2πt)≤ -0.9.

6.4.5. Frequency of oscillation

In Figure 6.26, the frequency responses for the cross-flow displacement of the cylinder in VIV for different gap ratios are compiled. In this figure, the ratio of the frequency of oscillation to the natural frequency in water is plotted versus reduced velocity. The nature of frequency response changes with the gap ratio G/D. For gap ratio greater than 3, the frequency response curves are the same in the synchronization regime. As the gap ratio reduced, the frequency response curve tended to move closer to the Strouhal line. In the case of lower gap ratios, the response frequency locked-on to the Strouhal shedding frequency rather than to the natural frequency as in the case of higher gap ratios. It is observed that at a reduced velocity value of 10, the frequency response curve tends to arch down to the frequency ratio value of one. Abrupt end in synchronization is observed when the frequency response ratio archs down to one. Probably, there is a phase shift or jump associated with arching down to the value one as in the case of the beginning of synchronization for VIV in unbounded fluid. It is hypothesized that such phase shift would result in abrupt end of synchronization.

For lower gap ratio G/D < 0.65, the f_{osc} follows the Strouhal frequency until U* ≈ 10 where its response separates towards frequency ratio 1 or 2, or follows the Strouhal frequency line as shown in Figure 6.26. In the first two cases, the range of synchronization extends further as shown in Figure 6.10, Figure 6.38, and Figure 6.17. In the case of G/D=0.157, it locks-on to the second harmonic of natural frequency in water (Figure 6.39). At high reduced velocity the maximum amplitude ratio has high value A/D ≈ 2 (Figure 6.38 and Figure 6.40), but the system is desynchronized for reduced velocity U*>12. The high amplitude ratio observed is due to intermittent jump in the response. The time series for reduced velocity greater than 12 and G/D = 0.157 is shown in Figure 6.27. In the case of G/D=0.405, it approaches the natural frequency in water (Figure 6.26 and Figure 6.31) and the system maintains higher amplitude and the end of the synchronization range wasn't observed (Figure 6.10, Figure 6.38, and Figure 6.30) within the limits of the LTFSW Channel. A possible explanation is that the frequency response did not completely reach the value of natural frequency in water. Once the frequency response equalizes with the natural frequency in water, the VIV response may become desynchronized. This was observed in the the cases where the synchronization range

ended abruptly when the frequency of oscillation reached the harmonics of natural frequency in water (Figure 6.10). The velocity could not be increased because of the limitation of the LTFSW Channel and the above statement wasn't checked.

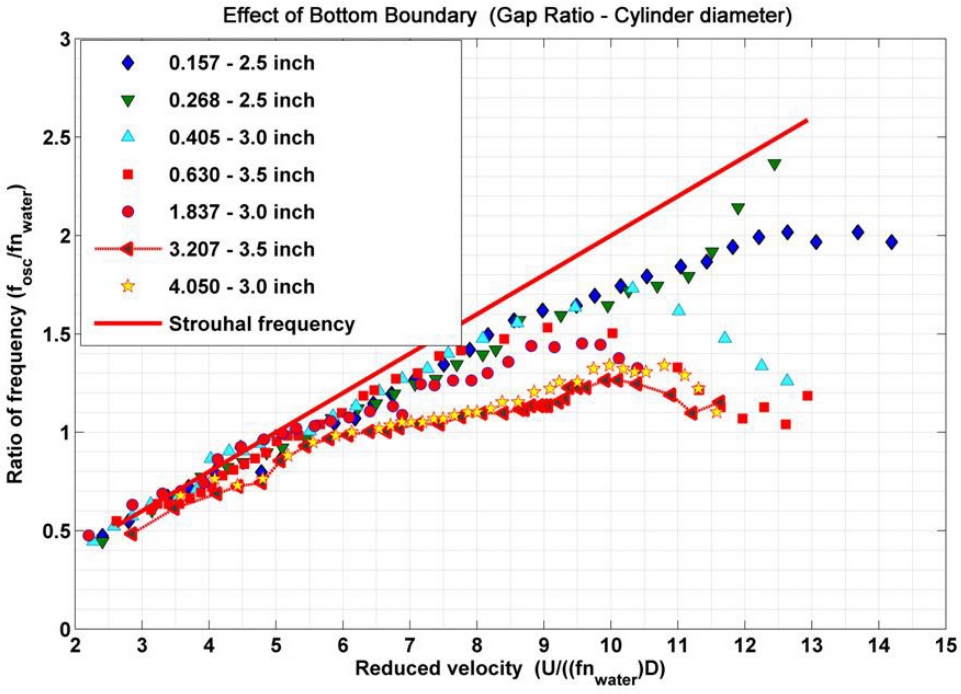

Figure 6.26. Compiled plot of the ratio of frequency of oscillation to the natural frequency in water versus reduced velocity for various gap ratio values.

The abrupt jump in amplitude at the end of synchronization (G/D = 0.157, 0.630, and 0.268) may be due to the frequency of response reaching the harmonic component of the natural frequency in water. Coincidence of the frequency of response and the harmonic component of the natural frequency in water would result in a phase shift between the forcing due to vortex shedding and displacement. Similar phase shift is observed in the case of a jump from initial branch to upper branch in unbounded VIV system (Ongoren and Rockwell 1988a). The phase shift is associated with the change in the phase of vortex shedding with respect to the displacement (Figure 6.22 and Figure 6.23). In the case of a cylinder in VIV closer to the bottom boundary, the shift in phase, when the frequency of response f_{osc} and the harmonic component of the natural frequency in water f_{nwater} coincide. This results in very low strength bottom vortices being shed from inner side of the cylinder (less forcing) and thus resulting in abrupt suppression of VIV.

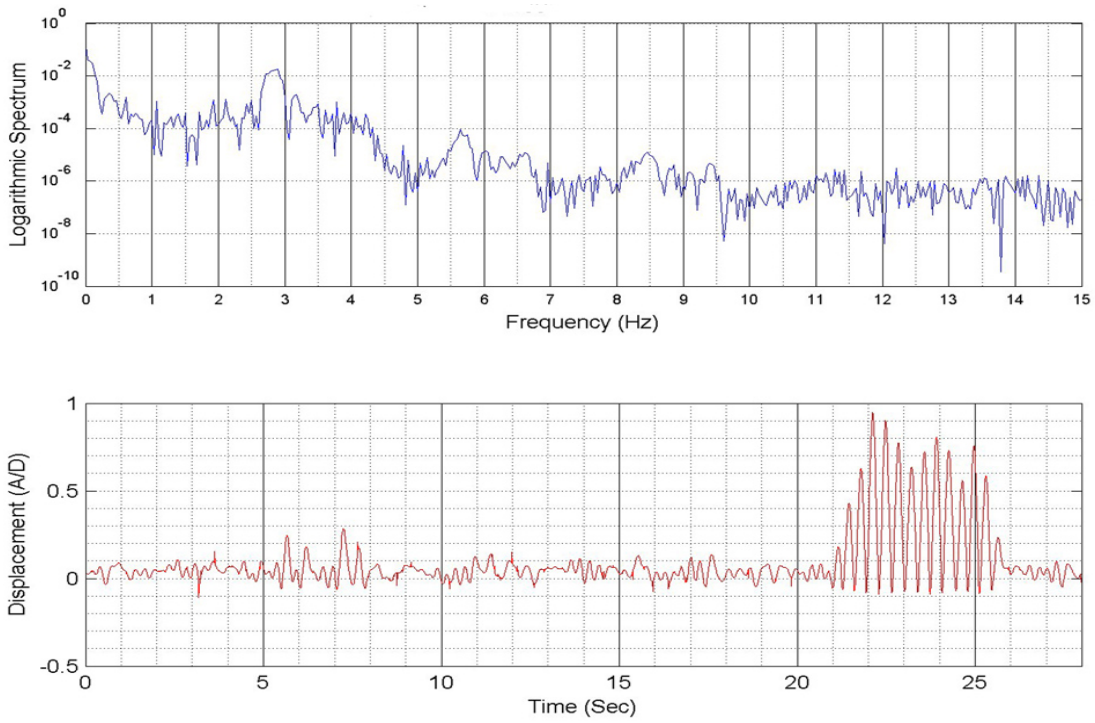

Figure 6.27. Frequency spectrum and time series of displacement ratio at velocity U = 1.25 m/s, for a gap ratio G/D = 0.157.

In the case of G/D =0.63, the frequency ratio increases until a value of 1.5 ($\frac{f_{osc}}{f_{n,water}} = \frac{3}{2}$) and the corresponding reduced velocity value is 9. Then the frequency ratio starts decreasing with increase in reduced velocity above 10 as shown in Figure 6.29. In the range where the frequency ratio is decreasing, the amplitude ratio starts decreasing drastically as shown in Figure 6.28.

In the case of G/D =0.405, the frequency ratio increases until a value of 1.75 ($\frac{f_{osc}}{f_{n,water}} = \frac{7}{4}$) and the corresponding reduced velocity value is 10.2. Then the frequency ratio starts decreasing with increase in reduced velocity above 10.2 as shown in Figure 6.31. In the range where the frequency ratio is decreasing, the amplitude ratio nearly remains the same until the frequency ratio reaches 1.5 ($\frac{f_{osc}}{f_{n,water}} = \frac{3}{2}$). When the frequency ratio reaches 1.5, the amplitude ratio reduces drastically at 1.5 and as the reduced velocity increases, the frequency decreases. But the amplitude ratio starts increasing as shown in Figure 6.30.

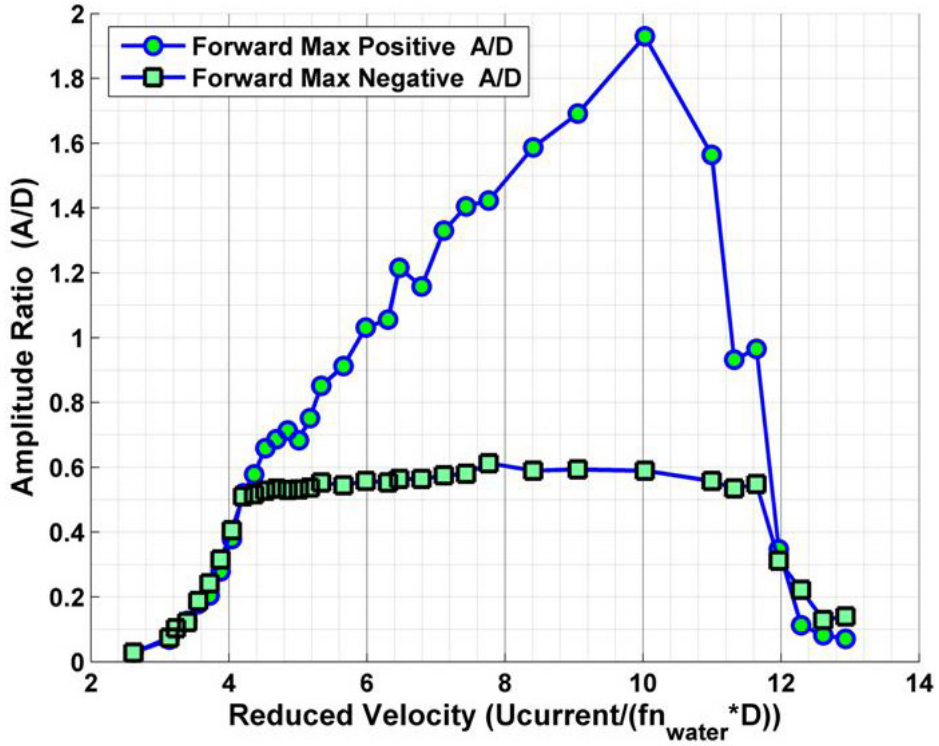

Figure 6.28. Positive and negative maximum amplitude ratio versus the reduced velocity for gap ratio, G/D = 0.63.

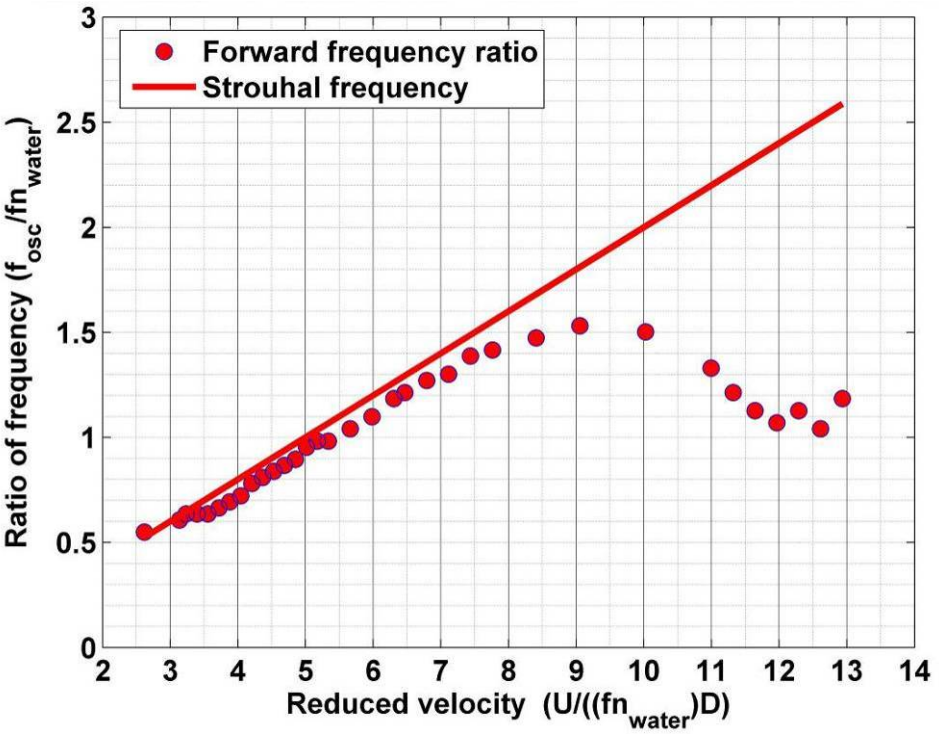

Figure 6.29. Ratio of frequency of oscillation to natural frequency in water versus the reduced velocity for gap ratio G/D = 0.63.

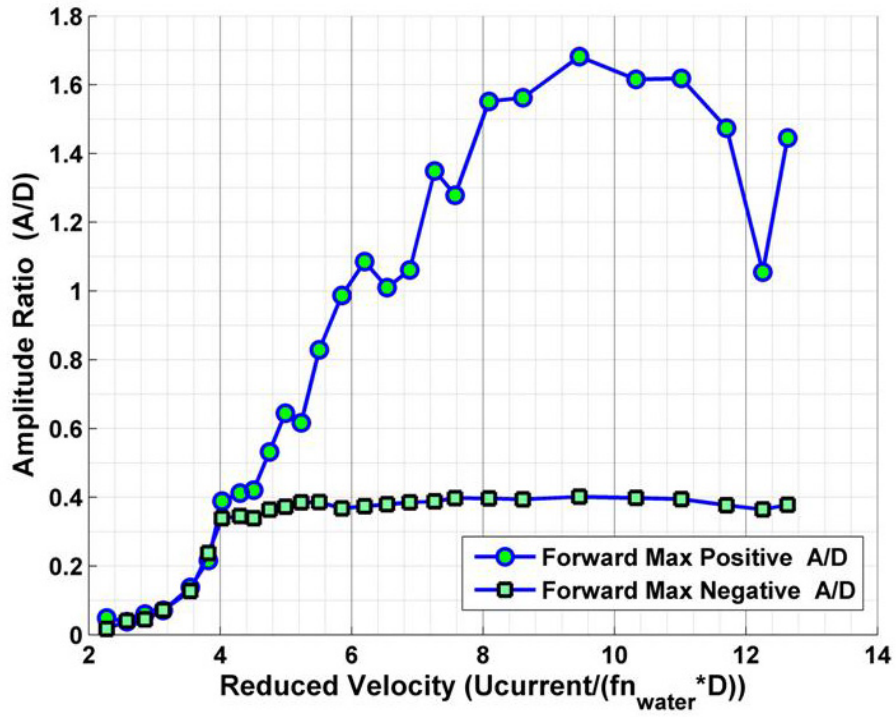

Figure 6.30. Positive and negative maximum amplitude ratio versus the reduced velocity for gap ratio, G/D = 0.405.

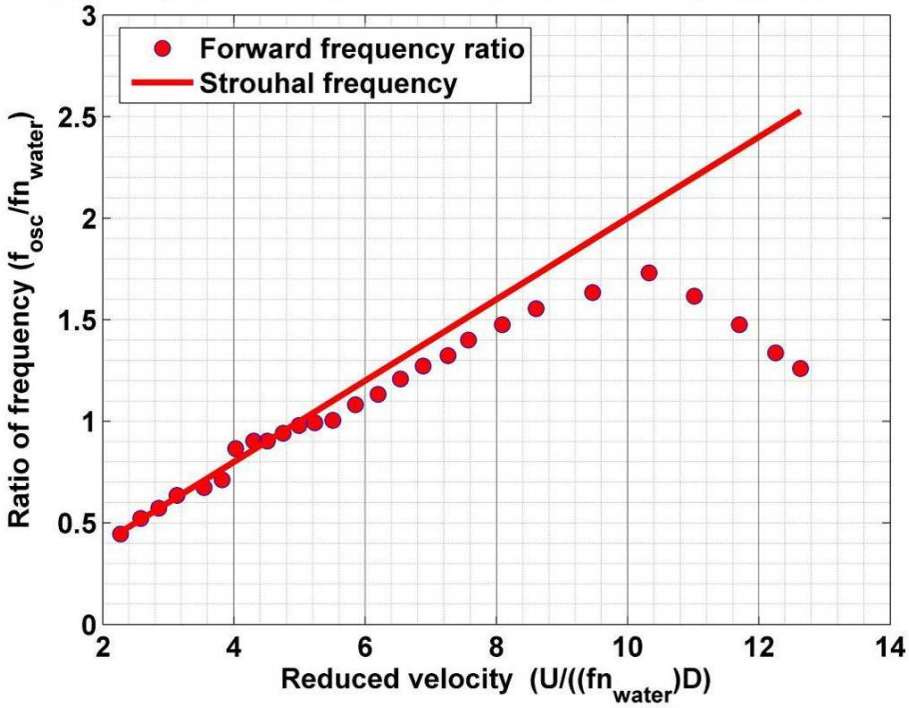

Figure 6.31. Ratio of frequency of oscillation to natural frequency in water versus the reduced velocity for gap ratio G/D = 0.405.

In the case of G/D =0.268, the frequency ratio keeps increasing along with the Strouhal line with a slope of 0.175 rather than 0.2. At a reduced velocity value of 8.2, the straight line trend breaks and the frequency tries to modulate and lock-in with the second harmonic natural frequency in water as shown in Figure 6.33. In the range of steady growth, the amplitude grows steadily and it is more like a linear system as shown in Figure 6.10, Figure 6.17, and Figure 6.32. As the reduced velocity increases above 10, the frequency ratio breaks away from the modulation and joins with the Strouhal line. During this range, the amplitude ratio plummets from high amplitude ratio of 1.8 to nearly zero amplitude of oscillation as shown in Figure 6.32.

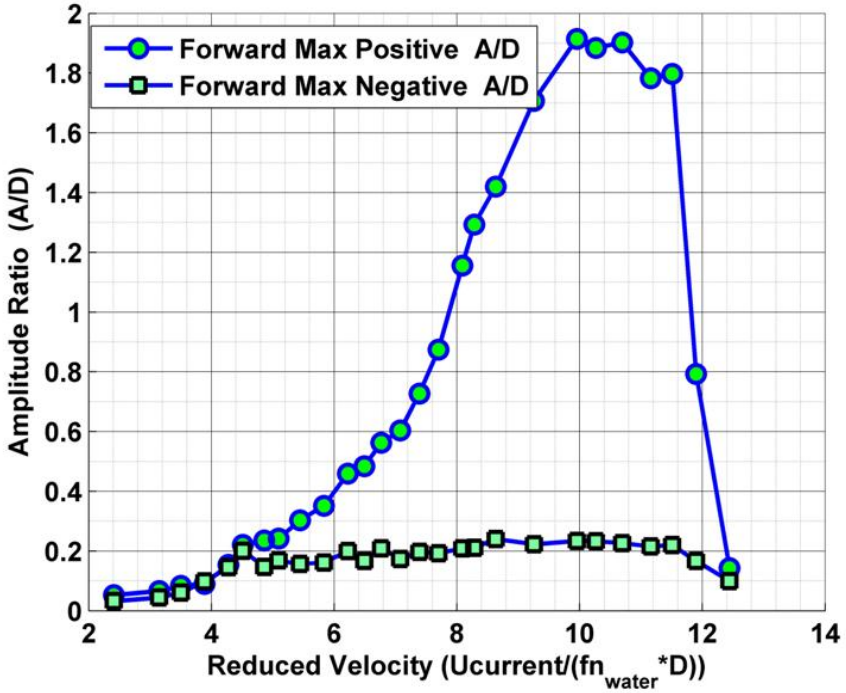

Figure 6.32. Positive and negative maximum amplitude ratio versus the reduced velocity for gap ratio, G/D = 0.268.

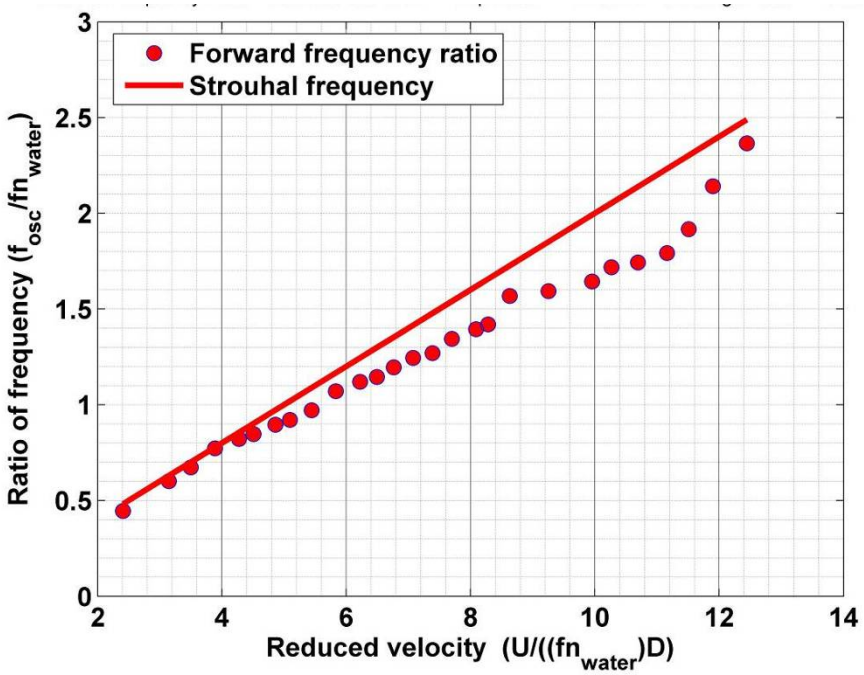

Figure 6.33. Ratio of frequency of oscillation to natural frequency in water versus the reduced velocity for gap ratio G/D = 0.268.

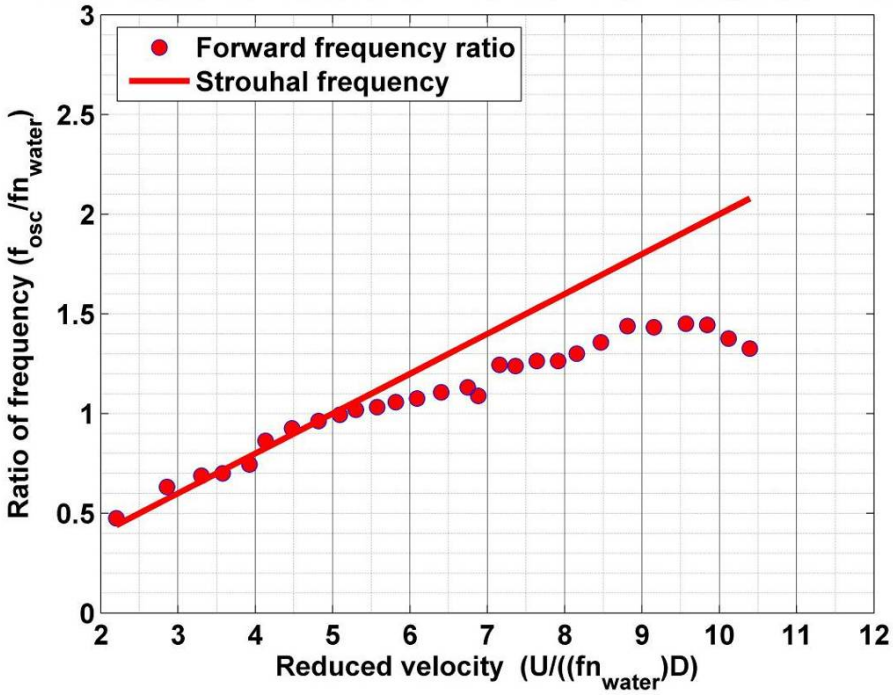

Figure 6.34. Ratio of frequency of oscillation to natural frequency in water versus the reduced velocity for gap ratio G/D = 1.87.

In the case of G/D =0.157, the frequency ratio keeps increasing along with the Strouhal line with a slope of 0.175 rather than 0.2. At a reduced velocity value of 9.0, the

straight line breaks the trend and the frequency of oscillation curves to lock-in with the second harmonic natural frequency in water as shown in Figure 6.39. In the range of steady growth, the amplitude grows steadily and it is more like a linear system as shown in Figure 6.10, Figure 6.17, and Figure 6.40. As the reduced velocity increases above 12, the frequency ratio locks-in with the second harmonic natural frequency in water. The frequency ratio reached a plateau at a value of 2. This lock-in of the frequency is associated with a jump in the amplitude ratio to a lower value. This behavior can be hypothesized as a phase shift in the shedding pattern. This could result in a sudden reduction in amplitude and this is similar to the jump observed from initial to upper branch. For this range, the amplitude ratio plummets to a nearly zero value but the maximum amplitude ratio (Figure 6.40) doesn't exhibit such behavior. The displacement is plotted in Figure 6.27 to show that there is intermittency in the character of displacement jumping between low and high amplitude of oscillation.

6.4.6. Boundary layer thickness

Proximity of the cylinder to the plate boundary brings the plate boundary layer and the cylinder's boundary layer and makes close enough for interference. The boundary layer transition of the plate usually occurs around the critical Reynolds number of 5×10^5 depending on the flow conditions and the surface of the plate. For preliminary calculations and simplicity, the thickness of the plate boundary layer is calculated assuming that the transition occurs at $Re_{plate} = 5 \times 10^5$. This results in an abrupt jump as shown in Figure 6.35, which is not true in reality.

The parameters are calculated using the formulaes in the Viscous fluid flow text book (White 1974). A summary of the formulae used is provided in the table below.

Quantity	Laminar	Turbulent
Boundary Layer Thickness	$5 \times Re^{-1/2}$	$0.14 \times Re^{-1/7}$
Displacement Thickness	$1.721 \times Re^{-1/2}$	$0.018 \times Re^{-1/7}$
Momentum Thickness	$0.664 \times Re^{-1/2}$	$0.0142 \times Re^{-1/7}$

Table 6.1. Boundary layer thickness for flat plate. Transition is assumed to occur at $Re = 5 \times 10^5$.

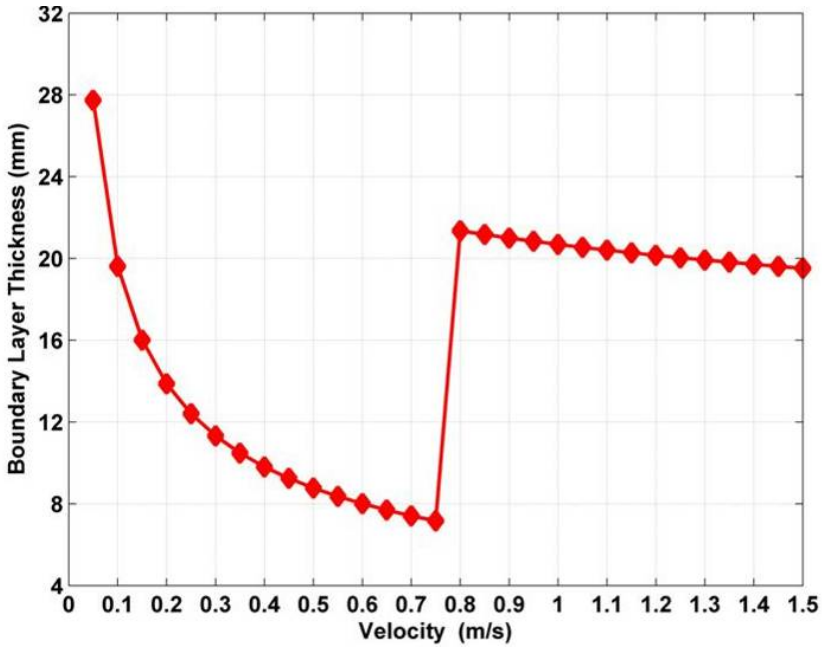

Figure 6.35. Boundary layer thickness on the plane bottom boundary where the cylinder is placed (0.65 m). At U = 0.75 m/s transition occurs from laminar to turbulent flow.

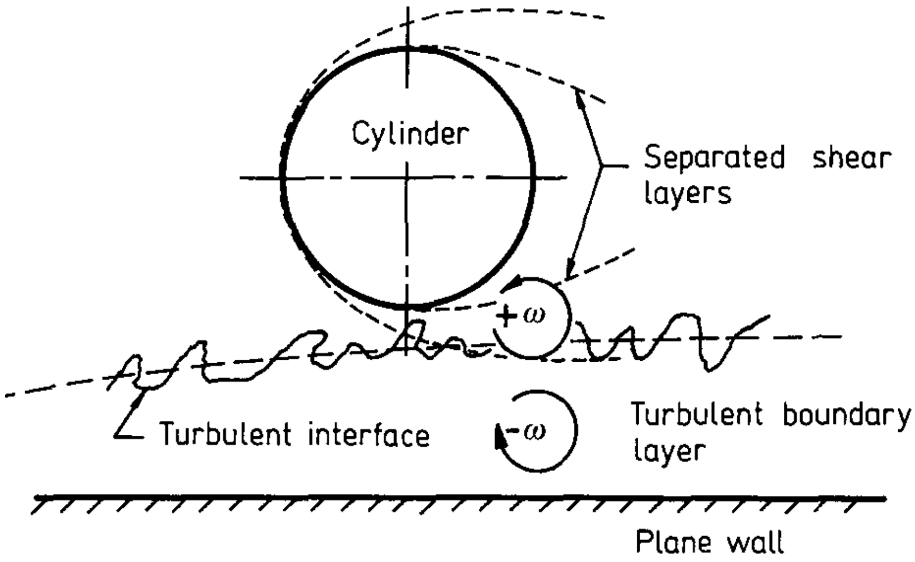

Figure 6.36 Schematic presentation of the interference mechanism between cylinder and wall (Taniguchi and Miyakoshi 1990).

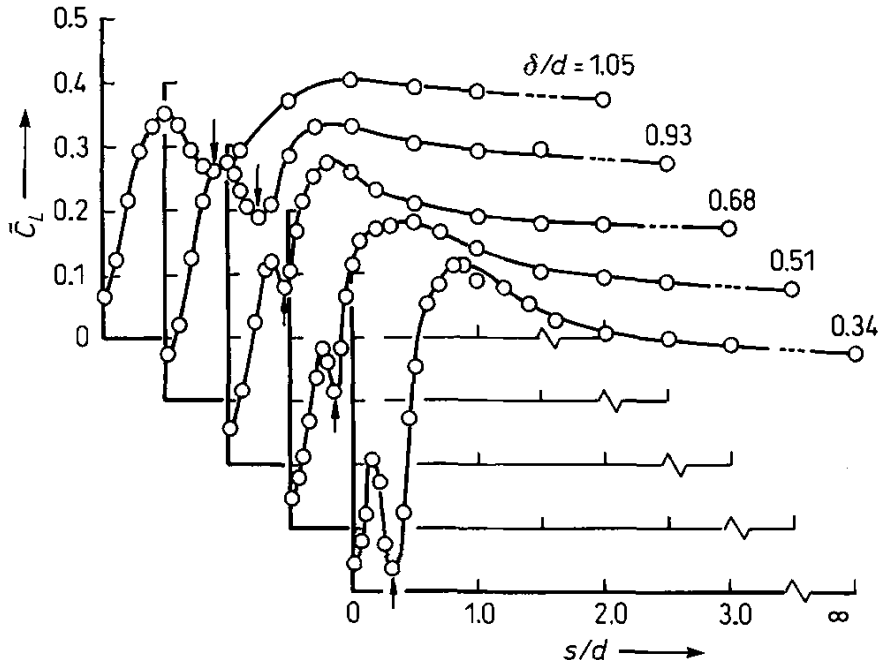

Figure 6.37. Fluctuating lift force versus gap height (Taniguchi and Miyakoshi 1990).

For a stationary cylinder near the bottom boundary, Taniguchi and Miyakoshi (1990) argued that the formation of two sided Kármán vortex streets can be abruptly disrupted when the outer part of the turbulent boundary layer of the bottom boundary comes in contact with the bottom surface of the cylinder. They called that gap value as critical value. Further, they argued that the suppression of the vortex at the bottom of the cylinder is due to the partial cancellation of vorticity in the separated shear layer from the cylinder by the opposite vorticity from the boundary layer of the bottom boundary. This effect is augmented by the interference of the turbulent eddies produced intermittently in the turbulent boundary layer of the plate into the outer layer of the separated shear layer of the cylinder. At gaps smaller than the critical value, the Kármán vortex street is not formed and only a one-sided vortex sheet is formed at the top of the cylinder. This results in strong reduction of the fluctuating fluid forces (Taniguchi and Miyakoshi 1990) for gap ratio smaller than the critical value. Price et al. (2002) observed in their experiments that opposite signed vorticity did not cancel out. They proposed that the inhibition of the regular Kármán vortex shedding was not likely to be due to the cross cancellation of the opposite vorticity from the boundary layer of the bottom boundary and the cylinder.

According to Price et al. (2002) there was a significant pairing between the vortices from the bottom of the cylinder and the bottom boundary.

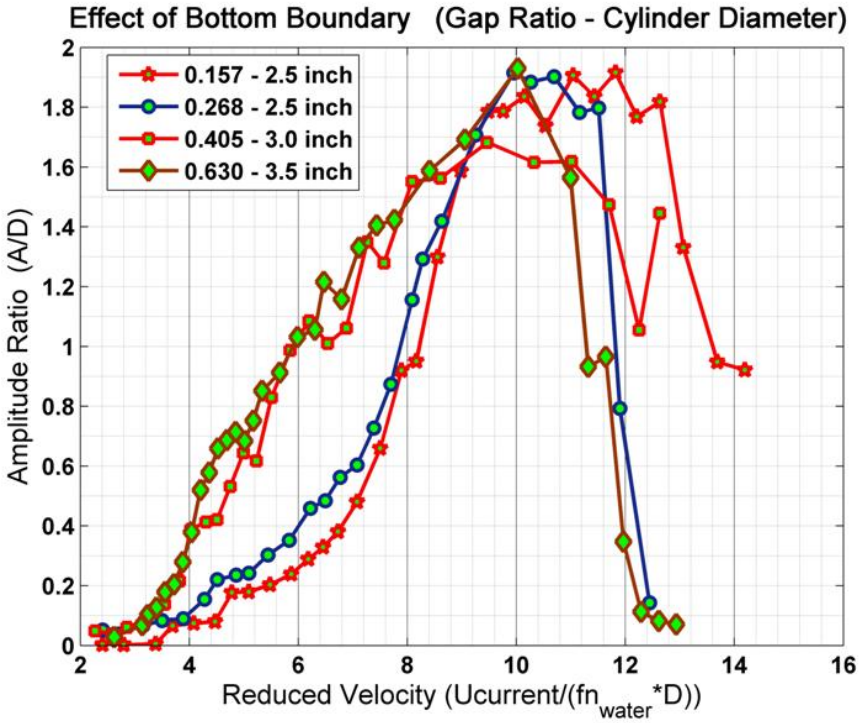

Figure 6.38. Amplitude ratio plotted as a function of reduced velocity for gap ratios 0.157, 0.268, 0.405, and 0.630.

In Figure 6.38, the growth in the amplitude response versus reduced velocity is concave for G/D = 0.405 and 0.623 and convex for G/D =0.157 and 0.268. In our experiments, the boundary layer thickness ratio δ/D (δ = 20mm) calculated was comparable the gap ratio for the case G/D = 0.157 (G = 10 mm), and G/D = 0.268 (G = 17mm) after transition. In the other two cases G/D = 0.405 (G = 30 mm) and 0.63 (G = 57 mm), the boundary layer thickness ratio δ/D (δ = 20mm) was smaller in comparison to the gap ratio. The difference in interaction between the boundary layer at the rigid bottom boundary and the vortex formation process might be the reason for the concavity in the growth of the amplitude response versus reduced velocity for G/D = 0.405 and 0.623 and convexity for G/D =0.157 and 0.268 (see Figure 6.38). The interaction of the boundary layer of the plate with the shear layer emanating from the bottom of the cylinder at low gap ratios depends on the state of the boundary layer (Lei et al. 1999; Taniguchi and Miyakoshi 1990). The mechanism of interaction of the bottom boundary layer with the

shear layer emanating from the bottom of the cylinder are not fully understood. Since no visualization was done in the present experiments, no definite conclusion can be made on the difference observed.

6.4.7. Hysterisis

Through out the present high damping VIV experiments, the classical hysterisis occurring at the beginning of synchronization range were not observed. At lower gap ratios, hysterisis is observed at the end of synchronization as shown in Figure 6.39, and Figure 6.40. At low Reynolds number VIV experiments, hysterisis occurs at the end of synchronization (Klamo 2006). The Bottom Induced Hysterisis (BIH) occurs at the end of synchronization and it prevails till the beginning of the synchronization as the velocity is reduced (going backwards). A detailed visualization study is required to understand the hysterisis at the end of synchronization.

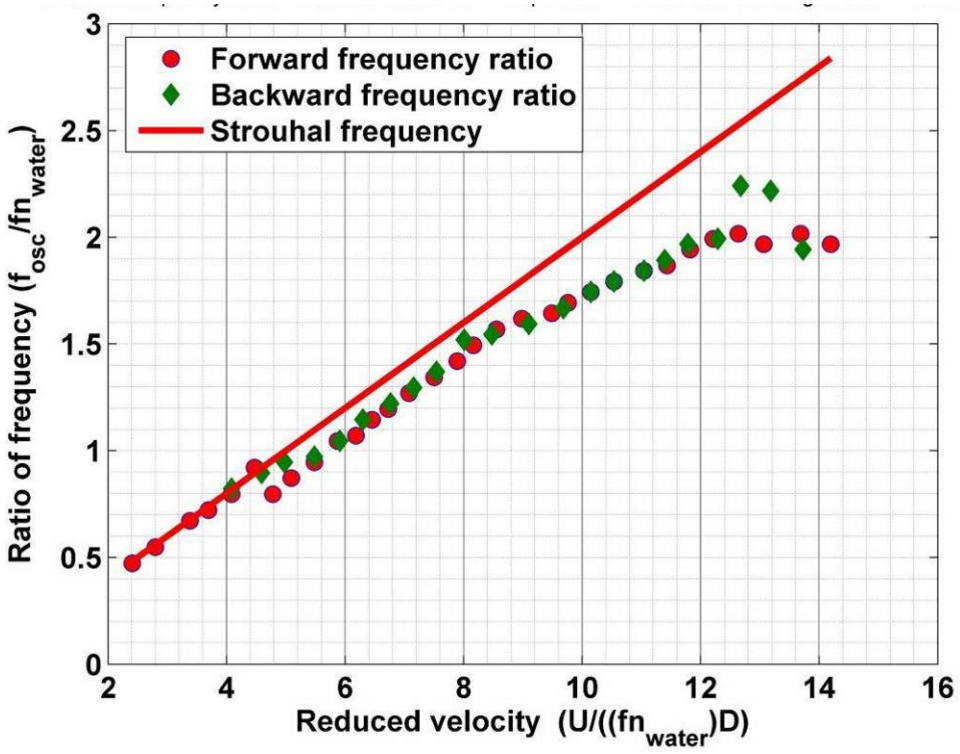

Figure 6.39. The ratio of frequency of oscillation with the natural frequency in water for both forward and backward velocity is plotted versus the reduced velocity for gap ratio 0.157.

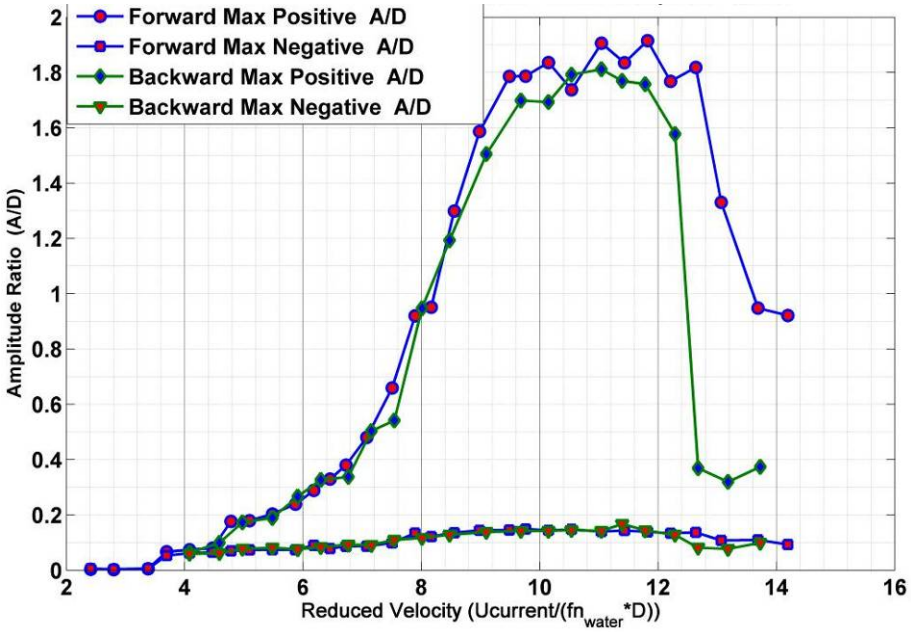

Figure 6.40. Hysterisis observed at the end of synchronization when maximum amplitude ratio for forward and backward velocity plotted versus the reduced velocity for gap ratio 0.157.

6.5. MAIN FINDINGS

VIV tests in the LTFSW Channel of the University of Michigan for Reynolds number in the range of [8×10^3 -1.5×10^5] have shown unmistakably the strong dependence of VIV of cylinders on proximity to a bottom boundary.

1. For gap ratio > 3.0, bottom boundary affect on VIV is negligible.
2. For gap ratio < 0.65, in comparison to gap ratio > 3.0, we observe the following:
    a. The positive amplitude of oscillation reached a maximum value of 2 diameters.
    b. The increased positive amplitude of oscillation is probably due to non-generation of bottom vortices. Thus, the top vortex strength increases since the top vortex is not partially diffused by the bottom vortex.
    c. The onset of synchronization is smoother than for G/D>3.0, where synchronization starts with a jump in A/D.
    d. The range of synchronization shifts to higher reduced velocities (U*).
    e. f_{osc} follows the Strouhal frequency until U*≈10, and above U*≈10 may follow three different paths. The frequency response either tries to lock on

to the natural frequency of the system in water, or second harmonic, or it follows the Strouhal frequency for stationary cylinder. In the first two cases, the range of synchronization extends further.

f. Boundary layer on the rigid bottom boundary plays an important role in the VIV response.

3. For $0.65<G/D<3.0$, the range of synchronization is unaffected but the amplitude of oscillation is reduced probably due to partial strength of the bottom vortex.
4. Occurrence of hysterisis:
    a. In all the present high damping VIV experiments, the classical hysterisis occurring at the beginning of the synchronization range was not observed.
    b. For $G/D < 0.65$, hysterisis was observed.
    c. Bottom induced hysterisis (BIH) occurs at the end of the synchronization.
    d. When BIH occurs, lock-in may result in $f_{osc}= f_{n,water}$ or $2* f_{n,water}$.

Chapter 7

EFFECT OF STRATEGICALLY DISTRIBUTED ROUGHNESS ON VIVACE

7.1. BACKGROUND

Control of vortex shedding around a bluff body has been a topic of interest for a long time. The benefits that are gained by the control of vortex shedding have been of interest in many fields such as ocean engineering, aerospace, control rods, pipelines, transmission wires, smoke stacks and etc.. In ocean engineering it's the suppression of vortex shedding that has been a topic of interest because of the detrimental effect of vortex induced vibration on the risers and underwater pipelines. On the other hand, the aerospace industry is interested in areas like lift enhancement, separation control, drag reduction, noise and vibration control. The control of vortex shedding can be achieved by both active and passive control. We will discuss only the passive-control of VIV giving emphasis on amplification of VIV.

Review on suppression of vortex shedding has been provided by (Zdravkovich 1981). He broadly classifies means for suppressing vortex shedding into three categories:

1. Disturbing the spanwise correlation, e.g. helical strakes, wires, studs or spheres, wavy separation body etc
2. Affecting the shear layer emanating at both the sides of the bluff body, e.g shrouds.
3. Preventing the interaction of the entrainment layer, e.g splitter plate, base-bleed.

In this dissertation alteration of the spanwise correlation using surface protrusion is studied. Effect of protrusions like thin wires and rough sand paper on stationary cylinders were first studied by (Fage and Warsap 1929). They noticed that for certain configurations of protrusions the distribution of pressure was altered and drag force was reduced. It was shown by (Naumann et al. 1966) that attaching broken separation wires staggered along the surface introduces reduction in the spanwise correlation by three-dimensional geometric disturbance. Reducing the spanwise correlation along the separation lines or shear layers correlated vortex shedding and the alternating force acting on the cylinder are weakened. Naumann et al. (1966) also showed that by attaching a continuous separation wire the correlation length increased and regular vortex shedding was observed even at critical Reynolds number.

Few researchers have used roughness strips to simulate high Reynolds number flow (Nakamura and Tomonari 1982) and to reduce the drag force on the circular cylinder (He et al. 2002).

In this dissertation, an experimental investigation on the fluid flow past an elastically mounted circular cylinder with two rectangular strips on the surface of the cylinder was conducted. Depending on the strip's width, roughness particle size, and location, response was of distinctly different character. With particular configurations, the amplitude of oscillation was either amplified or suppressed and the range of synchronization was increased or reduced. To the author's knowledge this is the first study in the control of VIV demonstrating both amplification and suppression using arranged roughness strip with a sharp edge.

7.1.1. Laminar-to-turbulent transition

The complex process involving the transition from a laminar to a turbulent boundary layer is not yet fully understood. A schematic version of turbulent boundary layer is shown in Figure 7.1. The boundary layer separation on a surface occurs due to adverse pressure gradient. If the separated shear layer is energized, the flow characteristic may change from a laminar to a turbulent or stay laminar, and reattach on the body surface downstream. The above process results in a slowly moving or nearly stagnant

fluid zone characterized by a stationary re-circulating vortex, called laminar separation bubble.

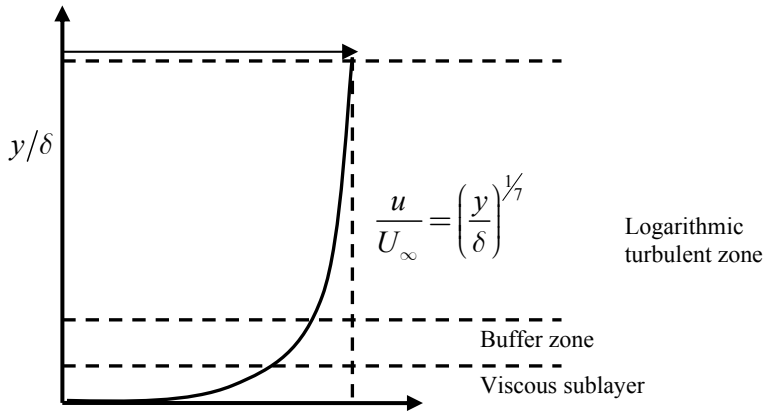

Figure 7.1. Schematic version of turbulent boundary layer velocity profile.

One of the boundary layer control methods involves the induction of a turbulent flow before separation by the introduction of geometrical discontinuities (turbulence stimulators) on the body surface (Igarashi 1985; Igarashi 1986). Placing the turbulence stimulators before the actual separation point destabilizes the laminar boundary layer and forces it to become turbulent.

In order to explain possibly what happens when the laminar boundary layer interacts with surface roughness, it is necessary to review the theory on laminar-to-turbulent transition and boundary layer stability. Transition can be divided into two main stages one is the receptivity stage and the second stage is amplification stage. In the receptivity stage the external disturbances in the flow due to surface roughness, free stream turbulence and acoustic noise are transformed into instability oscillations within the boundary layer. These internal disturbances usually decay, but a few get amplified and this depends on the 'receptivity' (Morkovin 1969). In the amplification stage, exponential growth of the few unstable internal disturbances which didn't decay occurs and turns into two-dimensional Tollmien–Schlichting (T–S) waves. Later the flow shifts from this two-dimensional state to a three-dimensional state, then to turbulent spots and then ultimately to turbulence. The above statements can be understood from Figure 7.2 which was reproduced from White's book (White 1974).

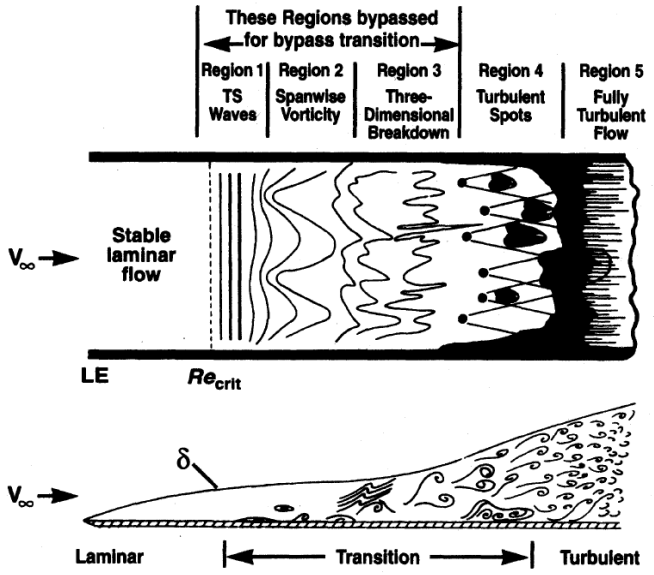

Figure 7.2. Natural boundary layer transition (White 1974).

In understanding the transition to turbulence, the issue of receptivity and stability needs to be studied. At present, the only solution which solves the stability problem is associated with the Orr-Sommerfeld equation, and is called 'linear stability theory'. Orr-Sommerfeld equation, involves the solution for the Navier-Stokes equation when a perturbation is superposed on the principal flow. Due to the difficulty in numerically modeling of the Navier-Stokes equation for higher Reynolds numbers, approximate methods such as asymptotic methods or Pohlhausen velocity profile can be used for this type of problem. Solving receptivity is more difficult than the stability problem (Duck et al. 1996).

Duck et al. (1996) excited the T-S waves using acoustic disturbances as a source of perturbation in combination with surface roughness, and they found that the effective generation of T-S waves occurs when the non-dimensional length of the roughness is $O(Re^{-3/8})$.

7.1.2. Roughness induced transition

For a bluff body, earlier transition from laminar to turbulent separation can occur due to the pressure gradient, step, roughness, and the nature of flow, i.e intensity of

turbulence. Surface irregularities induce laminar-to-turbulent transition by receiving and amplifying the disturbance within the laminar boundary layer. In real situations no surface is perfectly smooth and roughness can also play an important role in this process. To the author's knowledge, there exists no rigorous method in prediction of transition to turbulence on a surface with significant surface roughness. There are only few theories which try to throw some light on the roughness induced transition.

Distributed surface roughness has difficulty in actually explaining the surface roughness properties compared to the isolated roughness (see Figure 7.3 and Figure 7.4). Statistical properties on the vortex dynamics behind the roughness elements will be the better approach. The roughness generated turbulence is yet in the process of investigation. The transition can be predicted by a few theories based on empirical results, but this misses the physics of the problem (Tani 1969). Morkovin (1990) reviewed the effect of three-dimensional roughness and he concluded that depending on the relative size of the roughness in comparison to the boundary layer thickness or to the cylinder diameter the effect of roughness on the flow is different.

The Reynolds number regimes that are considered in this analysis fall in the TrSL3 and TrBL regimes. The figures representing these regimes are reproduced from the review papers of Norberg and Zdravkovich (see Figure 4.1, Figure 4.2, and Figure 4.3). In the present experiments, it is very crucial to understand the amount and configuration of roughness required to achieve the desired effect because the TrBL regime is very sensitive to turbulence (Achenbach 1971; Higuchi et al. 1989b).

By introducing isolated or distributed roughness around the body, discrete vortices in the scale of the roughness are formed. These highly energetic eddies formed behind the roughness elements are formed within the prevailing boundary layer and energizes the boundary layer. The small scale vortices in the boundary layer result in a partially or even fully turbulent boundary layer if it was initially laminar or enhance the turbulence within the turbulent boundary layer. In the case of an initial laminar boundary layer on a smooth circular cylinder at subcritical Reynolds numbers, transition of the boundary layer from laminar to turbulent results in gaining momentum and it could possibly help to overcome adverse pressure gradients and delay flow separation (Batham 1973).

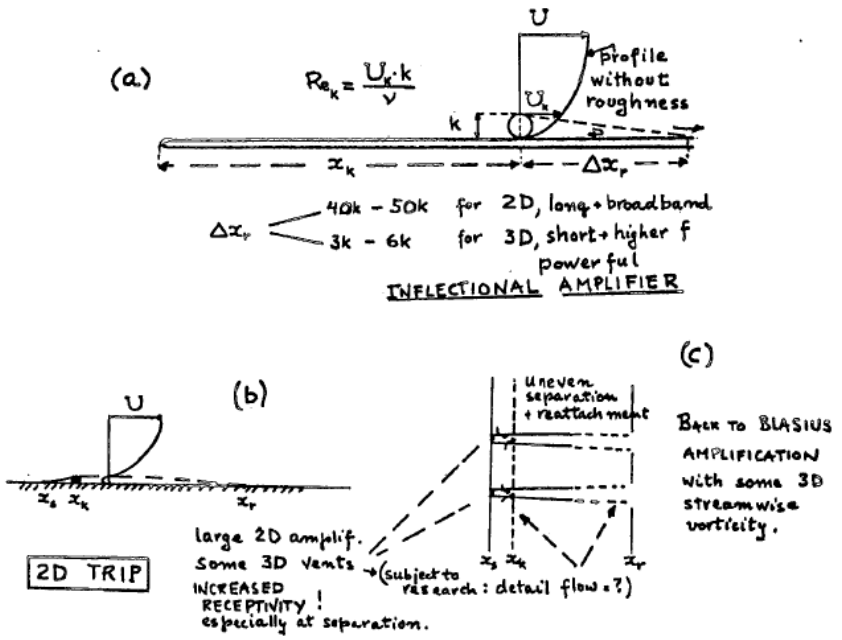

Figure 7.3. The process of transition by two dimensional roughness. [Reproduced from Morkovin (1990)].

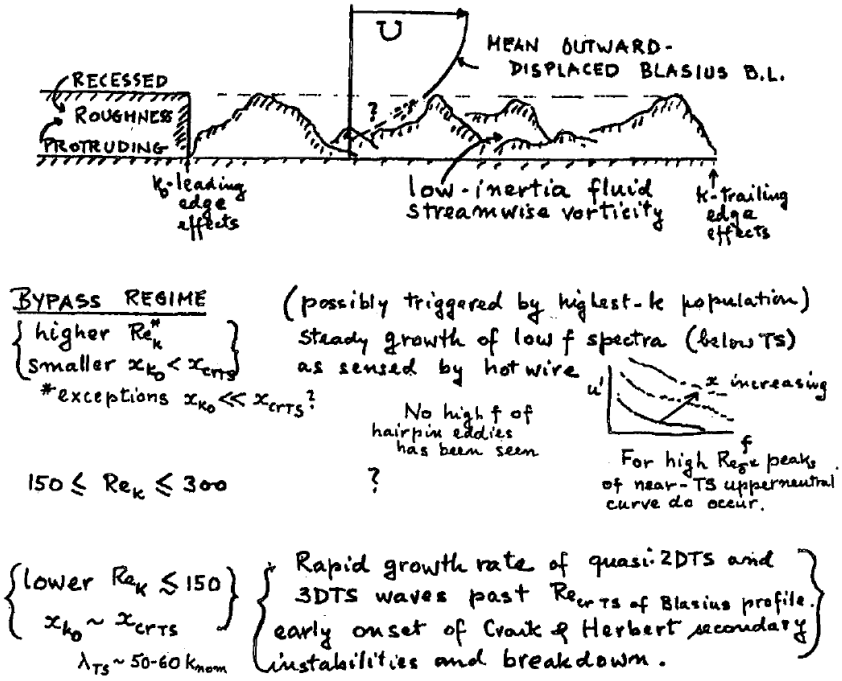

Figure 7.4. The process of transition by three-dimensional distributed roughness. [Reproduced from Morkovin (1990)].

Introducing roughness around a bluff body initiated transition and also resulted in the elimination of few flow regimes (Zdravkovich 1997). Achenbach and Heinecke

(1981) noted that the transition critical Reynolds number is reduced for a circular cylinder as the roughness height increases and they proposed a relation:

$$\mathrm{Re}_{crit} = \frac{6000}{\left(k_s/D\right)^{1/2}}$$

By introducing roughness uniformly around the body, the flow regimes TrS1 and TrS2 are eliminated (Zdravkovich 1997). But in the case of isolated roughness like a tripping wire, earlier formation of separation bubble can be induced (Igarashi 1986). Depending on the size of the roughness element, the separation bubble reattaches in a laminar or turbulent manner as shown in Figure 7.22.

For a smooth cylinder, boundary layer transition can occur with or without a transitional separation bubble. It is observed that the separation bubble may occur even in the subcritcal Reynolds number regime (Schewe 2001). A detailed investigation was done by Huang et al. (2006). They noticed that separation of a boundary layer shows significantly different flow patterns in two subranges of Reynolds number: $\mathrm{Re} < 0.55\times10^5$ and $\mathrm{Re} > 0.55\times10^5$. For $\mathrm{Re} < 0.55\times10^5$, a laminar separation mode occurs and for $\mathrm{Re} < 0.55\times10^5$ the separation bubble mode occurs (Figure 7.25). Separation bubble is sensitive to Tollmein-Schlichting (TS) waves and the amplification of the TS waves is sensitive to turbulence and the roughness of the cylinder (Pfeil and Orth 1990).

Pfeil and Orth (1990) investigated the sensitivity of the separation bubble to turbulence and the boundary layer transition with and without transitional separation bubbles. They found in their investigation that the separation bubble reacts very sensitively to changes in inlet turbulence. They also observed Tollmien-Schlichting waves in the separated shear layer just before transition.

7.1.3. Separation point

A literature survey on the separation point for an incompressible fluid flow around a circular cylinder shows that the time averaged separation angle results is sparse and widely diverse in the subcritical regime (Table 7.1).

Niemann and Hölscher (1990) and Coder (1971) argue that the diversity in the measurement of the separation point in the upper subcritical (TrSL3) and critical regime(TrBL) are caused by different factors: surface roughness, aspect ratios, and end

conditions of the cylinder, blockage ratio, turbulence intensity, and the experimental techniques employed. Depending on the experimental technique, there is a significant error bar for identification of the separation angle (Coder 1971). Huang et al. (2006) attributed the diversity for the separation point to the formation of separation bubble mode for Re $>5.5\times10^4$ using surface visualization. Huang also noticed that for Re $<5.5\times10^4$, the separation angle was 77° and for Re $>5.5\times10^4$ the separation angle was 74° but a bubble was formed after it. A similar observation was made by Coder for Re > 3×10^4, but he didn't attribute the observation to any particular reason. Using a roughness strip will allow the flow control method to accommodate the discrepancy in the separation point. Most of the present experiments were conducted in the laminar separation bubble regime (Huang et al. 2006).

Investigators	Separation Angle	Reynolds Number
Thom (1933)	73°-80°	4.6×10^5- 1.35×10^6
Nishimura and Taniike (2001)	76.2°	6.1×10^4
Achenbach (1968)	78°	10^5
Roshko (1954)	80°	1.45×10^5
Lee and Basu (1997)	82.5°	2.4×10^4 and 5.1×10^4
Fage and Falkner (1931)	82°	6×10^4
Son and Hanratty (1969)	85°- 75°	3×10^3 - 10^5
Schiller and Linke (1933)	87°-94°	$2.8\times10^3 - 4.1\times10^4$
Ballengee and Chen (1971)	91.5°	10^4 to 4.5×10^4
Roshko (1961)	95°-103°	8.4×10^6

Table 7.1. Separation angle measured by different investigators.

7.1.4. Oscillation of separation point

Mei and Currie (1969) found that for the vibrating cylinder, the range of angular displacement of the separation point was found to depend upon the vibration amplitude and frequency as shown in Figure 7.5. Maekawa and Mizuno (1967), Nishimura and Taniike (2001) and Dwyer and McCroskey (1973) observed that for a stationary cylinder

both the stagnation point and the separation points fluctuated with the oscillation of the wake. Maekawa and Mizuno (1967) measured the separation point of a circular cylinder for a Reynolds number range, Re = 3.7×10^4 ~2.8×10^5. In this range they observed an oscillation of the separation point between 78° - 90° as shown in Figure 7.6.

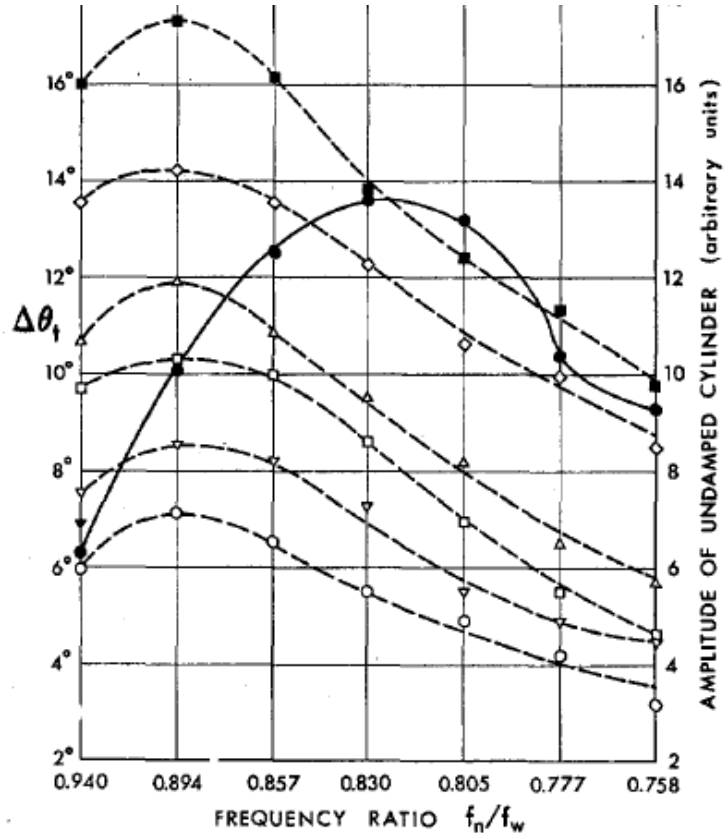

Figure 7.5. Total displacement of the separation point and the amplitude of the undamped cylinder versus frequency ratio (Mei and Currie 1969).

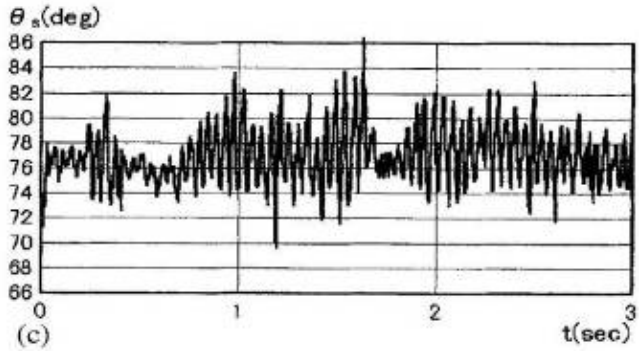

Figure 7.6. Oscillating separation point around a circular cylinder (Nishimura and Taniike 2001).

7.1.5. Effect of roughness strip on spanwise correlation

The use of roughness strips exploits the phenomenon that a straight line separation of the fluid flow around the body results in a correlated forcing on the cylinder. Straight line separation increases the spanwise correlation of the vortex shedding. An increase in spanwise correlation of vortex shedding increases the fluctuating lift force and subsequently amplifies vibration. Using a straight roughness strip is more effective than a trip wire because of the inherent nature of the oscillation of the separation point. The roughness strips accommodate the oscillatory nature of the separation point (78°-90°) because of their width. The roughness strip acts like a tripping wire used in conjunction with the vortex generators or turbulators.

The above stated, nature can be exploited to suppress VIV. If the separation length is discontinuous it will result in reducing the spanwise correlation along the separation lines or shear layers. Correlated vortex shedding and the alternating force acting on the cylinder are weakened. This can be achieved by introducing discontinuities in the roughness strip. That is, spanwise smooth and rough patches alternate. This would result in encouraging early separation at the rough patch and allowing natural separation at the smooth patch.

The loss in lift force for a smooth cylinder in the critical regime was speculated by Norberg (2003) to "spread spots". According to Norberg, the spread spots (Yokoi and Kamemoto 1992; Yokoi and Kamemoto 1993) can induce a feedback motion between the longitudinal streamwise vortices, and formation of Kármán vortices and separation resulting in spanwise undulations of the separation line. In the critical regime, as the roughness increases the spanwise correlation of vortex shedding also increases (Eaddy et al. 2002) as shown in Figure 7.7. From the above statements, the author believes that the surface roughness can be used to sustain and maximize VIV in the critical regime.

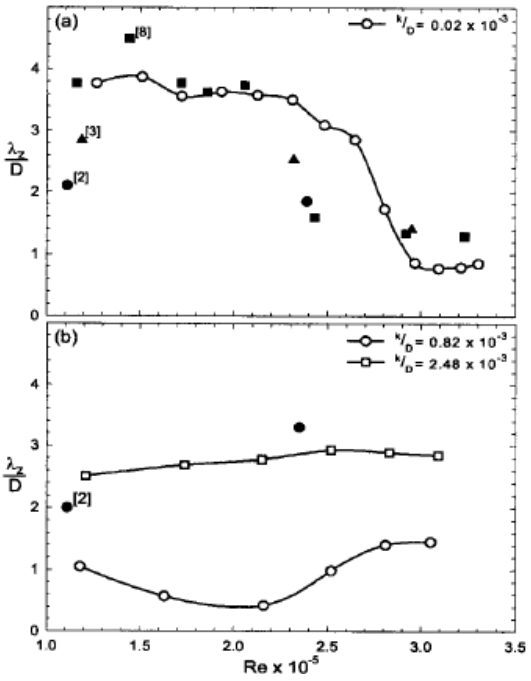

Figure 7.7. Axial correlation length for (a) smooth and (b) rough cylinders in low turbulence flow. [Reproduced from Eaddy et al. (2002)].

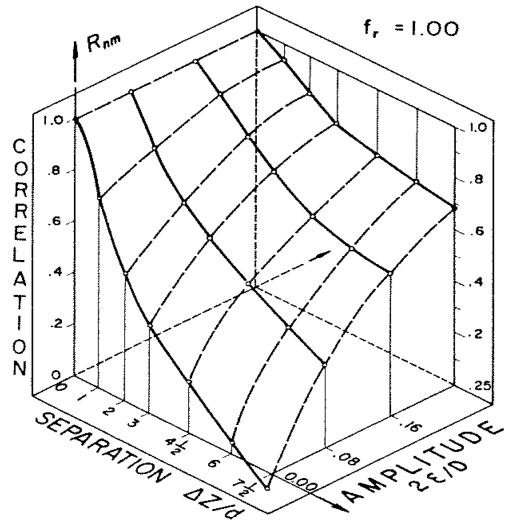

Figure 7.8. Variation of correlation coefficient R_{uu} between wake velocities along the span and at different amplitude rations. [Reproduced from Toebes (1969)].

The loss in spanwise correlation of vortex shedding is not only observed in the critical regime of Reynolds number but it is also observed in the middle and at the end of synchronization (Hover et al. 2004). Hover et al. (2004) proposes the loss in the end force correlation to the transition in wake states from 2S to 2P mode. For reduced velocity in

the initial part of the upper branch, they calculated a velocity correlation coefficient value of R <0.5 for spanwise separation of five diameters.

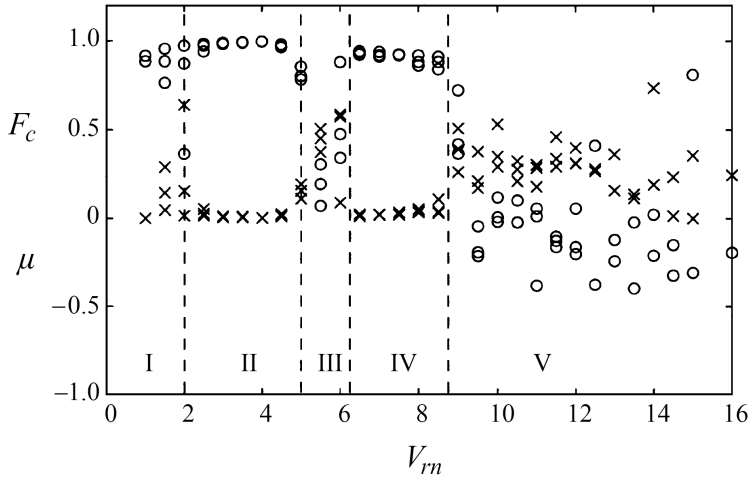

Figure 7.9. Force correlation coefficient $F_c(x)$ and standard deviation, $\mu(o)$ for free-vibration tests with the uniform cylinder. [Reproduced from Hover et al. (1998)].

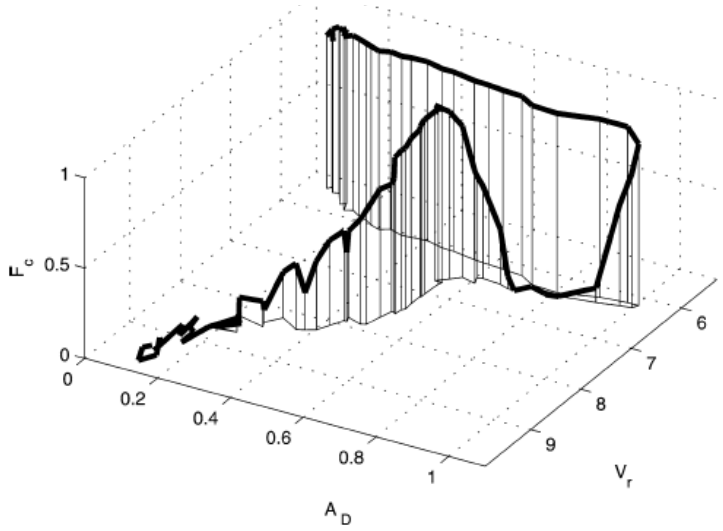

Figure 7.10. End lift force correlation coefficient F_c for free-vibration tests, as a function of amplitude and observed reduced velocity V_r. [Reproduced from Hover et al. (2004)].

In Figure 7.9, according to Hover et al. (1998) Region II corresponds to a correlated 2S wake structure, and Region IV is a correlated 2P regime. In Region III transition from 2S to 2P mode takes place and this result in reduction in the end force correlation and a corresponding increase in the value of the standard deviation. In Region

V, for higher reduced velocity, the end force correlation is typically negative, with increased scatter.

7.1.6. Effect of free-stream turbulence

In the case of flow around a circular cylinder, the characteristic effects of free-stream turbulence are similar to the effect of surface roughness on the cylinder, depending on the intensity and length scale of turbulence. Both the free stream turbulence in the flow and the surface roughness on the cylinder cause transition of Reynolds number, delay the flow separation (Fage and Warsap 1929; Sadeh and Saharon 1982), and reduce the mean drag coefficient (Fage and Warsap 1929). The sensitivity of turbulence on the flow around circular cylinders is in the TrSL3 (Norberg 1987; Norberg and Sunden 1987) and TrBL regime (Sadeh and Saharon 1982). When the turbulence scale is on the same order of magnitude as that of the boundary layer thickness it penetrates the boundary layer and energizes the boundary layer (Sadeh and Saharon 1982). The large-scale turbulence interacted with the Kármán vortices and larger scale were also perceived as a slow variation of the mean velocity (Sadeh and Saharon 1982). Sadeh et al. (Sadeh and Saharon 1982; Sadeh et al. 1970) used the vorticity amplification theory to explain the mechanism in which the free stream turbulence affects the flow around a circular cylinder.

The advantage of roughness induced turbulence over free stream turbulence is that the boundary layer is disturbed by the free stream turbulence from outside while the turbulence from the surface roughness turbulence acts inside the boundary layer and when the roughness element size is in the scale of the boundary layer it sheds vortices of the boundary layer scale. In the case of roughness induced turbulence, the scale and intensity of the turbulence generated can also be controlled. Bearman and Morel (1983) attributed the manner in which turbulence affects the flow around bluff bodies to the earlier transition of laminar shear layers to turbulent shear layers. Turbulence can increase entrainment between the turbulent shear layers, thus, increasing the negative base pressure. The free stream turbulence interaction with the mean flow depending on their scales and intensity can bring about distortion effects around the body and can

amplify or weaken some components (Bearman and Morel 1983; Sadeh and Saharon 1982).

7.1.7. Drag reduction

Drag force reduction for VIVACE is very important because this would reduce the offshore loads on the piles built to hold the device underwater. Reducing the drag force is an important engineering problem faced by offshore structures and other structures that are interacting with fluid. Achenbach in his experiments using distributed roughness around the cylinder did not find any reduction or increase in the drag coefficient in the subcritical regime but in the critical regime, the drag coefficient for a rough cylinder was higher than the smooth cylinder as shown in Figure 7.11.

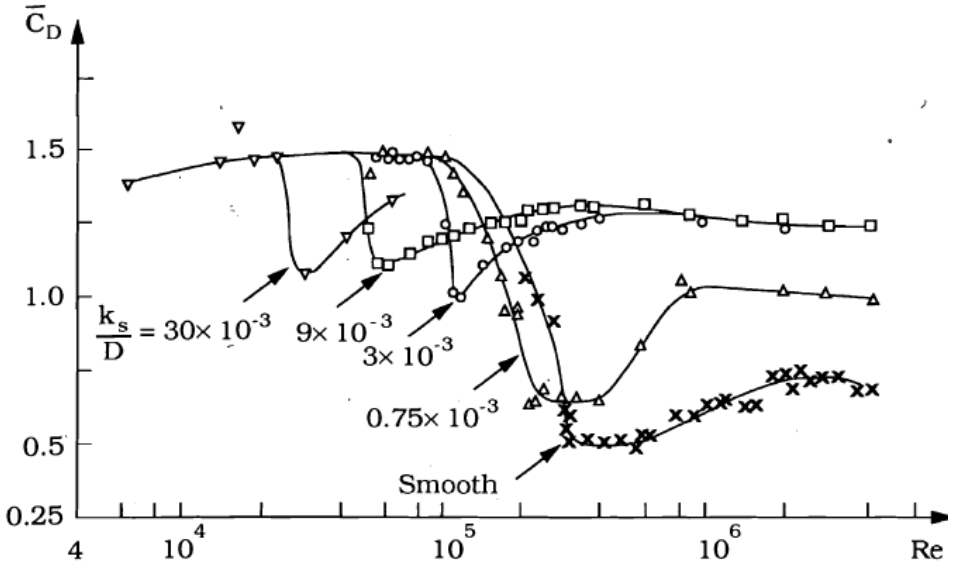

Figure 7.11. Drag coefficient of a circular cylinder at various surface roughness parameters k_s/D. [Reproduced from Achenbach and Heinecke (Achenbach and Heinecke 1981)].

He et al. (2002) in their experiments observed, when the roughness strips were attached to a smooth stationary cylinder at optimal locations (between 40° - 70°) the mean drag force reduced by 40% as shown in Figure 7.12, Figure 7.13, and Figure 7.14. He et al. (2002) proposed Reattachment Causes the Drag Reduction (RCDR) to explain the reduction in the drag force (see Figure 7.12, Figure 7.13, and Figure 7.14).

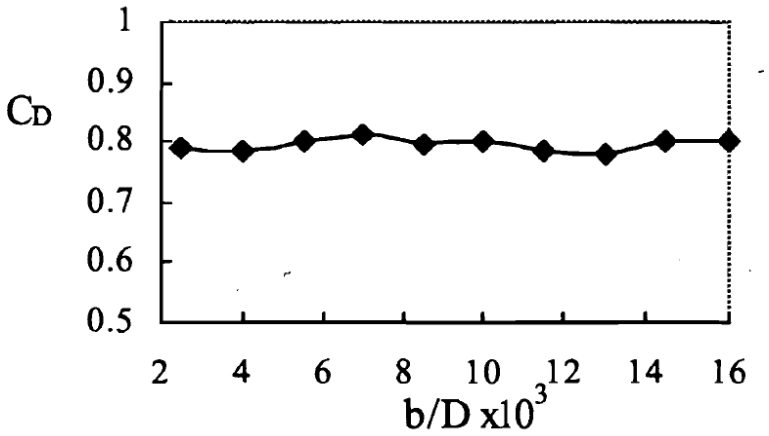

Figure 7.12. Drag coefficient versus width of the fixed strips. [Reproduced from (He et al. 2002)].

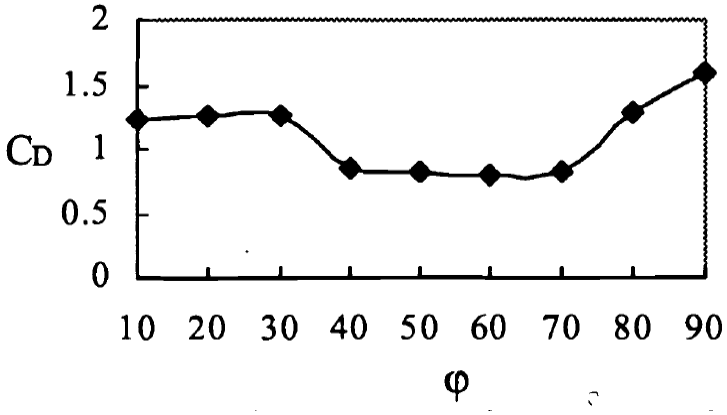

Figure 7.13. Drag coefficient versus arrangement angle of the fixed strips. [Reproduced from (He et al. 2002)].

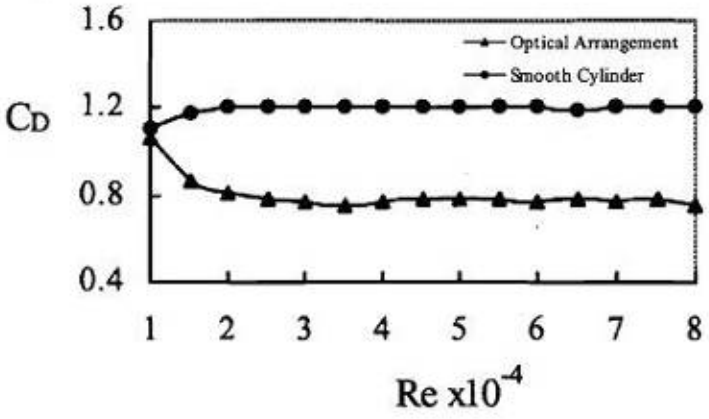

Figure 7.14. Reduction in the drag coefficient achieved by arranging the strips optimally. [Reproduced from (He et al. 2002)].

7.1.8. Vortex dynamics

Vortex dynamics can be classified on the basis of the transition Reynolds number range (Williamson 1996). For higher Reynolds number (Re > 350), transition from laminar to turbulent can happen in the separating shear layer or in the boundary layer. Zdravkovich has classified three subregimes within the **Tr**ansition from laminar to trubulent in the **S**hear **L**ayer (TrSL). He labeled them as TrSL1 ($350 \leq Re \leq 1{,}000–2{,}000$), TrSL2 ($1{,}000–2{,}000 \leq Re \leq 2–4\times10^4$) and TrSL3 ($2–4\times10^4 \leq Re \leq 1–2\times10^5$). The fluctuating lift coefficient varies in each regime as shown in Figure 4.1**,** Figure 4.2, and Figure 4.3.

In previously published VIV experiments, most of the laboratory measurements correspond to the TrSL1 and TrSL2 regimes. As was discussed in Chapter 4, the high amplitude of vibrations observed in our experiments are attributed to the TrSL3 regime, in which the present experiments fall.

In the regime $7\times10^3 < Re < 2\times10^4$, Lo and Ko (2001) observed pairing of small scale secondary vortices, which in turn play important roles in the formation of the large-scale primary vortices.

If the smaller scale vortices introduced by the roughness particle on the roughness strips constitute vortices shed at the secondary vortex frequency, this could result in a resonance condition. The resonance condition would result in amplification of Kármán vortices; a similar hypothesis has been presented by Duarte Ribeiro (1991).

The smaller scale turbulence intensity generated by the roughness strips will interact with the boundary layer and will constantly feed the vortex formation region. A similar interaction was seen by Duarte Ribeiro (1991) while using mesh screen between the turbulence generated by the mesh screen and the vortex formation region. Certain hypotheses from the previous Section regarding vortex amplification theory of free stream turbulence can be used to explain the effect of turbulence created by roughness strip. According to Sadeh et al. (1982; 1970) maximum amplification of turbulence occurs when the scale of turbulence is larger in magnitude than the boundary layer thickness but of the same order of magnitude . The maximum amplification of turbulence would result in stronger and correlated vortex shedding and consequently VIV.

7.2. PROBLEM DEFINITION

The goal was to study the effect of roughness strips distributed around the elastically mounted circular cylinders in a uniform flow. Different configurations of strips of distributed roughness were explored. The goals of these tests were to investigate the VIV response and in turn help to provide guidance for its control:

(i) To investigate the VIV response characteristics for various configurations of roughness strips.

(ii) To sustain VIV in the critical regime.

(iii) To assess the optimum configuration of roughness for VIV control.

7.3. SOLUTION APPROACH

The parameters varied in the model tests were; the cylinder diameter D, the flow speed U, the roughness distribution, the roughness size k, and the position of the roughness α_{bu}, α_{bl}, θ_u, θ_l as shown in Figure 7.16, Figure 7.17, and Figure 7.18. These tests are very important for the development of the VIVACE Converter, which converts flow kinetic energy of ocean/river currents to electricity.

Four models were used in the tests. All the smooth cylinders have length L=36″ (914mm) and were made of aluminum coated with polymer paint for surface smoothness and protection. Model diameters were 2.5″ (63.5mm), 3″ (76.2mm), 3.5″ (88.9 mm), 5″ (127mm). Amplitude of oscillation of elastically mounted smooth circular cylinders and elastically mounted circular cylinders with narrow roughness strips were measured over a Reynolds-number range 2.0×10^4 to 2.1×10^5 in a uniform flow. To obtain various values for the surface roughness of the test cylinder three grits of sand papers with equivalent roughness (k/D) 0.0014-0.0042 were used (Table 7.2, and Table 7.3). The roughness strips that were used were standard sand paper roll or strip with grit size 36, 80 and 120 of width 0.5″, 1″ and 2″ with known roughness. Grit refers to the average size of the abrasive. Sandpaper ‘grit’ refers to the number of abrasive particles per linear inch of sandpaper. Commonly referred to as grit, this number designation is determined by the amount of abrasive mineral that can pass through a mesh screen with specific size openings. Therefore, a 120 grit abrasive particle will pass through a mesh screen that has 120 openings in one inch square. The roughness strips were glued to the cylinder by

using double sided polyester tape. Different configurations of strips were used for the experiment and one of the parameters was the angle were the strip was placed in relation to the stagnation angle and it varied in between 47° - 160°. Hereafter the roughness strip of different roughness elements is represented as PGrit size, example: P120 refers to the roughness strip with grit size 120 and this characterizes the paper thickness and the roughness size as shown in Table 7.2 and Table 7.3. Schematic versions of the experimental setup and configurations are shown in Figure 7.16, Figure 7.17, and Figure 7.18. In Figure 7.16, the angles θ_u and θ_l is the measure of the circumferential angle that the roughness strip spans. In Figure 7.16, the angles α_{bu} and α_{bl} is the measure of the circumferential angle from where the upstream edge of the roughness strip begins. n Figure 7.17, k is the roughness element size an P is the thickness of the sandpaper including the roughness elements.

Sandpaper	**Grit size (10^{-6} m)**	**D =2.5″**	**D =3″**	**D =3.5″**	**D =5″**
	k	k/D	k/D	k/D	k/D
P36	538	-	-	-	0.0042
P80	201	0.0032	0.0026	0.0023	0.0016
P120	125	-	0.0016	0.0014	-

Table 7.2. The roughness element size of different sand paper and ratio with respect to the diameter.

Sandpaper	**Sandpaper thickness (10^{-6} m)**	**D =2.5″**	**D =3″**	**D =3.5″**	**D =5″**
	k+P	(k+P)/D	(k+P)/D	(k+P)/D	(k+P)/D
P36	1651	-	-	-	0.0130
P80	711	0.0112	0.0093	0.0080	0.0056
P120	508	-	0.0067	0.0057	-

Table 7.3 The roughness element plus the backing paper size of different sand paper and ratio with respect to the diameter.

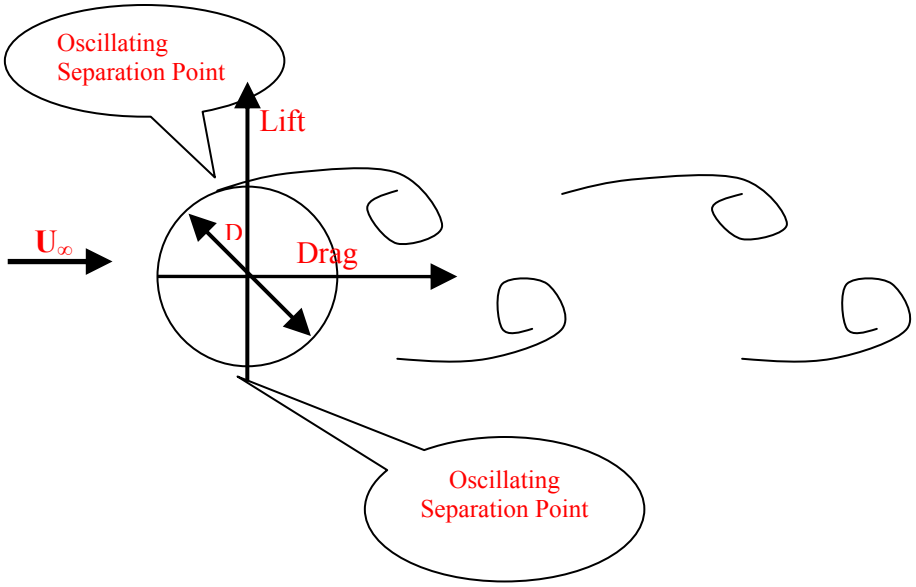

Figure 7.15. Vortex formation and wake.

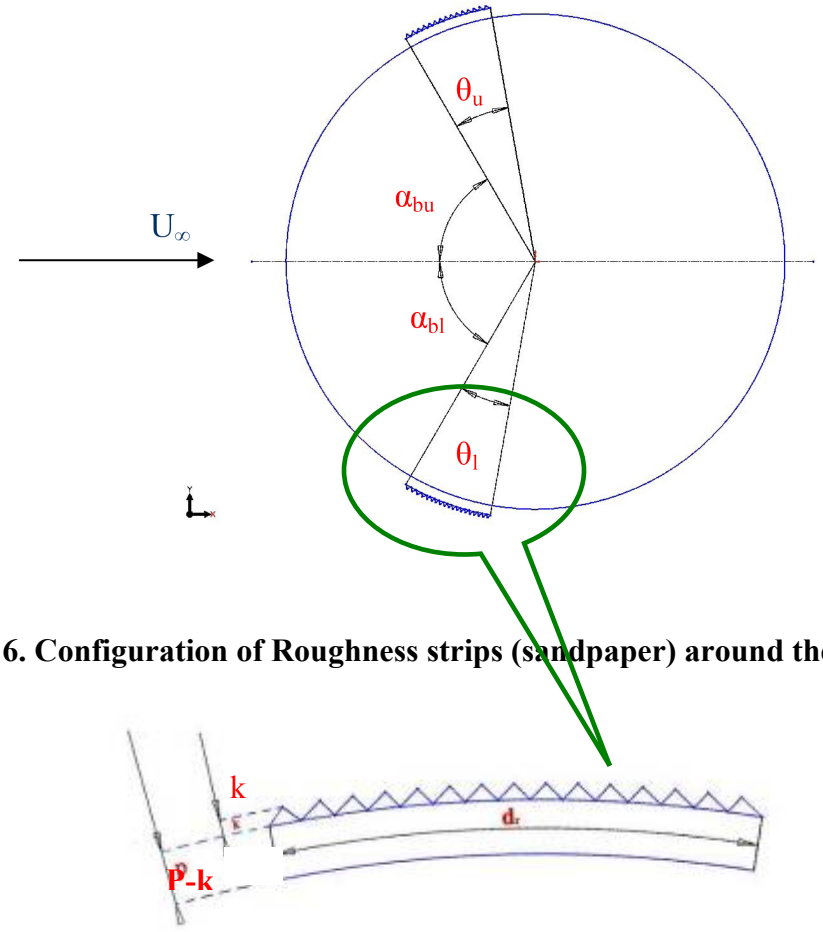

Figure 7.16. Configuration of Roughness strips (sandpaper) around the cylinder.

Figure 7.17 .Detailed sandpaper roughness.

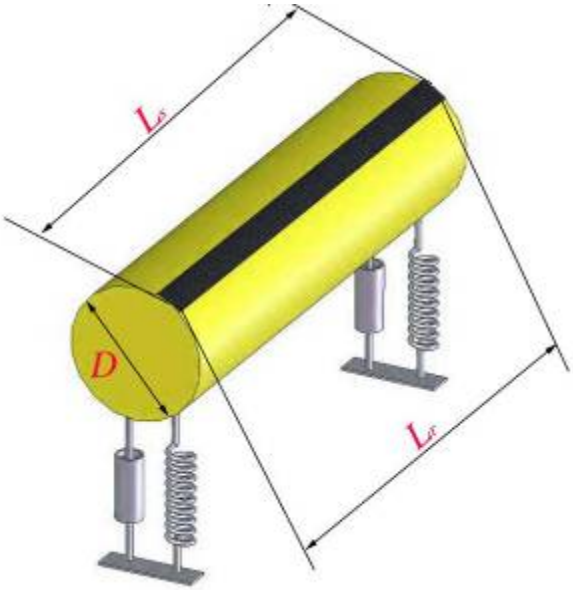

Figure 7.18 Experimental configuration.

7.4. RESULTS, OBSERVATIONS, AND DISCUSSION

At the beginning of our experiments, a smooth aluminum cylinder with no protective coating was left overnight in the LTFSW Channel submerged in water. It was then observed that the elastically mounted cylinder exhibited complete suppression of VIV throughout the synchronization range. This result was attributed to the uneven deposition of aluminum hydroxide. The aluminum deposits appeared to be randomly distributed and the size of excrescences was uneven. This resulted in both smooth and rough surface distributed in a uniform but random manner around the cylinder.

In the present experiments, the roughness of the sand strip weren't calibrated with Nikurdasae's equivalent sand roughness (White 1974) measurement due to lack of C_f measurement. Rather, Achenbach's (1968) result was used in calibrating the roughness used in the present experiments with Nikuradse's (Schlichting 1979), because Achenbach (1968) used similar grit size sandpaper.

With $k_s/D = 0.11\%$, Achenbach (1968) observed laminar separation at 1.3×10^5 and a separation angle of 82° which falls in the TrBL0 regime. At 2.4×10^5, Achenbach (1968) found reattachment of the boundary layer with a separation bubble. The flow separated at a separation angle of 135° with transition to start at an angle of 100° and the reattachment was manifested in the C_f and C_p curve. In the C_p curve for 2.4×10^5, an

adverse pressure recovery was noticed by reattachment as shown in Figure 7.27. In the case of reattached flow it is noted that the C_p curve behaves more like a potential flow in comparison with cases belonging to other regime. Achenbach (1968), noticed as the Reynolds number were increased to transcritical regime reattachment or separation bubble wasn't observed but turbulent separation was observed at an angle of 100°.

There are several studies on which part of the surface area on the cylinder does roughness play an important role. Fage and Warsap (1929) partially covered the smooth cylinder with glass paper strip and concluded that the least effective regions were $-37.5° < \theta < 37.5°$ and $-120° < \theta < 120°$ (Fage and Warsap 1929).

Hiemenz observed that shortly after the start of the adverse pressure gradient after an angle of 70° the flow separated, around 80° (White 1974). Fage and Falkner (1931) observed at Re 6×10^4, that the wall shear stress became maximum at 55° from the stagnation point.

In the cases of rough and smooth cylinders, the mean pressure distribution (C_p) around a cylinder doesn't vary between the cases operating in the TrSL2 and TrSL3 regime until the circumferential angle is 60° on both sides of the mean stagnation point (Figure 7.19). The pressure distribution is not similar in the transcritical regime when the boundary layer is turbulent. Higuchi et al. (1989b) mentioned that high Reynolds number flow can only be simulated using strips of roughness and not distributed roughness. One other observation that can be made from Figure 7.19 is that maximum differences in the pressure distribution occur between 60° and 90°. The above observation suggests that distributed roughness really doesn't modify the flow all over the cylinder and substantial modification of flow can be achieved by introducing roughness approximately in the 60°-85° bandwidth. The above conclusion was used as a guide for selecting the angle to place the roughness strips in our experiments.

Fage and Warsap (1929) also had concerns about the front edge of the sandpaper in their experiments. In effect the front edge of the sand paper acts like a tripping wire. The continuous edge straightens the separation line and correlation is increased. The roughness following acts like vortex stimulators and energizes the already turbulent flow and helps in successful reattachment of the boundary layer. The reattached boundary layer is energized depending on the size of the roughness. The results with smooth paper

and no roughness element confirm the above statement. Significant difference was seen in the response of the cylinder with and without roughness elements.

A discussion of the variability and oscillation of the separation point for both stationary and oscillating cylinder was presented in Sections 7.1.3 and 7.1.4. Fage and Warsap (1929) found that the tripping wires are very effective between the 45° and 65°. They also found that the effectiveness of tripping wires is maximized when the tripping wire is placed at 65° for Reynolds number 2.5×10^5. In Section 7.1.3 and Table 7.1, the variability of separation point along the circumference of the cylinder surface is shown for different Reynolds number and experimental setup. This variation and oscillation of the separation angle due to Reynolds number variation and VIV will handicap the use of the tripping wires. The roughness strips due to their wider width (b) could accommodate the variation of separation angle at different Reynolds number and the oscillation of separation point during VIV motion.

The impact of roughness on pressure distribution is a function of Reynolds number (Chakroun et al. 1997). They reported that for the same amount of roughness the pressure distribution around the cylinder show marked difference as the Reynolds number was varied as shown in Figure 7.19. In Figure 7.19, it is also shown that the pressure distribution can be altered dramatically when a characteristic roughness is distributed.

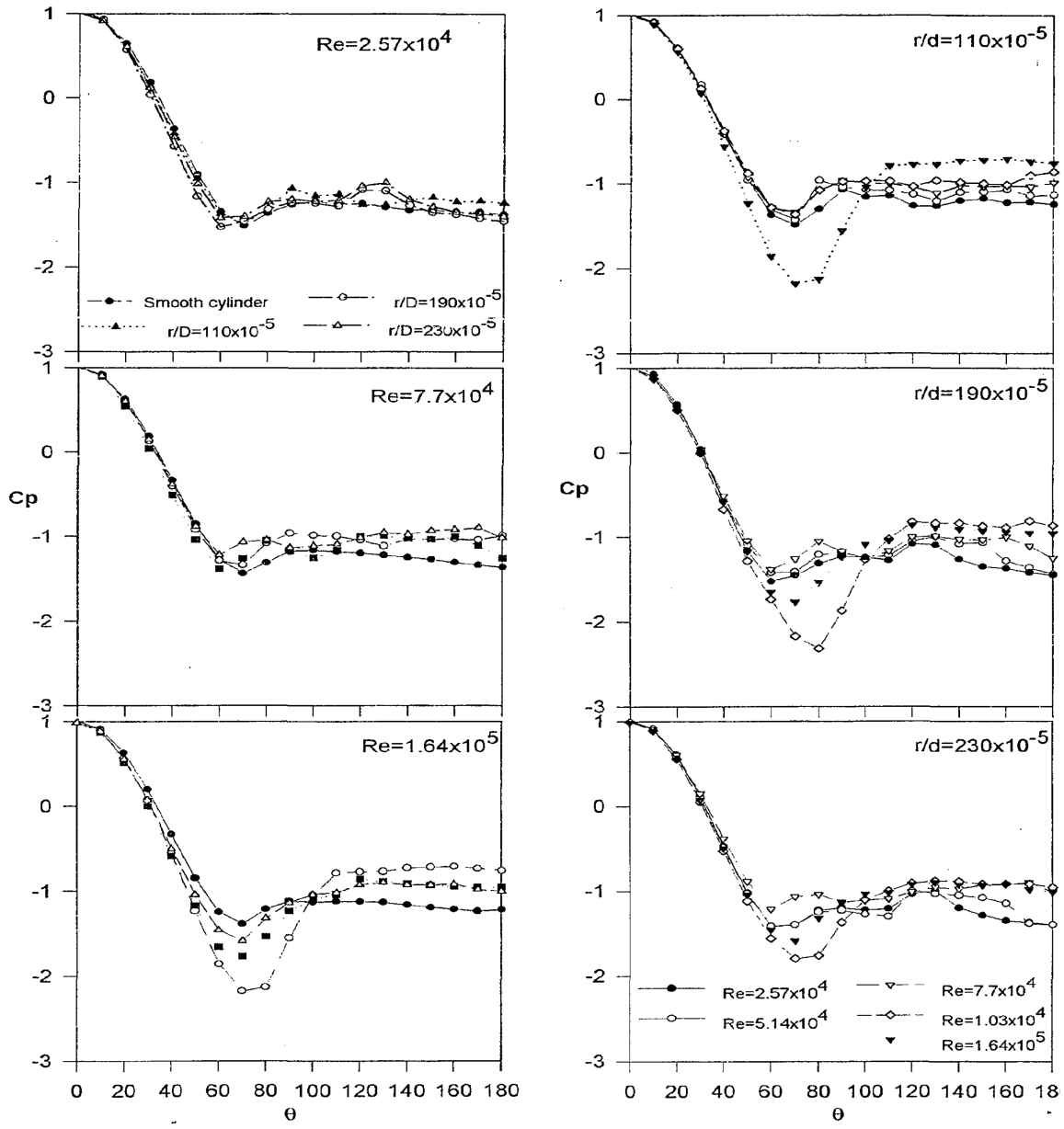

Figure 7.19. Variation of the pressure distribution around the cylinder with different roughness and at different Reynolds number. [Reproduced from Chakroun et al. (1997)].

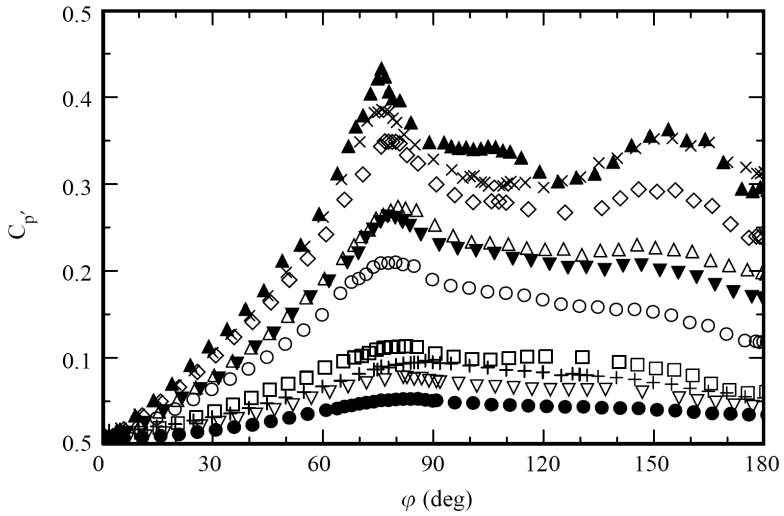

Figure 7.20. R.m.s. of fluctuating pressure distributions, C_p; for Re: +; 7:2 x 10^2; ●; 1:5 ×10^3; ▽; 4:4 x 10^3; □; 5.0x 10^3 ; ○ ; 6.1×10^3; ▼; 7.2×10^3; △ ; 8.1×10^3; ◊; 2.0 ×10^4; x; 6.1 ×10^4; ▲; 2.1 x 10^5: (Norberg 2003).

7.4.1. Boundary layer calculation

Considering a flow past a body, the influence of viscosity at higher Reynolds number is confined to a very thin layer in the immediate neighborhood of the body, where due to the influence of viscosity the flow adheres to the body. In that thin layer, the velocity of fluid increases from zero at the wall to its full value which corresponds to external frictionless flow. This layer is defined as boundary layer.

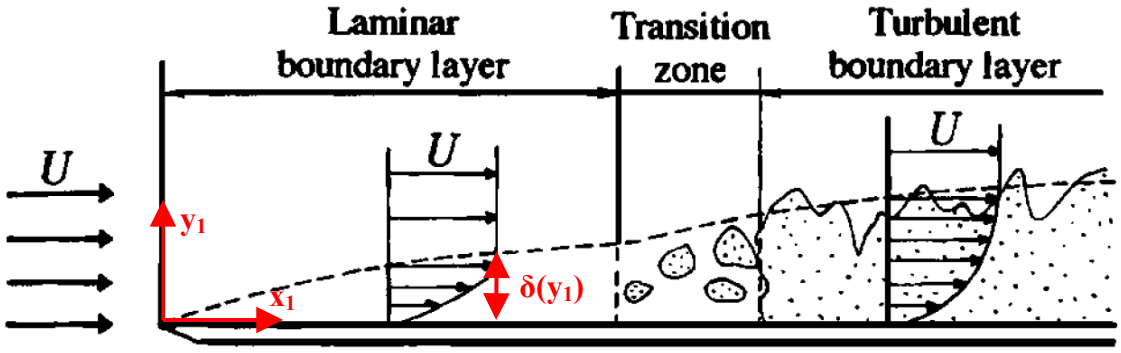

Figure 7.21. Development of boundary layer along a flat plate. [Reproduced from Nakayama et al (2000)].

Solution of the boundary layer equations are such that the velocity component u attains its main-stream value U only asymptotically. The thickness of the layer is therefore indefinite, as there is always some departure from the asymptotic value at any

finite distance y_1 from the surface. The scale of the boundary layer thickness can, be specified, however, adequately by certain lengths amenable to precise definition, both for experimental measurement and for theoretical calculation. These measures of boundary layer thickness are defined as follows:

1. Boundary Layer Thickness δ: This is defined as the y_1- location where u/U reaches 0.99%, that is the u- velocity becomes 99% of the edge velocity.

2. Displacement Thickness δ*: This is a measure of the outward displacement of the streamlines from the solid surface as a result of the reduced u- velocity within the boundary layer. For incompressible flow this quantity is defined as

$$\delta^* = \int_0^\infty \left[1 - \frac{u}{U}\right] dy_1$$

Even though boundary layer theory simplifies the Navier-Stokes equations significantly the boundary layer equations are numerically tasking. Integral boundary layer theory allows us to estimate displacement thicknesses with a minimal amount of effort.

The Pohlhausen integral method was used (Schlichting 1979) for estimation of the boundary layer characterisitcs. In our experiments, the general features of the mean flow past a cylinder with rough strips can be characterized by

- a very thin laminar boundary layer in the forward portion of the cylinder before the roughness strip
- transition following the laminar boundary layer,
- eventually turbulent separation further downstream.

The pressure measurement for different Reynolds number for a smooth cylinder in the subcritical regime is plotted in Figure 7.19 and Figure 7.27. In these figures the pressure distributions for a smooth cylinder are nearly similar before a circumferential angle of 60°. In other words, the characteristic change in the distribution of pressures for a smooth cylinder for Reynolds number regimes TrSL and TrBL occurs between 60° - 110°. This is one of the reasons that roughness or tripping mechanisms become more efficient for this part of the cylinder and essentially the place where the control of flow can be achieved.

Celik and Patel (1982) were among the few researchers who conducted boundary layer development experiments around a circular cylinder. They tripped the boundary

layer around a circular cylinder of 10.64″ diameter using tripping wire placed at angles 45° and 55° from the stagnation point at Re=4.4×10^5.

7.4.2. Separation bubble

To model the effect of a sandstrip on the flow around a circular cylinder, it is important to understand the effect that the edge of the sandstrip has on the flow. The edge of the sandstrip acts like a step and in a sense it acts like a tripping wire being conjugated with three-dimensional roughnesses after the tripping wire.

The flow around the cylinder with trip wire has been classified into three regimes such as A, C, and D by Igarashi as shown in Figure 7.22 (Igarashi 1986). Where in regime A the flow reattaches in a laminar manner beyond the wire with a separation bubble, in regime B the flow reattaches with a separation bubble as a turbulent boundary layer, and in regime C the flow separates at the wire. Regime B is the transition regime between A and C.

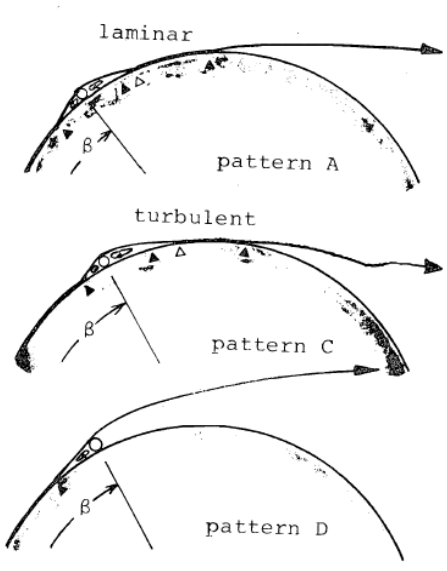

Figure 7.22. Different patterns associated with flow around the cylinder with trip wire.[Reproduced from Igarashi (1986)].

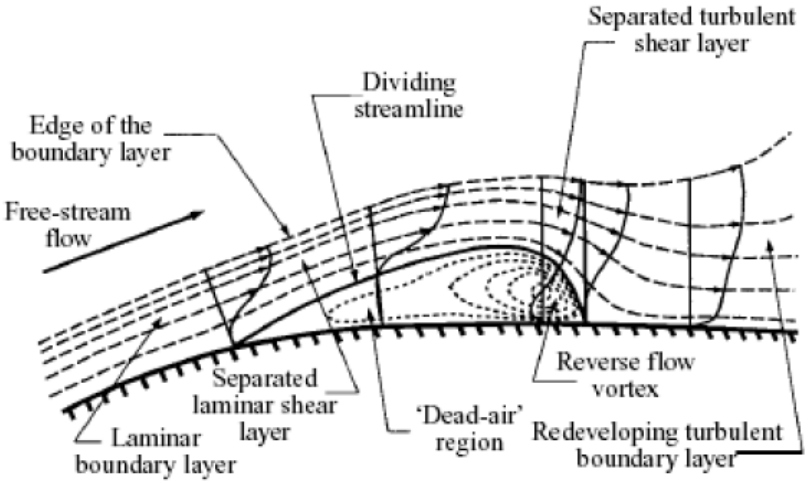

Figure 7.23. The time average structure of a laminar separation bubble. [Reproduced from (Alam and Sandham 2000)].

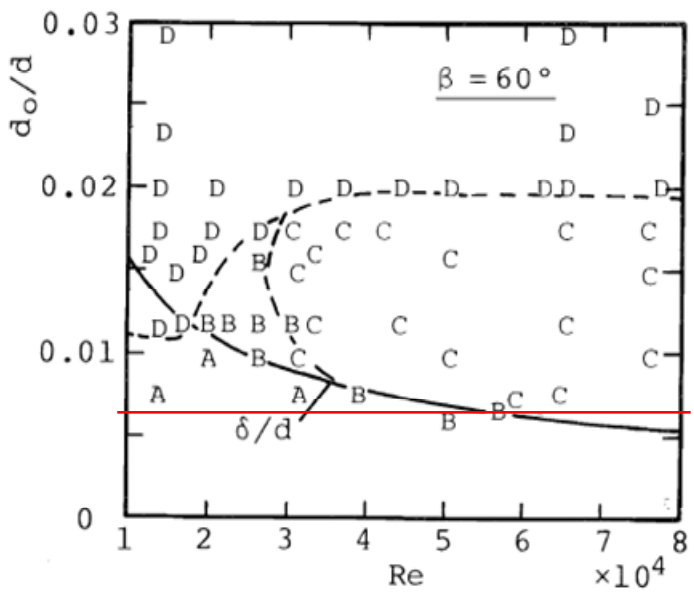

Figure 7.24. The variation of flow regime associated with Re and the ratio of the trip wire diameter and the diameter of the cylinder for a flow around the cylinder with trip wire. [Reproduced from Igarashi (1986)].

So cases A, B, and C can be considered as a separation bubble case. Separation bubble was observed by Higuchi et al. (Higuchi et al. 1989a) at Re= 0.8 x 10^5 and the separation bubbles existed in the range 60° - 90° from the stagnation point and they occur in cells along the span. Recently, Huang et al. (2006) observed separation bubbles at a lower Reynolds number of Re> 5.5 x 10^4 (see Figure 7.25). In general, a separation

bubble is classified based on the regime of the boundary layer at the separation and reattachment points as being laminar, transitional or turbulent. For a laminar separation bubble, the boundary layer is laminar at both the separation and reattachment points, while for a transitional bubble the boundary layer is laminar at separation and turbulent at reattachment. For a turbulent separation bubble the boundary layer is turbulent at both the separation and reattachment points. Case A (see Figure 7.22) is similar to the separation bubble on a smooth cylinder when the Reynolds number lies between 5.5 x 10^4-1 x 10^5. A separation bubble is characterized by its length and height. Depending on its length, it is classified as long and short separation bubble. The actual separation to reattachment length is not decisive whether a bubble should be termed long or short but rather the effect of the bubble on the static pressure distribution at the surface. The time average structure of a laminar separation bubble is shown in Figure 7.23.

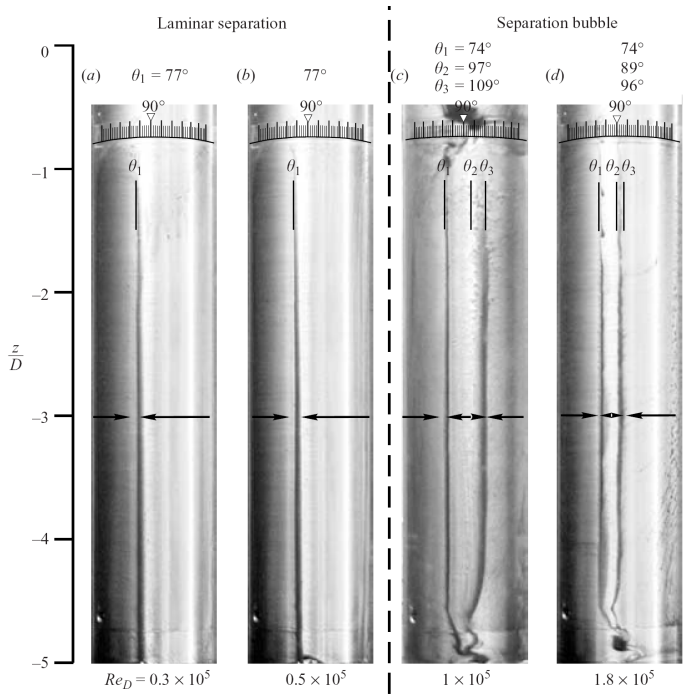

Figure 7.25. Surface oil-flow patterns of a circular cylinder at various Reynolds numbers. (a) Re = 0.3 × 10^5, (b) 0.5× 10^5, (c) 1.0× 10^5, (d) 1.8× 10^5. [Reproduced from Huang et al. (Huang et al. 2006)].

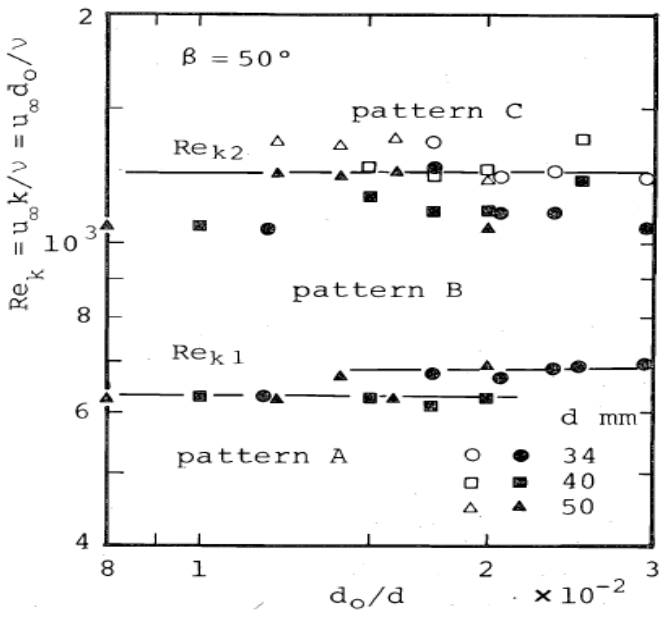

Figure 7.26. The variation of flow regime associated with Re_k (Reynolds number trip wire) and the diameter ratio of the trip wire for a flow around the cylinder with trip wire. [Reproduced from Igarashi (1986)].

Higuchi et al. (Higuchi et al. 1989a) investigated the flow around smooth circular cylinders in the Reynolds number range of $0.8 \times 10^5 < Re < 2 \times 10^5$ and they found intermittent boundary layer reattachment that occurred in cells along the span of the cylinder which resulted in a significant decrease in drag coefficient and a weakening of the vortex shedding.

Small separation bubbles can be considered to cause a minor perturbation of the pressure distribution around the cylinder and are, therefore, not harmful (Pfeil and Orth 1990). But, if the flow does not reattach shortly after separation, then either a long bubble is formed or the flow remains separated. These cases affect drastically the pressure distribution around the cylinder and in turn result in reduction of the lift and increase in drag force due to earlier separation.

In our experiments, the operational regime was A, B, and C in the Igarashi plot because the Re for the strips varied from 0 – 1300 in the cases where the strip was placed before 80° from the stagnation point (see Figure 7.24, and Figure 7.26). That is, our experiments were conducted in the transition from laminar to turbulent attachment regime. There was no confirmation made in our experiments by pressure measurements

around the cylinder. The author may yet suggest the following hypothesis on the behavior of reattachment. The influence of roughness element following the edge may act like a turbulator or vortex generator aiding in transition from laminar to turbulent reattachment.

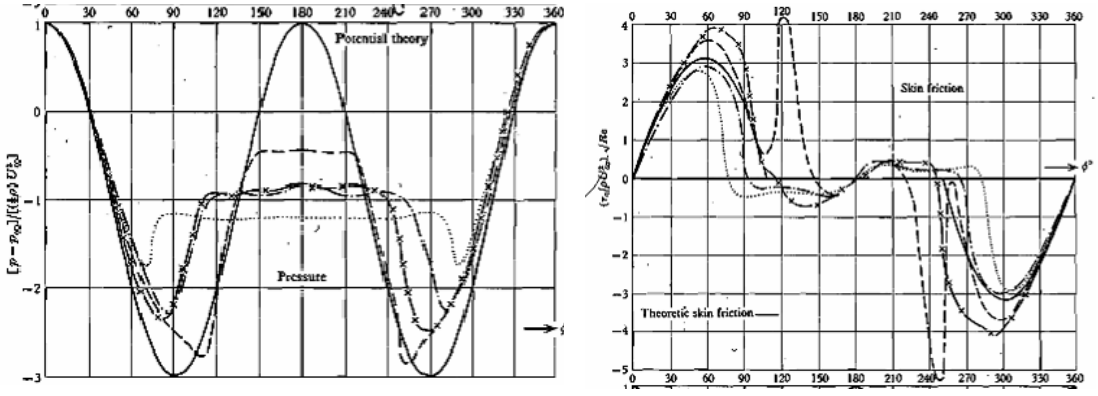

Figure 7.27. Comparison of the skin friction and pressure distribution at various Reynolds number. •••, Re = 1×10^5; — – —, 2.6×10^5; — —, 8.5 x 10^5; — x —,3.6 x 10^6. [Reproduced from Achenbach (1968)].

7.4.3. Synchronization in critical regime of Reynolds number

The roughness strips on the cylinder increase the correlation length in the critical regime and this results in increase of amplitude of oscillation and the width of the range of synchronization. In the critical regime, a loss in lift occurs as shown in Figure 4.3. The loss in correlated forcing or lift in the critical regime is attributed to the formation of a separation bubble that results in a highly irregular separation line and diminished correlation. But the presence of roughness strips aids in the transition process along a straight line and, thus, correlating the formation of separation bubble. This aids in sustenance of VIV even in the critical regime where vortex shedding is expected to be completely suppressed. In Figure 7.28, VIV for the 5″ cylinder is sustained for Reynolds number in the critical regime and the VIV is sustained at high amplitude ratio.

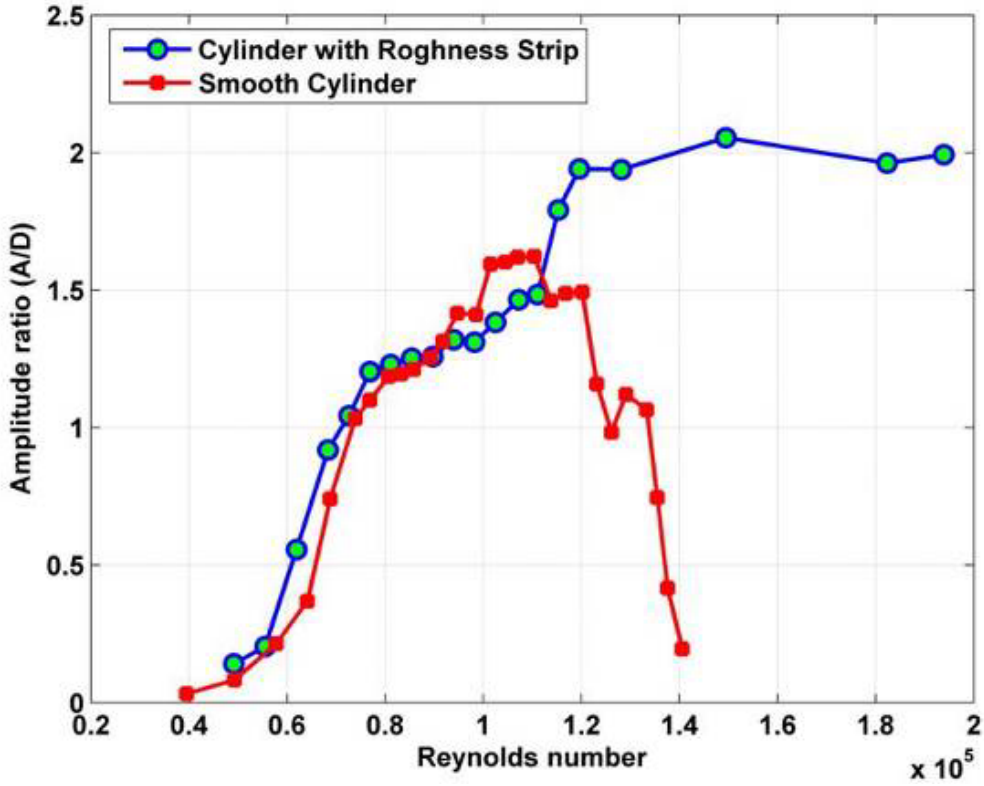

Figure 7.28. Comparison of the amplitude ratio and range of synchronization in terms of Reynolds number of a 5.0″ cylinder with and without roughness strip.

7.4.4. Wake strucutre

The roughness strips affect the wake mode of shedding as evidenced by the peak at higher harmonic components of vortex shedding in the displacement spectrum (see Figure 7.32). Williamson and Roshko in 1988 mapped the wake structure corresponding to the amplitude of oscillation and the reduced velocity or the wavelength that is defining the body trajectory (Williamson and Roshko 1988). In our experiments using roughness strips the corresponding amplitude and the reduced velocity are plotted against the Williamson and Roshko's map (Figure 7.37). It is noticed that the plot passes through the desynchronized region in the map and reaches the 2P+2S region in the map at higher reduced velocities. Further investigation was performed by using flow visualization and it was noticed that the number of vortices shed in half the period of oscillation increased to four as the velocity of the flow increased. Limitations of the LTFSW Channel made it impossible to proceed further with the experiments.

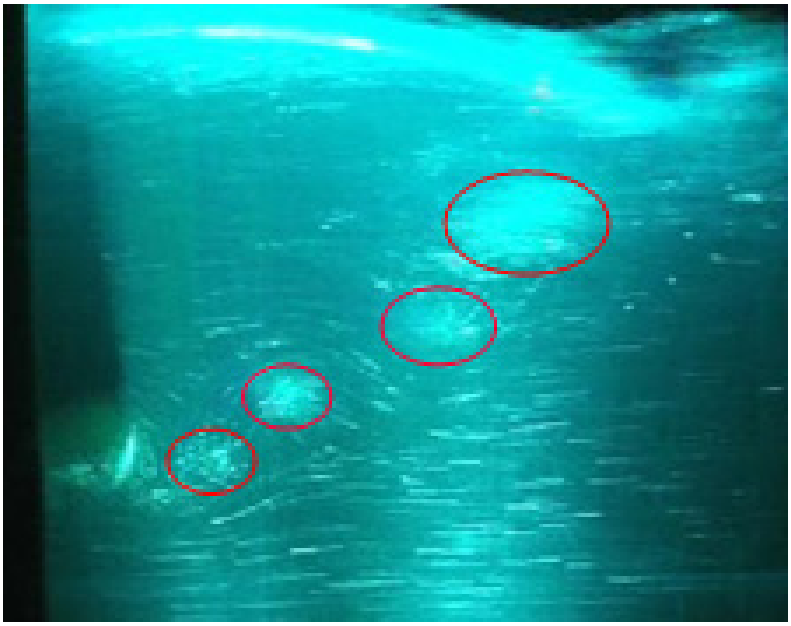

Figure 7.29. Preliminary visualization of the wake of an oscillating cylinder with rough strip showing four vortex structures in one half of the oscillation.

7.4.5. Higher harmonics in the spectral analysis of VIV response

Fourier spectra of the amplitude of oscillation are plotted for the cylinders with and without roughness strips and are shown in Figure 7.31 and Figure 7.32 for different velocities. From these spectra, it is observed that there is a major peak at the oscillation frequency. The most significant difference observed between the spectra of the cylinders with and without roughness strips is the increase in appearance of higher harmonic components. It has been previously demonstrated in Chapter 4 that the second harmonic components are observed at higher amplitude of oscillation in the smooth cylinder cases. This is attributed to the high Reynolds number of which the experiments were conducted. But in the case of cylinders with roughness strips the number of higher harmonics increased as well. The third and fourth higher harmonic components were exhibited and the amplitude of oscillation increased dramatically. The number of harmonic components increases with the velocity resulting in the increase in amplitude of oscillation. Williamson and Roshko's plot shows that as the amplitude of oscillation increases the number of vortices in the vortex structure might increase as shown in Figure 7.37. Jauvtis and Williamson (2004), in their two-degree of freedom VIV experiments, attributed the increase in amplitude of VIV to the increase in the strength of vortices being shed. Ziada

et al. (2005) noticed that in the case of finned tubes, even though the fins around the cylinder introduce streamwise vorticity and three-dimensional disturbances, it didn't aid in suppressing vortex shedding and instead it amplified the vortex shedding by concentrating a significant portion of the fluctuating energy into the vortex shedding frequency and its harmonic components. Occurrence of higher harmonics in the velocity fluctuations was noticed for finned tubes (Ziada et al. 2005) as shown in Figure 7.30. Ziada et al. (2005) noticed that the higher harmonic components increase as the fin density increased.

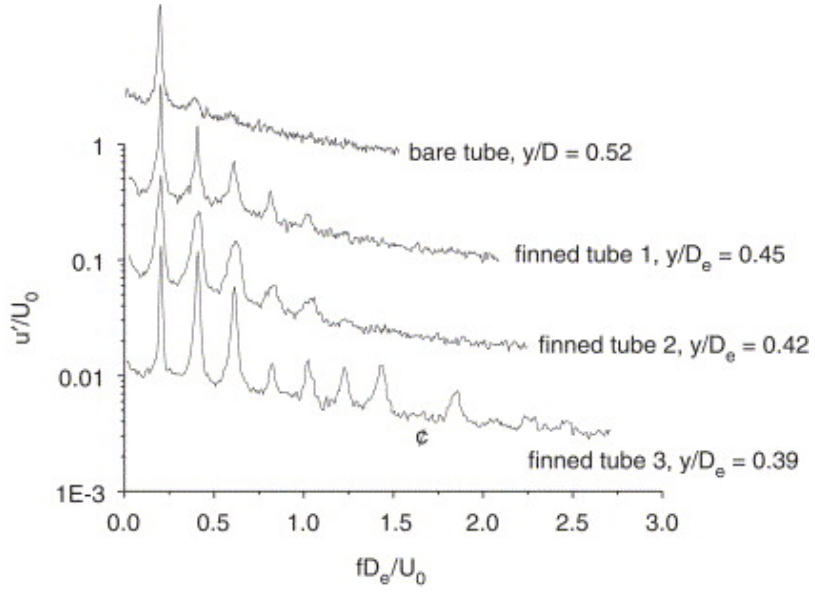

Figure 7.30. Spectra of velocity fluctuations for the bare and finned tubes. [Reproduced from Ziada et al. (2005)].

In a review paper on nonlinear stability theory (Stuart 1971), Stuart argues that for a boundary layer or shear layer, viscous and nonlinear terms cannot be neglected in the vorticity equation. Stuart attributes it to the terms arising from squares of the velocity fluctuations which would become comparable to the linear order terms for (ú/U≈3%). The inclusion of viscous and nonlinear terms leads to the generation of higher harmonics of the fundamental frequency of oscillation. For the finned case the enhancement of the higher harmonics of vortex shedding may be attributed to increase in the amplitude of velocity fluctuation (Ziada et al. 2005). Even though the scale of protuberances in the finned cylinder is several orders of magnitudes larger than the protuberance in the cylinders with roughness strips there are similarities in the response.

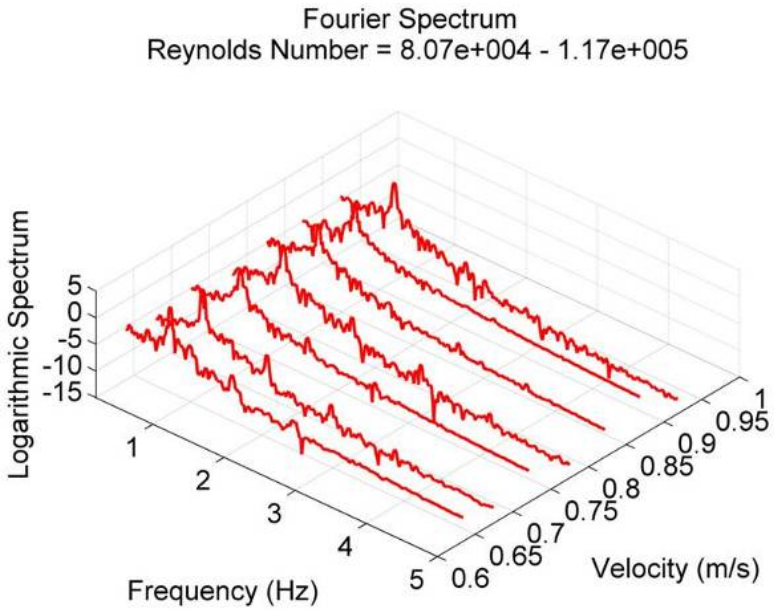

Figure 7.31 Power spectrum of displacement of smooth cylinder in VIV, as a function of velocity.

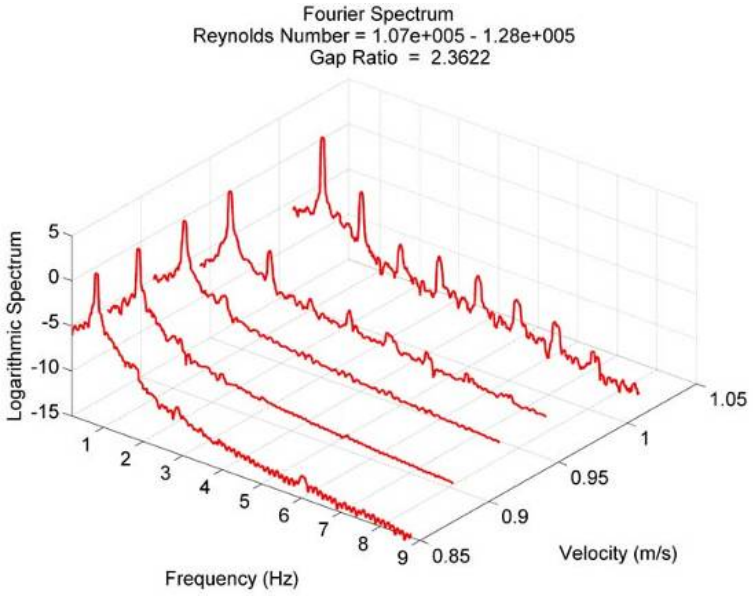

Figure 7.32 Power spectrum of displacement of 5″ cylinder with roughness strip (P80) in VIV, as a function of velocity.

7.4.6. Frequency of oscillation

The ratio of frequency of oscillation with respect to the natural frequency of the system in water showed interesting characteristic depending on the configuration of the

roughness strip. Results from the present experiments were classified in to two. This classification was based on the location of the separation point. The first classification included considered oscillating separation point lying within the bandwidth of the roughness strip. The second class included response where the roughness strips were just outside the bandwidth of the oscillating separation point and where the roughness strips interacts with the separated shear layer from the cylinder.

The upstream edge of the roughness strip at 80°

In this case the roughness strip and its elements interact with the shear layer separated from the cylinder. When the upstream edge of the roughness strip is at 80° it doesn't influence the separation point in most of the cases but it does influence the sher layer emanating after separation. In this case, the frequency of oscillation follows parallel to the Strouhal line $\left(\frac{0.2*U}{f_{n,water}D}\right)$ as shown in Figure 7.33. This implicates that the frequency of oscillation is locked on to the frequency of shedding rather than the natural frequency in water in the synchronization range. In the case of 5″ cylinder with P80 strips of width one inch, it behaves like a stationary cylinder but the constant is 0.185 rather than 0.2 to determine the frequency of oscillation using the Strouhal relation.

$$f_{osc} = f_{vs} = \frac{0.185*U}{D}$$

The amplitude of oscillation was reduced but the synchronization range was larger than in a smooth cylinder case as shown in Figure 7.34. In Figure 7.33 and Figure 7.34 the cases with four strips are plotted. The third and fourth strips are placed in the down stream side of the cylinder between angles of 117°-140°. In this case the roughness covered nearly 25% of the cylinder. In comparison with the two strip cases the four strip cases affected the amplitude in the reduced velocity range 4 to 6. Elsewhere it was having nearly the same magnitude and character as the two strip cases. The response character didn't change as the area of coverage of roughness increased from 12.5% (two-strips) to 25% (four-strips) emphasizing that the strategically located roughness was very effective in achieving the desired results, than in the cases where the roughnesses were distributed all around the cylinder.

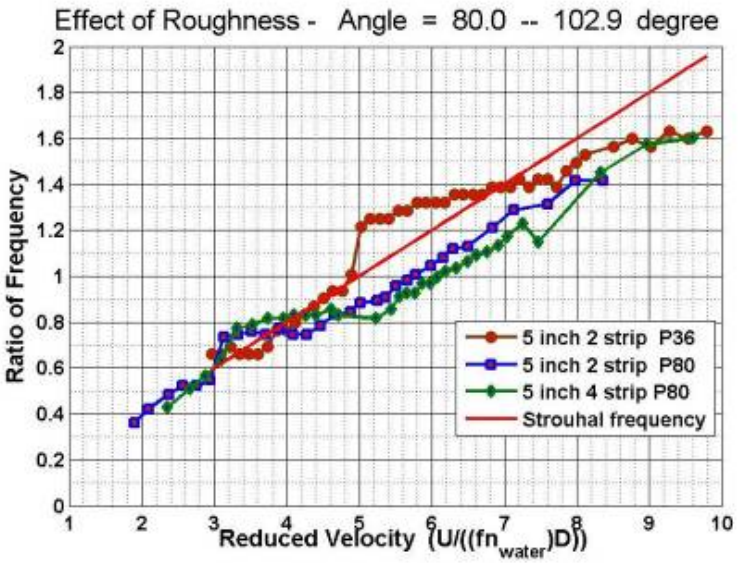

Figure 7.33. Compiled plot of ratio of response frequency (f*) for P36 and P80 roughness strips placed in between 80°– 102.9° symmetrically in the two strips case and two more strips placed symmetrically in between 117°-140° for 5″ cylinder as a function of reduced velocity.

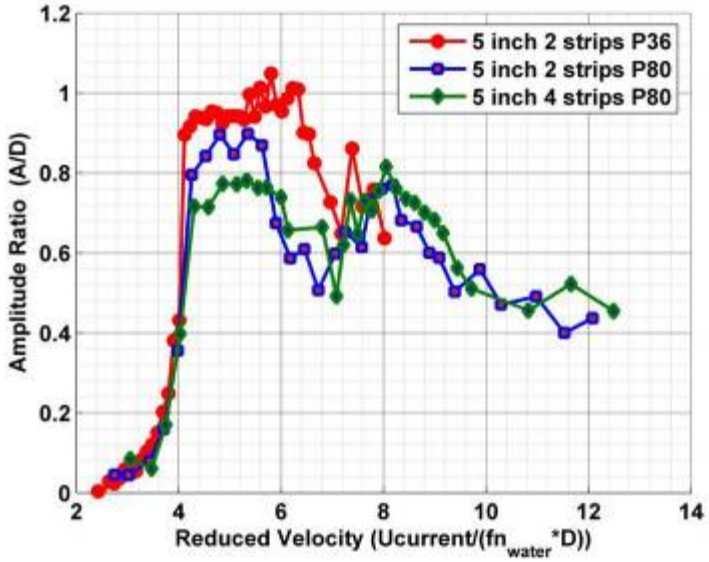

Figure 7.34. Compiled plot of amplitude ratio for P36 and P80 roughness strips placed between 80°– 102.9° symmetrically in the two strip case. In the four strip case and two more strips were placed symmetrically between 117°-140° for 5″ cylinder as a function of reduced velocity.

<u>The rear edge of the roughness strip at 80°</u>

In the case when the rear edge of the strip is located at 80° and the front edge located between 47°-64°, the frequency of oscillation locks to the natural frequency in

water (added mass calculated using potential theory). In the case of the 3.5″ cylinder, the frequency of oscillation initially increases and then curves downward to lock-in with the natural frequency in water as the reduced velocity is increased as shown in Figure 7.35 and Figure 7.43. As the frequency of oscillation curve curves downward toward the natural frequency in water, the amplitude of vibration starts increasing from the plateau of lesser amplitude vibration as shown in Figure 7.42 and Figure 7.45. Figure 7.41 compares the frequency ratio response of a 5″ cylinder with and without roughness strips. In the case of a cylinder with roughness strips, the locking on to the natural frequency is a perfect lock-in over a large range of reduced velocity. For the smooth cylinder, the locking of the frequency of oscillation with the natural frequency of the system in water was curved and this was attributed to the variation of the added mass because the actual added mass varies with the reduced velocity and with the amplitude of oscillation (Sumer and Fredsøe 1997). In the calculations, a constant potential added mass is used. But in the case of smooth cylinder VIV in air, due to the negligible added mass in comparison to the mass of the cylinder, a perfect locking on to the natural frequency of cylinder in air is observed.

In the case of the 3.5″ cylinder with four roughness strips attached, the frequency of oscillation locked in with the natural frequency in water as shown in Figure 7.35. For cylinders with two strips, the range of synchronization started at an earlier reduced velocity and a jump in the frequency of oscillation was observed at a reduced velocity equal to four. In the case of four strips, the range of synchronization started at an earlier reduced velocity and a jump in the frequency of oscillation was observed at a reduced velocity equal to 4.4.

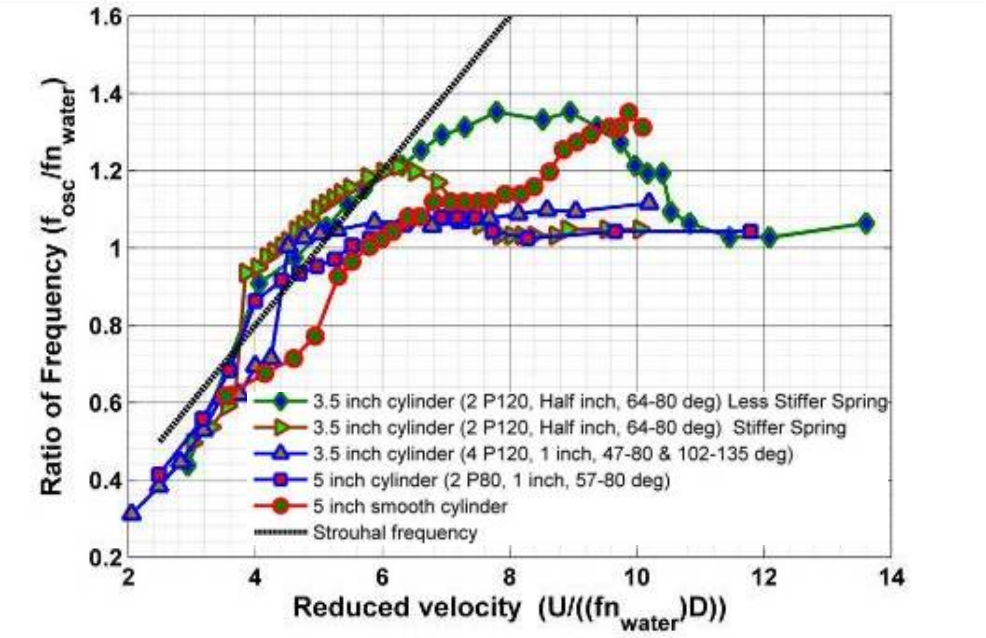

Figure 7.35. Compiled plot of ratio of response frequency (f*) for different configurations of roughness strip for 5″ and 3.5″ cylinder as a function of reduced velocity.

7.4.7. Change in character of the initial branch

Consider low Reynolds number and low mass and damping ratio VIV for a smooth cylinder. The initial branch character is shown in Figure 7.36. The VIV response within initial branch below reduced velocity of 4.3 is quasi-periodic and it locks-in with a value of 0.9 times the natural frequency in water. At a value of 4.7 it jumps to the upper branch which is about 1.04 times the natural frequency in water. In our experiments for a smooth cylinder case, a dent in the frequency ratio curve was observed in the initial branch regime and it is shown in Figure 7.41 and Figure 7.43. When a roughness strip was attached to the cylinder, the dent turns into a hump and the frequency increases above the Strouhal frequency as shown in Figure 7.35, Figure 7.36, Figure 7.41, and Figure 7.43. In comparison to the smooth cylinder, the amplitude of oscillation jumped at a lower value of reduced velocity and the synchronization started earlier than in the smooth cylinder case. Different configurations of the roughness strip and response are plotted in Figure 7.40, Figure 7.42, and Figure 7.45. In most of the cases the jump occurred at an earlier reduced velocity. In the case of the 5″ cylinder the jump in amplitude was nearly the same as in the smooth cylinder case as shown in Figure 7.40. In the case of 3.5″ cylinder,

the jump in the amplitude is lower in comparison to the smooth cylinder case as shown in Figure 7.42. In the plot of amplitude ratio versus the "true normalized reduced velocity," the characteristic change in the initial branch at an earlier reduced velocity is prominent as shown in Figure 7.38 and Figure 7.39. In Figure 7.38 and Figure 7.39, the difference in the initial branch response of smooth cylinder and the cylinder with rough strip is apparent in the higher Reynolds number cases. In the initial branch of the rough strip case, the response traverses through the parameter space of the 2S mode. In the case of the smooth cylinder the initial branch traverses the 2P mode regime. It is hypothesized that the characteristic change in the initial branch can be attributed to the roughness strip inducing earlier spanwise correlation and impacting the transition of wake states. The paper backing thickness (P) of the roughness strip increases the correlation length and the transition aided by the roughness element and the backing of the roughness strip. The above phenomenon may also be attributed to a high Reynolds number effect, which can be achieved only in the range where our experiments were conducted. Experiments designed to contrast high versus low Reynolds number behavior can be conducted in order to verify this.

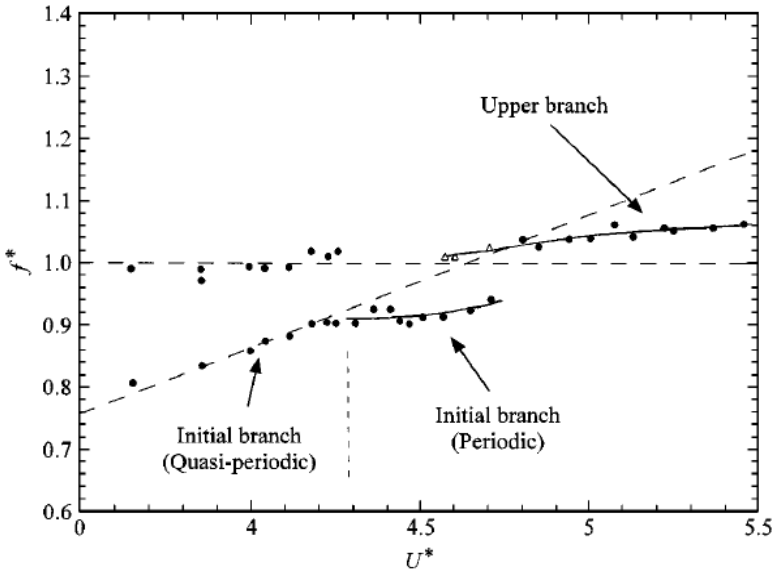

Figure 7.36. Frequency response plot of a VIV system with a low $(m^*+C_a)\zeta$. [Reproduced from (Khalak and Williamson 1999)].

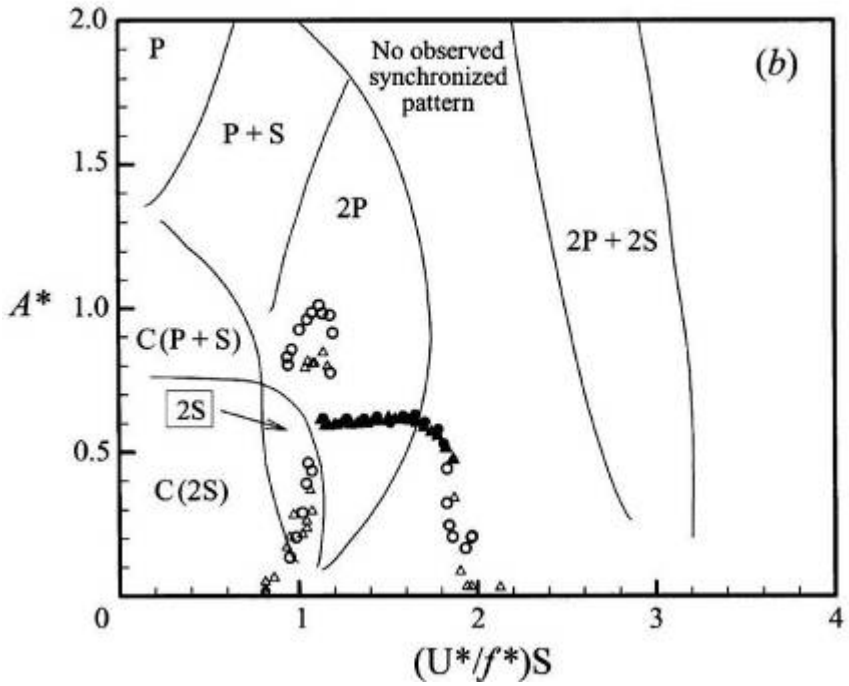

Figure 7.37. Williamson and Roshko plot interspersed with data of VIV systems with low $(m^*+C_a)\zeta$. [Reproduced from Williamson et al. (Williamson and Govardhan 2004)].

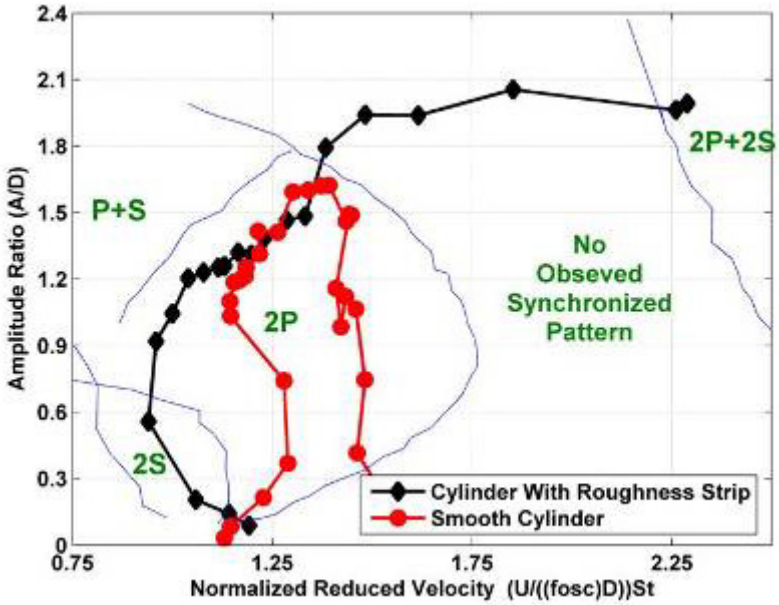

Figure 7.38. Response data of a 5″ cylinder with and without strips plotted using the "true normalized velocity" above the vortex mode regimes in Williamson and Roshko's map (Williamson and Roshko 1988).

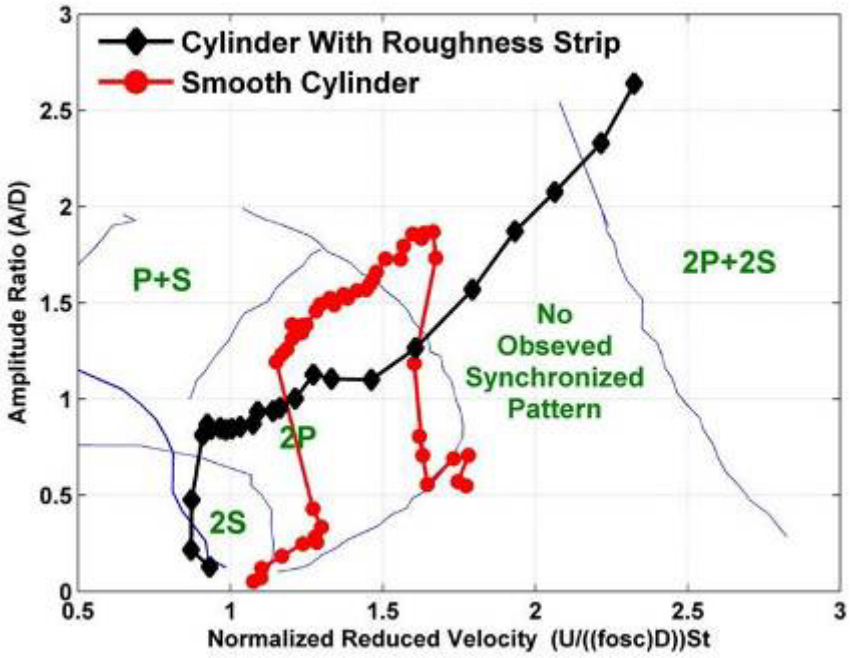

Figure 7.39. Response data of a 3.5″ cylinder with and without strips plotted using the "true" normalized velocity" above the vortex mode regimes in Williamson & Roshko's map (Williamson and Roshko 1988).

7.4.8. Roughness effects on the upper branch

In the plot of ratio of amplitude of oscillation versus the "true normalized reduced velocity", the upper branch jumps to a higher amplitude ratio as shown in Figure 7.38 and Figure 7.39. In Figure 7.38 and Figure 7.39, the amplitude of oscillation of cylinder with rough strip traverses into the parameter space with no observed synchronized pattern at higher values of "true normalized reduced velocity". The sustenance of VIV in this region can be hypothesized to result from the modification of flow pattern by extending the spanwise correlation by the roughness strip and velocity fluctuations by the roughness elements.

7.4.9. Amplitude of oscillation and width of synchronization range

Figure 7.40, Figure 7.42, and Figure 7.45 show the range of synchronization and the free response amplitudes, A/D, of transverse oscillation for a cylinder with and without the rough strips. For the 5″ cylinder case it is observed in Figure 7.38 that the response amplitude ratios for both the rough and smooth cylinders were nearly the same

until the smooth cylinder amplitude ratio reduces. An earlier reduction in amplitude ratio with respect to reduced velocity is observed for the case of 5″ smooth cylinder in comparison with the 3.5″ smooth cylinder as shown in Figure 7.40 and Figure 7.41. This earlier reduction in amplitude of oscillation for the 5″ smooth cylinder was attributed to the proximity of its operational Reynolds number to the critical regime. The roughness strips start taking effect at this point when the cylinder approaches the critical regime. Qualitatively, the strips help to sustain the vibration and also increase the vibration. In this case, the roughness strips were also able to increase the range of synchronization. This consequence can be attributed to straightening of the separation line by the roughness strip in the critical regime where the separation line for a smooth cylinder loses correlation of the vortex shed (Zdravkovich 1990a). One of the reasons for the extension of the synchronization regime can be related to the increase in correlation due to the roughness strips. Experiments performed by Hover et al. (1998) studied the nature of variation of force correlation with the reduced velocity and they divided the regime into five regimes. The fifth regime is the regime at the end of synchronization and the force correlation in this regime is nearly zero as shown in Figure 7.9. It can be hypothesized that in these cases the roughness strips are increasing the force correlation in this regime by straightening out the separation line and energizing the separated fluid with velocity fluctuations which are higher harmonics of the fundamental oscillation and then resulting in synchronizing the vibration with the shedding of vortices. In the case of a 5″ cylinder, the amplitude was limited due to the very close proximity to the free surface at these high amplitudes. The proximity of the cylinder to a free surface result in Coanda effect which was discussed in the previous chapter but with the roughness strip VIV was sustained.

In the case for the 3.5″ cylinder with the P120 strips placed between 64°-80°, the synchronization range starts earlier than the smooth cylinder. The initial amplitude of oscillation with the roughness strips is lower than the smooth cylinder and this is observed in other cases too with different roughness strip configurations which will be discussed later. The amplitude ratio of oscillation reached values of 2.7, which, to the author's knowledge, were never achieved before. Figure 7.42 and Figure 7.45 present two plots of the amplitude ratio of the 3.5″ cylinder with the P120 strips placed between 64°-80°. The difference between these two experiments is that they use different stiffness, so

their synchronization regimes are in different Reynolds number range. In Figure 7.45, it is observed that the amplitude ratio response for a less stiff spring and stiffer spring are different. The reason for this observation is attributed to the different Reynolds range in which they are operating. The range where the amplitude ratio was lower than the smooth cylinder was shorter for the case operating in high Reynolds number range in comparison to the case which was operating at a lower Reynolds number range. In the Reynolds number graph (see Figure 7.46), it is seen that the increase in amplitude ratio happens nearly at the same Reynolds number in both cases. This strongly advocates the existence of a critical Reynolds number based on roughness elements above which the effect of roughness strip is categorically different as shown in Figure 7.46. The analysis based on the critical roughness number is discussed in the next Section.

In the case of 3.5″ cylinder the amplitude of oscillation was reduced below the critical Reynolds number invariably with any configuration of the roughness strips as shown in Figure 7.45 and Figure 7.46. In some cases, the synchronization range exists for reduced velocity as high as 16. In Figure 7.45 for all the configurations that were used the synchronization range never ended due to the lab's limitations.

In Figure 7.46, for the 3.0″ cylinder case, the amplitude of oscillation and the range of synchronization reduced dramatically and even at high reduced velocity they didn't show as high amplitude of oscillation as the 3.5″ cylinder. In this case, VIV was suppressed. This can be attributed to the critical Reynolds number that must be reached before the roughness strips start increasing the amplitude and preserve the VIV. Due to the restriction of the channel capacity, higher Reynolds number could not be achieved for the 3.0″ cylinder. Due to time and resources restriction different configuration of roughness strip weren't performed for this particular case which is recommended for future work.

Figure 7.20 shows that the fluctuating pressure varies a lot between the 50°- 80° from the stagnation point. It is also seen that the fluctuating pressure increases with the Reynolds number and the pressure distribution can be drastically changed by right amount of roughness which is qualified by the operating Reynolds number (Figure 7.19).

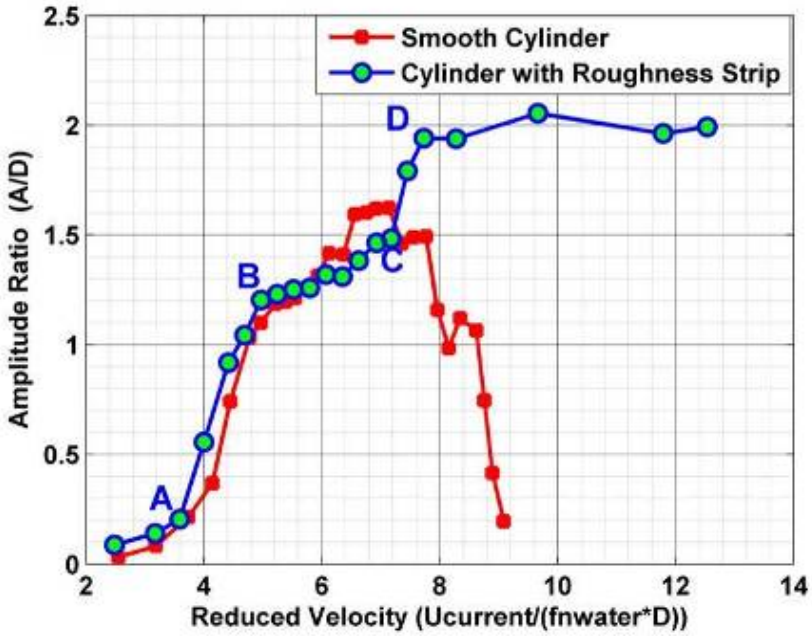

Figure 7.40. Comparison of the amplitude ratio and range of synchronization of a 5.0″ cylinder with and without roughness strip.

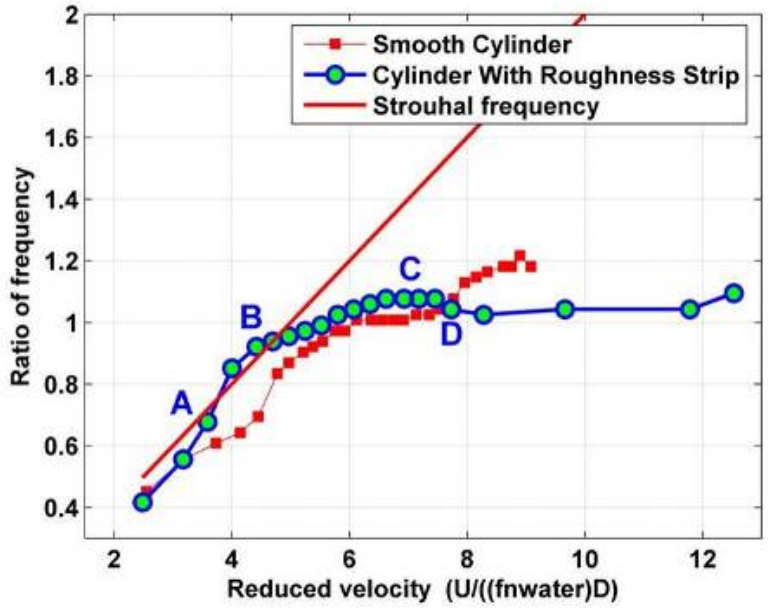

Figure 7.41. Comparison of the frequency ratio of a 5.0″ cylinder with and without roughness strips.

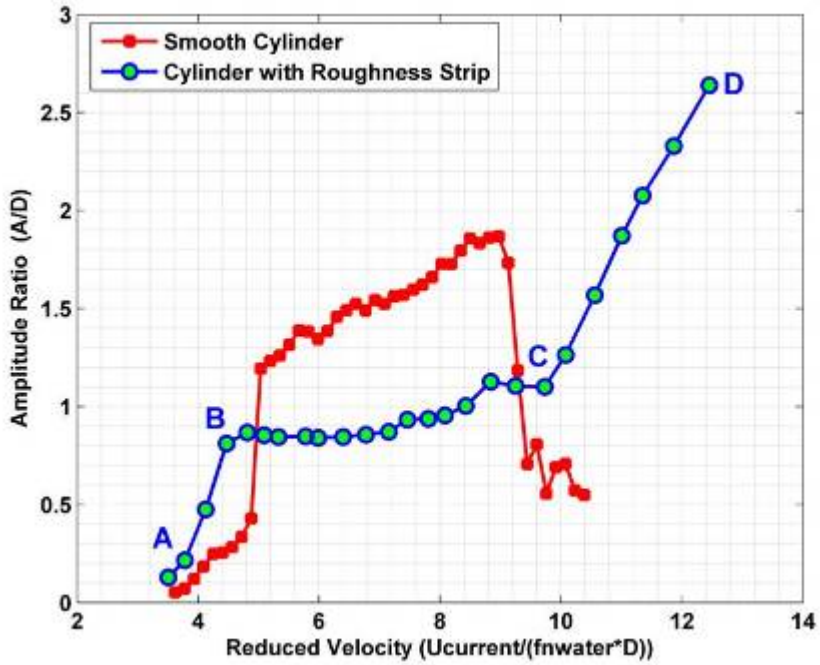

Figure 7.42. Comparison of the Amplitude ratio and range of synchronization of a 3.5″ cylinder with and without roughness strips.

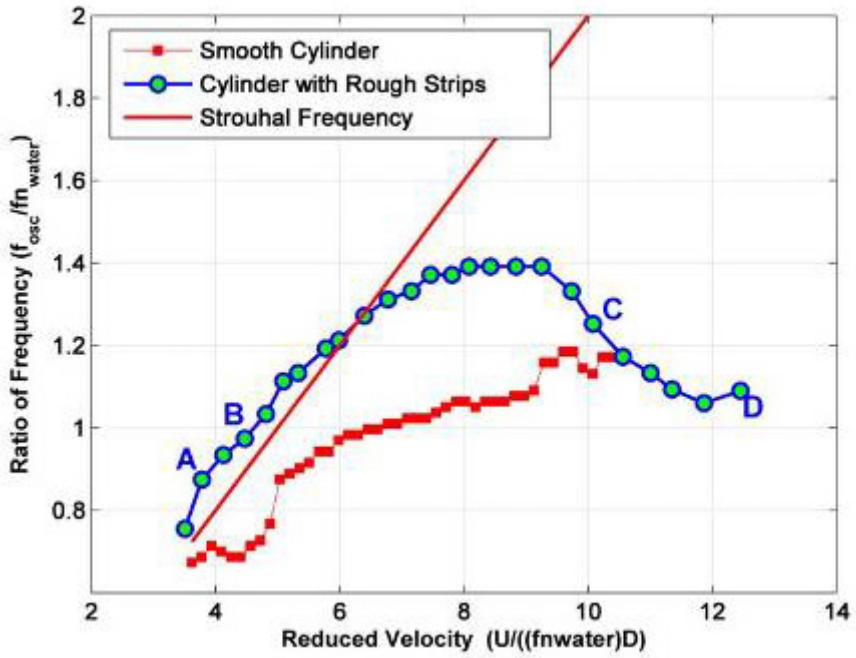

Figure 7.43. Comparison of the frequency ratio of a 3.5″ cylinder with and without roughness strips.

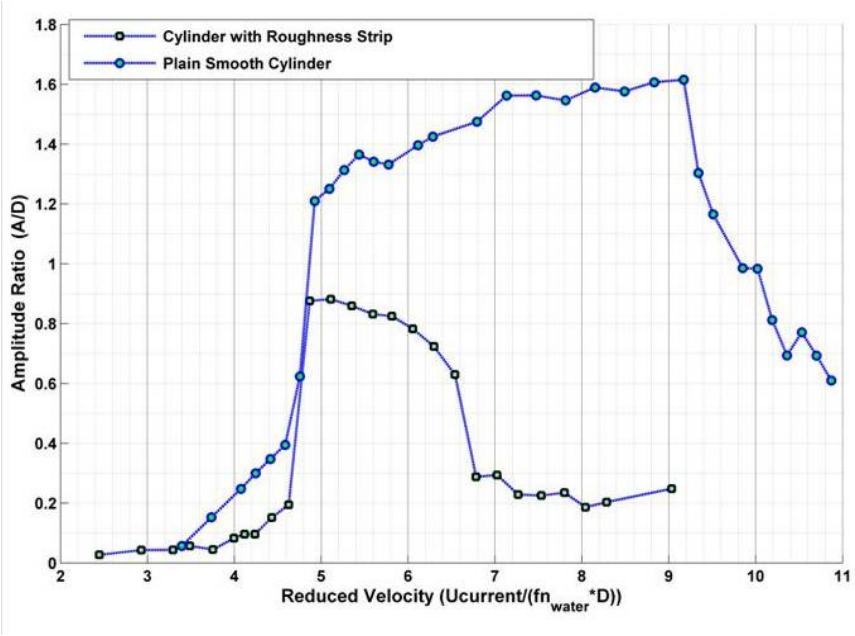

Figure 7.44. Comparison of the amplitude ratio and range of synchronization of a 3.0″ cylinder with and without roughness strip.

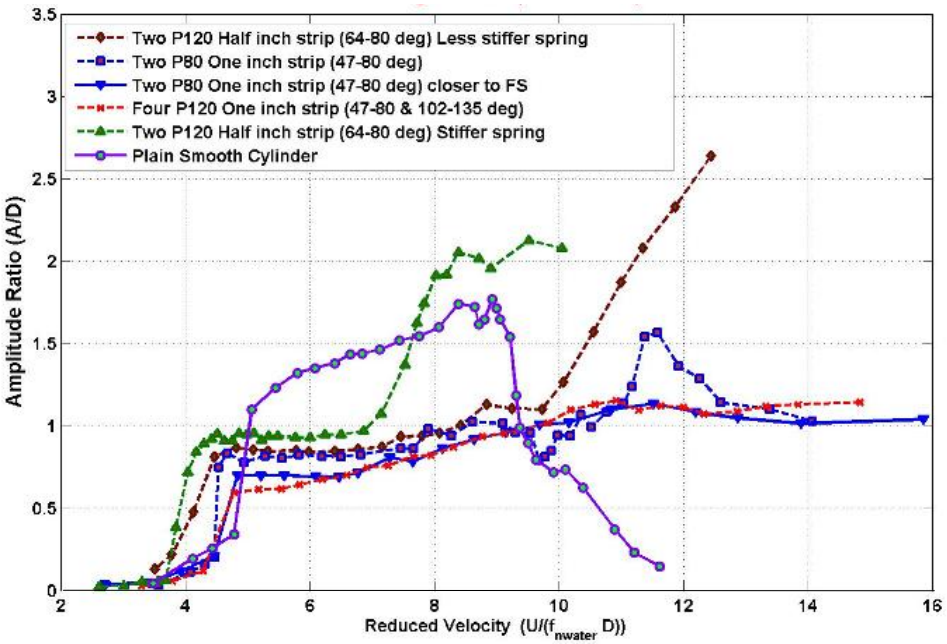

Figure 7.45. Response of 3.5″ cylinder with different configuration of roughness in comparison with the smooth cylinder. The synchronization regime did not end. In all cases at least two roughness strips are placed 80 degree from the mean stagnation point.

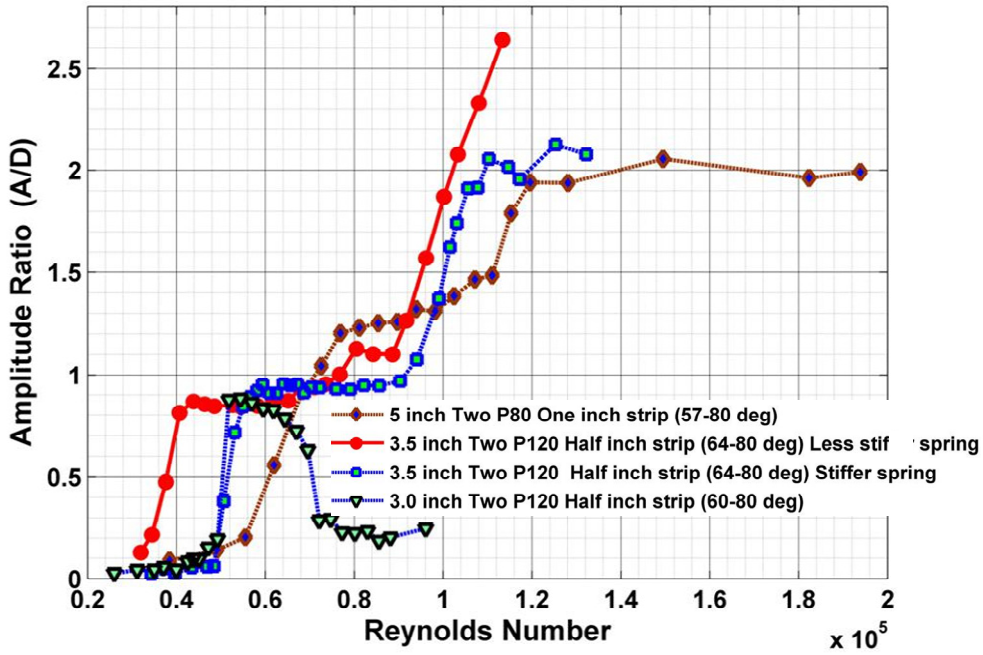

Figure 7.46. Response of 3.0″, 3.5″, and 5″ cylinder with roughness strips placed nearly at the same angle but the Reynolds number of the roughness were different. This figure shows the difference in characteristic response that can be achieved.

7.4.10. Critical roughness height and Reynolds number

The boundary layer transition induced by surface roughness is a more complicated phenomenon (Morkovin 1990). The classification of the effect of the roughness elements on the boundary layer is done based on the size of the roughness elements relative to the boundary layer thickness. If the roughness elements lie completely within the laminar sublayer it is argued that the roughness has least effect on the flow (Nikuradse 1933). The surface is regarded as hydraulically smooth or rough based on whether the roughness elements are completely embedded or not in the laminar boundary layer. When the height of the roughness elements is on the order of the boundary layer thickness of the laminar layer, horseshoe eddies are shed around the roughness element and aid in transition of the boundary layer from laminar to turbulent (Schlichting 1979). In the case of distributed roughness turbulent "spots" are formed behind the roughness element above a critical Reynolds number (Braslow 1960). Morkovin (Morkovin 1990) tries to explain partially what might be happening behind the rough particles in a sandpaper. In the case of sandpaper an agreement has never been

reached in which k or Re_k transition occurs, due to the random distribution of the sandpaper particle and statistical non-uniformities. The transition for a three-dimensional roughness is by the formation of hairpin eddies behind the roughness particle, but for a sandpaper the transition becomes complex and complicated because the elements are closely packed.

Several authors have come up with the concept of critical roughness. According to them critical roughness is the roughness size below which the flow is not affected by the roughness elements (Dryden 1953; Schlichting 1979). The critical roughness size is based on critical roughness Reynolds number (Dryden 1953). The critical roughness height for a single roughness elements (like tripping wires which would induce complete transition to turbulent flow for a flat plate) is $\frac{Uk}{\nu} \approx 826$ (Dryden 1953), where k is the size of the roughness element. For a distributed roughness, the critical roughness height is $\frac{Uk}{\nu} \approx 120$ (Schlichting 1979). In coming up with the critical roughness size for transition, Dryden, made use of the ratio of roughness height to the displacement thickness of the boundary layer at the roughness location (Schlichting 1979). Igarashi (1985; 1986) observed critical roughness number range for a tripping wire attached to the cylinder as $620 \leq \frac{Uk}{\nu} \leq 1220$ and turbulator or vortex generators attached to the cylinder as $600 - 700 \leq \frac{Uk}{\nu} \leq 1000 - 1200$.

Bradshaw (2000) argues that roughness does affect the flow if the flow is turbulent even if the size of the roughness element is smaller than the viscous sublayer.

In Figure 7.47 and Figure 7.48, the VIV response was plotted in terms of Re_k, and Re_{k+P}, where Re_k is the Reynolds number pertinent to the roughness element size (k) and where Re_{k+P}, is the Reynolds number pertinent to thickness of roughness strip (k+P). In Figure 7.48, it was observed, in the case of the 3.5″ and the 5″ cylinders with different operational Reynolds number (Re) the results collapsed evidencing that there is a critical value for the $Re_{k+P} \approx 600 - 700$. Above this critical value, the jump in the amplitude of oscillation to a higher value was observed (Figure 7.48). In Figure 7.47, the VIV response for both the cases of the 3.5″ and the 5″ cylinder with different operational Reynolds

number (Re) was plotted in terms of Reynolds number Re_k, and the results didn't collapse as well as in Figure 7.47. In Figure 7.47, for the case of the 3.5″ cylinder with different operational Reynolds number (Re) the plots collapsed (Figure 7.46). The jump in the amplitude of oscillation was observed above a critical value for the $Re_k \approx 120$ and it co-occurred with the $Re_{k+P} \approx 600$ -700. In the case of the 5″ cylinder the jump to high amplitude was observed for $Re_k \approx 180$ and it coincided with the $Re_{k+P} \approx 600$ -700. In the case of the 5″ cylinder, $Re_k \approx 120$ was achieved right after the unobvious early jump from initial to upper branch, Point A to Point B in Figure 7.40, and this could the reason why the amplitude was not affected. In the case of the 5″ cylinder the jump from the upper branch occurred at $Re_{k+P} \approx 600$ -700 even though $Re_k > 120$ were achieved earlier. In the case of 3.5″ cylinder with less stiff spring $Re_k \approx 120$ was achieved at the end of synchronization range of the smooth cylinder as seen in Figure 7.45 and the amplitude reduced by nearly half until $Re_{k+P} \approx 600$ -700 and $Re_k \approx 120$ was reached. In the case of the 3.5″ cylinder with stiffer spring the synchronization range was shifted to higher velocity/Reynolds number because of the shift in natural frequency. This implies $Re_k \approx 120$ was achieved at a lower reduced velocity as seen in Figure 7.45 and the amplitude plot was not less affected than for the 3.5″ cylinder case with less stiff spring. In all the 3.5″ cylinder cases with stiff and less stiff springs, the jump from the upper branch to higher amplitude of oscillation occurred at $Re_{k+P} \approx 600$ -700. The critical Reynolds number seen in the above cases $Re_{k+P} \approx 600$ -700 and $Re_k \approx 120$ is close to the critical Reynolds number observed for three-dimensional roughness element and two-dimensional roughness element (Schlichting 1979). In the above cases analyzed, the synchronization range belonged to $Re_D > 5 \times 10^4$.

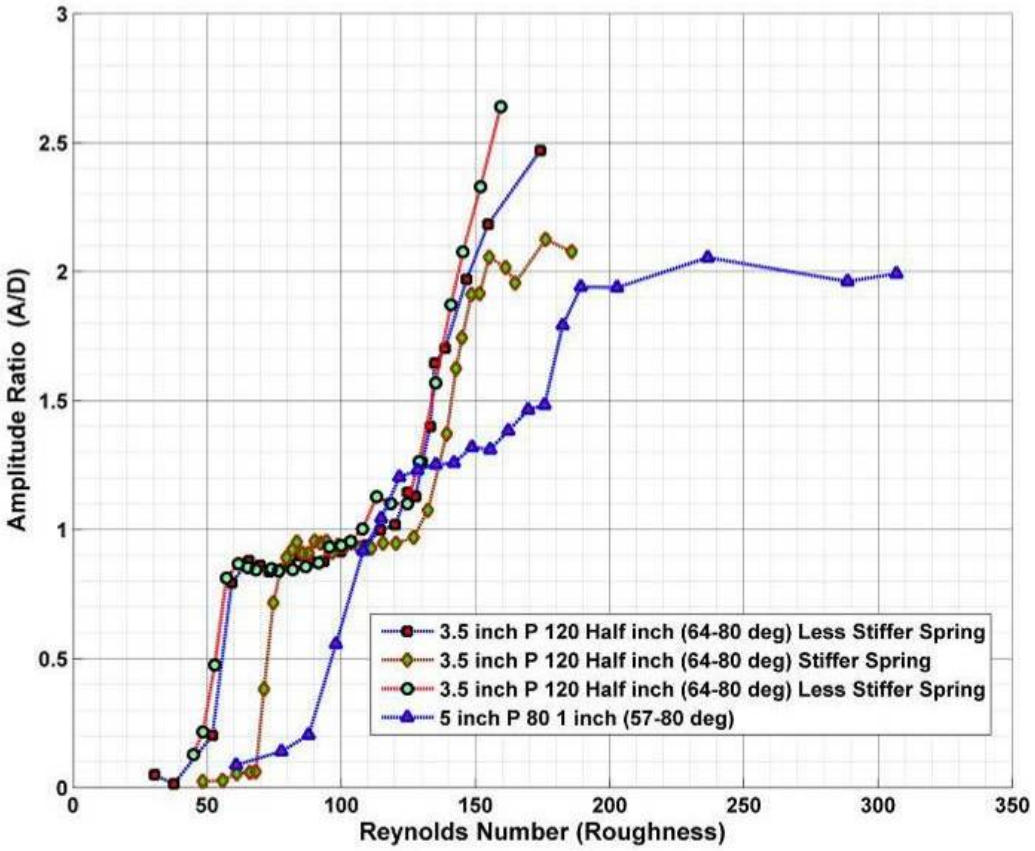

Figure 7.47. VIV Response of the 3.5″ and 5″ cylinders as a function of the Re_k.

Based on the critical Reynolds number in the above discussion, the following can be written

$$\frac{U(k+P)}{\nu} = 600, \tag{7.1}$$

$$\frac{Uk}{\nu} = 120. \tag{7.2}$$

From displacement thickness calculations,

$$\frac{\delta^*}{D} = \frac{0.4085}{\sqrt{\mathrm{Re}}} \text{ at } 60°. \tag{7.3}$$

Equation (7.1) and (7.2) can be rewritten as (7.4) and (7.5)

$$\frac{k+P}{D} = \frac{600}{\mathrm{Re}}, \tag{7.4}$$

$$\frac{k}{D} = \frac{120}{\mathrm{Re}}. \tag{7.5}$$

Therefore combining equation (7.4) ,(7.5), and (7.3), we can rewrite the relation as

$$\frac{k}{\delta^*} = \frac{120}{0.4085\sqrt{\mathrm{Re}}}, \tag{7.6}$$

$$\frac{k}{\delta^*} = 0.92, \text{ for Re} = 10^5, \tag{7.7}$$

$$\frac{k+P}{\delta^*} = 4.6447, \text{ for Re} = 10^5. \tag{7.8}$$

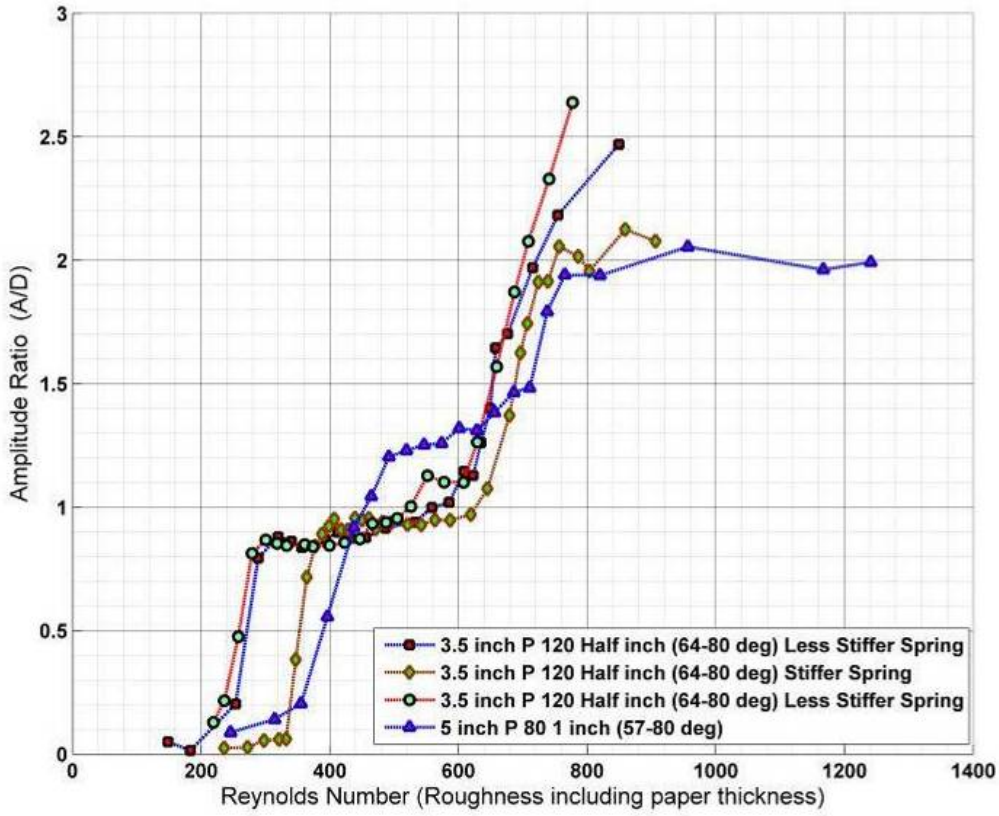

Figure 7.48. VIV Response of the 3.5 and 5″ cylinders as a function of the Re_{k+P}.

The experimental results for the high amplitude vibration cases of the 3.5″ and the 5.0″ cylinders with roughness strips are presented in Figure 7.49 through Figure 7.52 based on the ratio of roughness height to the boundary layer and ratio of roughness height to the displacement thickness. The effect of roughness can be analyzed using the roughness height in comparison with the displacement and boundary layer thickness. In Figure 7.51 and Figure 7.52 the displacement thickness for the 5″ cylinder is recalculated at 64° in order to compare with the 3.5″ cylinder. In our experiments, the transition in the response of VIV is observed when the ratio of roughness element size (k) to the

displacement thickness reaches one $\left(\frac{k}{\delta^*} \approx 1\right)$ and the ratio of roughness strip thickness (k+P) to the boundary layer thickness reaches 1.6 - 1.7$\left(\frac{k+P}{\delta^*} \approx 1.6-1.7\right)$. When $\frac{k}{\delta^*} < 1$, roughness elements are completely submerged underneath the displacement thickness and lower amplitude of oscillation is observed in the case of 3.5″ cylinder with roughness strips in comparison to the smooth cylinder (Figure 7.51). When the roughness element is larger than the displacement thickness it results in higher amplitude of oscillation (Figure 7.51). The reason for the above observation can be hypothesized to be the following: when $\frac{k}{\delta^*} \geq 1$, then Re_k exceeds 120 and this is the Reynolds number value around which transition in wake occurs behind a circular element and therefore when $\frac{k}{\delta^*} \geq 1$ small eddies/vortices are formed behind the roughness elements. Those energize the flow and result in delayed separation. To confirm the above statement visualization of the details behind roughness elements are needed.

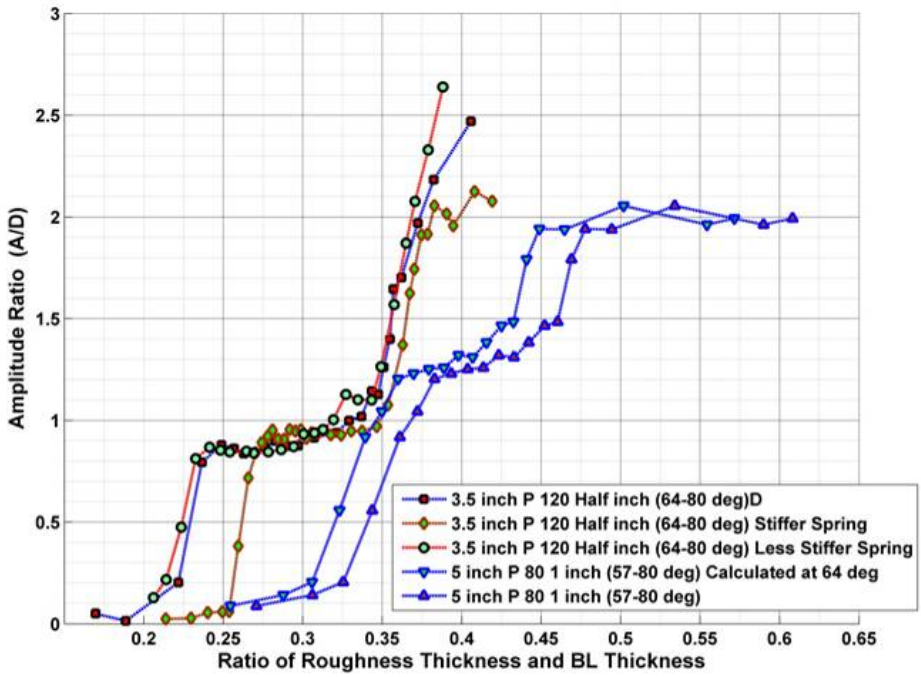

Figure 7.49. VIV response of the 3.5″ and the 5″ cylinders as a function of the ratio of roughness element size to the boundary layer thickness (k/δ).

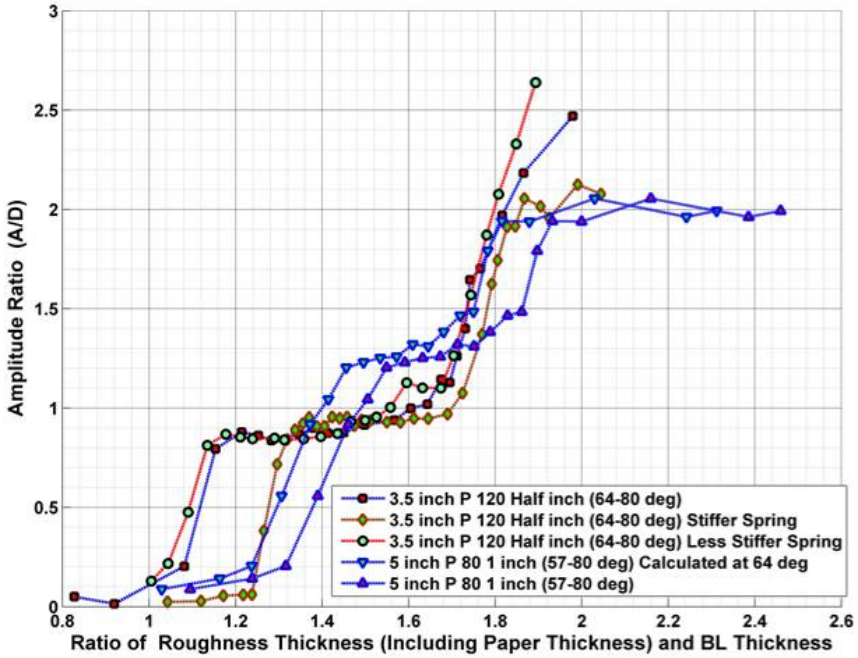

Figure 7.50. VIV response of the 3.5″ and the 5″ cylinders as a function of the ratio of the roughness element size plus backing paper thickness to the boundary layer thickness ((k+P)/δ).

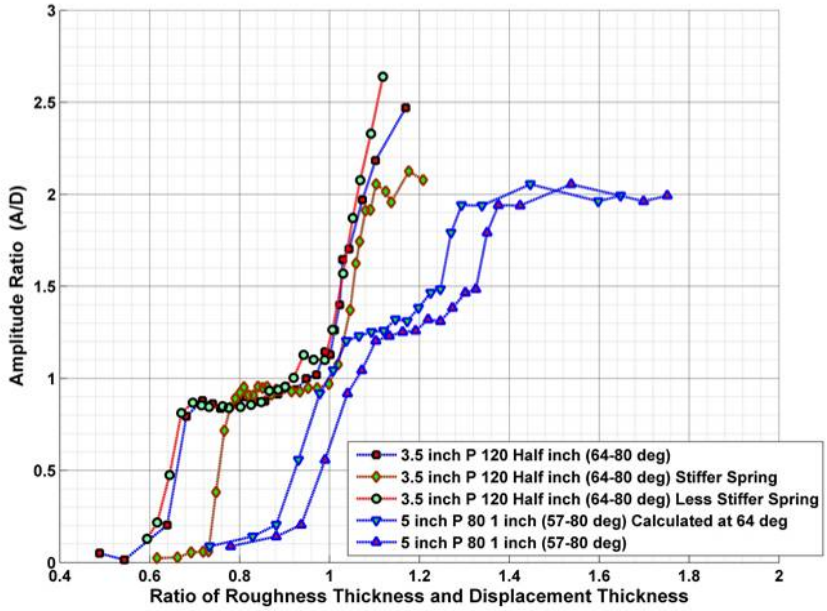

Figure 7.51. VIV response of the 3.5″ and the 5″ cylinders as a function of the ratio of roughness element size to the displacement thickness (k/δ^*).

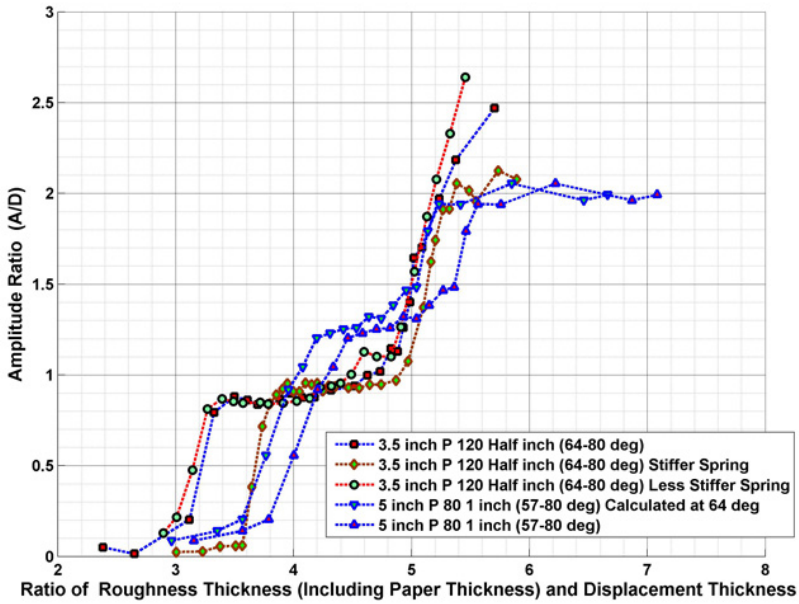

Figure 7.52. VIV response of the 3.5″ and the 5″ cylinders as a function of the ratio of roughness element size plus backing paper thickness to the displacement thickness ((k+P)/δ*).

The following conclusions are made from Figure 7.40 and Figure 7.42 based on the observation in the previous Sections:

- Roughness effects are prominent regardless of its relative magnitude to δ* or δ. Due to presence of roughness in a laminar boundary layer there is pressure loss in the flow around the cylinder and this would explain the loss in the amplitude of oscillation. The above statement was observed in Figure 7.49 to Figure 7.52.
- When $k > \delta^*$ it brings considerable momentum from the outer flow into the boundary layer. Eddies that are already generated at the edge of the roughness strips by tripping the boundary layer interact more vigorously with the roughness elements when $k > \delta^*$.
- For $k \approx \delta^*$ the vorticity generated by roughness is on the order of boundary layer vorticity and this enhances the strength of the large vortices because the boundary layer scale vorticity is absorbed into the large scale vortices.

- In Figure 7.40, point B matched for both smooth cylinder and cylinder with roughness strip. Concurrently at B, $Re_k = 120$, k introduces friction and results in pressure loss which would cause reduction in A/D, since $k = \delta^*$ at this Re_k it starts bringing turbulence in from higher momentum flow thus generating vorticity still at the boundary layer scale and therefore absorbable by the large vortex which counterbalances the friction change in A/D that we hypothesized.
- In Figure 7.40, point C coincides with the beginning of the desynchronization regime for a smooth cylinder. At point C in the case of 5″ cylinder with rough strips Re_{k+p} is approximately 750. When $Re_{k+p} > 600$ complete transition of laminar boundary layer to turbulent occurs (Schlichting 1979). At point C $Re_k > 120$ this in conjunction with the tripped boundary layer energizes by increasing vorticity. At point C the flow is tripped by the edge of the roughness strip and increase in correlation of transition is achieved thus resulting in sustenance of VIV and higher amplitude due to straight line separation.
- At point D for a 5″ cylinder, the cylinder is very close to the free surface. This is the upper bound for A/D and thus an endless increase in A/D is not observed as in the 3.5″ cylinder case. The interesting observation is that the presence of roughness strips was able to maintain VIV even in such a close proximity to the free surface as shown in Figure 7.40.
- Figure 7.42 shows for $Re_k < 120$ ($k < \delta^*$) a reduction in the amplitude of oscillation. When k is completely submerged in the displacement thickness, it still modifies the flow resulting in pressure loss due to the friction and thus reduces the amplitude of oscillation.
- In Figure 7.42 at Point C, the end of synchronization of the smooth cylinder VIV by coincidence of two phenomena, $Re_k = 120$ due to the roughness elements was achieved in the case of the cylinder with roughness strips. At $Re_k = 120$ momentum is added from the shed eddies behind the roughness elements causing continuous increase in A/D. Concurrently, $Re_{k+p} = 600$ also

occurs and this is the Reynolds number at which complete transition occurs for a two-dimensional roughness for $Re > 1 \times 10^5$ (Schlichting 1979).

7.4.11. Analysis of the spectral content

The spectral contents were studied between the bare smooth cylinder cases and the cylinders with roughness strips. To understand the change in the wake state, a direct method would be to use flow visualization techniques or wake velocity measurements. Since in our experiments flow visualization techniques or wake velocity measurement, and force measurement weren't done, the spectral content of the displacement was used to interpret the difference in the response. The influence of the higher harmonic components in the forces is less pronounced in the displacement spectrum in comparison to the force and wake velocity spectrum. To unveil the higher harmonic components, logarithmic spectra of the displacement histories were plotted. In the present high Reynolds number experiments, prominent higher harmonics components are seen for both the bare cylinders and the cylinders with rough strips. The reduced velocity values at which the domination of a particular higher harmonic component occurs are different for both cases. The higher harmonic components are present as the multiples of the oscillation frequency and where oscillation frequency is the same as the primary shedding frequency (forcing frequency) during lock-in. The higher harmonic components are the manifestation of the multiple vortices shed in one oscillation period. This proposes that the wake structure has regrouped in a distinctly separate manner for cylinder with rough strips. This regrouping has resulted in an increase in the amplitude and also an increase in the range of synchronization (Figure 7.40 and Figure 7.42).

To shed more light in the difference in response observed for cylinder with and without roughness strips as in Figure 7.40 and Figure 7.42, the spectral responses of these cases are analyzed.

For 3.5″ cylinder, the spectral contents corresponding to the reduced velocity for the whole range of experiments are plotted in Figure 7.53 through Figure 7.64. The bare cylinder and the cylinder with roughness strips are plotted alternatively in the order of the reduced velocity from Figure 7.53 to Figure 7.64. The spectrum plots explore the variation in magnitude of power in the frequency of oscillation, and the shift in

distribution of power and the growth of the harmonic components. In the case of smooth cylinder for reduced velocity less than 4.9 (Figure 7.53) the spectrum is characterized by less power in the oscillation frequency and broad-banded.

In the case of cylinder with roughness strips for reduced velocity less than 4.9, the spectral content is characterized by the narrow-banded spectrum with a peak at the oscillation frequency as shown in Figure 7.54. The stronger and narrower peak in the case of cylinder with roughness strips confirms earlier synchronization. The reason for the stronger and narrower peak can be attributed to the increase in correlation length of the spanwise shedding process and the modification of the wake structure by the roughness strips as shown in Figure 7.39. This is observed for all the cases with roughness strips regardless of the position, thickness, and the size of roughness elements as shown in Figure 7.45. The above reduced velocity range refers to the range before the jump from initial branch to upper branch. For the smooth cylinder case, the spectral contents for the reduced velocities between 4.9 and 7.1 are shown in Figure 7.55 and Figure 7.57. In these two figures, the spectra have more prominent peaks at the second and third harmonic components of the oscillation frequency. For the cylinder with roughness strips, the spectral contents for the reduced velocity between 4.8 and 7.2 are shown in Figure 7.56 and Figure 7.58. In these two figures, the spectra have small peaks at the second and third harmonic components of the oscillation frequency for reduced velocity less than 6. In Figure 7.56 and Figure 7.58 in comparison with Figure 7.55 and Figure 7.57, the magnitude of the power in the primary oscillation frequency is lower than the value of the primary oscillation frequency. In Figure 7.56 and Figure 7.58, the frequency of oscillation for a cylinder with roughness strips moves closer to the shedding frequency contrary to the bare smooth cylinder which tries to lock-in with the natural frequency (Figure 7.43).

As the reduced velocity increases above reduced velocity of 7.2, there is a steady increase in amplitude ratio for the smooth cylinder and there is also a modest steady increase in amplitude ratio for cylinder with roughness strips as shown in Figure 7.42. In the smooth cylinder case, the spectral components for the reduced velocity above 7.2 are shown in Figure 7.59 and Figure 7.61. In these figures the spectra have more prominent peaks at the second harmonic components of the oscillation frequency. In the case of the

cylinder with roughness strips the power in the higher harmonic components of the oscillation frequency are reduced but still present, as shown in Figure 7.60 and Figure 7.62.

Above reduced velocity of 9.6, for the smooth cylinder case, the spectral components are shown in Figure 7.63. In these figures the spectra at the primary oscillation frequency become broad banded and it has no conspicuous peaks at the second harmonic or third harmonic components of the oscillation frequency.

Above reduced velocity of 9.6, for the cylinder with roughness strips, the spectral contents are shown in Figure 7.62 and Figure 7.64, and in these figures the primary oscillation frequency in the spectrum are narrow banded and it has prominent peaks at the second harmonic or third harmonic components of the oscillation frequency.

At reduced velocity higher than 11 and when the ratio of amplitude of oscillation reached the value of 1.9, the spectral contents had prominent second harmonic and as the reduced velocity increased to 11.9 the third harmonic peak came into prominence and it continued for reduced velocity of 12.5 and the amplitude of oscillation reached 2.7. Tests were stopped at that point to prevent damage to the LTFSW Channel.

The following conclusions are hypothesized from the spectral analysis of the 3.5″ smooth cylinder and with roughness strips attached:

- For reduced velocity less than 4, there are multiple peaks at the shedding and natural frequency of the system. The shedding character is predominantly the regular Kármán vortex shedding, that is the 2S mode of vortex shedding.
- For reduced velocity greater than 4, and less than 4.9, in the case of smooth cylinder the peak at the oscillation frequency is broad banded and there are no conspicuous higher harmonics observed.
- For a cylinder with roughness strips, in the cases for reduced velocity greater than 4 and less than 5, a strong peak at the oscillation frequency and peak at the third, fourth and fifth harmonics of the oscillation frequency (Figure 7.54) were observed. This implies that 2S and P+S or 2P and 2S type of wake structures along the span occurs. The roughness strips transitions the wake from 2S to P+S or 2P and 2S behind the cylinder at an earlier reduced velocity. The observed strong peak at the oscillation frequency is also attributed to the correlation

increase aided by the roughness strips. The transition in the wake structure from 2S to P+S or 2P and 2S along the span near the jump from initial to upper branch had been observed by Hover et al. (2004) and Davis (2001) in their work on the three dimensionality of vortex shedding.

- For a cylinder with roughness strips, in the cases for reduced velocity greater than 10.6, a strong peak at the oscillation frequency reappears after it has been denigrated between reduced velocity 9 and 10. The reappearance of strong peak at oscillation frequency for reduced velocity greater than 10.6 was associated with peak at the second harmonic, proposing a 2P + 2S structure present which can be corroborated by overlaying the response on the Williamson and Roshko map (Figure 7.39). For reduced velocity greater than 11.3, strong peaks were associated with multiple harmonics at second, third and fourth harmonics proposing a wake structure where four vortices are shed per oscillation cycle that is 4P (Figure 7.29).
- In the case of the smooth cylinder, for reduced velocity greater than 10.6, the frequency spectrum become broad banded and the synchronization range ended due to the loss in spanwise correlation length.

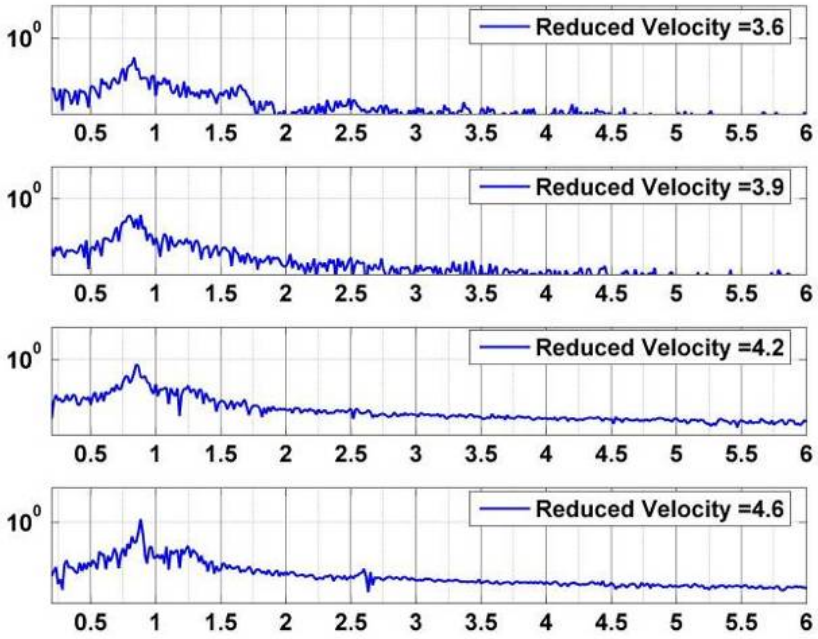

Figure 7.53. Spectra of displacement time series for a 3.5″ smooth cylinder for reduced velocity, 3.6 - 4.6.

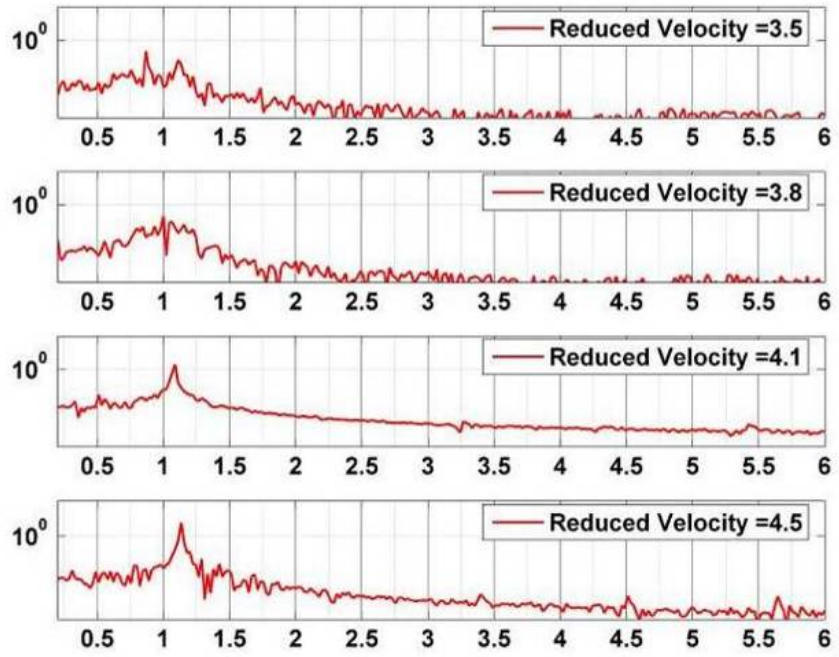

Figure 7.54. Spectra of displacement time series for a 3.5″ cylinder with roughness strip for reduced velocity, 3.5 - 4.5.

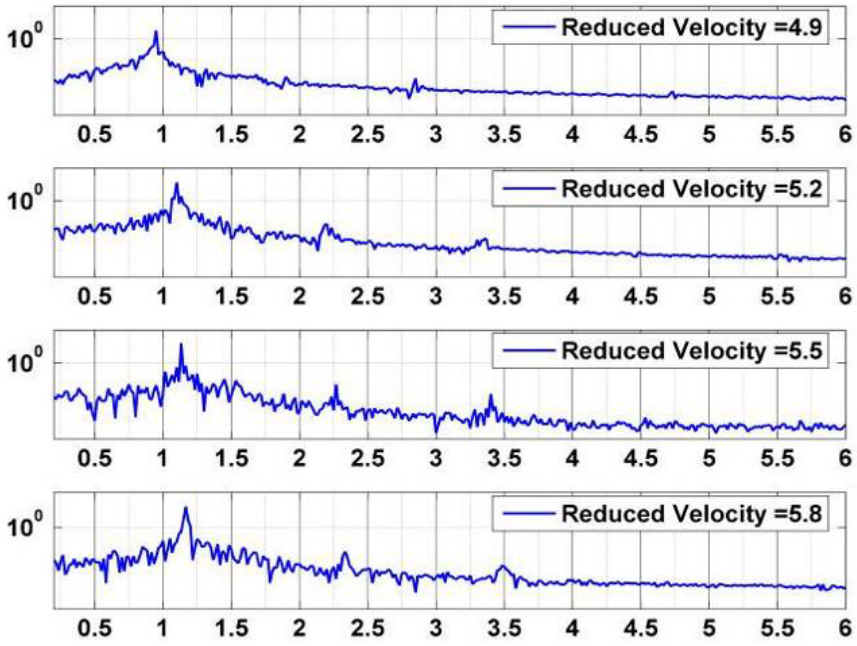

Figure 7.55. Spectra of displacement time series for a 3.5″ smooth cylinder for reduced velocity, 4.9-5.8.

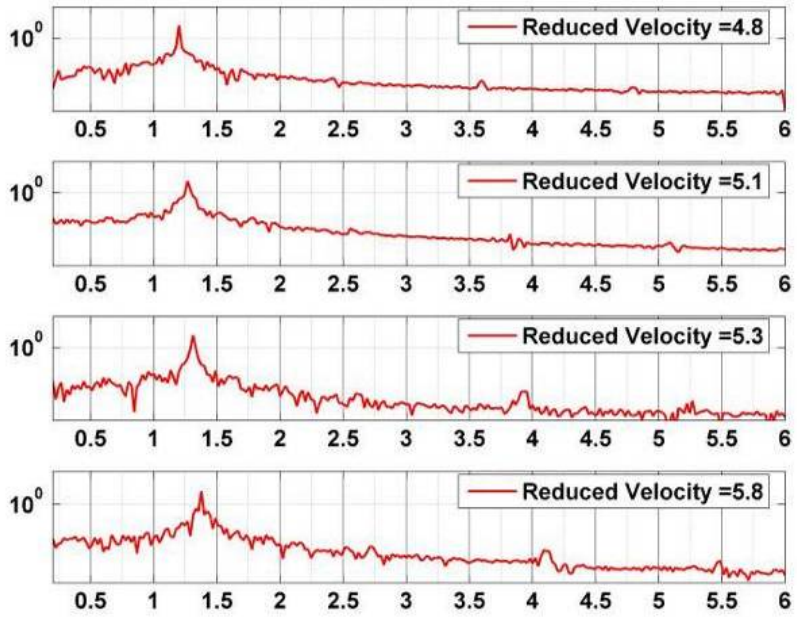

Figure 7.56. Spectra of displacement time series for a 3.5″ cylinder with roughness strip for reduced velocity, 4.8 – 5.8.

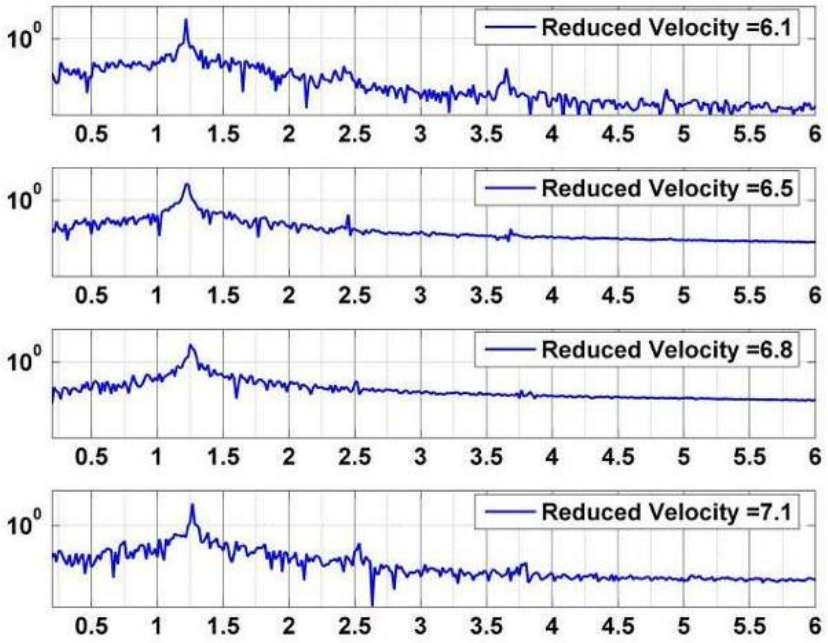

Figure 7.57. Spectra of displacement time series for a 3.5″ smooth cylinder for reduced velocity, 6.1-7.1.

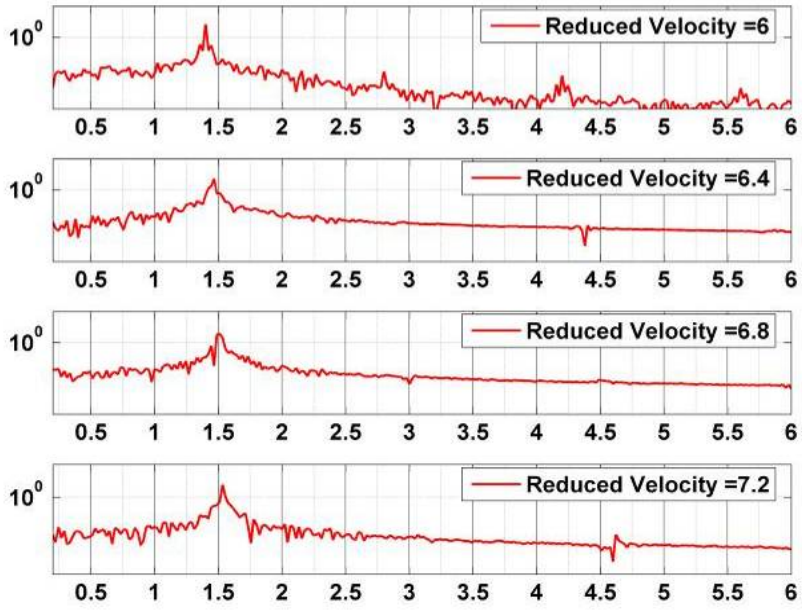

Figure 7.58. Spectra of displacement time series for a 3.5″ cylinder with roughness strip for reduced velocity, 6 0– 7.2.

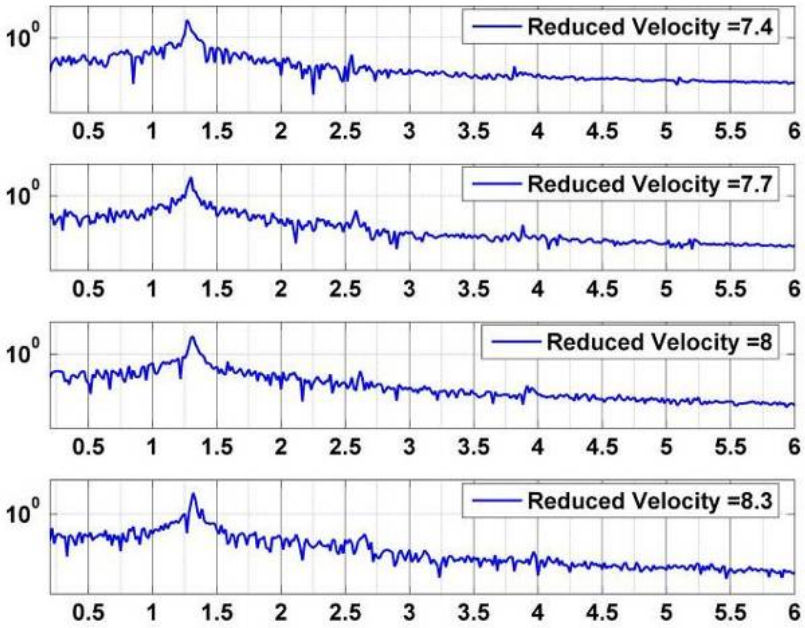

Figure 7.59. Spectra of displacement time series for a 3.5″ smooth cylinder for reduced velocity, 7.4-8.3.

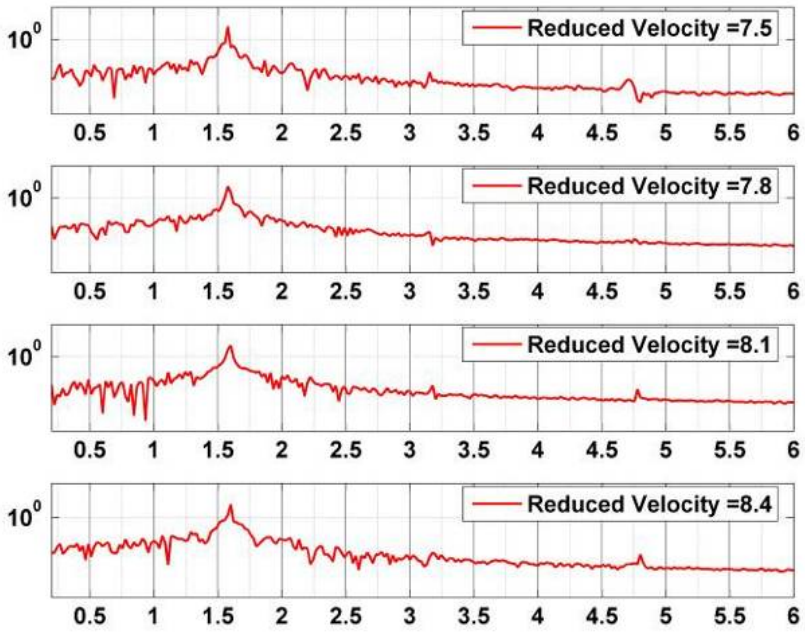

Figure 7.60. Spectra of displacement time series for a 3.5″ cylinder with roughness strip for reduced velocity, 7.5– 8.4.

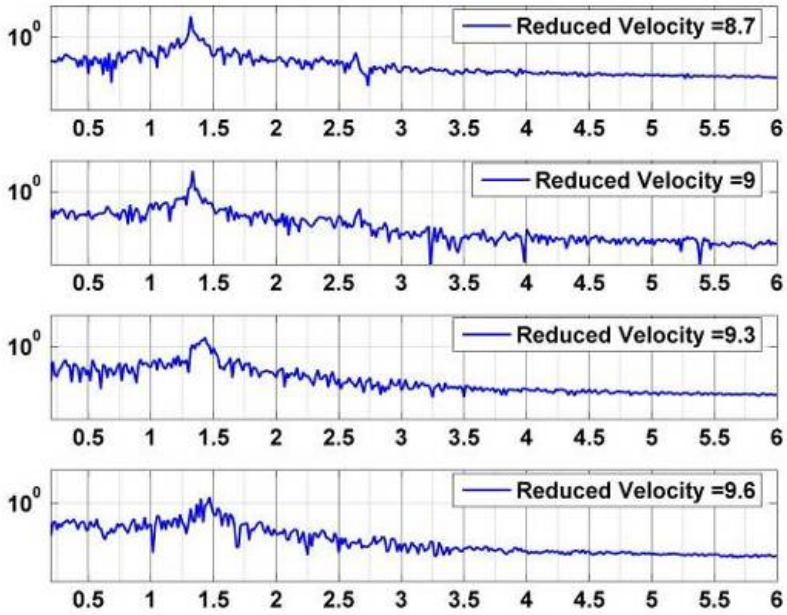

Figure 7.61. Spectra of displacement time series for a 3.5″ smooth cylinder for reduced velocity, 8.7-9.6.

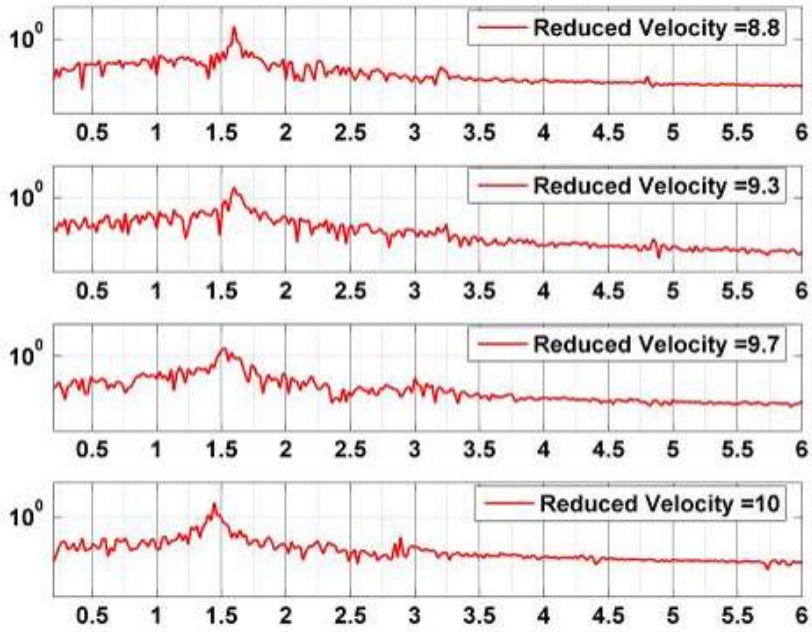

Figure 7.62. Spectra of displacement time series for a 3.5″ cylinder with roughness strip for reduced velocity, 8.8 – 10.

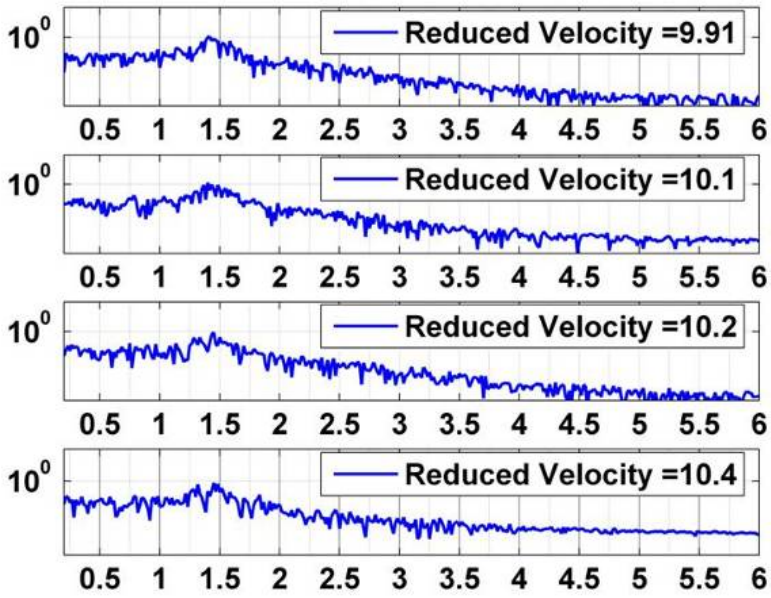

Figure 7.63. Spectra of displacement time series for a 3.5″ smooth cylinder for reduced velocity, 9.9-10.4.

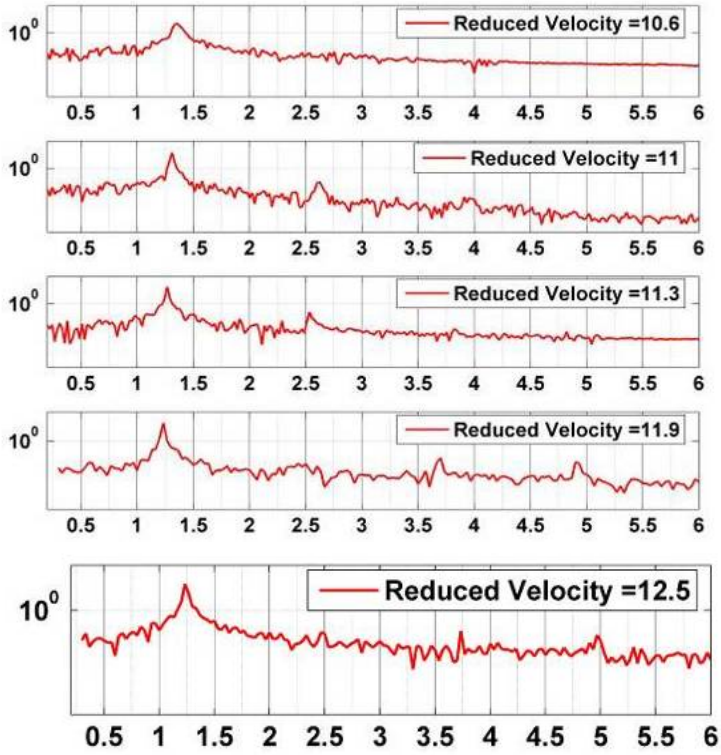

Figure 7.64. Spectra of displacement time series for a 3.5″ cylinder with roughness strip for reduced velocity, 10.6 – 12.5.

The spectral components corresponding to the reduced velocity for a 5″ smooth cylinder and cylinder with roughness strips are plotted from Figure 7.65 to Figure 7.74. In the case of the 5″ cylinder the Reynolds number regime is higher than the 3.5″ cylinder.

In the case of smooth cylinder for reduced velocity less than 4.45 as shown in Figure 7.65 the spectrum is characterized by power in the oscillation frequency. The power was distributed in the higher harmonic frequencies. This is a character of high Reynolds number and it was discussed in Chapter 4. In the case of the cylinder with roughness strips for reduced velocity less than 4.0, the spectral content is characterized by a sharper narrow-banded spectrum at the oscillation frequency as shown in Figure 7.65.

It is noticed at around reduced velocity of value 4 (point A in Figure 7.40 and Figure 7.42) a smooth cylinder has multiple peaks at the harmonic components of the oscillation frequency and a broad-banded small peak at the natural frequency of the system as shown in Figure 7.64. In Figure 7.66, at reduced velocity of 4, for a cylinder

with roughness strips, the peak is sharp at the oscillation frequency and there is no power distribution between the natural frequency and other higher harmonic components. For reduced velocity less than 4.45, the frequencies of oscillation were higher than the similar case of smooth cylinder. The stronger and narrower peak in the case of cylinder with roughness strips confirms earlier synchronization. The smooth cylinder has similar characteristic at the higher reduced velocity of 4.45.

In the case of a smooth cylinder, for reduced velocity between point B and C in Figure 7.40 and Figure 7.42 the accretion of power in the higher harmonic components occurs and is shown in Figure 7.67, Figure 7.69, Figure 7.71, and Figure 7.73. In the case of a cylinder with roughness strips for reduced velocity between point B and C in Figure 7.40 and Figure 7.42, the higher harmonics are not as conspicuous as in the smooth cylinder case as shown in Figure 7.68, Figure 7.70, and Figure 7.72. At the end of synchronization for the smooth cylinder case for reduced velocity between point C and D in Figure 7.40 and Figure 7.42 the power spectrum at the oscillation frequency becomes broad-banded and the higher harmonic components aren't present as shown in Figure 7.75 and Figure 7.75. In the case of a cylinder with roughness strips, for reduced velocity between point C and D in Figure 7.40 and Figure 7.42 the power spectrum is still narrow banded at the oscillation frequency and the higher harmonic components are prominent as shown in Figure 7.74. In Figure 7.74, 2^{nd}, 3^{rd}, 4^{th}, 5^{th}, 6^{th}, 7^{th}, and 8^{th} harmonics of the oscillation frequency are seen for a reduced velocity of 8.28. The resolution of spectrum reduces as the reduced velocity increases and it might be due to the reason that for reduced velocities greater than 8.28 the recording time was reduced due to the restriction of the lab conditions.

For a cylinder with roughness strips, in the cases of reduced velocity greater than 7, the reappearance of multiple higher harmonics with dominant second harmonic and small peaks at the 3^{rd}, 4^{th}, 5^{th}, 6^{th}, 7^{th}, and 8^{th} harmonics suggesting a 2P + 2S structure present which was corroborated by overlaying the response on the Williamson and Roshko map (Figure 7.38).

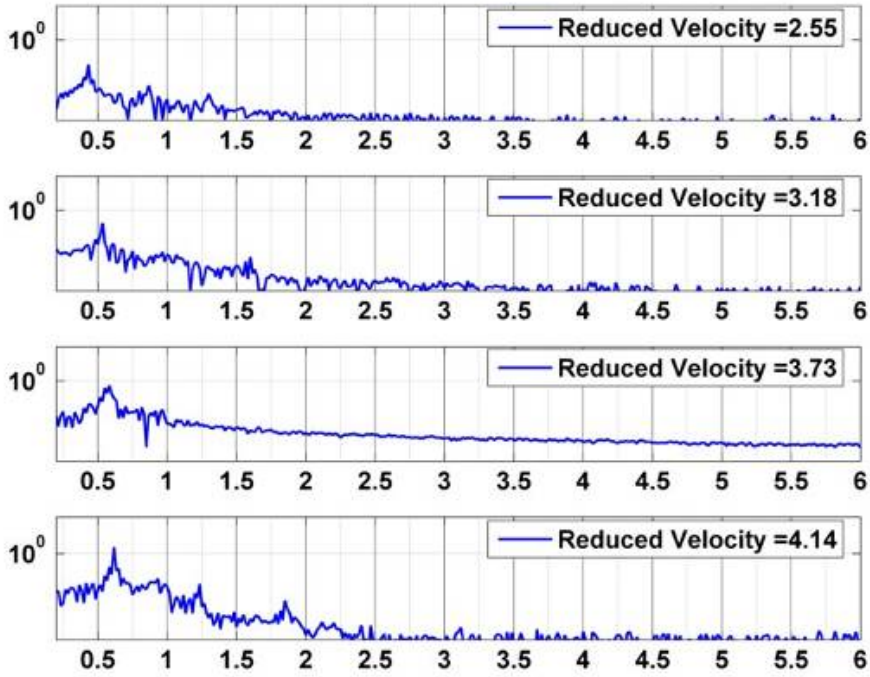

Figure 7.65. Spectra of displacement time series for a 5″ smooth cylinder for reduced velocity, 2.55-4.14.

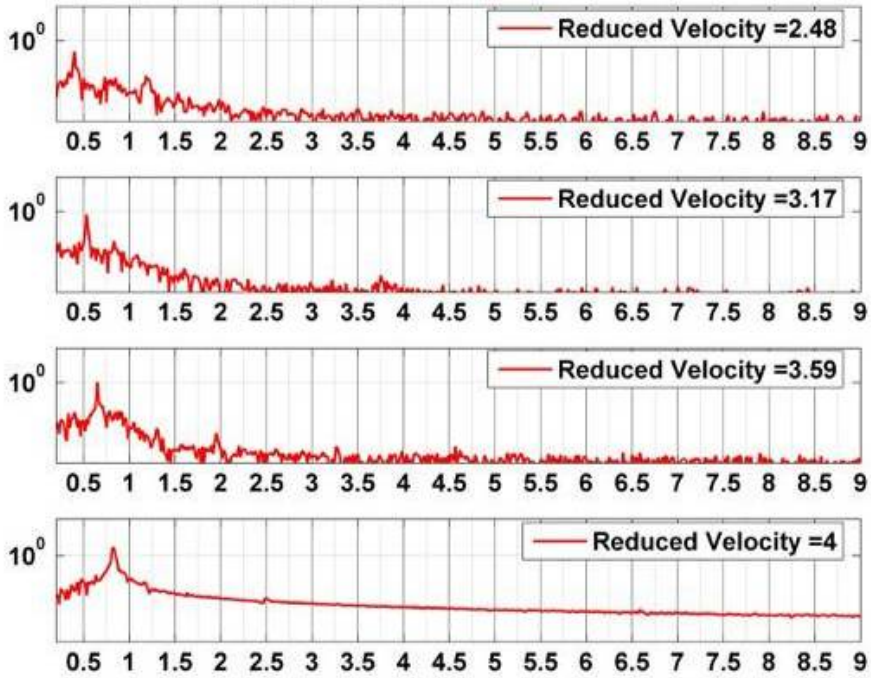

Figure 7.66. Spectra of displacement time series for a 5″ cylinder with roughness strip for reduced velocity, 2.48-4.00.

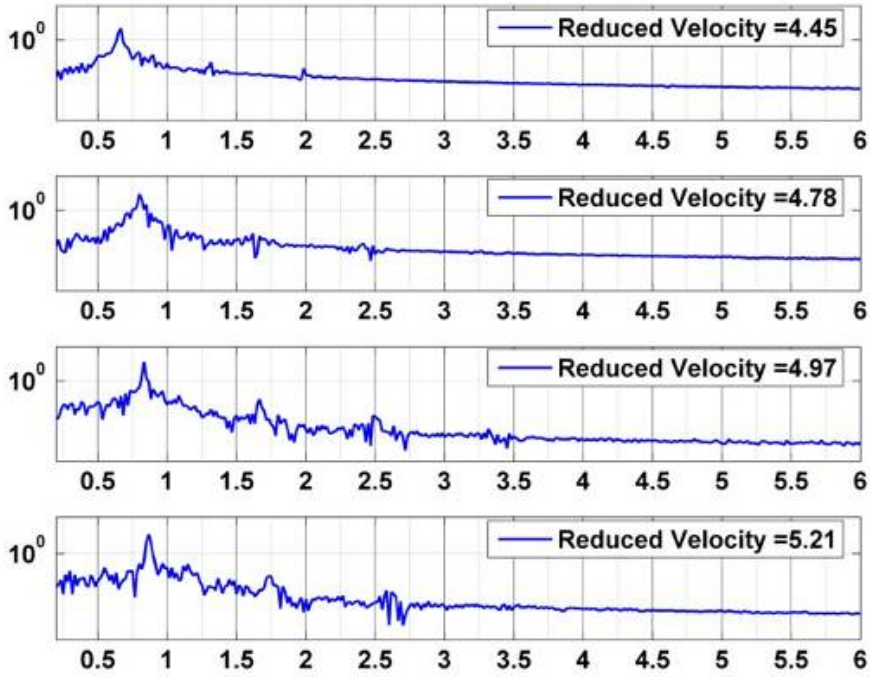

Figure 7.67. Spectra of displacement time series for a 5″ smooth cylinder for reduced velocity, 4.45-5.21.

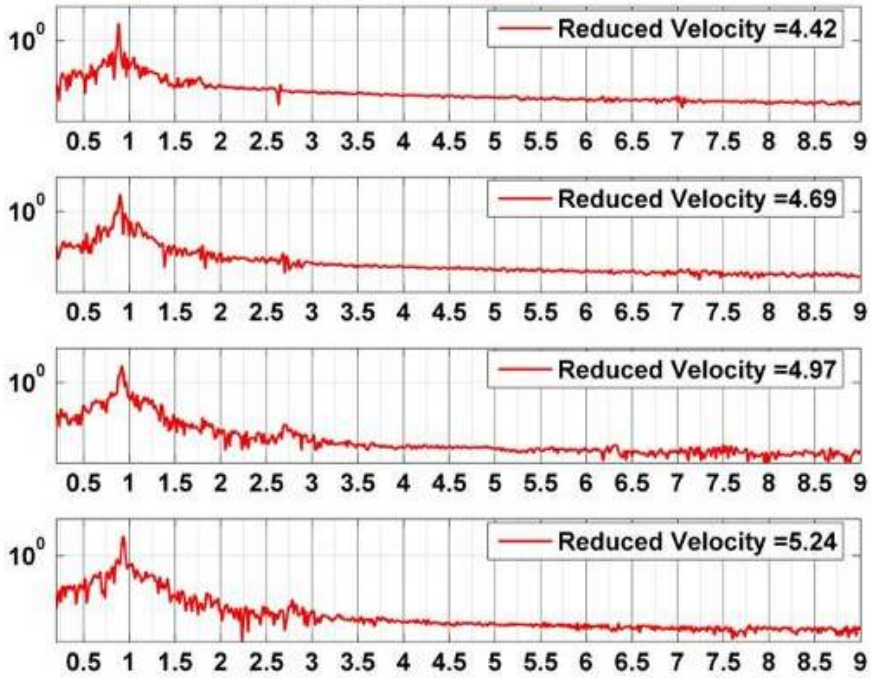

Figure 7.68. Spectra of displacement time series for a 5″ cylinder with roughness strip for reduced velocity, 4.42-5.24.

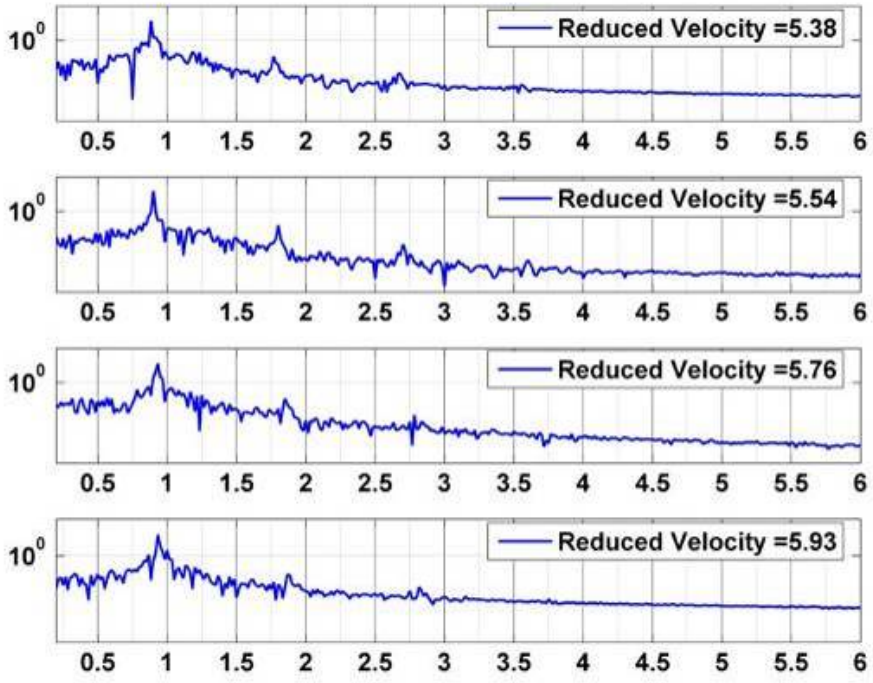

Figure 7.69. Spectra of displacement time series for a 5″ smooth cylinder for reduced velocity, 5.38-5.93.

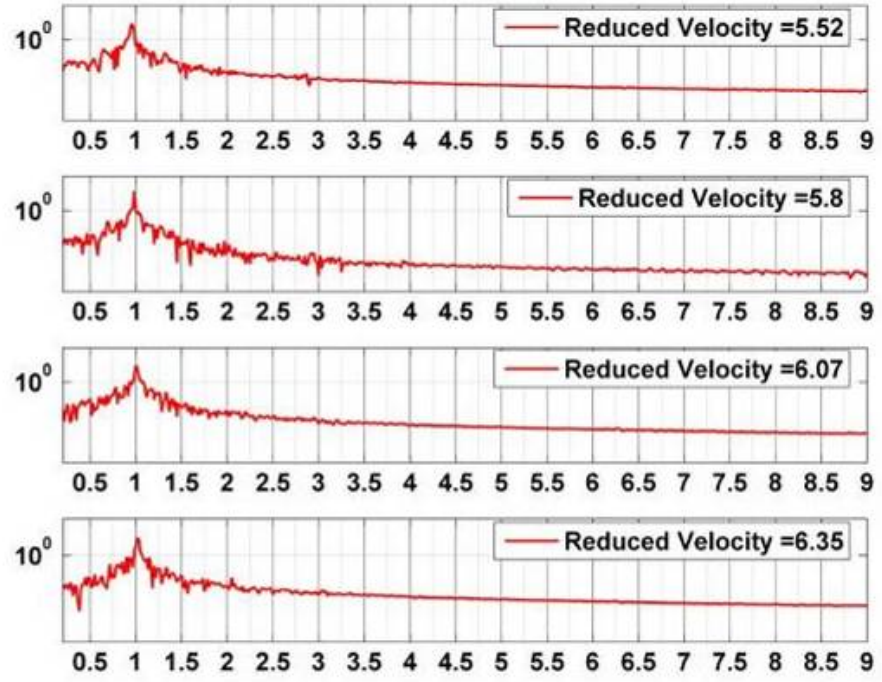

Figure 7.70. Spectra of displacement time series for a 5″ cylinder with roughness strip for reduced velocity, 5.52-6.35.

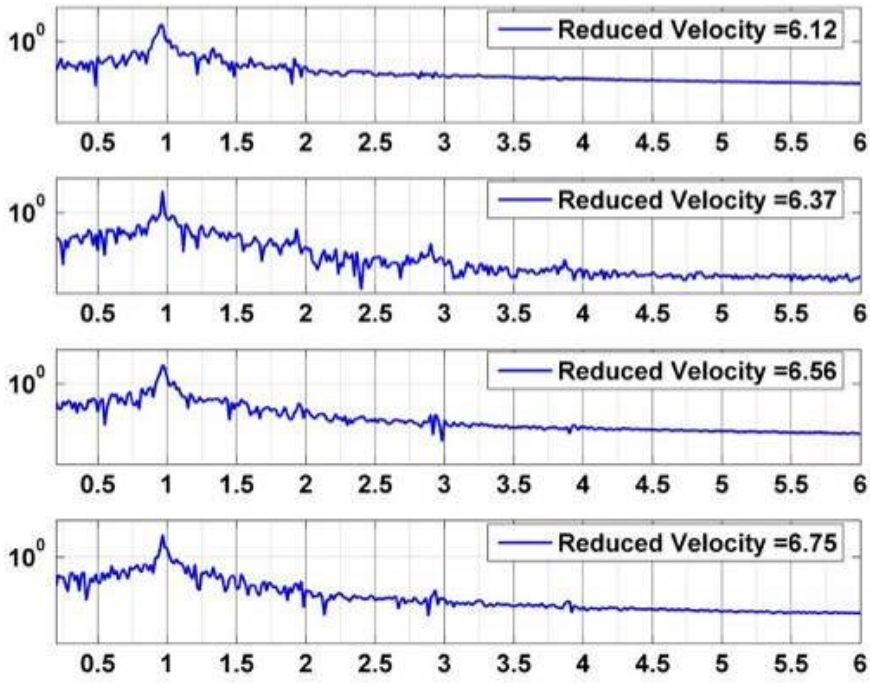

Figure 7.71. Spectra of displacement time series for a 5″ smooth cylinder for reduced velocity, 6.12-6.75.

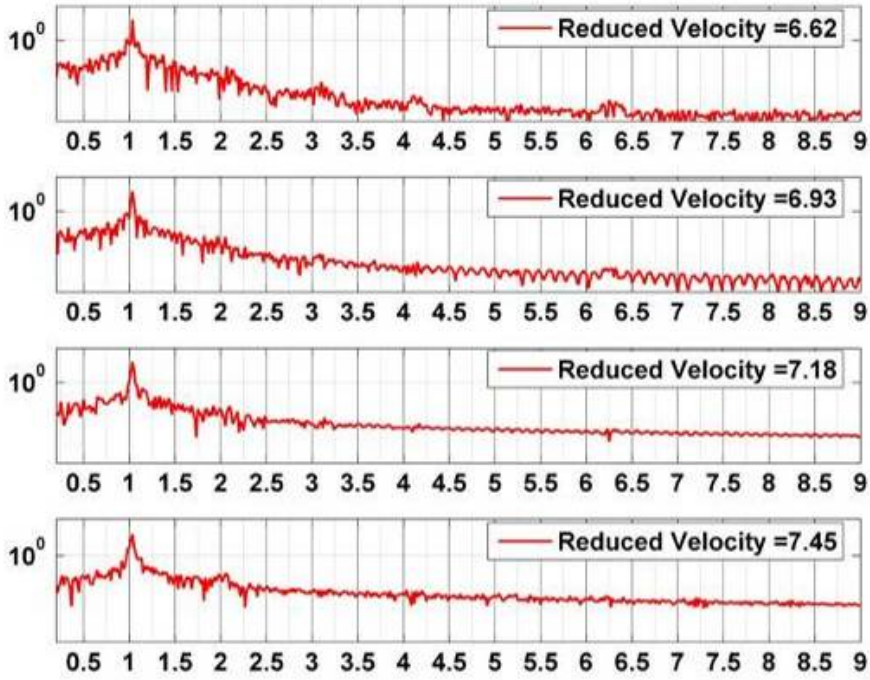

Figure 7.72. Spectra of displacement time series for a 5″ cylinder with roughness strip for reduced velocity, 6.62-7.45.

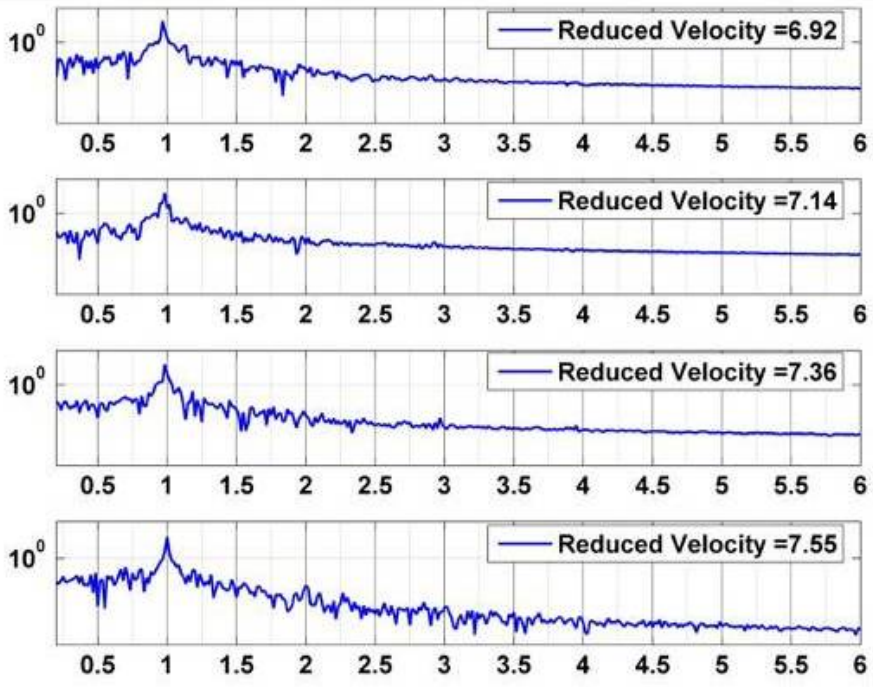

Figure 7.73. Spectra of displacement time series for a 5″ smooth cylinder for reduced velocity, 6.92-7.55.

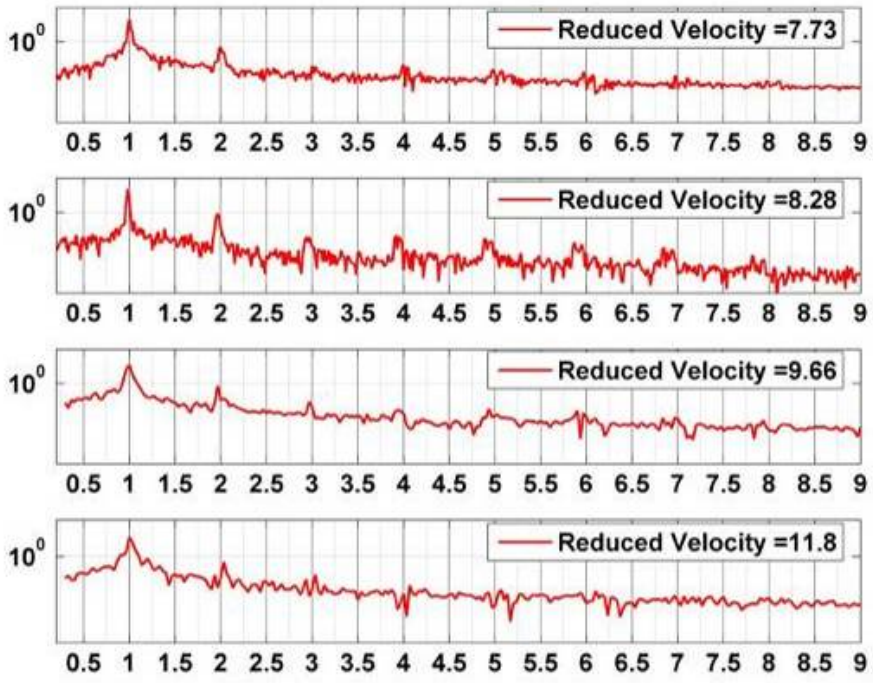

Figure 7.74. Spectra of displacement time series for a 5″ cylinder with roughness strip for reduced velocity, 7.73-11.8.

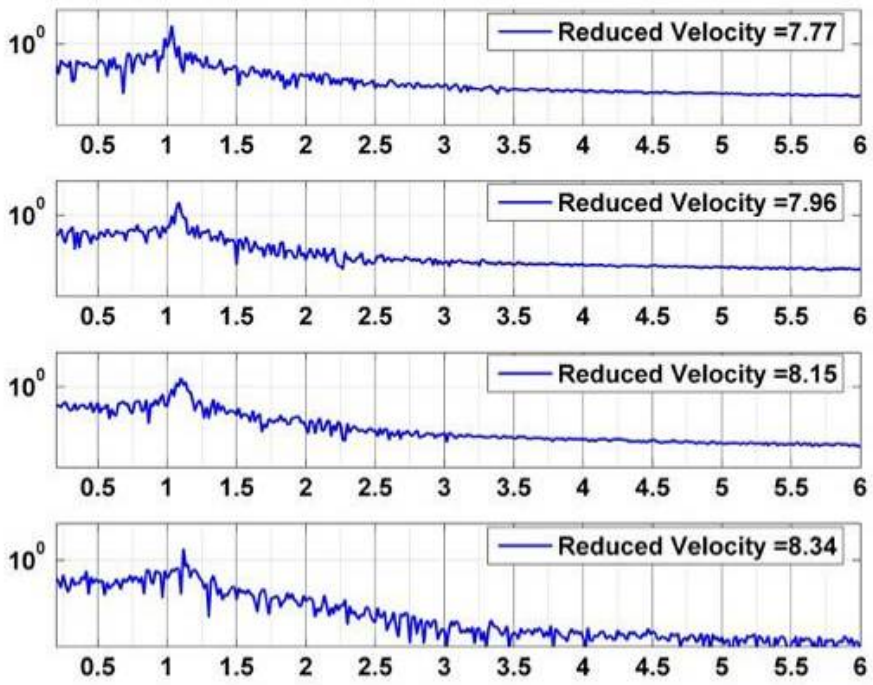

Figure 7.75. Spectra of displacement time series for a 5″ smooth cylinder for reduced velocity, 7.77-8.34.

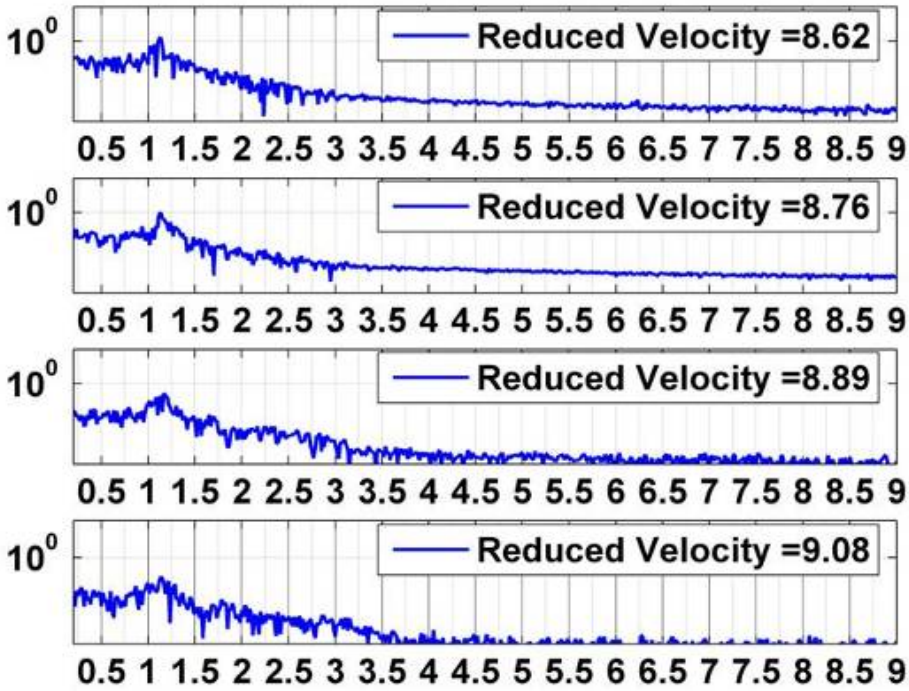

Figure 7.76. Spectra of displacement time series for a 5″ smooth cylinder for reduced velocity, 8.62-9.08.

7.5. MAIN FINDINGS

To increase the harnessed power of VIVACE, the lift coefficient, the amplitude of oscillation needs to be enhanced and both are related to the amount of circulation of the vortices being shed. The expansion of range of synchronization of VIV is another design requirement of VIVACE and it is achieved by increasing the correlation length. The results of the present experimental investigation presented in this chapter provide new information concerning the effect of roughness strips around a circular cylinder in VIV in the TrSL3 regime. A passive technique of increasing the amplitude of oscillation of a cylinder in VIV by inducing transition of boundary layer from laminar to turbulent with the aid of strategically located roughness strip has been successfully developed. The added roughness, when designed and implemented appropriately, affects in a predetermined way the boundary layer, the separation of the boundary layer, the level of turbulence, the wake, the drag and lift forces, and consequently the VIV, and the fluid-structure interaction.

The results of the cylinder with roughness strips, undergoing vortex induced vibration in the TrSL3 regime with a high $(m^*+C_a)\zeta$ is summarized as follows:

1. Roughness strip can be designed to maintain synchronization and increase A/D, even in the critical Reynolds number regime, 1×10^5 - $2\times10^5 < Re < 3.5\times10^6$- 6×10^6, where coherent vortex shedding along span is lost in the case of smooth cylinder, (see Figure 7.28, and Figure 7.46)
2. The sensitive part of modification of the cylinder with roughness strip was identified between 57°- 80°, which is in the range of the oscillating separation point. When the roughness strips were attached to the cylinder between 57°- 80° the range of synchronization and amplitude ratio (A/D) of the VIV response increased. (see Figure 7.40 and Figure 7.42)
3. When the roughness strips were attached to the cylinder between a circumferential angle 57°- 80°, the frequency characteristic of the synchronization range at high amplitude of oscillation/higher reduced velocity was found to be $f_{osc} = f_{n,water}$. For a smooth cylinder with $f_{osc} \approx f_{n,water}$, the oscillation frequency locks-in with a detuning away from the natural frequency in water.

4. Reduction of VIV can be achieved by arranging the roughness strip in multiple other configurations where the spanwise separation is disrupted resulting in reduction of the correlation length. This topic is of great interest in engineering applications, because circular cylindrical structures and other bluff bodies in fluid flow appear in many engineering disciplines such as offshore, civil, aerospace, mechanical, nuclear engineering. For example in offshore engineering, frequently marine risers and pipelines operate in VIV. Similarly, SPAR platforms, legs of tension leg platforms, mooring lines, marine cables, cooling towers, car antennas, and nuclear fuel control rods also operate often in VIV. Roughness strips when distributed properly provides the possibility of reducing/suppressing VIV without significant increase in drag.
5. When the roughness strips were attached to the cylinder aft of an angle of 80°, the range of synchronization was increased but the amplitude ratio (A/D) of the VIV response decreased (see Figure 7.34).
6. When the roughness strips were attached to the cylinder aft of an angle of 80°, the frequency characteristic of the synchronization range for a cylinder with roughness strip was similar to the case with roughness strip between 57°-80° in the beginning of the synchronization. For higher reduced velocity it follows the Strouhal line (see Figure 7.33).
7. In the present experiments an amplitude ratio of 2.7 was achieved and the range of synchronization didn't end within the feasible range of the experiments.
8. In general, the roughness strips induced an earlier start of synchronization by increasing the spanwise correlation length of the vortex shedding process (see Figure 7.38, and Figure 7.39).
9. A critical Reynolds number based on the roughness element size and the paper backing thickness was determined, above which the roughness strip was effective for enhancing the vibration. Below this critical Reynolds number ($Re_{k+P} < 600$, $Re_k < 120$) the roughness strip reduces the amplitude ratio in the original synchronization region. An optimal designed roughness can enhance the vibration without affecting the original synchronization range, which was observed in the 5″ cylinder case.

10. When the roughness element was on the order of the boundary layer, the flow around the cylinder was modified and the separation point was moved downstream.
11. In the preliminary visualization, the wake constituted four vortices shed per half-cycle. Strategically, arranged roughness can affect lock-in (synchronization) frequency.

Chapter 8

CONCLUSIONS AND RECOMMENDATIONS FOR FUTURE WORK

8.1. CONCLUSIONS

In this chapter we discuss the final conclusions based on the investigations performed to study various hydrodynamic aspects of the, VIVACE (Vortex Induced Vibrations Aquatic Clean Energy) Converter. Suggestions are made for further research needed to improve performance of the VIVACE Converter. Investigations performed in this Dissertation on VIVACE Converter shed light on various aspects of VIV which have been not explored before. This was made possible because the fundamental model of VIVACE is a highly damped VIV system with relatively high Reynolds number. Therefore, further investigation on hydrodynamic aspects of VIVACE will complement VIV knowledge available in the open literature.

In the present study, VIVACE Converter has been designed and tested. In our experiments, it was shown that the VIVACE Converter extracts energy successfully and efficiently from fluid flow by enhancing rather than spoiling vortex shedding and enhancing rather than suppressing VIV and harnessing rather than mitigating VIV energy.

The major conclusions of this dissertation are:

1. The VIVACE Converter complies with the requirements set by the California Energy Commission and the US DOE. VIVACE is viable even for low speed and low-

head flows, providing an advantage over watermills or dams. Additional advantages include consistency of current flow and its availability all year round; broad range of synchronization, which allows efficient extraction of energy with minor and slow adjustment of basic design parameters such as the spring stiffness and induced damping; its ability to extract even more energy in the case of velocity surge to 5 knots and higher; its scalability, modularity, and design flexibility, which allow for a broad range of applications. In our early experiments, maximum harnessed power of $0.307\times\frac{1}{2}\rho U^3 DL$ was achieved in the case of a single VIVACE modulo. The corresponding integrated harnessed power in that particular test was $P_{\text{VIVACE}}=0.22\times\frac{1}{2}\rho U^3 DL$ with a theoretical upper limit based on measurements of $P_{\text{UL-VIVACE}}= 0.37\times\frac{1}{2}\rho U^3 DL$. The velocity for the particular test was U =0.840m/sec = 1.63knots. The range of synchronization and the amplitude of oscillation were reduced at the expense of energy generation.

2. In our experiments, the VIVACE tests were performed in the TrSL3 regime of Reynolds number. This regime was not explored before. In our experiments a strong dependence of VIV on Reynolds number was observed. In the TrSL3 regime, the high amplitude of oscillation was sustained at high damping. This proves to be an ideal regime for VIVACE operation. Amplitude of 1.9 diameters was achieved for a smooth cylinder in VIV even with high damping imposed and it is attributed to the TrSL3 regime of Reynolds number in which VIVACE was operating. The present VIV system falls in the tail-end of the Griffin plot with its high $(m^*+C_a)\zeta$. Still high amplitude was achieved and maintained due to the effect of Reynolds number. In our experiments the range of synchronization of the upper branch and the amplitude ratio of VIV increase with increasing Reynolds number. Due to the high damping imposed on the VIV system, the lower branch was lost. Due to the high damping imposed on the VIV system to simulate VIVACE, the hysteresis phenomenon observed at the beginning of synchronization was also lost. In our experiments in the TrSL3 regime of Reynolds number it was observed that Reynolds number has a stronger influence than the mass ratio on A/D.

3. In this dissertation a strong dependence of VIV on the proximity to the free surface was shown. The effect of free surface is of interest in other bluff body applications which are close to the free surface. A strong Froude number dependence on the response was shown. In the present investigation, it was found that proximity to free surface reduced the range of synchronization of VIV and the amplitude ratio. Proximity to free surface introduced hysteresis at the end of synchronization for moderate gap ratio. At lower values of gap ratio hysterisis was observed both at the beginning and end of the synchronization range due to flipping between wake states. At a critical value of the Froude number, VIV is suppressed and it is attributed to change in stability of the vortex shedding process. At high values of Froude number and low values of gap ratio, the vortex formation process transforms from absolute to convective instability. This is achieved by skewing the wake and resulting in the formation of a long separation bubble instead of alternate shedding.

4. In our experiments, the contrast in the VIV response in close proximity to a rigid boundary was studied. In the present experiments, it was shown that for gap ratio > 3.0, the bottom boundary effect on VIV is negligible. For intermediate gap ratio (0.65<G/D <3.0), the range of synchronization is unaffected but the amplitude of oscillation is reduced probably due to partial strength of the bottom vortex. Below a critical gap ratio the character of VIV response was altered. For low gap ratio (0.65>G/D) the positive amplitude of oscillation was higher than the VIV of a cylinder in unbounded fluid. The amplitude reached a value of 2 diameters. This increase in amplitude has been hypothesized to the non-generation of bottom vortices. The top vortex strength increased since the top vortex is not partially diffused by the bottom vortex. In the case of VIV near a bottom boundary, the range of synchronization shifted to higher reduced velocities (U_r) than in the unbounded VIV cases. A steady increase in amplitude was observed at the beginning of synchronization rather than a jump as observed in the unbounded fluid cases.

5. Enhancement of amplitude of oscillation of VIV is needed to increase the harnessed power of VIVACE (Bernitsas and Raghavan 2007a). The expansion of range

of synchronization of VIV is another design requirement of VIVACE and it was achieved by roughness strips. Roughness strips were added to the surface of a cylinder in VIV. The added roughness, when designed and implemented appropriately, affects in a predetermined way the boundary layer, the separation of the boundary layer, the level of turbulence, the wake, the drag and lift forces, and consequently VIV and fluid-structure interaction. In the present experiments, the goal of increasing the amplitude of oscillation was achieved by attaching the roughness strips to the cylinder between 57°-80°. The range of synchronization and amplitude ratio (A/D) of the VIV response increased. In the present experiments, an unprecedented amplitude ratio of 2.7 was achieved and no end to the range of synchronization was observed within the LTFSW Channel capabilities. In general, the roughness strips induced an earlier start of synchronization by increasing the spanwise correlation length of vortex shedding. Based on the roughness element size and the paper backing a critical Reynolds number was determined above which the roughness strip was effective in enhancing VIV. Below this critical Reynolds number ($Re_{k+P} < 600$, $Re_k < 120$) the roughness strip reduces the amplitude ratio in the original synchronization region. Above this critical Reynolds number, an increase in amplitude ratio was observed. An optimally designed roughness can enhance the vibration without affecting the original synchronization range, which was observed in the 5″ cylinder case. When the roughness element was in the order of the boundary layer, the flow around the cylinder was modified and the separation point was moved downstream. In the preliminary visualization, the wake constituted of four vortices shed per half cycle. Strategically arranged roughness can affect lock-in (synchronization) frequency. At the beginning of the synchronization range for a cylinder with a roughness strip $f_{osc}=f_{Strouhal}$ where as for a smooth cylinder $f_{osc}\approx f_{n,water}$.

6. Even though the aim of the present research topic was to enhance VIV, it is worth mentioning that reduction of VIV was also achieved by a strategically arranged roughness strip (Patent pending (Bernitsas and Raghavan 2007b)). This topic is of great interest to the offshore industry application and several other engineering disciplines.

8.2. RECOMMENDATIONS FOR FUTURE RESEARCH

Future developments of the VIVACE Converter at the level of a single module:

(i) Optimization of the hydrodynamics of VIV by studying vortex shedding mode under high damping, vortex strength enhancement, and shedding phase.

(ii) Optimization of the range of synchronization and the amplitude of VIV under high damping.

(iii) Selection of the Power Take-Off system.

(iv) Investigation of the impact of wake mode on energy extraction, which requires maintaining high amplitude VIV over a broad range of synchronization.

(v) Optimization the harnessed energy for a given m*, by varying the spring stiffness K_{spring}.

(vi) Optimization of the harnessed energy for a given m*, by varying the electrical load (damping) and identifying the system character for various damping value.

In the present experiments, only a single modulo of VIVACE was investigated and multiple tests would be required to understand the hydrodynamics of cluster of VIVACE modules. The areas of promising improvement for a VIVACE power plant are:

(vii) Optimization of the trade-off between complexity and high energy density.

(viii) Optimization of the configuration of the array of VIVACE cylinders in three-dimensional ocean space.

Recommendations for future study of VIV aspects of VIVACE

(ix) In the TrSL3 regime of Reynolds number, systematically investigate the effect of damping ratio and mass ratio on VIV to complete the data set in the mass damping plots.

(x) In the TrSL3 regime of Reynolds number, investigate the wake behind a cylinder in VIV operating by measuring the wake velocity and by flow visualization techniques. These measurements and observations will clarify the role of the shear layer in the increase in lift and amplitude of oscillation.

(xi) Flipping between the wake states for a cylinder in VIV needs to be investigated by using flow visualization techniques. This would shed light on the cessation of vortex shedding observed at the end of synchronization.

(xii) The observation of the absence of a jump in the initial part of synchronization for a cylinder in VIV closer to a boundary (rigid or free surface) needs to be studied by visualization.

(xiii) System Identification for VIV is challenging but will facilitate optimization of energy extraction and design of the VIVACE Converter. A simple linear model is used in the present experiments and by most of the other investigators. They model phenomenologically VIV using a Van der Pol oscillator or modified Van der pol oscillators, coupled or uncoupled. Each of these models has limitations in predicting system response with variation in Reynolds number because of the fluid character is not modeled by the Van der Pol oscillator. To accurately model the fluid part, a few investigators used the Ginzburg-Landau and Stuart-Landau equations to model the fluid part and which has yet to reach maturity in modeling VIV. So, there is a necessity for a robust model, this could include the nonlinear character of VIV response in different Reynolds number regimes.

(xiv) The modification of the flow with roughness strips needs to be explored by wake velocity measurement and visualization. The wake velocity measurements reports the velocity fluctuations behind the cylinder and could possibly explain the lock-in observed between the frequency of oscillation and natural frequency in cases where the strips

are attached before 80°. In other cases where the strips were attached after 80° the lock-in was observed between the frequency of oscillation and the Strouhal frequency.

(xv) The different VIV response character needs to be identified in the parameter space of Reynolds number, roughness element size and reduced velocity for different configurations of roughness strips.

(xvi) Lift and drag forces need to be measured for the cylinder in VIV at high Reynolds number. This complements the present data by adding the data lacking in the TrSL3 regime. The lift-force measurement could be used to understand the phase characteristic of the shedding mode and also explain the absence of jump observed in cylinders close to the boundary.

(xvii) Further tests need to be done to study the suppression of VIV using roughness strips. even though this study is not relevant to VIVACE. It may have an impact on other industries where suppression of VIV is required.

(xviii) For the design of a VIVACE bank, the study of multiple cylinder interaction is a necessity. The flow dynamics is more complicated than in the case of a single cylinder in VIV. Galloping of cylinders has been observed for two cylinders in VIV. There is very limted information for optimal design of a VIVACE bank. This study with multiple cylinders will help in defining efficiency of larger VIVACE applications in a less controversial manner.

References

[1]. Achenbach, E., (1968), "Distribution of Local Pressure and Skin Friction around a Circular Cylinder in Cross-Flow up to Re = 5×10^6," *Journal of Fluid Mechanics*, 34(4), 625-639.

[2]. Achenbach, E., (1971), "Influence of Surface Roughness on the Cross-Flow around a Circular Cylinder," *Journal of Fluid Mechanics*, 46(2), 321-335.

[3]. Achenbach, E., and Heinecke, E., (1981), "On Vortex Shedding from Smooth and Rough Cylinders in the Range of Reynolds Numbers 6×10^3 to 5×10^6," *Journal of Fluid Mechanics*, 109, 239-251.

[4]. Alam, M., and Sandham, N. D., (2000), "Direct Numerical Simulation of 'Short' Laminar Separation Bubbles with Turbulent Reattachment," *Journal of Fluid Mechanics*, 410, 1-28.

[5]. Anagnostopoulos, P., (2000a), "Numerical Study of the Flow Past a Cylinder Excited Transversely to the Incident Stream. Part 1: Lock-in Zone, Hydrodynamic Forces and Wake Geometry," *Journal of Fluids and Structures*, 14(6), 819-851.

[6]. Anagnostopoulos, P., (2000b), "Numerical Study of the Flow Past a Cylinder Excited Transversely to the Incident Stream. Part 2: Timing of Vortex Shedding, Aperiodic Phenomena and Wake Parameters," *Journal of Fluids and Structures*, 14(6), 853-882.

[7]. Anand, N. M., (1985), "Free Span Vibrations of Submarine Pipelines in Steady and Wave Flows," Ph.D thesis, Norwegian Institute of Technology, Trondheim, Norway.

[8]. Anand, N. M., and Torum, A., (1985), "Free Span Vibration of Submerged Pipelines in Steady Flow and Waves," *Proceedings of International Symposium on Separated Flow Atround Marine Structures*.

[9]. Angrilli, F., Di Silvio, G., and Zanardo, A., (1972), "Hydroelasticity Study of a Circular Cylinder in a Water Stream," *Flow-Induced Structural Vibrations*, 504-512.

[10]. Atsavapranee, P., Benaroya, H., and Wei, T., (1998), "Vortex Dynamics in the near Wake of a Freely-Oscillating Cylinder," *Proceedings of the FEDSM'98*, 1-6.

[11]. Batham, J. P., (1973), "Pressure Distributions on Circular Cylinders at Critical Reynolds Numbers," *Journal of Fluid Mechanics*, 57(3).

[12]. Bearman, P. W., (1984), "Vortex Shedding from Oscillating Bluff Bodies," *Annual review of fluid mechanics. Vol. 16*, 195-222.

[13]. Bearman, P. W., and Currie, I. G., (1979), "Pressure-Fluctuation Measurements on an Oscillating Circular Cylinder," *Journal of Fluid Mechanics*, 91(pt 4), 661-677.

[14]. Bearman, P. W., and Davies, M. E., (1975), "Vortex Shedding from Oscillating Bluff Structures," Colorado State University, U.S.A.

[15]. Bearman, P. W., and Morel, T., (1983), "Effect of Free Stream Turbulence on the Flow around Bluff Bodies," *Progress in Aerospace Sciences*, 20(2-3), 97-123.

[16]. Bearman, P. W., and Zdravkovich, M. M., (1978), "Flow around a Circular-Cylinder near a Plane Boundary," *Journal of Fluid Mechanics*, 89(Nov), 33-&.

[17]. Bedard, R., and Previsic, M., (2005), "Survey and Characterization, Tidal in Stream Energy Conversion (Tisec) Devices," EPRI.

[18]. Bedard, R., Previsic, M., Siddiqui, O., Hagerman, G., and Robinson, M., (2005), "Final Survey and Characterization Tidal in Stream Energy Conversion (Tisec) Devices," EPRI–TP–004 NA Report November 9, 2005.

[19]. Ben Simon, Y., (2005), "Highly Damped Vortex Induced Vibrations of Circular Cylinder " Professional degree thesis, University of Michigan.

[20]. Bernitsas, M. M., Ben-Simon, Y., Raghavan, K., and Garcia, E. M. H., (2006a), "The VIVACE Converter: Model Tests at High Damping and Reynolds Number around 10^5," *Proceedings of the International Conference on Offshore Mechanics and Arctic Engineering - OMAE*.

[21]. Bernitsas, M. M., and Raghavan, K., (2005a), "Fluid Motion Energy Converter," USPTO, 11/272,504.

[22]. Bernitsas, M. M., and Raghavan, K., (2005b), "Fluid Motion Energy Converter," I. P. Application, Serial No.PCT/US05/040773.

[23]. Bernitsas, M. M., and Raghavan, K., (2007a), "Enhancement of Vortex Induced Forces and Motion through Surface Roughness Control," U of M Ref. 3737. HDP Ref. 2115-003737/PS1.

[24]. Bernitsas, M. M., and Raghavan, K., (2007b), "Reduction of Vortex Induced Forces and Motion through Surface Roughness Control," U of M Ref. 3757. HDP Ref. 2115-003757/PS1.

[25]. Bernitsas, M. M., Raghavan, K., Ben-Simon, Y., and Garcia, E. M. H., (2006b), "VIVACE (Vortex Induced Vibrations Aquatic Clean Energy): A New Concept in Generation of Clean and Renewable Energy from Fluid Flow," *Proceedings of the International Conference on Offshore Mechanics and Arctic Engineering - OMAE*.

[26]. Bernitsas, M. M., Raghavan, K., and Maroulis, D., (2007), "Effect of Free Surface on VIV for Energy Harnessing at 8×10^3 <Re< 1.5×10^5 " *Proceedings of the International Conference on Offshore Mechanics and Arctic Engineering - OMAE* San Diego.

[27]. Bishop, R. E. D., and Hassan, A. Y., (1964), "The Lift and Drag Forces on a Circular Cylinder Oscillating in a Flowing Fluid," *Proceedings of the Royal Society (London)*, 277, 51-75.

[28]. Blackburn, H. M., and Henderson, R. D., (1999), "A Study of Two-Dimensional Flow Past an Oscillating Cylinder," *Journal of Fluid Mechanics*, 385, 255-286.

[29]. Blevins, R. D., (1990), *Flow-Induced Vibration*, Van Nostrand Reinhold Co, NY.

[30]. Bloor, M. S., (1964), "The Transition to Turbulence in the Wake of a Circular Cylinder," *Journal of Fluid Mechanics*, 19, 290-304.

[31]. Bradshaw, P., (2000), "A Note On "Critical Roughness Height" And "Transitional Roughness"," *Physics of Fluids*, 12(6), 1611-1614.

[32]. Brankovic, M., and Bearman, P. W., (2006), "Measurements of Transverse Forces on Circular Cylinders Undergoing Vortex-Induced Vibration," *Journal of Fluids and Structures*, 22(6-7), 829-836.

[33]. Braslow, A. L., (1960), "Review of the Effect of Distributed Surface Roughness on Boundary-Layer Transition," *NASA-TM-79879* NASA Center: Langley Research Center.

[34]. Braza, M., Chassaing, P., and Ha Minh, H., (1986), "Numerical Study and Physical Analysis of the Pressure and Velocity Fields in the near Wake of a Circular Cylinder," *Journal of Fluid Mechanics*, 165, 79-130.

[35]. Brede, M., Eckelmann, H., and Rockwell, D., (1996), "On Secondary Vortices in the Cylinder Wake," *Physics of Fluids*, 8(8), 2117-2124.

[36]. Brika, D., and Laneville, A., (1993), "Vortex-Induced Vibrations of a Long Flexible Circular Cylinder," *Journal of Fluid Mechanics*, 250, 481-508.

[37]. Carberry, J., (2001), "Wake States of a Submerged Oscillating Cylinder and of a Cylinder beneath a Free-Surface," Ph.D. thesis, Monash University.

[38]. Carberry, J., (2002), "Wake States of a Submerged Oscillating Cylinder and of a Cylinder beneath a Free-Surface," Ph.D. thesis, Monash University, Australia, Clayton.

[39]. Carberry, J., Sheridan, J., and Rockwell, D., (2001), "Forces and Wake Modes of an Oscillating Cylinder," *Journal of Fluids and Structures*, 15(3-4), 523-532.

[40]. Carberry, J., Sheridan, J., and Rockwell, D., (2002a), "Controlled Oscillations of a Cylinder: Forces and Wake Modes," *European Journal of Mechanics - B/Fluids*, 23(1).

[41]. Carberry, J., Sheridan, J., and Rockwell, D., (2002b), "Vortex Forces on an Oscillating Cylinder," *American Society of Mechanical Engineers, Applied Mechanics Division, AMD*, 275-282.

[42]. Carberry, J., Sheridan, J., and Rockwell, D., (2004), "Cylinder Oscillations beneath a Free-Surface," *European Journal of Mechanics, B/Fluids*, 23(1), 81-88.

[43]. Celik, I., and Patel, V. C., (1982), "Boundary-Layer Development on Circular Cylinders," *Boundary-Layer Meteorology*, 24, 281-293.

[44]. Chakroun, W. M., Abdel-Rahman, A. A., and Quadri, M. M. A., (1997), "Fluid Characteristics for Flow Past a Rough Circular Cylinder," *AIAA-1997-713A*.

[45]. Chen, S. S., (1987), *Flow-Induced Vibration of Circular Cylindrical Structures*, Washington, DC, Hemisphere Publishing Corp.

[46]. Chyu, C., Lin, J. C., Sheridan, J., and Rockwell, D., (1995), "Karman Vortex Formation from a Cylinder: Role of Phase-Locked Kelvin-Helmholtz Vortices," *Physics of Fluids*, 7(9), 2288-2290.

[47]. Chyu, C., and Rockwell, D., (1996a), "Evolution of Patterns of Streamwise Vorticity in the Turbulent near Wake of a Circular Cylinder," *Journal of Fluid Mechanics*, 320, 117-137.

[48]. Chyu, C. K., and Rockwell, D., (1996b), "Near-Wake Structure of an Oscillating Cylinder: Effect of Controlled Shear-Layer Vortices," *Journal of Fluid Mechanics*, 322, 21-49.

[49]. Clark, R. O., (1999), "Apparatus for Generating Electricity from Flowing Fluids," USPTO, US Pat. 6153944, 6153944.

[50]. Coder, D. W., (1971), "Location of Separation on a Circular Cylinder in Crossflow as a Function of Reynolds Number," Naval ship research and development center, Bethesda MD.

[51]. Davies, M. E., (1976), "Comparison of Wake Structure of a Stationary and Oscillating Bluff Body, Using a Conditional Averaging Technique," *Journal of Fluid Mechanics*, 75, 209-231.

[52]. Davis, J. T., (2001), "Velocity Characteristics in the Wake of an Oscillating Cylinder," S.M thesis, Massachusetts Institute of Technology. .

[53]. Dean, R. B., Milligan, R. W., and Wootton, L. R., (1977), "Study of Flow-Induced Vibration ", London, UK.

[54]. Ding, J., Balasubramanian, S., Lokken, R., and Yung, T., (2004), "Lift and Damping Characteristics of Bare and Staked Cylinders at Riser Scale Reynolds Numbers," *Proceedings of Offshore Technology Conference Paper No. 16341*.

[55]. Dryden, H. L., (1953), "Review of Published Data on the Effect of Roughness on Transition from Laminar to Turbulent Flow," *Journal of the Aeronautical Sciences*, 20(7), 477-482.

[56]. Duarte Ribeiro, J. L., (1991), "Effects of Surface Roughness on the Two-Dimensional Flow Past Circular Cylinders. Ii. Fluctuating Forces and Pressures," *Journal of Wind Engineering and Industrial Aerodynamics*, 37(3), 311-326.

[57]. Duck, P. W., Ruban, A. I., and Zhikharev, C. N., (1996), "The Generation of Tollmien-Schlichting Waves by Free-Stream Turbulence," *Journal of Fluid Mechanics*, 312, 341-371.

[58]. Dwyer, H. A., and McCroskey, W. J., (1973), "Oscillating Flow over a Cylinder at Large Reynolds Number," *Journal of Fluid Mechanics*, 61(4).

[59]. Eaddy, M., Melbourne, W. H., and Sheridan, J., (2002), "Surface Roughness Effects on Circular Cylinders at High Reynolds Numbers," *American Society of Mechanical Engineers, Applied Mechanics Division, AMD*, 187-193.

[60]. Energetech, http://www.energetech.com.au/

[61]. Fage, A., and Falkner, V. M., (1931), "Further Experiments on the Flow around a Circular Cylinder," *Aero. Res. Counc. Lond. Rep. Mem*, 1369, 1-13.

[62]. Fage, A., and Warsap, J. H., (1929), "The Effects of Turbulence and Surface Roughness on the Drag of a Circular Cylinder," *Aero. Res. Comm. R. and M*, 1283.

[63]. Feng, C. C., (1968), "The Measurements of Vortex-Induced Effects in Flow Past a Stationary and Oscillating Circular and D-Section Cylinders," M.Sc thesis, University of British Columbia.

[64]. Ferguson, N., and Parkinson, G. V., (1967), "Surface and Wake Flow Phenomena of the Vortex-Excited Oscillation of a Circular Cylinder," *ASME Journal of Engineering for Industry*, 89, 831-838.

[65]. Fredsoe, J., Sumer, B. M., Andersen, J., and Hansen, E., (1987), "Transverse Vibrations of a Cylinder Very Close to a Plane Wall," *Journal of Offshore Mechanics and Arctic Engineering*, 109(1), 52-60.

[66]. Fredsoee, J., Sumer, B. M., Andersen, J., and Hansen, E., (1987), "Transverse Vibrations of a Cylinder Very Close to a Plane Wall," *J. OFFSHORE MECH. ARCTIC ENG.*, 109(1), 52-60.

[67]. Fujarra, A. L. C., Meneghini, J. R., Pesce, C. P., and Parra, P. H. C. C., (1998), "An Investigation of Vortex-Induced Vibration of a Circular Cylinder in Water," *Conference on Bluff Body Wakes and Vortex-Induced Vibrations*.

[68]. Gerrard, J. H., (1966), "The Mechanics of the Formation Region of Vortices Behind Bluff Bodies," *Journal of Fluid Mechanics*, 25(2), 401-413.

[69]. Gharib, M., and Weigand, A., (1996), "Experimental Studies of Vortex Disconnection and Connection at a Free Surface," *Journal of Fluid Mechanics*, 321, 59-86.

[70]. Gharib, M. R., (1999), "Vortex-Induced Vibration, Absence of Lock-in and Fluid Force Deduction," Ph.D thesis, California Institute of Technology.

[71]. Gopalkrishnan, R., (1993), "Vortex Induced Forces on Oscillating Bluff Cylinders," Sc.D thesis, Massachusetts Institute of Technology,.

[72]. Govardhan, R., (2000), "Vortex Induced Vibration of Two and Three Dimensional Bodies," Ph.D thesis, Cornell University, Ithaca.

[73]. Govardhan, R., and Williamson, C. H. K., (1999), "Modes of Vortex Formation and Frequency Response for a Freely-Vibrating Cylinder," *Journal of Fluid Mechanics*.

[74]. Govardhan, R., and Williamson, C. H. K., (2000), "Modes of Vortex Formation and Frequency Response of a Freely Vibrating Cylinder," *Journal of Fluid Mechanics*, 420, 85-130.

[75]. Govardhan, R., and Williamson, C. H. K., (2002), "Resonance Forever: Existence of a Critical Mass and an Infinite Regime of Resonance in Vortex-Induced Vibration," *Journal of Fluid Mechanics*, 473(473), 147-166.

[76]. Govardhan, R., and Williamson, C. H. K., (2005), "Revealing the Effect of Reynolds Number on Vortex-Induced Vibrations Using Controlled Negative and Positive Damping," *Conference on Bluff Body Wakes and Vortex-Induced Vibrations (BBVIV4)*.

[77]. Govardhan, R. N., and Williamson, C. H. K., (2006), "Defining the 'Modified Griffin Plot' in Vortex-Induced Vibration: Revealing the Effect of Reynolds Number Using Controlled Damping," *Journal of Fluid Mechanics*, 561, 147-80.

[78]. Grass, A. J., Raven, P. W. J., Stuart, R. J., and Bray, J. A., (1984), "Influence of Boundary Layer Velocity Gradients and Bed Proximity on Vortex Shedding from Free Spanning Pipelines," *Journal of Energy Resources Technology, Transactions of the ASME*, 106(1), 70-78.

[79]. Griffin, O. M., and Ramberg, S. E., (1974), "Vortex-Street Wakes of Vibrating Cylinders," *Journal of Fluid Mechanics*, 66(Part 3), 553-576.

[80]. Griffin, O. M., Skop, R. A., and Ramberg, S. E., (1975), "The Resonant Vortex-Excited Vibrations of Structures and Cable Systems," *Offshore Technology Conference*.

[81]. Gu, W., Chyu, C., and Rockwell, D., (1994), "Timing of Vortex Formation from an Oscillating Cylinder," *Physics of Fluids*, 6(11), 3677-3682.

[82]. Guilmineau, E., and Queutey, P., (2002), "Numerical Simulation of Vortex Shedding from an Oscillating Circular Cylinder," *Journal of Fluids and Structures*, 16, 773-794.

[83]. Hammache, M., and Gharib, M., (1989), "A Novel Method to Promote Parallel Vortex Shedding in the Wake of Circular-Cylinders," *Physics of Fluids a-Fluid Dynamics*, 1(10), 1611-1614.

[84]. Hammache, M., and Gharib, M., (1991), "An Experimental-Study of the Parallel and Oblique Vortex Shedding from Circular-Cylinders," *Journal of Fluid Mechanics*, 232, 567-590.

[85]. He, C., Long, T., Xin, M., and Chung, B. T. F., (2002), "An Experimental Investigation of Flow Past a Circular Cylinder with Rectangular Strips," *American Society of Mechanical Engineers, Heat Transfer Division*, 59-63.

[86]. Higuchi, H., Farell, C., and Kim, H. J., (1989a), "On Flow Separation and Reattachment around a Circular Cylinder at Critical Reynolds Numbers," *Journal of Fluid Mechanics*, 200, 149-171.

[87]. Higuchi, H., Kim, H. J., and Farell, C., (1989b), "On Flow Separation and Reattachment around a Circular Cylinder at Critical Reynolds Numbers," *Journal of Fluid Mechanics*, 200, 149-171.

[88]. Hover, F. S., Davis, J. T., and Triantafyllou, M. S., (2004), "Three-Dimensionality of Mode Transition in Vortex-Induced Vibrations of a Circular Cylinder," *European Journal of Mechanics, B/Fluids*, 23(1), 29-40.

[89]. Hover, F. S., Techet, A. H., and Triantafyllou, M. S., (1998), "Forces on Oscillating Uniform and Tapered Cylinders in Crossflow," *Journal of Fluid Mechanics*, 363, 97-114.

[90]. Hoyt, J. W., and Sellin, R. H. J., (2000), "A Comparison of Tracer and Piv Results in Visualizing Water Flow around a Cylinder Close to the Free Surface," *Experiments in Fluids*, 28(3), 261-265.

[91]. Huang, R. F., Chen, J. M., and Hsu, C. M., (2006), "Modulation of Surface Flow and Vortex Shedding of a Circular Cylinder in the Subcritical Regime by a Self-Excited Vibrating Rod," *Journal of Fluid Mechanics*, 555, 321-352.

[92]. Huerre, P., and Monkewitz, P. A., (1990), "Local and Global Instabilities in Spatially Developing Flows," *Annual Review of Fluid Mechanics*, 22, 473-537.

[93]. Energy Statistics, Data and Analysis, http://www.eia.doe.gov/emeu/international/contents.html

[94]. Igarashi, T., (1985), "Effect of Vortex Generators on the Flow around a Circular-Cylinder Normal to an Airstream," *Bulletin of the Jsme-Japan Society of Mechanical Engineers*, 28(236), 274-282.

[95]. Igarashi, T., (1986), "Effect of Tripping Wires on the Flow around a Circular-Cylinder Normal to an Airstream," *Bulletin of the JSME*, 29(255), 2917-2924.

[96]. Jacobsen, V., Bryndum, M. B., and Nielson, R., (1984), "Cross-Flow Vibrations of a Pipe Close to a Rigid Boundary," *Journal of Energy Resources Technology*, 106, 451-457.

[97]. Jauvtis, N., and Williamson, C. H. K., (2002), "Vortex-Induced Vibration of a Cylinder in Two Degrees of Freedom," *Conference on Bluff Body Wakes and Vortex-Induced Vibrations (BBVIV3) (4P)*.

[98]. Jauvtis, N., and Williamson, C. H. K., (2003), "Vortex-Induced Vibration of a Cylinder with Two Degrees of Freedom," *Journal of Fluids and Structures*, 17(7), 1035-1042.

[99]. Jauvtis, N., and Williamson, C. H. K., (2004), "The Effect of Two Degrees of Freedom on Vortex-Induced Vibration at Low Mass and Damping," *Journal of Fluid Mechanics*, 509, 23-62.

[100]. Keefe, R. T., (1962), "Investigation of the Fluctuating Forces on a Stationary Circular Cylinder in a Subsonic Stream and of the Associated Sound Field," *The Journal of the Acoustical Society of America*, 34, 1711-1714.

[101]. Khalak, A., and Williamson, C. H. K., (1996), "Dynamics of a Hydroelastic Cylinder with Very Low Mass and Damping," *Journal of Fluids and Structures*, 10(5), 455-472.

[102]. Khalak, A., and Williamson, C. H. K., (1997a), "Fluid Forces and Dynamics of a Hydroelastic Structure with Very Low Mass and Damping," *Journal of Fluids and Structures*, 11(8), 973-982.

[103]. Khalak, A., and Williamson, C. H. K., (1997b), "Investigation of Relative Effects of Mass and Damping in Vortex-Induced Vibration of a Circular Cylinder," *Journal of Wind Engineering and Industrial Aerodynamics*, 69-71, 341-350.

[104]. Khalak, A., and Williamson, C. H. K., (1999), "Motions, Forces and Mode Transitions in Vortex-Induced Vibrations at Low Mass-Damping," *Journal of Fluids and Structures*, 13(7-8), 813-851.

[105]. Klamo, J. T., (2006), "Effects of Damping and Reynolds Number on Vortex-Induced Vibrations," Ph.D thesis, California Institute of Technology.

[106]. Klamo, J. T., Leonard, A., and Roshko, A., (2005), "On the Maximum Amplitude for a Freely Vibrating Cylinder in Cross-Flow," *Journal of Fluids and Structures*, 21(4), 429-434.

[107]. Klamo, J. T., Leonard, A., and Roshko, A., (2006), "The Effects of Damping on the Amplitude and Frequency Response of a Freely Vibrating Cylinder in Cross-Flow," *Journal of Fluids and Structures*, 22(6-7), 845-856.

[108]. Koopmann, G. H., (1967), "On the Wind-Induced Vibrations of Circular Cylinders," M.S. thesis, Catholic University of America.

[109]. Krishnamoorthy, S., Price, S. J., and Paidoussis, M. P., (2001), "Cross-Flow Past an Oscillating Circular Cylinder: Synchronization Phenomena in the near Wake," *Journal of Fluids and Structures*, 15(7), 955-980.

[110]. Lashkov, I. A., Sokolova, I. N., and Shumilkina, E. A., (1992), "Jet Flow on Ribbed Curved Surfaces," *Rossiiskaia Akademiia Nauk Izvestiia Mekhanika Zhidkosti i Gaza*, 1, 177-179.

[111]. Lei, C., Cheng, L., and Kavanagh, K., (1999), "Re-Examination of the Effect of a Plane Boundary on Force and Vortex Shedding of a Circular Cylinder," *Journal of Wind Engineering and Industrial Aerodynamics*, 80(3), 263-286.

[112]. Liao, J. C., Beal, D. N., Lauder, G. V., and Triantafyllou, M. S., (2003a), "Fish Exploiting Vortices Decrease Muscle Activity," *Science*, 302(5650), 1566-1569.

[113]. Liao, J. C., Beal, D. N., Lauder, G. V., and Triantafyllou, M. S., (2003b), "The Karman Gait: Novel Body Kinematics of Rainbow Trout Swimming in a Vortex Street," *Journal of Experimental Biology*, 206(6), 1059-1073.

[114]. Lin, J. C., and Rockwell, D., (1999), "Horizontal Oscillations of a Cylinder beneath a Free Surface: Vortex Formation and Loading," *Journal of Fluid Mechanics*, 389, 1-26.

[115]. Lin, J. C., Sheridan, J., and Rockwell, D., (1996), "Near-Wake of a Perturbed, Horizontal Cylinder at a Free-Surface," *Physics of Fluids*, 8(8), 2107-2116.

[116]. Lin, J. C., Towfighi, J., and Rockwell, D., (1995), "Instantaneous Structure of the near-Wake of a Circular Cylinder: On the Effect of Reynolds Number," *Journal of Fluids and Structures*, 9(4), 409-418.

[117]. Lo, K. W., and Ko, N. W. M., (2001), "At the Upper Transition of Subcritical Regime of a Circular Cylinder," *Journal of Fluids Engineering*, 123, 422-434.

[118]. Lu, X. Y., and Dalton, C., (1996), "Calculation of the Timing of Vortex Formation from an Oscillating Cylinder," *Journal of Fluids and Structures*, 10(5), 527-541.

[119]. Lundgren, T., and Koumoutsakos, P., (1999), "On the Generation of Vorticity at a Free Surface," *Journal of Fluid Mechanics*, 382, 351-366.

[120]. Maekawa, T., and Mizuno, S., (1967), "Flow around Separation Point and in near-Wake of a Circular Cylinder," *Physics of Fluids*, 10(9p2), S184-&.

[121]. Maki, K. J., (2005), "Transom Stern Hydrodynamics," Ph.D thesis, University of Michigan, Ann Arbor.

[122]. Marine Turbines, http://www.marineturbines.com/home.htm

[123]. Mei, V. C., and Currie, I. G., (1969), "Flow Separation on a Vibrating Circular Cylinder," *Physics of Fluids*, 12(11), 2248-2254.

[124]. Meneghini, J. R., and Bearman, P. W., (1993), "Numerical Simulation of High Amplitude Oscillatory-Flow About on a Circular Cylinder Using a Discrete Vortex Method," *Proc. AIAA Shear Flow Conference*, 1-11.

[125]. Meneghini, J. R., and Bearman, P. W., (1995), "Numerical Simulation of High Amplitude Oscillatory Flow About a Circular Cylinder," *Journal of Fluids & Structures*, 9(4), 435-455.

[126]. Miyata, H., Shikazono, N., and Kanai, M., (1990), "Forces on a Circular Cylinder Advancing Steadily beneath the Free-Surface," *Ocean Engineering*, 17(1-2), 81-104.

[127]. Moe, G., Holden, K., and Yrrervoll, P. O., (1994), "Motion of Spring Supported Cylinders in Subcritical and Critical Water Flows," *Proceedings of the International Offshore and Polar Engineering Conference*, 3, 468-475.

[128]. Moe, G., and Overvik, T., (1982), "Current-Induced Motions of Multiple Risers," *Behaviour of Off-Shore Structures*, 618-639.

[129]. Moe, G., and Wu, Z. J., (1990), "The Lift Force on a Cylinder Vibrating in a Current," *Journal Offshore Mechanics and Arctic Engineering*, 112, 297-303.

[130]. Morison, J. R., O'Brien, M. P., Johnson, J. W., and Schaaf, S. A., (1950), "The Force Exerted by Surface Waves on Piles," *Petroleum Transactions*, 189, 149-154.

[131]. Morkovin, M. V., (1969), "Critical Evaluation of Transition from Laminar to Turbulent Shear Layers with Emphasis on Hypersonically Travelling Bodies," *Critical Evaluation of Transition from Laminar to Turbulent Shear Layers with Emphasis on Hypersonically Traveling Bodies*, 68-149.

[132]. Morkovin, M. V., (1990), "On Roughness-Induced Transition: Facts, Views, and Speculations," *Instability and Transition*, 1, 281-295.

[133]. MPSC, (2005), "Capacity Needs Forum Status Report," *U-14231* Michigan Public Service Commission

[134]. Nakamura, H., and Igarashi, T., (2004), "Variation of Nusselt Number with Flow Regimes Behind a Circular Cylinder for Reynolds Numbers from 70 to 30000," *International Journal of Heat and Mass Transfer*, 47(23), 5169-5173.

[135]. Nakamura, Y., and Tomonari, Y., (1982), "Effects of Surface Roughness on the Flow Past Circular Cylinders at High Reynolds Numbers," *Journal of Fluid Mechanics*, 123, 363-378.

[136]. Nakayama, Y., Boucher, R. F., and Knovel (Firm), (2000), *Introduction to Fluid Mechanics*, Butterworth-Heinemann, Oxford [England] ; Woburn, Mass.

[137]. Naumann, A., Morsbach, M., and Kramer, C., (1966), "The Conditions of Separation and Vortex Formation Past Cylinders," *NATO AGARD Conference Proceedings in Separated Flow*.

[138]. Niemann, H. J., and Hoelscher, N., (1990), "Review of Recent Experiments on the Flow Past Circular Cylinders," *Journal of Wind Engineering and Industrial Aerodynamics*, 33(1-2), 197-209.

[139]. Nikuradse, J., (1933), "Laws for Flows in Rough Pipes," *VDI-Forchungsheft 361*, 4, 4.

[140]. Nishimura, H., and Taniike, Y., (2001), "Aerodynamic Characteristics of Fluctuating Forces on a Circular Cylinder," *Journal of Wind Engineering and Industrial Aerodynamics*, 89(7-8), 713-723.

[141]. Nishino, T., Roberts, G. T., and Zhang, X., (2007), "Vortex Shedding from a Circular Cylinder near a Moving Ground," *Physics of Fluids*, 19(2), -.

[142]. Norberg, C., (1987), "Effect of Reynolds Number and a Low-Intensity Freestream Turbulence on the Flow around a Circular Cylinder," The Department of Applied Thermodynamics and Fluid Mechanics, Chalmers University, Goteborg, Sweden

[143]. Norberg, C., (1994), "Experimental Investigation of the Flow around a Circular Cylinder: Influence of Aspect Ratio," *Journal of Fluid Mechanics*, 258, 287-316.

[144]. Norberg, C., (2001), "Flow around a Circular Cylinder: Aspects of Fluctuating Lift," *Journal of Fluids and Structures*, 15(3-4), 459-469.

[145]. Norberg, C., (2003), "Fluctuating Lift on a Circular Cylinder: Review and New Measurements," *Journal of Fluids and Structures*, 17(1), 57-96.

[146]. Norberg, C., and Sunden, B., (1987), "Turbulence and Reynolds Number Effects on the Flow and Fluid Forces on a Single Cylinder in Cross Flow," *Journal of Fluids and Structures*, 1(3), 337-357.

[147]. Novak, M., and Tanaka, H., (1975), "Pressure Correlations on a Vibrating Cylinder," *Proceedings of the 4th International Conference on Wind Effects on Buildings and Structures*, 227-232.

[148]. Okajima, A., Nakamura, A., Kosugi, T., and Uchida, H., (2002), "Flow-Induced in-Line Oscillation of a Circular Cylinder," *Conference on Bluff Body Wakes and Vorlex-Induced Vibrations*.

[149]. Ongoren, A., and Rockwell, D., (1988a), "Flow Structure from an Oscillating Cylinder. Part 1. Mechanisms of Phase Shift and Recovery in the near Wake," *Journal of Fluid Mechanics*, 191, 197-223.

[150]. Ongoren, A., and Rockwell, D., (1988b), "Flow Structure from an Oscillating Cylinder. Part 2. Mode Competition in the near Wake," *Journal of Fluid Mechanics*, 191, 225-245.

[151]. OPT, "Ocean Power Technology, Http://Www.Oceanpowertechnologies.Com."

[152]. Testimony to the Us Congress, Http://Epw.Senate.Gov/107th/Tay_0530.Htm,

[153]. Owen, J. C., Bearman, P. W., and Szewczyk, A. A., (2001), "Passive Control of VIV with Drag Reduction," *Journal of Fluids and Structures*, 15(3-4), 597-605.

[154]. Pelamis, "Pelamis, Ocean Power Delivery."

[155]. Pfeil, H., and Orth, U., (1990), "Boundary-Layer Transition on a Cylinder with and without Separation Bubbles," *Experiments in Fluids*, 10(1), 23-32.

[156]. Pontes, M. T., and Falcao, A., (2001), "Ocean Energies: Resources and Utilization," *Proceedings of 18th WEC Congress*, Buenos Aires.

[157]. Prandtl, L., and Tietjens, O. G., (1957), *Fundamentals of Hydro and Aeromechanics*, Dover Publications.

[158]. Prasad, A., and Williamson, C. H. K., (1997), "The Instability of the Shear Layer Separating from a Bluff Body," *Journal of Fluid Mechanics*, 333, 375-402.

[159]. Price, S. J., Sumner, D., Smith, J. G., Leong, K., and Paidoussis, M. P., (2002), "Flow Visualization around a Circular Cylinder near to a Plane Wall," *Journal of Fluids and Structures*, 16(2), 175-191.

[160]. Raghavan, K., Bernitsas, M. M., and Maroulis, D., (2007a), "Effect of Bottom Boundary on VIV for Energy Harnessing at 8×10^3 <Re< 1.5×10^5 " *Proceedings of the International Conference on Offshore Mechanics and Arctic Engineering - OMAE* San Diego.

[161]. Raghavan, K., Bernitsas, M. M., and Maroulis, D., (2007b), "Effect of Reynolds Number on Vortex Induced Vibrations," *IUTAM Symposium*, Hamburg, Germany.

[162]. Ramberg, S. E., and Griffin, O. M., (1976), "Velocity Correlation and Vortex Spacing in Wake of a Vibrating Cable," *Journal of Fluids Engineering-Transactions of the ASME*, 98(1), 10-18.

[163]. Reichl, P., Hourigan, K., and Thompson, M., (2003a), "The Unsteady Wake of a Circular Cylinder near a Free Surface," *Flow, Turbulence and Combustion*, V71(1), 347-359.

[164]. Reichl, P., Hourigan, K., and Thompson, M., (2003b), "The Unsteady Wake of a Circular Cylinder near a Free Surface," *Flow Turbulence and Combustion*, 71(1-4), 347-359.

[165]. Reichl, P., Hourigan, K., and Thompson, M. C., (2005), "Flow Past a Cylinder Close to a Free Surface," *Journal of Fluid Mechanics*, 533, 269-296.

[166]. Reichl, P. J., (2001), "Flow Past a Cylinder Close to a Free Surface. ," Ph.D. thesis, Monash University.

[167]. Rood, E. P., (1995), "Free Surface Vorticity," Fluid Vortices (Fluid Mechanics and Its Applications) S. I. Green, ed., Springer.

[168]. Roshko, A., (1954), "On the Development of Turbulent Wakes from Vortex Streets," *NACA Report 1191*.

[169]. Roshko, A., (1961), "Experiments on the Flow Past a Circular Cylinder at Very High Reynolds Number," *Journal of Fluid Mechanics*, 10(3), 345-356.

[170]. Roshko, A., and Fiszdon, W., (1969), "On the Persistence of Transition in near Wake. ," Problems of Hydrodynamics and Continuum Mechanics.

[171]. Roshko, A., Steinolfson, A., and Chattoorgoon, V., (1975), "Flow Forces on a Cylinder near a Wall or near Another Cylinder," *Proceedings of the 2nd National Conference on Wind Engineering Research*.

[172]. Sadeh, W. Z., and Saharon, D. B., (1982), "Turbulence Effect on Crossflow around a Circular Cylinder at Subcritical Reynolds Numbers," NASA, Washington, D.C.

[173]. Sadeh, W. Z., Sutera, S. P., and Maeder, P. F., (1970), "Investigation of Vorticity Amplification in Stagnation Flow," *Zeitschrift Fur Angewandte Mathematik Und Physik*, 21(5), 717-&.

[174]. Saelim, N., (2003), "Flow Past a Cylinder: Effect of Surface Modification on Structure of the near-Wake " Ph. D thesis, Lehigh University.

[175]. Sainsbury, R. N., and King, D., (1971), "The Flow Induced Oscillation of Marine Structures," *Proceedings of Institute of Civil Engineering*, 269-302.

[176]. Sarpkaya, T., (1978), "Fluid Forces on Oscillating Cylinders," *Journal of Waterway Port Coastal Ocean Division*, 104(4), 275-290.

[177]. Sarpkaya, T., (1979), "Vortex-Induced Oscillations: A Selective Review," *Journal of Applied Mechanics*, 46(2), 241-258.

[178]. Sarpkaya, T., (1995), "Hydrodynamic Damping, Flow-Induced Oscillations, and Biharmonic Response," *Journal of Offshore Mechanics and Arctic Engineering*, 117(4), 232-238.

[179]. Sarpkaya, T., (2004), "A Critical Review of the Intrinsic Nature of Vortex-Induced Vibrations," *Journal of Fluids and Structures*, 19(4), 389-447.

[180]. Schewe, G., (2001), "Reynolds-Number Effects in Flow around More-or-Less Bluff Bodies," *Journal of Wind Engineering and Industrial Aerodynamics*, 89(14-15), 1267-1289.

[181]. Schiller, L., and Linke, W., (1933), "Pressure and Frictional Resistance of a Cylinder at Reynolds Numbers 5000 to 40000," National Advisory Committee Aeronautics, Technical Memorandum.

[182]. Schlichting, H., (1979), *Boundary Layer Theory: Seventh Edition*.

[183]. Sheridan, J., Carberry, J., Lin, J. C., and Rockwell, D., (1998), "On the near-Wake Topology of an Oscillating Cylinder," *Journal of Fluids and Structures*, 12(2), 215-220.

[184]. Sheridan, J., Lin, J. C., and Rockwell, D., (1995), "Metastable States of a Cylinder Wake Adjacent to a Free Surface," *Physics of Fluids*, 7(9), 2099-2101.

[185]. Sheridan, J., Lin, J. C., and Rockwell, D., (1997), "Flow Past a Cylinder Close to a Free Surface," *Journal of Fluid Mechanics*, 330, 1-30.

[186]. Singh, S. P., and Mittal, S., (2005), "Vortex-Induced Oscillations at Low Reynolds Numbers: Hysteresis and Vortex-Shedding Modes," *Journal of Fluids and Structures*, 20(8), 1085-1104.

[187]. Stansby, P. K., (1974), "The Effects of End Plates on the Base Pressure Coefficient of a Circular Cylinder," *Aeronautical Journal*, 78 , 757.

[188]. Stuart, J. T., (1971), "Nonlinear Stability Theory," *Annual Review of Fluid Mechanics*, 3, 347-&.

[189]. Sugimoto, T., Saito, S., Matsuda, K., Okajima, A., Kiwata, T., and Kosugi, T., (2002), "Water Tunnel Experiments on in-Line Oscillation of a Circular Cylinder with a Finite Span Length," *Conference on Bluff Body Wakes and Vortex-Induced Vibrations*.

[190]. Sumer, B. M., and Fredsoe, J., (1997), *Hydrodynamics around Cylindrical Structures*, World Scientific Pub Co Inc

[191]. Sumer, B. M., and Fredsøe, J., (1997), "Hydrodynamics around Cylindrical Structures," *Hydrodynamics Around Cylindrical Structures*.

[192]. Szepessy, S., (1993), "On the Control of Circular Cylinder Flow by End Plates," *European Journal of Mechanics B/Fluids*, 12(2), 217-244.

[193]. Szepessy, S., and Bearman, P. W., (1992), "Aspect Ratio and End Plate Effects on Vortex Shedding from a Circular Cylinder," *Journal of Fluid Mechanics*, 234, 191-217.

[194]. Szepessy, S., and Bearman, P. W., (1993), "Analysis of a Pressure Averaging Device for Measuring Aerodynamic Forces on a Circular Cylinder," *Experiments in Fluids*, 16, 120-128.

[195]. Taneda, S., (1965), "Experimental Investigation of Vortex Streets," *Journal of the Physical Society of Japan*, 20(9), 1714-1721.

[196]. Tani, I., (1969), "Boundary-Layer Transition," *Annual Review of Fluid Mechanics*, 1(1), 169-196.

[197]. Tanida, Y., Okajima, A., and Watanabe, Y., (1973), "Stability of a Circular Cylinder Oscillating in Uniform Flow or in a Wake," *Journal of Fluid Mechanics*, 61(4), 769-784.

[198]. Taniguchi, S., and Miyakoshi, K., (1990), "Fluctuating Fluid Forces Acting on a Circular-Cylinder and Interference with a Plane Wall - Effects of Boundary-Layer Thickness," *Experiments in Fluids*, 9(4), 197-204.

[199]. Techet, A. H., Hover, F. S., and Triantafyllou, M. S., (1998), "Vortical Patterns Behind a Tapered Cylinder Oscillating Transversely to a Uniform Flow," *Journal of Fluid Mechanics*, 363, 79-96.

[200]. Technomare, (1996), "Wave Energy Project Results: The Exploitation of Tidal Marine Currents."

[201]. Thorpe, T. W., (1998), ""An Overview of Wave Energy Technologies"," *An Overview of Wave Energy Technologies*.

[202]. Toebes, G. H., (1969), "The Unsteady Flow and Wake near an Oscillating Cylinder," *ASME Journal of Basic Engineering*, 91, 493-505.

[203]. Triantafyllou, G. S., and Dimas, A. A., (1989), "Interaction of Two-Dimensional Separated Flows with a Free Surface at Low Froude Numbers," *Phys. Fluids A*, 1(11), 1813-1821.

[204]. Triantafyllou, G. S., Triantafyllou, M. S., and Chryssostomidis, C., (1986), "On the Formation of Vortex Streets Behind Stationary Cylinders," *Journal of Fluid Mechanics*, 170, 461-477.

[205]. Triantafyllou, M. S., Dahl, J. M., and Hover, F. S., (2006), "Two-Degree-of-Freedom Vortex-Induced Vibrations Using a Force Assisted Apparatus," *Journal of Fluids and Structures*, 22(6-7), 807-18.

[206]. Tsahalis, D. T., and Jones, W. T., (1981), "Vortex-Induced Vibrations of a Flexible Cylinder near a Plane Boundary in Steady Flow," *Proceedings - Annual Offshore Technology Conference*, 1, 367-381.

[207]. Unal, M. F., and Rockwell, D., (1988a), "On Vortex Formation from a Cylinder .2. Control by Splitter-Plate Interference," *Journal of Fluid Mechanics*, 190, 513-529.

[208]. Unal, M. F., and Rockwell, D., (1988b), "On Vortex Formation from a Cylinder. Part 1. The Initial Instability," *Journal of Fluid Mechanics*, 190, 491-512.

[209]. United States Patent Office (Uspto), http://www.uspto.gov/

[210]. Vikestad, K., (1998), "Multi-Frequency Response of a Cylinder Subjected to Vortex Shedding and Support Motions," Ph.D thesis, NTNU, Norway.

[211]. Vikestad, K., Vandiver, J. K., and Larsen, C. M., (2000), "Added Mass and Oscillation Frequency for a Circular Cylinder Subjected to Vortex-Induced Vibrations and External Disturbance," *Journal of Fluids and Structures*, 14(7), 1071-1088.

[212]. Walker, D. T., Lyzenga, D. R., Ericson, E. A., and Lund, D. E., (1996), "Radar Backscatter and Surface Roughness Measurements for Stationary Breaking Waves," *Proceedings of the Royal Society - Mathematical, Physical and Engineering Sciences (Series A)*, 452(1952), 1953-1984.

[213]. WaveNet, (2003), "Results from the Work of the European Thematic Network on Wave Energy," Eurpean Community.

[214]. WEC, (2001), "Survey of Energy Resources," World Energy Council, London.

[215]. Wei, T., and Smith, C. R., (1986), "Secondary Vortices in the Wake of Circular Cylinders," *Journal of Fluid Mechanics*, 169 , Aug. 1986, 513-533.

[216]. West, G. S., and Apelt, C. J., (1982), "Effects of Tunnel Blockage and Aspect Ratio on the Mean Flow Past a Circular Cylinder with Reynolds Numbers between 10^4 and 10^5

[217]. " *Journal of Fluid Mechanics*, 114, 361-377.

[218]. White, F. M., (1974), *Viscous Fluid Flow.* , McGraw-Hill, New York.

[219]. Williamson, C. H. K., (1985), "Sinusoidal Flow Relative to Circular Cylinders," *Journal of Fluid Mechanics*, 155, 141-174.

[220]. Williamson, C. H. K., (1989), "Oblique and Parallel Modes of Vortex Shedding in the Wake of a Circular Cylinder at Low Reynolds Numbers," *Journal of Fluid Mechanics*, 206, 579-627.

[221]. Williamson, C. H. K., (1996), "Vortex Dynamics in the Cylinder Wake," *Annual Review of Fluid Mechanics*, 28, 477-539.

[222]. Williamson, C. H. K., and Govardhan, R., (2004), "Vortex-Induced Vibrations," *Annual review of fluid mechanics. Vol.36 2004*, 413-55.

[223]. Williamson, C. H. K., and Jauvtis, N., (2004), "A High-Amplitude 2t Mode of Vortex-Induced Vibration for a Light Body in Xy Motion," *European Journal of Mechanics, B/Fluids*, 23, 107-114.

[224]. Williamson, C. H. K., and Roshko, A., (1988), "Vortex Formation in the Wake of an Oscillating Cylinder," *Journal of Fluids and Structures*, 2(4 , Jul. 1988), 355-381.

[225]. WMCE, (2003), "Ocean Enegy Systems, Status and Research and Development Priorities ".

[226]. Wu, J., Sheridan, J., Welsh, M. C., and Hourigan, K., (1996), "Three-Dimensional Vortex Structures in a Cylinder Wake," *Journal of Fluid Mechanics*, 312, 201-222.

[227]. Yang, B., Gao, F. P., Wu, Y. X., and Li, D. H., (2006), "Experimental Study on Vortex-Induced Vibrations of Submarine Pipeline near Seabed Boundary in Ocean Currents," *China Ocean Engineering*, 20(1), 113-121.

[228]. Yokoi, Y., and Kamemoto, K., (1992), "Initial Stage of a Three-Dimensional Vortex Structure Existing in a Two-Dimensional Boundary Layer Separation Flow. (Observation of Laminar Boundary Layer Separation over a Circular Cylinder by Flow Visualization)," *JSME International Journal, Series 2: Fluids Engineering, Heat Transfer, Power, Combustion, Thermophysical Properties*, 35(2), 189-195.

[229]. Yokoi, Y., and Kamemoto, K., (1993), "Initial Stage of a Three-Dimensional Vortex Structure Existing in a Two-Dimensional Boundary Layer Separation Flow (Visual Observation of Laminar Boundary Layer Separation over a Circular Cylinder from the Side of a Separated Region)," *JSME International Journal, Series B: Fluids and Thermal Engineering*, 36(2), 201-206.

[230]. Yoshitake, Y., Sueoka, A., Yamasaki, M., Sugimura, Y., and Ohishi, T., (2004), "Quenching of Vortex-Induced Vibrations of Towering Structure and Generation of Electricity Using Hula-Hoops," *Journal of Sound and Vibration*, 272(1-2), 21-38.

[231]. Zdravkovich, M. M., (1981), "Review and Classification of Various Aerodynamic and Hydrodynamic Means for Suppressing Vortex Shedding," *Journal of Wind Engineering and Industrial Aerodynamics*, 7(2), 145-189.

[232]. Zdravkovich, M. M., (1982), "Modification of Vortex Shedding in the Synchronization Range," *American Society of Mechanical Engineers*, 104, 513-517.

[233]. Zdravkovich, M. M., (1985), "Forces on a Circular-Cylinder near a Plane Wall," *Applied Ocean Research*, 7(4), 197-201.

[234]. Zdravkovich, M. M., (1990a), "Conceptual Overview of Laminar and Turbulent Flows Past Smooth and Rough Circular-Cylinders," *Journal of Wind Engineering and Industrial Aerodynamics*, 33(1-2), 53-62.

[235]. Zdravkovich, M. M., (1990b), "On Origins of Hysteretic Responses of a Circular-Cylinder Induced by Vortex Shedding," *Zeitschrift Fur Flugwissenschaften Und Weltraumforschung*, 14(1-2), 47-58.

[236]. Zdravkovich, M. M., (1997), *Flow around Circular Cylinders Volume 1: Fundamentals*, Oxford Science Publications.

[237]. Zhu, Q., Lin, J. C., Unal, M. F., and Rockwell, D., (2000), "Motion of a Cylinder Adjacent to a Free-Surface: Flow Patterns and Loading," *Experiments in Fluids*, 28(2-6), 559-575.

[238]. Ziada, S., Jebodhsingh, D., Weaver, D. S., and Eisinger, F. L., (2005), "The Effect of Fins on Vortex Shedding from a Cylinder in Cross-Flow," *Journal of Fluids and Structures*, 21(5-7 SPEC. ISS.), 689-705.